NUMERICAL AND EXPERIMENTAL INVESTIGATIONS OF BLOOD FLOW WITH APPLICATION TO VASCULAR BYPASS SURGERIES

A DISSERTATION

SUBMITTED TO THE DEPARTMENT OF ELECTRICAL ENGINEERING

AND THE COMMITTEE ON GRADUATE STUDIES

OF STANFORD UNIVERSITY

IN PARTIAL FULFILLMENT OF THE REQUIREMENTS

FOR THE DEGREE OF

DOCTOR OF PHILOSOPHY

Joy Paochi Ku

December 2003

© Copyright by Joy Paochi Ku 2004
All Rights Reserved

I certify that I have read this dissertation and that, in my opinion, it is fully adequate in scope and quality as dissertation for the degree of Doctor of Philosophy.

Charles A. Taylor (Principal Advisor)
Assistant Professor of Mechanical Engineering and Surgery

I certify that I have read this dissertation and that, in my opinion, it is fully adequate in scope and quality as dissertation for the degree of Doctor of Philosophy.

Dwight G. Nishimura (Co-Advisor)
Associate Professor of Electrical Engineering

I certify that I have read this dissertation and that, in my opinion, it is fully adequate in scope and quality as dissertation for the degree of Doctor of Philosophy.

Norbert J. Pelc
Professor of Radiology

I certify that I have read this dissertation and that, in my opinion, it is fully adequate in scope and quality as dissertation for the degree of Doctor of Philosophy.

Christopher K. Zarins
Professor of Surgery

Approved for the University Committee on Graduate Studies:

Abstract

In planning operations for patients with cardiovascular disease, vascular surgeons rely on their training, past experiences with patients with similar conditions, and diagnostic imaging data. However, variability in patient anatomy and physiology makes it difficult to quantitatively predict the surgical outcome for a specific patient *a priori*. A simulation-based medical planning system that utilizes three-dimensional finite element analysis (3D FEA) methods and patient-specific anatomic and physiologic information to predict changes in blood flow distribution and flow patterns resulting from surgical bypass procedures has been developed. However, in order to apply these computational methods, their accuracy must first be determined.

In this dissertation, velocity and flow measurements acquired with phase contrast magnetic resonance imaging (PC-MRI) techniques were compared against those predicted using the 3D FEA methods for a bypass geometry. Studies were performed both in a phantom model of a stenosed vessel with a bypass graft and in pigs that had undergone thoraco-thoraco aortic bypass graft procedures.

The phantom experiments consisted of comparisons of flow rates and flow patterns at five distinct locations in the model and under both a lower and higher Reynolds number, thus examining a range of flow complexities not investigated by previous studies. These experiments highlighted the differences between PC-MRI and the 3D FEA methods and resulted in the development of post-processing steps critical for the fair comparison of results from the two techniques. They were also used to examine the sensitivity of the 3D FEA results to various input parameters, such as the geometric model.

The methods developed for the phantom experiments were applied to comparisons between the 3D FEA results and the PC-MRI data for the more challenging *in vivo* experiments. Flow distributions and flow patterns were modeled and compared against

PC-MRI measurements acquired at two locations in the porcine studies. These comparisons are the first *in vivo* investigations of these simulation methods for bypass surgery planning purposes and as such, they represent an important step towards this new paradigm in medicine.

Acknowledgments

I have been extremely fortunate to have had many amazing people be a part of my life during these seven years that I have been a graduate student here at Stanford. Without them, this Ph.D. would not have been possible, and certainly, would not have been as memorable.

My research advisor, Charles Taylor, has been one of my most ardent supporters. While few professors were willing to spend time and resources on a Master's student who wanted to work on a small research project in a one-year time frame, Charley did. Throughout my time here at Stanford, Charley has continued to provide both encouragement and guidance, whether it is deciding if I should continue in the Ph.D. program or how to overcome the frustration that is common to research. From Charley, I have also learned more than I ever wanted to know about finite element analysis.

I am also grateful to the rest of my committee members. My co-advisor, Dwight Nishimura, provided helpful suggestions for my research and first introduced me to MR. Norbert Pelc has been indispensable to my research; his knowledge of MR combined with his good sense of humor and his patience made him an excellent person from whom to learn. Finally, I want to express my appreciation to Christopher Zarins for sharing his vast experiences in vascular surgery with me and for helping to plan the *in vivo* experiments.

The experiments described in this thesis required the assistance of numerous people, and I thank them for their help. Frank Arko, with his entertaining stories in the surgical suite, and Anthony Lee, who helped develop the original protocol for the *in vivo* experiments, were the surgeons for the *in vivo* experiments described here. Frandics Chan, Kris Wedding, and Michael Markl were the MR imaging gurus for these experiments and helped me work through many of the imaging problems we encountered. Anne Sawyer-Glover kept the MR system running smoothly, and Wendy Baumgardner

and Diane Howard assisted with the *in vivo* experiments. For the *in vitro* experiments, I want to recognize Chris Elkins for building a pump that actually works in the MR suite and for coming in at odd hours to run the experiments with me. I would also like to thank Ryan Wicker and Gilbert Palafox of the University of Texas El Paso for providing me with the phantom model that was used.

Running the experiments and collecting the data was only half of the work. Software was needed to process this data, and because this is research, a single commercial package did not exist that would do everything I wanted to do with the data. Over the years, I have used over a dozen different programs to process my data and generate and analyze my simulation results, and I want to thank all those who provided me with code and software help: Ken Wang, Tom Brosnan, David Parker, Sean Spicer, Andrew Fu, Dolf Van Der Heide, and Ken Jansen of Rensselaer Polytechnic Institute. In particular, I want to thank Nathan Wilson, who enhanced the primary software tool for my project, answered my many questions about programming in Tcl/Tk, and kept all the lab's computers up and running, even responding to computer SOS calls on the weekends! I also received help from Wendy Ong, Greg Chan, Valerie Favier, Ryan Spilker, and Bev Tang in processing these mega data sets.

The women of P224 have been wonderful colleagues and friends. Many, many thanks to Mary Draney, who was here when I first started at Stanford and who has helped me in every way imaginable—helping me run my experiments, answering MR questions, teaching me Adobe Photoshop tricks, helping me move. Brooke Steele sat next to me for most of my graduate school career and I will miss having her to bounce ideas off of and to share life's ups and downs. Mary O'Connell was a great source of encouragement (and of yoga mats and tennis shoes, too), and Joan Greve, with her enthusiasm and openness, has been a great role model. I also want to thank the rest of the Cardiovascular Biomechanics Research Lab members for sharing their knowledge and insights with me and for making this a fun place to work.

I also want to express my gratitude to all my friends, for they have helped keep balance in my life. In particular, I want to thank Maggie Tan, Mike Timbol, and Kevin Hwang for not disowning me for having "defected" from U.C. Berkeley to Stanford and

for reminding me about the important things in life. Cathy Chiu, Susan Houghton, and Jenny Liu have remained the best girlfriends despite the distance between us. And finally, I credit Ted Ko with jump starting my thesis writing with his crazy negative reinforcement scheme. His support and friendship have meant much to me during this past year.

Lastly, I want to recognize my family. Thanks to my sisters, Mary and Nancy, for listening, sharing, and along with Gooey, adding silliness and laughter to my life. My parents have influenced me in more ways than they can ever know, and I thank them for their love and support over all these years.

Financial support was provided by Hewlett-Packard through a Resident Fellowship, a NIST-ATP grant, the Ayers Foundation, the American Heart Association through a Western States Affiliate pre-doctoral fellowship, NIH grant P41RR09784, and the Lucas Foundation.

Table of Contents

1 Introduction 1

1.1 Cardiovascular Disease 1

1.2 Role of Hemodynamics in Bypass Graft Surgery 2

1.2.1 Bypass Graft Surgery Terminology 2

1.2.2 Surgery Planning 3

1.2.3 Bypass Graft Failures 4

1.2.4 Utilizing Hemodynamics to Increase the Effectiveness of Bypass Surgery 4

1.3 Magnetic Resonance Imaging 6

1.4 Computational Methods 7

1.4.1 Background 7

1.4.2 *In Vitro* Validation of Computational Methods 8

1.4.3 *In Vivo* Validations 10

1.5 Contributions 11

1.6 Organization 12

2 Investigating Hemodynamics 13

2.1 Hemodynamic Concepts 13

2.1.1 Fluid Properties 14

2.1.2 Fluid Energy 15

2.1.3 Wave Reflections 17

2.1.4 Flow Patterns 18

2.2 Magnetic Resonance Imaging 20

2.2.1 Magnetic Resonance Physics 20

2.2.2 Magnetic Resonance Angiography 23

2.2.3 Phase-Contrast Magnetic Resonance Imaging 27
2.3 Image-Based Modeling 42
2.3.1 Methods for Image-Based Geometric Models 43
2.3.2 Mesh Generation Techniques 45
2.3.3 Geodesic 46
2.4 Computational Hemodynamic Methods 55
2.4.1 Governing Equations 55
2.4.2 Finite Element Methodology 56
2.4.3 Spectrum™ Solver 58
3 Sensitivity of PC-MRI Measurements 61
3.1 Baseline Correction of PC-MRI Data 61
3.1.1 Method 62
3.1.2 Results and Discussion 64
3.1.3 Conclusion 69
3.2 Effect of Imaging Parameters on PC-MRI Measurements 70
3.2.1 Method 71
3.2.2 Results and Discussion 77
3.2.3 Conclusion 92
3.3 Temporal Smoothing of PC-MRI Data 93
3.3.1 Method 94
3.3.2 Results and Discussion 95
3.3.3 Conclusion 98
4 Low Flow *In Vitro* Experiment 100
4.1 Experimental Protocol 101
4.1.1 Experimental Set-Up 101
4.1.2 Data Acquisition 103
4.1.3 Numerical Simulations 106
4.2 Convergence Studies 108
4.3 Comparison Method 114
4.3.1 Spatial Averaging 119

4.3.2 Periodic Averaging 120
4.3.3 Conclusions 123
4.4 Numerical Simulation Results 124
4.4.1 Comparison to PC-MRI 124
4.4.2 Flow and Velocity Patterns 127
4.5 Limitations of Experimental Data 128
4.6 Sensitivity of Numerical Simulations 135
4.6.1 Effect of Geometric Model on Numerical Simulations 135
4.6.2 Effect of Inlet Velocities on Numerical Simulations 147
4.7 Discussion 151
4.8 Summary 155
5 High Flow *In Vitro* Experiment 156
5.1 Methods 157
5.1.1 Experimental Set-Up 157
5.1.2 Data Acquisition 159
5.1.3 Numerical Simulations 162
5.1.4 Post-Processing of the Numerical Simulations 164
5.2 Comparison of Numerical Simulation Results to PC-MRI 164
5.2.1 Comparison of Flows 164
5.2.2 Comparison of Velocity Patterns 166
5.3 Sensitivity of Experimental Data 173
5.4 Sensitivity of Numerical Simulations 176
5.4.1 Effect of Geometry on Numerical Simulations 176
5.4.2 Post-Processing Effects on the Numerical Simulations 185
5.5 Discussion 189
5.6 Summary 191
6 *In Vivo* Experiment 193
6.1 Experimental Protocol 194
6.1.1 Surgical Procedure 195
6.1.2 Magnetic Resonance Imaging 197

6.1.3 Pressure Measurements 200
6.2 Validation of Numerical Simulation Methods 202
6.2.1 Predicting Flow Rates and Flow Distributions 203
6.2.2 Predicting Velocity Patterns 215
6.2.3 Summary 227
6.3 Comparison of Physiology with Bypass Open and Closed 228
6.3.1 Methods 228
6.3.2 Physiologic Results 231
6.3.3 Sensitivity of Pressure Measurements 237
6.3.4 Discussion 238
6.3.5 Conclusion 240
7 Conclusions and Future Work 242
7.1 Contributions and Significance 242
7.2 Recommendations for Future Investigations 244
8 Appendix A: Effect of Repetition Time on Flow Measurements 247
9 Appendix B: Spectrum Input File 249
10 Appendix C: Physiology Observed With Open and Occluded Bypass Grafts 257
11 Bibliography 265

List of tables

Number *Page*

Table 4.1: Signal-to-noise ratios and theoretically computed standard deviations of velocities for the PC-MRI data for the low Reynolds number *in vitro* experiment 134

Table 5.1: Signal-to-noise ratios and theoretically computed standard deviations of velocities for the PC-MRI data for the high Reynolds number *in vitro* experiment 174

Table 6.1: Imaging parameters for segmented k-space PC-MRI data 197

Table 6.2: Imaging parameters for 2D cine PC-MRI data 198

Table 6.3: Velocity encodings for the 2D cine PC-MRI data 198

Table 6.4: Average baseline corrections applied to the PC-MRI images for the 4 slice planes for the eight pig experiments 208

Table 6.5: Inlet Reynolds numbers (Re) for the 8 pigs 209

Table 6.6: Theoretically computed standard deviations of flow measurements acquired with PC-MRI. 210

Table 6.7: List of factors to assess usability of data for comparisons between numerically computed and PC-MRI-acquired velocity patterns. 217

List of figures

Number *Page*

Figure 1.1: Example of a bypass graft. 2

Figure 1.2: Diagram of a bypass graft attached to a host artery with a stenosis. 3

Figure 2.1: Velocity profiles for different types of laminar flow. 18

Figure 2.2: Effect of magnetic fields on the magnetization vector. 21

Figure 2.3: Saturation of spins. 23

Figure 2.4: Maximum intensity projection images with and without grad warp correction. 26

Figure 2.5: Comparison of tube diameter with and without grad warp correction. 27

Figure 2.6: Cine PC-MRI sequence. 30

Figure 2.7: Segmented k-space sequence. 32

Figure 2.8: Effect of interpolation using the linear dilation model. 33

Figure 2.9: Underestimation of velocities due to slice plane angle. 35

Figure 2.10: Comparison of thresholding versus the level set method. 39

Figure 2.11: Process for creating geometric models. 47

Figure 2.12: Effect of paths on geometric model of vessel junction. 48

Figure 2.13: Effect of manually chosen points on resulting spline path. 49

Figure 2.14: Contours resampled with different number of points. 51

Figure 2.15: Effect of contour spacing on geometry. 51

Figure 2.16: Effect of contour alignment on a solid model. 52

Figure 2.17: Velocity mapping algorithm. 54

Figure 2.18: Staggered solution strategy employed by the Spectrum™ Solver. 58

Figure 3.1: Regions used in baseline correction experiment. 62

Figure 3.2: Average flow waveforms using different orders of baselining. 64

Figure 3.3: Comparison of flows using baseline correction functions computed

using different regions. 65
Figure 3.4: Comparison of zeroth order velocity correction functions based on different regions of interest. 66
Figure 3.5: Comparison of first order velocity correction functions based on different regions of interest. 67
Figure 3.6: Comparison of second order velocity correction functions based on different regions of interest. 68
Figure 3.7: Comparison of baseline correction functions for velocities in the anterior-posterior direction using different regions of interest 69
Figure 3.8: Straight rigid tube for testing effects of imaging parameters on PC-MRI measurements. 71
Figure 3.9: Experimental set-up for assessing the effect of imaging parameters on PC-MRI measurements. 72
Figure 3.10: Comparison of contours obtained from thresholding. 74
Figure 3.11: An average flow waveform based on approximately 20 cycles acquired with an ultrasonic flow probe. 76
Figure 3.12: Comparison of flows at different time points during the experiment studying the effect of the plane angle on PC-MRI velocity measurements. 76
Figure 3.13: Comparison of flows at the beginning and end of the experiment studying the effect of temporal resolution on the PC-MRI flow measurements. 77
Figure 3.14: Eight points used to examine the repeatability of velocity measurements acquired with PC-MRI 79
Figure 3.15: Repeated measurements of velocity using a segmented k-space sequence ..80
Figure 3.16: Repeated measurements of velocity using a cine sequence 81
Figure 3.17: Variability in through-plane velocity contours, as measured with a segmented k-space PC-MRI sequence 82
Figure 3.18: Variability in through-plane velocity contours, as measured with a cine PC-MRI sequence 83

Figure 3.19: Repeatability of flow measurements acquired with different PC-MRI sequences 84
Figure 3.20: Comparison of the average through-plane velocity acquired with a two-dimensional cine PC-MRI sequence for different angles between the prescribed plane and the tube axis 85
Figure 3.21: Comparison of the average through-plane velocity acquired with a segmented k-space PC-MRI sequence for different angles between the prescribed plane and the tube axis 86
Figure 3.22: Comparison of the average flows acquired with a two-dimensional cine PC-MRI sequence for different angles between the prescribed plane and the tube axis 87
Figure 3.23: Comparison of the average flows acquired with a segmented k-space PC-MRI sequence for different angles between the prescribed plane and the tube axis 88
Figure 3.24: Comparison of areas of region of interest for PC-MRI sequences for different plane angles. 89
Figure 3.25: Comparison of through-plane flows acquired with a cine PC-MRI sequence for 3 components of velocity and for 1 component of velocity 91
Figure 3.26: Comparison of through-plane flows measured with a segmented k-space PC-MRI sequence 92
Figure 3.27: Comparison of flow waveforms acquired using different PC-MRI sequences 93
Figure 3.28: Temporal smoothing of velocities for low Reynolds flow acquired with a cine, 3 components of velocity PC-MRI sequence 96
Figure 3.29: Temporal smoothing of velocities for high Reynolds flow acquired with a cine, 3 components of velocity PC-MRI sequence 97
Figure 3.30: Absolute differences in the velocity waveforms due to temporal smoothing under low Reynolds conditions 98
Figure 3.31: Absolute differences in the velocity waveforms due to temporal smoothing under high Reynolds conditions 98

Figure 4.1: Phantom model and imaging slice planes for the *in vitro* flow experiments 102
Figure 4.2: Diagram of the phantom model 103
Figure 4.3: Diagram of the experimental set-up for the low flow *in vitro* flow experiment 104
Figure 4.4: Example of the in-plane velocity components at the inlet (plane A) during peak flow 107
Figure 4.5: Comparison of flows through the (a) aorta (plane C) and (b) the graft (plane F) for simulations of different mesh sizes 109
Figure 4.6: Comparison of flows through the (a) aorta (plane C) and (b) the graft (plane F) for simulations run with a different number of time steps per cycle. 109
Figure 4.7: Comparison of through-plane velocity contours at the aorta proximal to the coarctation (plane C in Figure 4.1) for different mesh sizes 111
Figure 4.8: Comparison of through-plane velocity contours at the graft (plane F in Figure 4.1) for different mesh sizes 112
Figure 4.9: Comparison of through-plane velocity contours at the aorta distal to the bypass, also referred to as the outlet, (plane E in Figure 4.1) for different mesh sizes. 113
Figure 4.10: Comparison of through-plane velocity contours at the aorta proximal to the coarctation (plane C in Figure 4.1) for different number of time steps per cycle 114
Figure 4.11: Comparison of through-plane velocity contours at the graft (plane F in Figure 4.1) for different number of time steps per cycle 115
Figure 4.12: Comparison of through-plane velocity contours at the aorta distal to the bypass, also referred to as the outlet, (plane E in Figure 4.1) for different number of time steps per cycle 116
Figure 4.13: Comparison of the through-plane velocity simulation results at a given slice location versus averaged over 5 slices for the aorta distal to the coarctation (plane D) during late-deceleration 117

Figure 4.14: Comparison of the through-plane velocity simulation results at a given slice location versus averaged over 5 slices for the aorta distal to the coarctation (plane D) during peak flow 118
Figure 4.15: Periodicity is observed in the flow measurements through both the (a) proximal coarctation (plane C) and (b) the graft (plane F) for single cycle data, as well as for the data based on the average of 8 simulation cycles.....121
Figure 4.16: Periodicity is observed in the through-plane velocity contours in the aorta proximal to the coarctation (plane C) for both the single cycle data and for the data based on the average of 8 simulation cycles.....122
Figure 4.17: The through-plane velocities at the aorta distal to the bypass, also referred to as the outlet, (plane E) are not periodic for the single cycle data but are periodic for the data based on the average of 8 simulation cycles.....123
Figure 4.18: Velocity magnitudes as computed from the numerical simulations 125
Figure 4.19: Comparison between flows from PC-MRI and the numerical simulations (finite element analysis, FEA) at the (a) proximal coarctation (plane C), (b) graft (plane F), and (c) inlet (plane A). 126
Figure 4.20: Comparisons in the aorta proximal to the bypass graft, also referred to as the downstream inlet (plane B) location, of through-plane velocities computed numerically using finite element analysis (FEA) and those acquired with PC-MRI.....129
Figure 4.21: Comparisons in the aorta between the proximal anastomosis and the coarctation, also referred to as the proximal coarctation (plane C) location, of through-plane velocities computed numerically using finite element analysis (FEA) and those acquired with PC-MRI.....130
Figure 4.22: Comparisons at the distal coarctation (plane D) location of through-plane velocities computed numerically using finite element analysis (FEA) and those acquired with PC-MRI 131

Figure 4.23: Comparisons at the bypass graft (plane F) location of through-plane velocities computed numerically using finite element analysis (FEA) and those acquired with PC-MRI 132
Figure 4.24: Comparisons at the distal aorta, also referred to as the outlet (plane E), of through-plane velocities computed numerically using finite element analysis (FEA) and those acquired with PC-MRI.....133
Figure 4.25: Flow measurements acquired with an ultrasonic flow probe demonstrate the repeatability of the flow that was output by the pump.....134
Figure 4.26: Graphical user interface for analyzing the shape of a solid model.....136
Figure 4.27: Comparison of three models of the bypass phantom.....137
Figure 4.28: Quantitative comparison of three geometric models of the phantom.....139
Figure 4.29: Comparison of flow waveforms for simulations based on three different geometric models.....140
Figure 4.30: Comparison of through-plane velocity contours in the aorta proximal to the bypass, also referred to as the downstream inlet (plane B), for three geometric models of the phantom.....142
Figure 4.31: Comparison of through-plane velocity contours at the aorta proximal to the coarctation but distal to the bypass (plane C) for three geometric models of the phantom.....143
Figure 4.32: Comparison of through-plane velocity contours in the aorta distal to the coarctation (plane D) for three geometric models of the phantom.....144
Figure 4.33: Comparison of through-plane velocity contours in the bypass graft (plane F) for three geometric models of the phantom.....145
Figure 4.34: Comparison of through-plane velocity contours in the aorta distal to the graft, also referred to as the outlet (plane E), for three geometric models of the phantom 146
Figure 4.35: Comparison of two different inlet velocity profiles at peak flow.....148
Figure 4.36: Comparison of flow waveforms for simulations run with two different inlet velocity profiles 148

Figure 4.37: Comparison of through-plane velocity contours at five different locations for different inlet velocity boundary conditions.....149
Figure 5.1: Set-up for the high flow *in vitro* experiment 158
Figure 5.2: Diagram of the experimental set-up for the high flow *in vitro* study 159
Figure 5.3: Example of measurements of flow acquired with the ultrasonic flow probe 160
Figure 5.4: Phantom model for the *in vitro* flow experiments. Planes A-F indicate locations where PC-MRI data was acquired for the high flow experiment 161
Figure 5.5: In-plane velocity components at the inlet (plane A) during peak flow.....163
Figure 5.6: Comparison of flow waveforms measured with PC-MRI and those from the numerical simulations 165
Figure 5.7: Velocity magnitudes as computed from the numerical simulations for cycle 9 167
Figure 5.8: Comparisons in the aorta proximal to the bypass graft, also referred to as the downstream inlet (plane B) location, of through-plane velocities computed numerically using finite element analysis (FEA) and those acquired with PC-MRI.....168
Figure 5.9: Comparisons in the aorta proximal to the coarctation (plane C) of through-plane velocities computed numerically using finite element analysis (FEA) and those acquired with PC-MRI.....169
Figure 5.10: Comparisons in the aorta distal to the coarctation (plane D) of through-plane velocities computed numerically using finite element analysis (FEA) and those acquired with PC-MRI 170
Figure 5.11: Comparisons in the aorta distal to the bypass graft, also referred to as the outlet (plane E), of through-plane velocities computed numerically using finite element analysis (FEA) and those acquired with PC-MRI 171
Figure 5.12: Comparisons in the bypass graft (plane F) of through-plane velocities computed numerically using finite element analysis (FEA) and those acquired with PC-MRI.....172

Figure 5.13: Repeatability of output from flow pump, as measured with the ultrasonic flow probe 175
Figure 5.14: Comparison of PC-MRI measurements. The sum of the flows through the host vessel and through the graft should equal the flow at the inlet and the flow at the outlet....176
Figure 5.15: Comparison of geometric models (a) constructed from MRA data and (b) based on the CAD drawing 177
Figure 5.16: Quantitative comparison of two geometric models of the phantom 178
Figure 5.17: Comparison of flow waveforms measured with PC-MRI and those from the numerical simulations 179
Figure 5.18: Comparison of through-plane velocity contours in the aorta proximal to the bypass graft, also referred to as the downstream inlet location (plane B), for two geometric models of the phantom 181
Figure 5.19: Comparison of through-plane velocity contours in the aorta proximal to the coarctation (plane C) for two geometric models of the phantom 182
Figure 5.20: Comparison of through-plane velocity contours in the aorta distal to the coarctation (plane D) for two geometric models of the phantom 183
Figure 5.21: Comparison of through-plane velocity contours in the aorta distal to the bypass, also referred to as the outlet (plane E), for two geometric models of the phantom 184
Figure 5.22: Comparison of through-plane velocity contours in the bypass graft (plane F) for two geometric models of the phantom....185
Figure 5.23: Comparison of through-plane velocity isocontour patterns with and without spatial averaging 187
Figure 5.24: Effect of temporal averaging on the numerical simulation results 188
Figure 6.1: Diagram of the *in vivo* experiment protocol 194
Figure 6.2: External occluders used to control whether the bypass graft was open or closed 196
Figure 6.3: Equipment set-up for acquiring pressure measurements 201
Figure 6.4: Set-up for pressure transducer calibration 202

Figure 6.5: Process for generating the numerical simulation results.....205
Figure 6.6: Comparison of flow results from simulations using 240 time steps per cycle and different mesh sizes: 120,000 elements, 548,000 elements, 1 million elements, and 1.8 million elements 206
Figure 6.7: Comparison of flow results from simulations using a different number of time steps per cardiac cycle and a 548,000 element mesh.....206
Figure 6.8: Comparison of average flow rates measured with PC-MRI and computed by numerical simulations for eight animals 211
Figure 6.9: Comparison of flow distributions between PC-MRI flow measurements and numerically computed quantities 212
Figure 6.10: Comparison of flow waveforms acquired with PC-MRI and computed with numerical simulation techniques over one cardiac cycle for eight pigs.....213
Figure 6.11: Sensitivity of the flow solutions to the equivalent-circle radius of the coarctation contour for pig E 214
Figure 6.12: Velocity profile prescribed at inlet of numerical simulations for pig G 216
Figure 6.13: Models used for the numerical simulation of velocity patterns for Pig G ..218
Figure 6.14: Velocity magnitudes from the numerical simulation of Pig G 220
Figure 6.15: Comparison of flow waveforms from the numerical simulations and from PC-MRI.....221
Figure 6.16: Periodicity of flow waveforms from averaged numerical simulation results 222
Figure 6.17: Comparison of flows at the inlet with sum of flows through the aorta and the bypass graft 222
Figure 6.18: Comparisons in the aorta proximal to the coarctation of through-plane velocity patterns computed numerically using finite element analysis (FEA) and those acquired with PC-MRI 224
Figure 6.19: Comparisons in the bypass graft of through-plane velocity patterns computed numerically using finite element analysis (FEA) and those acquired with PC-MRI.....225

Figure 6.20: Pressure measurements acquired in the proximal and distal porcine aorta....229
Figure 6.21: Obtaining an average representative cycle from a pressure waveform 230
Figure 6.22: Comparison of pressure waveform characteristics for the bypass-open and bypass-closed state....233
Figure 6.23: Comparison of flow waveform characteristics for the bypass-open and bypass-closed state....234
Figure 6.24: Comparison of average heart rates for the bypass-open and bypass-closed state....235
Figure 6.25: Physiologic changes observed in Pig F for the bypass-open and bypass-closed states....236
Figure 6.26: Determination of drift in pressure transducer measurements....237
Figure 6.27: Circuit representations of (a) the stenosis (bypass-closed condition) and (b) the stenosis and bypass (bypass-open condition)....239

Chapter 1

Introduction

A journey of a thousand miles begins with a single step.
~Chinese proverb

1.1 Cardiovascular Disease

Cardiovascular disease is the leading cause of death in the world, having contributed to 29% of deaths worldwide in the year 2001 [1]. In industrialized countries, the impact of cardiovascular disease is even larger. In 2000, 1 of every 2.5 deaths in the United States was caused by cardiovascular disease [2]. Approximately 75% of these deaths were attributed to atherosclerosis, a disease process in which lipids, calcium, cellular waste products, and other substances accumulate in the intima, or the inner-most layer of an artery, under a layer of smooth muscle cells and connective tissue fibers referred to as a fibrous cap. The formation of these atherosclerotic plaques can result in vessel lumen narrowing and ischemia, or low blood flow, while plaque rupture, in which the fibrous cap degrades or detaches, could cause additional complications, such as thrombosis or clotting, which may cause vessel occlusion downstream.

Hemodynamic factors that have been implicated in the development of atherosclerotic plaques and intimal thickening, a condition that is hypothesized to lead to atherosclerotic plaques, include low shear stress, flow separation and stasis, and shear stress oscillation [3-6]. It has been postulated that regions with flow separation and low shear stress

promote the accumulation of atherogenic material in the intima [7]. Shear stress oscillation, which is related to flow oscillation, is theorized to produce a disorganized endothelial cell structure with large gap junctions between cells, which would also increase the absorption of atherogenic substances. Other studies have found that the product of the shear stress level and the residence time affect platelet activation, a key step in the formation of thrombi [8].

1.2 Role of Hemodynamics in Bypass Graft Surgery

A primary goal in treating vascular disease is to restore blood flow to ischemic regions. Bypass graft surgery is a treatment option in which a blood vessel or synthetic graft (see Figure 1.1) is placed in the body to provide an alternate path for blood flow, thus minimizing the effects of the diseased artery on the downstream blood flow. In 1999 in the United States alone, an estimated 688,000 bypass surgeries were performed, of which 571,000 were coronary artery bypass procedures and the remaining 117,000 were bypass operations performed on other arteries [9].

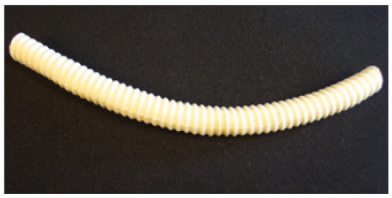


Figure 1.1: Example of a bypass graft.

1.2.1 Bypass Graft Surgery Terminology

In discussing bypass graft surgeries, it is helpful to first define the specialized terminology that is used. Figure 1.2 is a diagram of a stenosed, or narrowed, artery with a bypass graft. "Anastomosis" is the term for the connection between the graft and the native artery. The upstream anastomosis is referred to as the "proximal anastomosis," while the downstream anastomosis is termed the "distal anastomosis." The location where the outer portion of the graft attaches to the host vessel is defined to be the "toe," while the "heel" refers to the location where the inner portion of the graft is attached to

the host vessel. The arterial wall opposite the junction is referred to as the "floor" of the anastomosis.

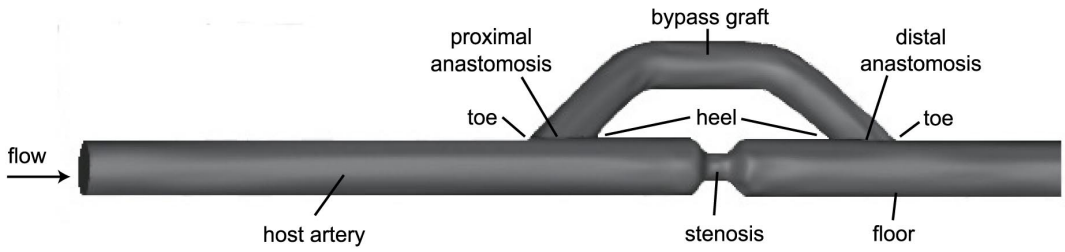


Figure 1.2: Diagram of a bypass graft attached to a host artery with a stenosis.

1.2.2 Surgery Planning

When planning a bypass graft procedure, vascular surgeons must determine the location and manner for attaching the graft and the type of graft to use. The placement of the anastomosis depends on factors such as the location of collateral vessels and the extent of the disease. The anastomosis can be performed end-to-end, where the end of the graft is directly sutured to the end of the host artery, or end-to-side, where the end of the graft is beveled and attached to the side of the host artery. Side-to-side anastomoses are also possible but are rarely used in clinical practice. The graft itself can be synthetically manufactured from fabric or polymers, or it can be a blood vessel from another part of the patient's body, from another human, or from an animal. The vascular surgeon also decides upon the size and length of the graft that is needed.

While cost and ease of implementation influence a vascular surgeon's decisions, the primary criteria when planning a procedure is its effectiveness. It is critical that the bypass procedure sufficiently restore blood flow to the ischemic regions of the body. Furthermore, the surgeon is concerned about the graft's long-term patency, or ability to remain open and functional, and the potential for complications, such as infection and the structural breakdown of the graft. An understanding of the hemodynamic factors that potentially lead to bypass graft failure is therefore valuable for planning more effective surgeries.

1.2.3 Bypass Graft Failures

Up to 10% [10-14] of bypass graft procedures fail within 30 days of surgery. These are termed early bypass graft failures and can usually be attributed to technical errors, such as the introduction of a kink in the graft, the patient's tendency to form clots, or a poor surgical planning decision, such as choosing a location for the distal anastomosis that does not permit sufficient blood to reach the downstream vessels [10, 11].

Late failures, those that occur 30 days or more after placement of the graft, are frequently caused by graft occlusion. Over a period of 5 to 10 years, approximately 30% to 60% [12-17] of bypass grafts will become stenosed or occluded, leading to a need for revascularization or amputation. The incidence of bypass graft occlusion varies, depending on the anatomy involved, the length of time since the operation, and the type of graft that was utilized. For instance, the cumulative patency rate for vein grafts used for femoropopliteal bypass graft procedures was 73% 5 years after surgery, compared with the 35% patency rate for prosthetic grafts in that same time period [13]. The stenosis and occlusion of grafts can result from intimal thickening or atherosclerotic plaque, which, as previously mentioned, have been hypothesized to be due to local hemodynamic factors, such as flow recirculation and low wall shear stresses.

Bypass graft failures also occur because of anastomotic aneurysms, which are connective tissue sacs that develop because of a gap between the graft and the host artery. Possible causes of this gap include turbulent flow, compliance mismatch between the graft and the host artery, and weak sutures [18, 19]. Anastomotic aneurysms can lead to complications, such as thrombosis, distal embolization, or rupture. However, their incident rate is only on the order of 10% [16, 19-21].

1.2.4 Utilizing Hemodynamics to Increase the Effectiveness of Bypass Surgery

The ideal bypass graft surgery would be designed to avoid the adverse flow conditions associated with bypass graft failure. For example, since low flows are associated with the development of intimal thickening and there is an inverse relationship between the cross-sectional area of the graft and the velocities through the graft, the surgeon should select a bypass graft of small diameter to ensure high flow through the graft during rest.

However, the resistance of a bypass graft is inversely related to the cube of the diameter, so a larger graft is desirable to ensure that it does not inhibit flow to the vessels downstream. In particular, varying physiologic states, including exercise, must be considered since a bypass graft sized for resting conditions might be flow-limiting under exercise conditions.

Numerous studies have examined the effects of other geometric factors on local hemodynamics. For example, changes to the anastomosis angle have been shown to affect both the flow patterns and the flow distribution. A study by Zhang and colleagues on 30 male rats showed that a proximal anastomosis angle of 45^o or 90^o results in approximately 10% more flow through the bypass graft than an anastomosis angle of 135^o [22]. Furthermore, *in vitro* experiments suggest that smaller distal end-to-side anastomosis angles result in less flow disturbances. Specifically, Hughes and How observed flow separations at the toe of the anastomosis for angles of 30^o and 45^o, but not at 15^o [23]. This is similar to the results of Ojha, *et. al*, in which flow separations occurred at the toe for angles of 30^o, 45^o, and 60^o, but not at 20^o [24]. For larger anastomosis angles, the vortices that form in the proximal outflow segment are found to be larger in size and composed of higher velocities [25]. Since flow recirculation and flow separation regions have been associated with the development of intimal thickening and atherosclerotic plaque, the angle of the anastomosis is an essential factor in planning a successful bypass graft procedure.

An understanding of the outflow conditions is also vital to planning a successful bypass graft procedure. In an experiment with 27 dogs, Greenstein and colleagues found that lower outflow rates resulted in fewer patent bypass grafts [26]. Similar results were observed in patients with a polytetraluoroethylene femoropopliteal or femoral-distal bypass. The 2-year patency rate for these bypass grafts for patients with "good" angiographic run-off was 50%, but it dropped to 9% if the angiographic run-off was "poor" [27]. This finding is consistent with fluid dynamic principles. Poor outflow conditions correspond to a higher outlet resistance, making it more difficult for blood to flow through the vessel of interest. Since the resulting low blood flow rates in the graft

could promote intimal thickening and the development of atherosclerotic plaque, outflow conditions need to be considered when planning a bypass graft surgery.

Another parameter that affects the flow patterns is the flow rate. At higher flow rates, particle accumulation, which occurs along the heel of the distal end-to-side anastomosis and is indicative of flow recirculation or low flow regions, decreases dramatically [28]. In other instances, higher velocities produce a separation zone that does not exist at lower velocities, as observed near the toe of the anastomosis for an anastomosis angle of 60^{o} [25].

The nature of the flow in the arterial segment proximal to the distal anastomosis also influences the flow patterns. *In vitro* experiments show that flow separation occurs in the anastomosis when greater than 10% of the flow from the graft exits through the proximal arterial segment; however, flow separation is not seen at this location when the proximal arterial segment is occluded [23, 29, 30]. Under conditions of prograde flow, in which blood flows downstream along the proximal segment towards the distal anastomosis, the flow patterns change considerably. In the case of a stenosis upstream of the distal anastomosis, a strong jet is generated in the native arterial segment that leads to flow separation along both arterial walls and a more symmetric profile downstream of the anastomosis relative to when the proximal arterial segment is occluded [31].

These examples show the effects that surgical decisions can have on the hemodynamics in a bypass graft geometry. The results of these experiments, while not applicable to a specific patient situation, do provide general guidelines for surgeons when planning their operations.

1.3 Magnetic Resonance Imaging

Flow dynamics in bypass grafts have been measured using various techniques. Particle image velocimetry (PIV) and laser Doppler anemometry (LDA) have been utilized to study flow patterns in *in vitro* models but are inappropriate for *in vivo* applications. Of the *in vivo* imaging techniques that are currently available—x-ray angiography, computed tomography (CT), ultrasound, and magnetic resonance imaging (MRI)—MRI provides

the most useful information for studying and simulating *in vivo* blood flow patterns. X-ray angiography is limited to providing qualitative flow information in a single two-dimensional plane and is an invasive procedure. CT cannot measure blood flow, and furthermore, it exposes the subject to ionizing radiation. Ultrasound can be used to acquire three-dimensional anatomic and physiologic data, but this is limited to certain anatomic regions. Furthermore, through-plane velocity profiles cannot be obtained. On the other hand, with MRI it is possible to obtain detailed velocity measurements over a region of space, so flows and velocity profiles can be accurately computed. MRI also provides three-dimensional anatomic information, which can provide insights into the observed flow patterns and are needed for computer simulations (see Section 1.4). Moreover, MRI is not invasive and does not expose the subject to any ionizing radiation.

Two common MRI techniques for quantitatively measuring velocities are tagging and phase-contrast (PC-MRI). Tagging involves using magnetization to non-invasively impose a grid structure onto a region of interest. This grid structure evolves over time, according to the motion of the objects in the region of interest. Analysis of the changing grid structure produces velocity information. PC-MRI measures the magnetization phase, which is directly related to velocity under certain conditions. While both methods have been utilized to acquire velocity and motion information, PC-MRI can be used to measure velocities in three dimensions with potentially higher spatial resolution [32], and is therefore more favorable for studying blood flow and velocity patterns.

1.4 Computational Methods

1.4.1 Background

Blood flow and velocity patterns can also be studied using computational simulation methods. The simplest of these computational models is the lumped parameter model, which describes blood vessel networks using global quantities such as resistance, inductance, and capacitance. One-dimensional finite-element models describe the vessels in more detail, dividing the network of vessels into small segments, each characterized by a length and diameter. While these models can be used to predict blood flow rates and

distributions fairly accurately [33], they are unable to provide any information about three-dimensional flow features, such as recirculation or flow separation. On the other hand, simulations using three-dimensional models can capture these blood flow patterns. As previously discussed, these flow features may play a role in the development of arterial disease, and as such, the three-dimensional models may also be more useful than the one-dimensional models in understanding disease formation and planning effective surgeries.

These numerical methods have been used extensively to study the relationship between the fluid mechanics of blood and the development of arterial disease [34-39] and to test hypotheses regarding the effects of different parameters of bypass graft surgery on hemodynamics [40-42]. Recently, Taylor, *et al*. described a comprehensive system for simulation-based medical planning to enable the preoperative assessment of alternate treatment plans [43]. In this system, three-dimensional finite-element simulation methods were utilized to predict blood flow and pressures in postoperative models given patient-specific anatomic and physiologic data.

The advantage of using numerical simulations for these investigations is its ease of use over physical testing. Numerical simulations can provide a more complete description of hemodynamic conditions than experimental fluid mechanical methods. Furthermore, numerical models can be readily modified to assess the effects of a given parameter, such as the bypass graft angle or the graft-to-host-artery diameter. The usefulness of these numerical simulations, though, depends on their accuracy. Simplifying assumptions about the underlying physics, the properties of blood and blood vessels, the geometry of the blood vessels, and the accuracy of the numerical methods can all affect how well the numerical simulation models blood flow.

1.4.2 *In Vitro* Validation of Computational Methods

Numerous *in vitro* validation studies have been performed to verify the accuracy of the results predicted using numerical simulation methods. One of the simpler geometries studied was a curved tube. Comparisons between laser Doppler anemometry (LDA) measurements and numerical simulation results for non-Newtonian, pulsatile flow in this

model were excellent [44]. Validation experiments using more anatomically relevant geometries also demonstrated the accuracy of these numerical simulation methods. Good agreement in velocity profiles was found in bifurcated models, such as the carotid artery [45-47] and the coronary arteries [48]. Numerical predictions and hydrogen bubble visualizations of flow patterns in an idealized bypass graft with an occluded native artery compared well qualitatively [49]. Sun, *et al.* showed a reasonable agreement between PC-MRI velocity measurements and numerical simulation results for steady flow in a straight cylinder with a partial obstruction, a geometry similar to that of a stenosed vessel [50]. Numerically computed flow velocities in a plane through the center of the slightly more complex geometry of an expansion in a cylinder, followed by a constriction and another expansion, have also proven to be qualitatively similar to those measured using Fourier velocity encoding MRI techniques [51].

Additionally, several variations of the end-to-side anastomosis model have been investigated. Taylor, *et al.* and Lei, *et al.* both evaluated numerically computed velocity profiles for pulsatile flow in a distal end-to-side anastomosis model, in which 20% of the flow exited through the proximal arterial segment [52, 53]. Both investigations demonstrated favorable agreement between the numerical simulations and the LDA measurements. Furthermore, velocity profiles from simulations of steady flow through distal end-to-side anastomoses with an occluded proximal segment matched both PC-MRI measurements [54] and photochromic dye tracer measurements [36, 55]. Even more complex flow, such as that of pulsatile flow in a non-planar distal end-to-side anastomosis with an occluded proximal segment, have been accurately predicted using numerical simulation methods [56]. Bertolotti, *et al.* have also demonstrated reasonably accurate predictions of pulsatile flows in a model of a host artery with a stenosis and a distal end-to-side anastomosis [57]. However, their methodology required specification of the inlet waveforms for both the host artery and the graft section upstream of the distal anastomosis. This approach is unsuitable for surgical planning purposes, where the flow through the bypass graft section is not known *a priori*.

The agreement obtained between numerical and *in vitro* experimental results is encouraging. However, to date, no studies, other than that by Bertolotti and colleages

[57], are known to have validated these methods for the more complicated geometry of a bypass graft attached to a stenosed artery via end-to-side anastomoses. Moreover, *in vitro* experiments fail to incorporate all the complexities observed *in vivo*. For example, the models are rigid and do not replicate the compliant nature of blood vessels, and the blood-mimicking materials used in the experiments are typically homogenous fluids, rather than suspensions of cells in plasma like blood. Other simplications may include using steady flow, instead of pulsatile flow, and using non-physiologic Reynolds numbers. Furthermore, these *in vitro* studies have been performed using idealized geometric and/or physiologic parameters, so the results do not accurately describe the blood flow for a specific patient.

1.4.3 *In Vivo* Validations

Thus far, few *in vivo* validations have been performed because non-invasive methods for obtaining both *in vivo* measurements of blood flow and high resolution three-dimensional anatomic information have not been available. Long, *et al.* have utilized MRI to examine the accuracy of simulation methods in the aorto-iliac bifurcation region [58] and in the carotid artery [59] for one subject. In both of these studies, inlet and outlet velocity boundary conditions were specified using MRI data, and the predicted velocity was compared with MRI data on a plane midway between the inlet and outlet. Similarly, the comparison study by Steinman and colleagues in the human carotid artery utilized simulation results in which idealized velocity profiles were prescribed at the inlet and one of the outlets [38]. While this approach is reasonable for investigations where the flow distribution can be fully specified, it is not applicable to surgery planning where the flow distribution is not known *a priori*.

A limited number of *in vivo* validation studies have utilized a traction-free or uniform constant pressure boundary condition at the outlets, an approach that is suitable for surgery planning. Xu and colleagues' comparison of ultrasound velocity measurements with numerical simulation results was one of the earliest *in vivo* validation studies performed. They compared computed results and flow measurements through two different canine ilio-femoral bifurcation models [60]. Significant errors were observed in

the ultrasound-acquired velocity vectors in regions of secondary flow, which could explain the discrepancy between the numerical simulations and the measurements. This experiment involved relatively low inlet flows and small diameters, and consequently, low Reynolds numbers.

Validation studies performed on larger vessels with higher inlet flows have been limited in scope and yielded variable results. A comparison for one location at one time point in the human ascending aorta showed reasonable qualitative agreement between velocities obtained with PC-MRI and those computed using numerical simulation techniques [61]. Wood and colleagues also performed a validation experiment in the aorta of one subject and showed results for one slice at 3 consecutive time points in the cardiac cycle [62]. Both of these studies involved relatively simple geometries with one input and one output. On the other hand, investigations of a total cavopulmonary connection, in which the superior and inferior vena cava are attached to the right pulmonary artery, found significant differences between the MR-measured and numerically computed velocity profiles [63]. Migliavacca, *et al.* attributed these differences to the simplifying assumptions used in the simulations.

1.5 Contributions

While previous investigations have compared numerical predictions of blood flow and velocities with physical measurements, they have generally focused on geometries with a single input and output or with a bifurcation. To date, no known studies have validated numerical simulation methods for the more complex geometry of a stenotic vessel with a bypass graft under conditions that are suitable for surgical planning purposes. For surgical planning, limited flow information is available *a priori*. Moreover, since anatomic and physiologic conditions differ between subjects, a simulation method for surgical planning would need to be subject-specific.

This thesis undertakes this validation study both *in vitro* and *in vivo*. Specifically, the contributions of this work are as follows:

1. Blood flow distribution and velocity patterns were quantified in an *in vitro* model of a thoraco-thoraco aortic bypass procedure using cine PC-MRI and computational methods. The effect of imaging and computational parameters on the measured and simulated velocity fields was assessed, and comparisons between the computational and imaging data were made.
2. Hemodynamic conditions, including flow rate, velocity fields, and pressure losses were quantified in a porcine model of a thoraco-thoraco aortic bypass procedure using cine PC-MRI and MR-compatible pressure transducers. The effect of closing the bypass on pressure and flow rate was determined.
3. Numerical simulations of blood flow in the thoraco-thoraco aortic bypass procedure were performed. It was demonstrated that numerical methods could be used to predict blood flow distribution between the native aorta and the bypass graft to within 10% of PC-MRI measurements obtained in 8 pigs. Furthermore, initial results showed that the predicted velocity profiles agreed favorably with cine PC-MRI data.

1.6 Organization

Chapter 2 provides background information on fluid dynamics, magnetic resonance imaging, image-based modeling techniques, and numerical simulation methods. Chapter 3 describes the sensitivity of PC-MRI measurements, while Chapters 4 and 5 present the results of using numerical simulation techniques to study the hemodynamics of a phantom model of a stenotic vessel with a bypass graft at low and high flow rates, respectively. Chapter 6 compares the results of the numerical simulation against the PC-MRI measurements for the case of a stenotic vessel with a bypass graft *in vivo*. In addition, comparisons are made between "bypass open" and "bypass closed" conditions. Finally, Chapter 7 summarizes the findings of this work and discusses areas for further investigation.

Chapter 2

Investigating Hemodynamics

The learning and knowledge that we have, is, at the most, but little compared with that of which we are ignorant.
~Plato

In 1628, William Harvey postulated a new theory about blood in the body. In contrast to the popular idea of the time that food was converted into blood, Harvey proposed the idea that blood circulated around the body, with blood being pumped from the heart into the arteries and returning to the heart via the veins. Since that time, much has been learned about the properties of blood, how it circulates throughout the body, and the potential role of blood flow in disease. Multiple approaches have been utilized to increase our understanding of blood flow. The current hemodynamic, or blood fluid mechanic, theories are summarized in Section 2.1. Section 2.2 describes magnetic resonance imaging techniques that are used to study blood flow. Computational simulation methods can also be used to expand our knowledge about blood flow. The image-based modeling techniques which enable subject-specific simulations are described in Section 2.3, while Section 2.4 focuses on the theory and methods for numerical simulation techniques.

2.1 Hemodynamic Concepts

Blood is a complex substance, consisting of platelets, red blood cells, and white blood cells suspended in a plasma. Classical fluid mechanical theory, though developed for simpler fluids, can be used to model and provide a basic understanding of blood flow.

2.1.1 Fluid Properties

Viscosity is one of the most important characteristics of a fluid, describing how easily the fluid moves when a force is applied to it. Mathematically, this can be expressed as the ratio of shear stress, or the tangential force applied to a given surface area of the fluid, to the shear rate, or velocity gradient:

$$\mu = \frac{\tau}{\dot{\gamma}} \tag{2.1}$$

where μ is the viscosity, τ is the shear stress, and $\dot{\gamma}$ is the shear rate. Viscosities vary with both temperature and pressure. In general, viscosities of liquids increase with pressure and decrease with temperature. A fluid, such as water, whose viscosity is constant at a given temperature and pressure is known as a Newtonian fluid.

Blood is a non-Newtonian fluid, since under certain conditions, its viscosity decreases as the shear rate increases. In blood, this shear-thinning behavior is attributed to the aggregation of red blood cells. Since flow is proportional to shear rate, higher average shear rates result in higher flow rates and therefore a decrease in the tendency of red blood cells to accumulate. The reduction in the hematocrit, or the concentration of red blood cells in the blood, results in a lower viscosity. A shear-thinning fluid will have higher velocity gradients at solid walls than a Newtonian fluid. For shear rates above 100 s^{-1}, though, the viscosity of blood has been observed to be constant [64-66].

The viscosity of blood also depends on the hematocrit. The shear-thinning phenomenon only occurs for hematocrit ratios above approximately 12%. Below a hematocrit ratio of 12%, blood behaves like a Newtonian fluid [64, 65]. Normal human blood with hematocrit ratios ranging from 40% to 45% [66] does display shear-thinning characteristics. Furthermore, since a larger hematocrit ratio results in increases in the blood viscosity, conditions which alter it, such as disease and dehydration, can produce changes in the viscosity of blood.

The diameter of the tube or vessel also affects the viscosity of blood. Fahraeus and Lindqvist showed that the viscosity of blood remains constant in tubes larger than approximately 0.3 mm in diameter [67]. Below this threshold, the viscosity decreases as

the tube diameter decreases. This trend is due to the lower hematocrit ratio that is observed in smaller vessels [65]. Thus, although blood is a non-Newtonian fluid, in vessels with diameters greater than 0.3 mm and shear rates greater than 100 s^{-1}, it can be considered a Newtonian fluid. Measurements of normal human blood viscosity yield values between 3.0 and 5.5 cP at a shear rate of 230 s^{-1} [66].

Other properties that are useful in modeling and understanding fluid flow are density and compressibility. The density ρ of a fluid is the ratio of its mass m to its volume V:

$$\rho = \frac{m}{V} \tag{2.2}$$

Fluids with a constant density everywhere are considered homogenous. Like viscosity, the density of blood varies with its hematocrit. The different concentrations of red blood cells in blood will produce slight changes in the density of whole blood. However, in vessels with diameters that are significantly larger than that of a red blood cell, blood can modeled as a homogenous fluid [68]. In humans, the density of blood is 1.06 g/cm^3 [69].

Compressibility describes a fluid whose density changes depending on the level of the pressure applied to it. For incompressible liquids, the following equation for the conservation of mass applies:

$$\nabla \bullet \bar{\mathrm{v}} = \frac{\partial \mathrm{v}_x}{\partial x} + \frac{\partial \mathrm{v}_y}{\partial y} + \frac{\partial \mathrm{v}_z}{\partial z} = 0 \tag{2.3}$$

where $\bar{\mathrm{v}}$ is the velocity field. Within normal physiologic pressures, blood can be considered incompressible [68].

2.1.2 Fluid Energy

Fluid energy can be categorized as either potential or kinetic energy. Within the arterial system, there are two sources of potential energy: an intravascular pressure, that is primarily due to the contraction of the heart, and a gravitational potential energy, which is related to the fluid density and the height of the measurement relative to a given reference point. The kinetic energy is related to the blood density and velocity.

Changes in either the kinetic or potential energy will result in flow. The resistance R is defined as the difference in fluid energy ΔE needed to produce a given amount of mean flow Q:

$$R = \frac{\Delta E}{Q} \tag{2.4}$$

Oftentimes, the kinetic energy and the gravitational potential energy terms are ignored, so that resistance simplifies to a ratio between intravascular pressure differences ΔP and the mean flow Q:

$$R = \frac{\Delta P}{Q} \tag{2.5}$$

For the case of steady flow of a homogenous, Newtonian fluid through a straight, rigid cylinder, the resistance can then be expressed as

$$R = \frac{8l\mu}{\pi r^4} \tag{2.6}$$

where μ is the viscosity, l is the cylinder length, and r is the cylinder radius. This quantity represents the pressure gradient needed to produce a given flow.

Additional energy losses can occur due to changes in kinetic energy. Factors such as acceleration or deceleration of the fluid, changes in vessel diameter, branching, and vessel curvature alter the fluid velocity magnitudes and/or directions, and produce differences in kinetic energy.

For pulsatile flow, the more general concept of impedance is employed to relate the pressure waveform to the flow waveform. Impedance Z is defined as:

$$Z(\omega) = \frac{P(\omega)}{Q(\omega)} \tag{2.7}$$

where ω is the frequency, P is pressure, and Q is flow. This definition is more accurately termed "input impedance," since it is dependent on downstream impedances, and not just the local fluid and vessel properties. The impedance at zero frequency, or steady flow, is

the resistance. Similar to resistance, impedance is a measure of how much energy, or pressure, loss is needed to achieve a given flow. Total impedance can be computed using the following formulae:

impedances in series: $$Z_{total} = Z_1 + Z_2 + Z_3 + ... \quad (2.8)$$

impedances in parallel: $$\frac{1}{Z_{total}} = \frac{1}{Z_1} + \frac{1}{Z_2} + \frac{1}{Z_3} + ... \quad (2.9)$$

where Z_1, Z_2, Z_3 are impedances of downstream vessels.

2.1.3 Wave Reflections

The concept of impedance also plays a role in wave transmission and reflection theory. This theory, originally applied to electric transmission lines, has been used to explain the pressure and flow waveforms observed in the arterial system [70]. The idea is that impedance mismatches, where the impedance differs from one segment of a system to the next, cause wave reflections that add to or subtract from the incident wave to produce the final waveform that is observed. Changes in vessel diameter and vessel distensibility are two factors that cause impedance mismatches in the arterial system and lead to wave reflections. The relationships between the reflected and incident waves are defined as follows:

$$P_r = \frac{Z_2 - Z_1}{Z_2 + Z_1} P_i \quad (2.10)$$

$$Q_r = \frac{Z_1 - Z_2}{Z_1 + Z_2} Q_i \quad (2.11)$$

where Z_1 is the upstream impedance, Z_2 the downstream impedance, P_r the reflected pressure wave, P_i the incident pressure wave, Q_r the reflected flow wave, and Q_i the incident pressure wave.

2.1.4 Flow Patterns

2.1.4.1 Types of Flow

Laminar flow describes fluid that moves in layers over one another, resulting in a smooth, orderly motion. One example of laminar flow is plug flow, shown in Figure 2.1(a), where the axial velocity remains relatively constant across the cross-sectional area of the tube. Since the walls have a velocity of zero, this profile results in steep velocity gradients near the walls. Plug flow can be observed at the entrance of a tube.

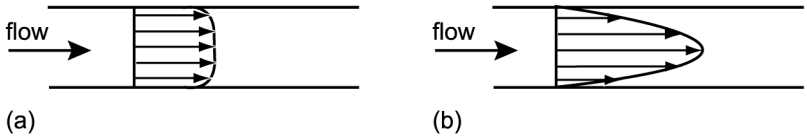


Figure 2.1: Velocity profiles for different types of laminar flow. (a) Plug flow. (b) Poiseuille or parabolic flow.

Poiseuille, or parabolic, flow, another type of laminar flow, occurs downstream of the tube entrance in the fully developed flow regime, where the velocity profile remains constant. The distance from the tube entrance to the beginning of the fully developed flow region is termed the entrance length. An approximate value for the entrance length L_e can be determined from the following equation:

$$L_e \approx 0.06\,\mathrm{Re}\cdot d \tag{2.12}$$

where Re is the Reynolds number, described below, and d is the diameter of the tube. In parabolic flow, the axial velocities vary with the square of the tube radius, with the maximum velocity occurring at the center of the tube and the minimum velocities occurring along the walls of the tube, as seen in Figure 2.1(b). Parabolic flows develop under conditions of steady flow of a Newtonian fluid through a long, straight, rigid cylinder. Strictly speaking, these conditions do not exist in the cardiovascular system. Pulsatile, fully-developed flow for an incompressible, Newtonian fluid through a straight cylinder, also known as Womersley flow, is a more appropriate model of blood flow in the arterial system than Poiseuille flow, but nevertheless still a crude approximation that neglects the compliance, branching, and curvature effects that exist in reality.

The Reynolds number, which is the ratio of inertial forces to viscous forces on the fluid, identifies whether or not a fluid is in the laminar flow regime. For a cylindrical tube, this parameter Re depends on the tube diameter D, the mean velocity U, the fluid density ρ and dynamic viscosity μ:

$$\mathrm{Re} = \frac{\rho D U}{\mu} \tag{2.13}$$

Fluids with a Reynolds number less than 2000 in a cylinder are considered laminar, while a Reynolds number greater than 3000 indicates turbulent flow. Unlike smooth, orderly laminar flow, turbulent flow is characterized by random, fluctuating motion, making it difficult to predict and model. Turbulent flow is not generally observed in normal, healthy vessels. However, under pathologic conditions, such as distal to a stenosis, or a narrowing of the artery, turbulent flow may exist. Fluids with a Reynolds number between 2000 and 3000 are in a transitional stage, in which the flow is primarily laminar with occasional disturbances that are dampened out downstream. The values identifying these different flow states are valid for flow in a straight, rigid cylinder and will vary for flow under other conditions.

The Womersley number is a measure of the transient inertial effects to viscous ones and can be expressed as

$$\mathrm{Wo} = \sqrt{\frac{\rho \omega r^2}{\mu}} \tag{2.14}$$

where r is the radius of the tube, ω is the frequency at which the flow is pulsating, ρ is the fluid density, and μ is the dynamic viscosity of the fluid. Generally speaking, higher Womersley numbers result in flatter velocity profiles.

2.1.4.2 Boundary Layer Separation

The boundary layer refers to the fluid layer that is closest to the wall. Typically, this layer flows downstream following the contour of the wall. However, in situations where there is a decrease in the forward velocity coupled with an adverse pressure gradient, such that there is higher pressure downstream than upstream, this layer breaks away from

the wall. This phenomenon is termed flow separation. Flow separation tends to occur along curved walls, at branch points, and where the tube diameter changes. The points along the wall where the flow separation begins and ends have a shear stress of zero and are called separation and reattachment points, respectively. Complex flow patterns, such as flow recirculation, are often observed where flow separation occurs.

2.1.4.3 Vortices

A vortex describes fluid moving in a circular path around an axis. The speed at which this fluid rotates is inversely proportional to its distance from the axis. Vortices are important because of their ability to generate large forces and pressure fluctuations. For instance, they are hypothesized to affect plaque rupture [71]. Vortices are commonly observed in regions of flow separation, where a low pressure region is generated. Fluid moves upstream into these low pressure regions, initiating a circular movement that leads to a vortex. The behavior of vortices is strongly dependent on the Reynolds number, becoming more complex and unpredictable as the Reynolds number increases. Vortices eventually disappear due to viscous effects, becoming smaller vortices and eventually dissipating into heat. In some cases, instabilities in the shear layer where vortices are formed cause the vortices to break away and move downstream. This phenomena is referred to as "vortex shedding." Vortex shedding has been theorized to affect platelet deposition, which is associated with intimal hyperplasia and atherosclerosis [72].

2.2 Magnetic Resonance Imaging

2.2.1 Magnetic Resonance Physics

Magnetic resonance (MR) measures the magnetic moments of “spins,” or nuclei with an odd number of protons and/or an odd number of neutrons. Although several elements possess a magnetic moment, typical *in vivo* applications are tuned to examine hydrogen-1.

The spins interact with externally applied magnetic fields to provide signals that can be used to reconstruct meaningful images. Normally, the spins are randomly oriented

and cancel each other, thus producing a net magnetic moment of zero. However, in the presence of an external magnetic field B_0, the spins become oriented in the direction of B_0 (conventionally referred to as the longitudinal or z direction). Since the spins are aligned in the same direction, they produce a non-zero magnetization vector. The spins also resonate at the Larmor frequency ω:

$$\omega = \gamma B \tag{2.15}$$

where γ is the gyromagnetic ratio, a constant that depends on the atom, and B is the applied magnetic field. In the MR system, the B_0 field is constantly on, and the spins are considered to be at equilibrium under this condition.

During imaging, a second magnetic field, the radiofrequency (RF) or B_1 field, is applied in the transverse, or x-y plane, and excites the spins, causing them to rotate away from equilibrium and towards the transverse plane (Figure 2.2). The resulting changes in magnetization in the transverse plane induce a change in flux, that in turn causes a change in voltage, which is detected by an RF coil. The time between one RF excitation and the next is the repetition time T_R, and the time from the RF excitation to the center of the data read-out period is the echo time T_E.

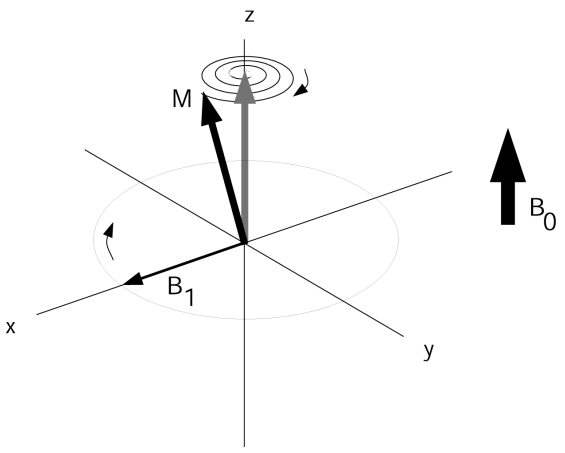


Figure 2.2: Effect of magnetic fields on the magnetization vector M. Application of the B_0 field causes the spins to line up in the direction of the field, producing a net magnetization in that direction. This is depicted by the gray arrow along the z axis. Upon turning on the B_1 field in the x-y plane, the spins begin to tip away from the z axis towards the x-y plane. Recall, also, that the spins are rotating at the Larmor frequency. The resulting motion of the magnetization vector is a spiral pattern, as shown. *Courtesy of Dwight Nishimura.*

Once the B_1 field is turned off, the spins relax towards equilibrium. The rate at which they recover their magnetization in the longitudinal direction is governed by the time constant T_1, and the rate at which the transverse component of their magnetization disappears is governed by T_2. T_1 and T_2 are material-dependent properties which can be exploited to produce contrast between different materials in the body.

Lastly, linear gradient fields are applied so that spatial information may be obtained. With the application of a linear gradient field, the frequency at which a spin resonates is related to its location in space. For example, if a gradient G_x is applied in the x-direction, the spins experience a total magnetic field B:

$$B = B_0 + G_x x \tag{2.16}$$

and resonate at a frequency ω:

$$\omega = \gamma(B_0 + G_x x) \tag{2.17}$$

The fact that the application of linear gradient fields can create a relationship between the resonant frequency and spatial position is key to constructing an MR image.

As described above, changes in magnetization ultimately result in changes in voltage, which are detected and used to fill k-space, a domain where each point represents a spatial frequency component of the image. The k-space data can then be Fourier transformed to produce the images that are used clinically. The terms "phase encode" and "frequency encode" describe ways of altering gradients so that they can be used to determine spatial location in k-space. A phase-encoded gradient field produces changes in magnetization phase which vary in proportion to the distance along a given direction, whereas a frequency-encoded gradient field alters the resonant frequency of the magnetization, as described in Equation (2.17). By utilizing both encoding methods, it is possible to fill in k-space. A common data acquisition scheme acquires data for one row of k-space at a time, with the phase encode varying for each RF excitation. Other acquisition schemes include collecting data along a spiral trajectory and interleaving the data collection.

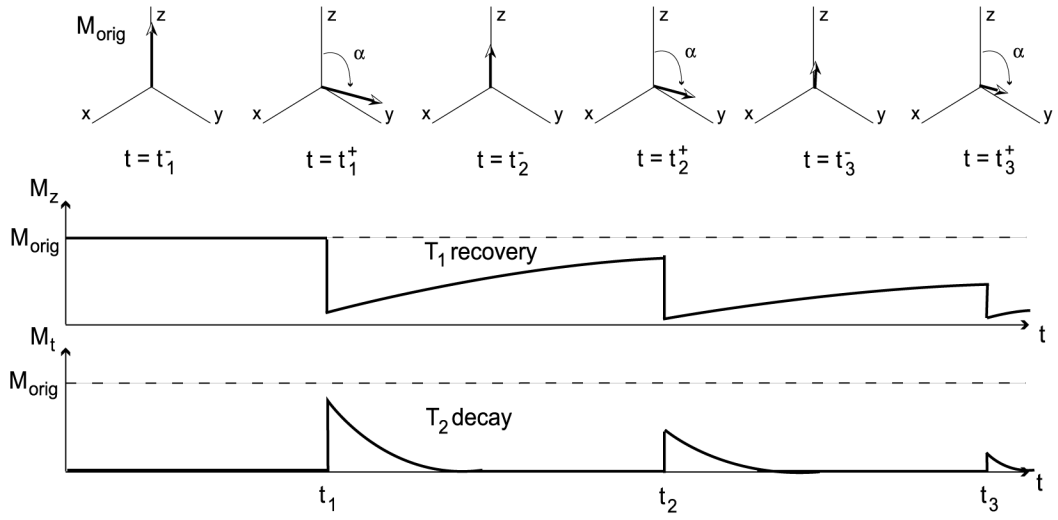


Figure 2.3: Saturation of spins. The spins originally have a longitudinal magnetization component M_z equal to M_{orig}. Their transverse (x-y) magnetization component M_t is zero. Upon excitation at time t_1, the spins are rotated away from the z-axis by a flip angle α, resulting in a transverse magnetization value of $M_{orig}\sin(\alpha)$. The time between t_1 and t_2 is long enough for complete T_2 decay, so that there is no transverse magnetization at time t_2^-. However, this same time interval is insufficient for complete recovery of the longitudinal magnetization component, so at t_2^-, M_z has a value slightly less than M_{orig}. Therefore, upon excitation at time t_2, the resulting transverse magnetization component is less than it was at t_1. Subsequent excitations result in smaller and smaller magnetizations, leading to spin saturation.

2.2.2 Magnetic Resonance Angiography

2.2.2.1 Principles of Magnetic Resonance Angiography

Magnetic resonance angiography (MRA) provides an image of the blood vessels and can be used to identify regions with low blood flow. The time-of-flight (TOF) method is one way to generate MRA images. It depends on flow-related enhancement, in which moving spins have a larger magnetization, and hence, higher signal, than static spins. Flow-related enhancement is produced by repeatedly exciting the spins in an imaging slice. The time between excitations is short compared to T_1, or the time it takes the spins to recover their longitudinal magnetization, so each subsequent excitation results in a smaller magnetization being tipped down into the transverse plane. The final steady-state magnetization is therefore much smaller than the original magnetization (Figure 2.3). The spins produce a low signal and are considered "saturated." On the other hand,

moving spins do not remain in the imaging slice, so they are not repeatedly excited and do not become saturated and are able to generate much higher signals. This contrast between the high signal of flowing spins and the low signal of static spins produces MRA images.

The addition of a contrast agent, such as gadolinium, can further enhance the contrast between the lumen of a blood vessel and the static regions. These contrast agents decrease the T_1 times of the material to which they are added. Therefore, the spins of the contrast-enhanced material recover faster than before, which makes it possible to excite them at a higher rate without saturating them. However, at this higher excitation rate, the static spins will become even more saturated and produce lower signals. Thus, the contrast between the modified material and static spins is increased. This type of MRA is sometimes referred to as contrast-enhanced magnetic resonance angiography (CE-MRA).

2.2.2.2 CE-MRA Accuracy and Sensitivity

CE-MRA is generally considered an improvement over the traditional TOF-MRA techniques. Because saturation effects are much less of a concern when acquiring CE-MRA data, imaging parameters, such as the number of excitations, flip angle, and repetition time T_R, which influence spin saturation, are not as critical to obtaining images with good contrast. Furthermore, the shorter T_1 values of the contrast-enhanced blood allow for improved temporal resolution and shorter overall scan times, decreasing the effects of motion blurring and other time-related artifacts.

Scan times can be reduced if one accepts a decrease in spatial resolution. The larger voxel sizes make it more difficult to accurately determine the vessel boundary. Hoogeveen, *et al.* studied the effect of spatial resolution on TOF-MRA data for steady flow in a 5.3 mm diameter tube and determined that at least 3 pixels were needed across the diameter in order to acquire accurate diameter measurements [73]. A smaller pixel-to-diameter ratio distorted the tube shape. Although this experiment was performed using TOF-MRA data, it is also applicable to CE-MRA data, which generally has better contrast.

Moreover, the decrease in spatial resolution can lead to signal loss due to intravoxel phase dispersion, in which the signals from the spins within a voxel are not coherent and cancel each other out. This would occur in situations of complex or turbulent flows and is a more significant problem in larger voxels, which contain more spins.

It is also worth noting that in order to increase the temporal resolution as much as possible, CE-MRA sequences currently do not use flow compensation, a technique in which the position- or velocity-dependent phase shifts are designed to always be zero. (See Section 2.2.3.1 for more details). Without flow compensation, these phase shifts, if not consistent throughout a voxel, would result in signal loss due to intravoxel phase dispersion. This is a notable problem in regions such as a stenosis, where accelerating, complex flow can exist. Experiments performed in a Plexiglas model of a 90% stenosis showed significant signal loss when flow compensation was not used [74]. This signal loss leads to an underestimation of the vessel lumen. In a study of 100 patients, CE-MRA underestimated the lumen size in 7 cases [75]. It was proposed that the lack of flow compensation was one cause for this underestimation.

In vitro experiments by Evans and colleagues also indicate that fractional echo can affect the signal loss in CE-MRA images. Fractional echo, also referred to as partial echo or asymmetrical sampling echo, acquires a percentage of k-space and then utilizes an interpolation scheme to fill in the rest of k-space. By not acquiring all the data needed to fill k-space, echo times and total scan times can be decreased. Examination of images of steady flow through a tube with a 90% stenosis found that the lower the fractional echo, the smaller the area of signal loss [74]. This study suggested that the smaller gradient magnitudes and durations which occur with lower fractional echoes are the reason for the decrease in signal loss. Furthermore, the experimental results showed that with fractional echo, there is little difference in signal loss regardless of whether flow compensation is used. In contrast, flow compensation had a large impact on signal loss for full echo sequences.

In summary, CE-MRA is capable of producing accurate anatomic images. As with any imaging modality, the accuracy is limited by the spatial resolution. Increased spatial resolution produces more accurate images. CE-MRA is also dependent on laminar flows,

and in regions where this assumption does not hold true, such as downstream of a stenosis, signal loss can occur and the image will not reflect the true geometry. Flow compensation and fractional echo can minimize the signal loss.

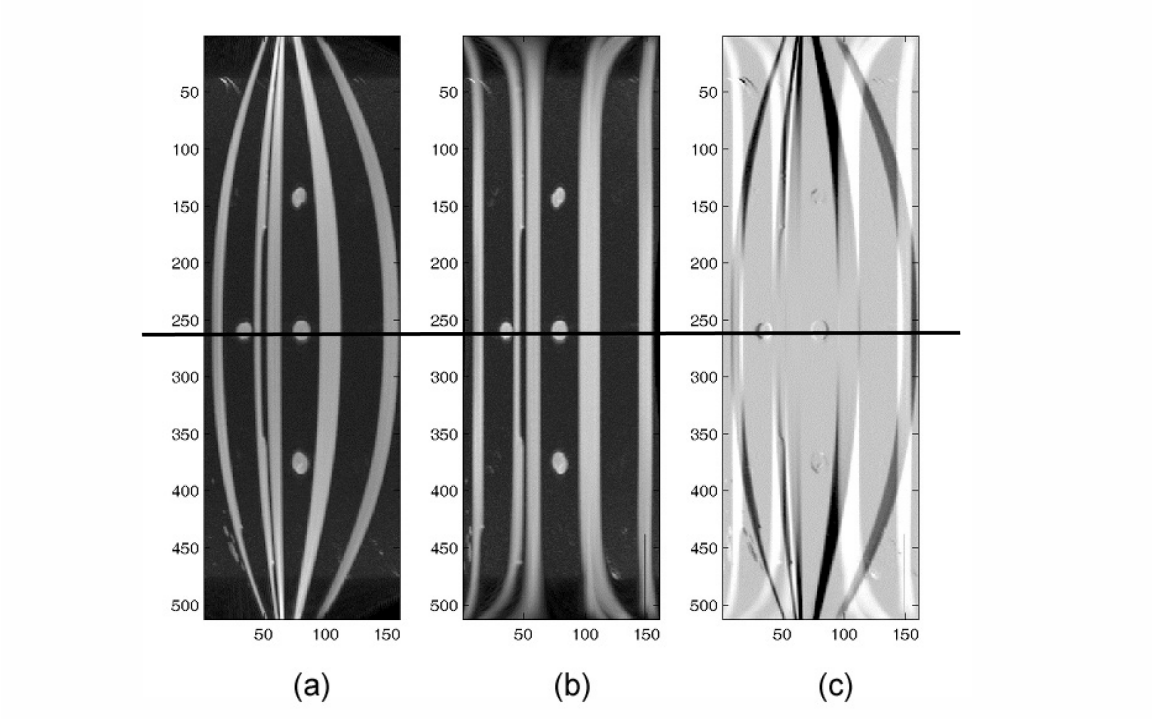


Figure 2.4: Maximum intensity projection images with and without grad warp correction. These are sagittal views of a series of tubes both parallel and perpendicular to this view. The black line through the center of the images is the center of the field of view, which was 48 cm. All quantities are in mm. (a) The uncorrected image shows severe distortion of the tubes. Note the curvature that is introduced by the grad warping. The tubes are also tapered at the ends, leading to a large underestimation of the tube diameter at these locations. (b) The corrected image produces tubes that are much straighter and more uniform in diameter. (c) This is a subtraction image highlighting the differences between the corrected and uncorrected images. *Courtesy of Mary T. Draney.*

2.2.2.3 Grad Warp Correction

Image distortion can also occur when gradient non-linearities are not accounted for. Equation (2.17) describes how the frequency of the spins can be directly mapped to a spatial position, assuming that the gradients are known. If the physically applied gradient differs from what the MR reconstruction algorithm assumes, then the MR signals will be mapped to an incorrect location. These gradient non-linearities not only result in incorrect positioning of an object, but can also cause changes in the object shape and size. This problem is commonly referred to as the "grad warp" problem. While commercial

MR systems currently correct for gradient non-linearities in-plane, they generally do not correct for the non-linearities in the slice direction.

Draney and colleagues have examined the distortion that occurs due to these non-linearities [76]. Experiments were performed on long tubes filled with gadolinium-doped water. Figure 2.4 demonstrates the severe distortions that can occur, with the straight tubes appearing curved in the images. Figure 2.5 shows that errors greater than 10 mm can occur in the diameter measurement. Note that the true diameter was approximately 25 mm, so that a 10-mm error was significant. The errors were larger further from the center of the field of view, with measureable errors occurring at distances greater than 70 mm from the center. An algorithm similar to what is currently used for correcting non-linearities in-plane can be applied to correct for the non-linearities in the slice direction.

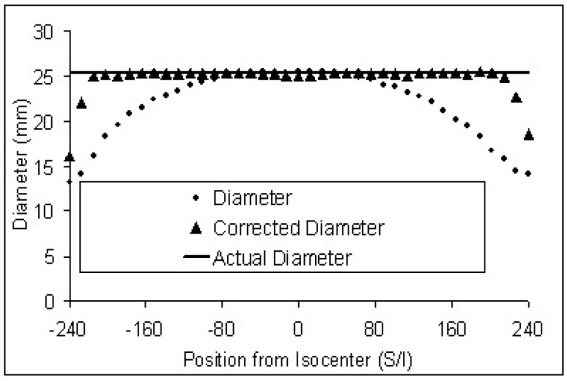


Figure 2.5: Comparison of tube diameter as measured from images with and without grad warp correction. *Courtesy of Mary T. Draney.*

2.2.3 Phase-Contrast Magnetic Resonance Imaging

While the flow enhancement technique described in Section 2.2.2 can be used to image flow, it is limited in the quantitative information it can provide. MRI methods based on the magnetization phase are more valuable for quantitative velocity measurements in multiple dimensions. With the application of a linear gradient field, the phase can be related to the velocity of an object.

2.2.3.1 Principles of Phase-Contrast Magnetic Resonance Imaging

The phase ϕ is a measure of how much a spin has rotated over a given amount of time t:

$$\phi = \int_0^t \omega(\tau) d\tau \tag{2.18}$$

where $\omega(\tau)$ is the frequency at which the spin rotates. Ignoring the contribution from the main field B_0, which is the same for all spins, and generalizing the linear gradient field $G(\tau)$ and the location of the spins $r(\tau)$ so that they vary with time τ, Equation (2.17) can be rewritten as:

$$\omega(\tau) = \gamma(G(\tau) \bullet r(\tau)) \tag{2.19}$$

Using the Taylor series expansion, the location of the spins can be expressed as:

$$r(\tau) = r_o + v\tau + \frac{1}{2} a\tau^2 + \ldots \tag{2.20}$$

where r_o is the position at time 0, v is velocity, and a is acceleration. For the x direction, substitution of Equations (2.19) and (2.20) into Equation (2.18) yields the following expression for the phase:

$$\phi(t) = \gamma \left[x_o \int_0^t G_x(\tau) d\tau + v_x \int_0^t G_x(\tau) \tau d\tau + \frac{1}{2} a_x \int_0^t G_x(\tau) \tau^2 d\tau + \ldots \right] \tag{2.21}$$

If velocity is constant and higher-order terms can be ignored, the phase is then proportional to the velocity:

$$\phi(t) = \gamma \left[x_o \int_0^t G_x(\tau) d\tau + v_x \int_0^t G_x(\tau) \tau d\tau \right] \tag{2.22}$$

$$\phi(t) = \gamma(x_o M_0(t) + v_x M_1(t)) \tag{2.23}$$

where $M_0(t) = \int_0^t G_x(\tau) d\tau$ is the zeroth moment of the x gradient and $M_1(t) = \int_0^t G_x(\tau) \tau d\tau$

is the first moment of the *x* gradient. Therefore, the phase of an object provides information about the object's velocity.

This relationship is the basis of Fourier velocity encoding, a time-consuming method for acquiring the velocity distributions at each position in space. The more clinically useful technique for measuring velocities is phase-contrast magnetic resonance imaging (PC-MRI). PC-MRI assumes that a single velocity can be assigned to each voxel in space. To decrease the sensitivity of the phase measurements to static magnetic field inhomogeneities, phase differences are usually measured:

$$\Delta\phi = \gamma v_x \Delta M_1 \tag{2.24}$$

In this way, phase shifts that are the same for both M_1 values, such as those due to static magnetic field inhomogeneities, cancel each other out. The phase difference thereby reflects only the velocity and the change in the first moment. These phase shifts are usually achieved by subtracting data acquired using two bipolar gradients of different amplitudes. Note that the typical MR pulse sequence is also designed so that M_0 is zero at the measurement time, so that term is dropped.

The phase difference can be converted to a velocity measurement if the value of the velocity encoding, or v_{enc}, is known. The v_{enc} is associated with a phase difference of 180^o, or π radians, and is the maximum absolute velocity that can be unambiguously measured:

$$v_{enc} = \frac{\pi}{\gamma \Delta M_1} \tag{2.25}$$

The velocity for a given voxel is then:

$$v = \frac{\Delta\phi}{\gamma \Delta M_1} = \Delta\phi\left(\frac{v_{enc}}{\pi}\right) \tag{2.26}$$

The method is therefore able to measure phases from -180^o to $+180^o$, or correspondingly velocities from $-v_{enc}$ to $+v_{enc}$. Aliasing results when the absolute value of the phase difference is greater than 180^o. For instance, a phase difference of 200^o is

indistinguishable from a phase of -160°. Therefore, it is important to choose a v_{enc} that is greater than the largest velocity that will be measured.

2.2.3.2 Segmented k-Space PC-MRI Versus Cine PC-MRI

Different implementations of PC-MRI exist: cine PC-MRI [77, 78] and segmented k-space PC-MRI [79-81]. The primary difference between them is the number of phase encodes that are acquired within one cardiac cycle, resulting in trade-offs between total scan time and temporal resolution.

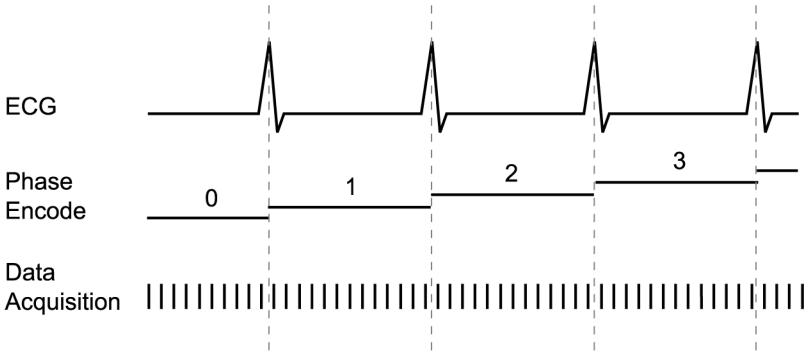


Figure 2.6: Cine PC-MRI sequence. Data is continuously acquired, while the phase encoding gradient changes whenever a trigger from the ECG (or the plethysmograph) occurs. This results in one line of k-space being acquired for each cardiac cycle.

In cine PC-MRI, data is continuously acquired. The value of the phase encoding is constant over a cardiac cycle, only changing when a trigger from the electrocardiogram (ECG) or plethysmograph is observed (Figure 2.6). This results in one line of k-space being acquired for each cardiac cycle. The total time T_{total} to acquire data with a cine sequence is:

$$T_{total} = n_{PE} \cdot NEX \cdot RR \tag{2.27}$$

where n_{PE} is the number of phase encodes (equivalent to the number of lines in k-space), NEX is the number of excitations to average together, and RR is the period of one cardiac cycle. Note that the total scan time is independent of parameters such as T_R and T_E. The actual number of frames n_{frames} acquired per cardiac cycle is:

$$n_{frames} = \left(\left(1 + n_{vel} \right) \cdot T_R \cdot HR \right)^{-1} \tag{2.28}$$

where HR is the heart rate in beats per second, n_{vel} is the number of velocity components, or velocity directions, being acquired, and T_R is the repetition time in seconds.

With a segmented k-space acquisition scheme, several phase encodes are acquired for each cardiac cycle. As with cine PC-MRI, data is continuously acquired. However, instead of acquiring just one new phase encode with each ECG or plethysmograph trigger, multiple phase encodes are acquired (Figure 2.7). Since more phase encodes are acquired per cardiac cycle, the total scan time can be considerably shorter than the equivalent cine sequence. For the segmented k-space sequence, the total scan time T_{total} is:

$$T_{total} = NEX \cdot RR \cdot \left(\frac{n_{PE}}{n_{vps}} \right) \tag{2.29}$$

where again n_{PE} is the number of phase encodes, NEX is the number of excitations to average together, and RR is the period of one cardiac cycle. n_{vps} is the number of phase encoding lines acquired per cardiac cycle, also referred to as the number of views per segment. The significantly shorter scan times enable the acquisition of data within one breathhold, thereby removing artifacts due to respiratory motion. The cost of the shorter scan time is a poorer temporal resolution relative to the cine sequence. The equation for the temporal resolution is similar to that for the cine sequence, with an additional factor due to the number of views per segment n_{vps}:

$$n_{frames} = \left(\left(1 + n_{vel} \right) \cdot n_{vps} \cdot T_R \cdot HR \right)^{-1} \tag{2.30}$$

Assuming that all the parameters are the same for the two sequences and that the segmented k-space sequence utilizes two views per segment, then the cine sequence would result in twice as many actual frames per cycle as the segmented k-space sequence, meaning that the temporal resolution for the cine sequence is twice that of the segmented k-space sequence.

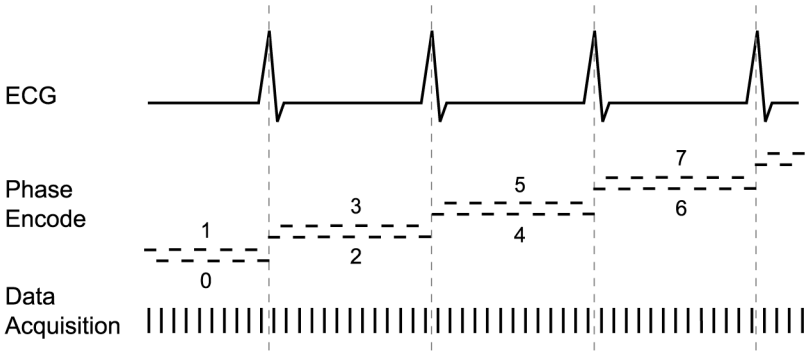


Figure 2.7: Segmented k-space sequence. Data is continuously acquired. Multiple phase encoding gradients are applied during each cardiac cycle, thereby acquiring multiple lines in k-space for each cycle. In this figure, 2 lines of k-space are acquired per cardiac cycle. In other words, there are 2 views per segment. The trigger from the ECG (or the plethysmograph) signals that a new set of phase encoding gradients should be applied.

Two levels of interpolation are then applied to the data, whether acquired with a cine or segmented k-space sequence. Since each phase encode, or in the case of segmented k-space, each set of phase encodes, is acquired during a different cardiac cycle and the period of the cardiac cycle can vary from heartbeat to heartbeat, the time period over which data is collected for each phase encode can differ. To account for these differences, a linear dilation method is typically used to interpolate the data so that they all range over the same time period. The linear dilation model simply stretches the data in time, assuming that the percentage of the cardiac cycle that corresponds to systole remains the same regardless of how long the cardiac cycle is (Figure 2.8). Physiologically, though, a lengthening or shortening of the cardiac cycle primarily results in a lengthening or shortening of diastole, respectively. Therefore, interpolation using the linear dilation model does not produce a completely physiologically accurate data set.

Additionally, interpolation is required to generate the user-specified number of frames per cardiac cycle. Linear interpolation is applied to the acquired data to produce a continuous function, which is then sub-sampled to the desired number of frames per cardiac cycle. The interpolation step is equivalent to a low-pass filtering operation, where high frequencies, which correspond to rapidly changing variations in the waveform as seen during systole, are attenuated. Frayne and Rutt demonstrated this effect on cine

PC-MRI measurements and showed that smaller T_R values cause less attenuation of high frequencies and thereby produce more accurate peak velocity and flow waveforms [82].

With this understanding of how the data is acquired and how interpolation can affect the data, it is now possible to examine the accuracy and precision of PC-MRI measurements under different conditions.

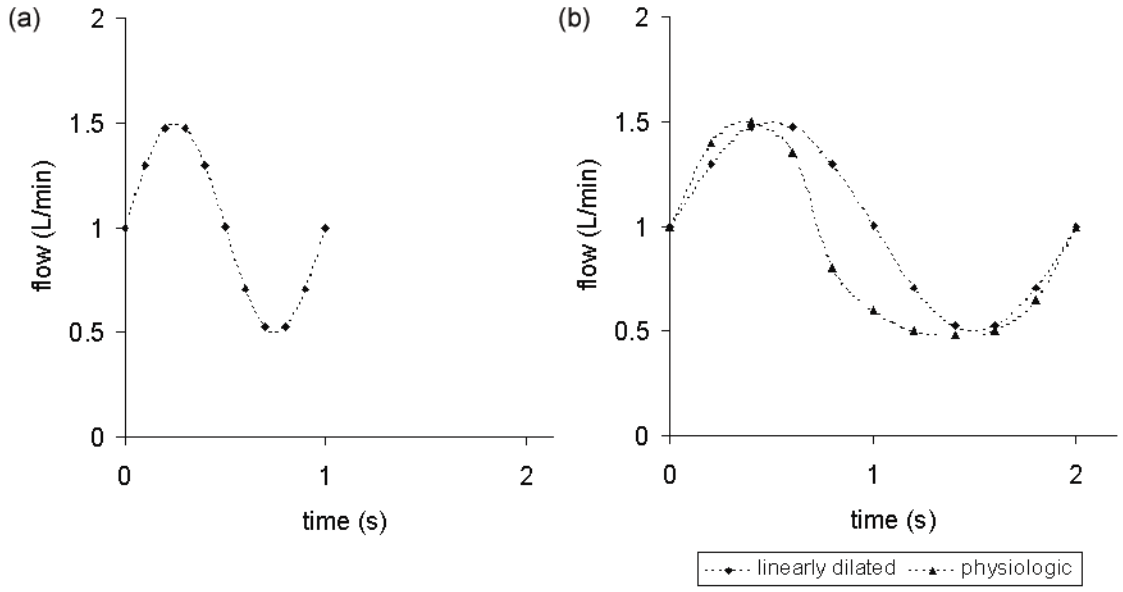


Figure 2.8: Diagram simulating the effect of interpolation using the linear dilation model. (a) A data set with an original period of 1 second. (b) The diamonds correspond to the dilation, or stretching, of the data in time to a period of 2 seconds. However, physiologically, an increase in the period of the cardiac cycle results primarily in an increase in the diastolic portion of the cardiac cycle, as represented by the triangles.

2.2.3.3 Accuracy of Velocity Measurements

Accuracy indicates how well a measurement compares to the true value, whereas precision assesses the repeatability of a measurement. In this section, the accuracy of PC-MRI velocity measurements is considered. The precision of these measurements is deferred to Section 2.2.3.5.

A number of experiments have been performed examining the accuracy of PC-MRI velocity measurements under various conditions. In straight tubes, velocity profiles have been validated against theoretical predictions for both steady flow [83] (upstream Reynolds number of 500) and pulsatile flow [84]. The pulsatile flow experiment studied a

mean flow of 15 mL/s through a 0.95 cm diameter tube at 3 frequencies: 0.55 Hz, 1.0 Hz, and 2.0 Hz. The linear regression fit between the PC-MRI measurements and the analytic velocities had a slope of 0.998 ± 0.002, with a coefficient of determination of r^2 = 0.997. Relative to the temporal and spatial velocity average, there was a root-mean-square error of 7.5%. Root-mean-square differences of 9-13% relative to the peak velocity were found when comparing PC-MRI measurements against analytic results for flow in a tube with a sinusoidal input, while the difference was 4% with a triangle input waveform [85]. The error at the wall was equivalent to or larger than the error at the center of the tube.

PC-MRI velocity measurements have also been compared against other imaging modalities. Comparisons against peak velocities measured with Doppler ultrasound in the human abdominal aorta showed reasonable agreement [86]. In the slightly more complex geometry of a stenosis in a straight tube, comparisons have been made between PC-MRI measurements and laser Doppler anemometry (LDA) measurements [87]. Three diameters upstream of the stenosis, the velocity profiles measured with LDA and PC-MRI were similar. However, at 0.5 diameters upstream of the stenosis and at 1.5 and 6 diameters downstream of the stenosis, the PC-MRI measurements deviated significantly from those acquired with LDA.

Modifying the imaging parameters can improve the accuracy of the velocity measurements. In their study with a stenotic model, Siegel and colleagues demonstrated that an improved signal-to-noise ratio, such as can be achieved by increasing the averaging, increased the accuracy of the PC-MRI velocity measurements [87]. Steinman, *et al*.'s study of displacement artifacts, in which the velocity is mapped to an incorrect spatial location or an incorrect velocity is mapped to the correct spatial location, demonstrated that the error in velocity measurement was dependent on both the sequence timing parameters and on the flow conditions. By comparing PC-MRI measurements with numerical simulations of blood flow both with and without displacement artifacts, they concluded that displacement artifacts tended to occur in regions of complex flow, such as at an anastomosis, and that 3D PC-MRI is less sensitive to displacement artifacts than 2D PC-MRI because of sequence timing parameters [88]. Additional errors may

occur due to non-linearities in the gradient fields. Similar to the grad-warping errors described in Section 2.2.2.3, the gradient inhomogeneities can also distort the velocity measurements up to 25%, but can be corrected during post-processing [89]. Furthermore, in voxels containing both moving and static particles, such as near a wall, partial volume effects occur. Partial volume effects result in an underestimation of the velocity of the moving particles, since the velocity for the voxel is a weighted average of the velocities of both the moving and static elements. These effects can be minimized by enhancing the signal from the moving particles and suppressing the signal from the static particles [90]. An underestimation of velocity components can also occur if the slice plane is not prescribed to be perpendicular to the flow direction (See Figure 2.9) [90].

These experiments have demonstrated the feasibility of using PC-MRI to acquire accurate velocity data. However, in areas of complex flow, such as downstream of a stenosis or at an anastomotic junction, PC-MRI may not be as accurate. Furthermore, the accuracy of the velocity measurements acquired with PC-MRI is highly dependent on the imaging parameters. Changes in the imaging parameters that improve the signal-to-noise ratio, such as increasing slice thickness and increasing the averaging, and that improve the contrast between the moving and static particles can improve the accuracy of PC-MRI measurements. Moreover, minimizing the sequence timing parameters and ensuring that the slice plane is perpendicular to the flow direction diminishes the effects of imaging errors.

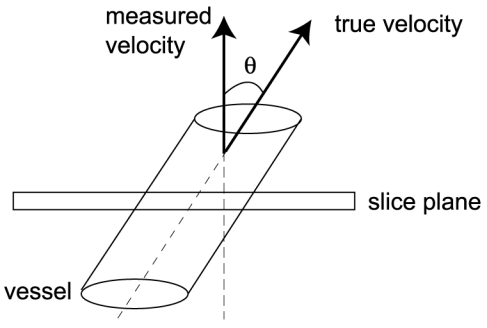


Figure 2.9: Underestimation of velocities due to slice plane angle. When the slice plane is not perpendicular to the vessel axis, the measured velocity component will underestimate the true velocity component by a factor of cos(θ), where θ is the angle between the vessel axis and the normal to the slice plane.

2.2.3.4 Accuracy of Flow Measurements

2.2.3.4.1 Computing Flow from Velocity Measurements

Volumetric flow Q (in mL/s) can be computed as follows:

$$Q = A \cdot \bar{v} \tag{2.31}$$

where A is the area in cm^2 of the region of interest and $\bar{v}$ is the spatially averaged velocity in cm/s over that region of interest. While this is a straightforward computation, difficulty arises in setting imaging parameters to achieve the desired degree of accuracy and determining the region of interest (See Section 2.2.3.4.3).

Post-processing techniques can also cause variation in the flow computations. In this research, two custom software programs were used for computing flow measurements from PC-MRI data: *vcalc* and *Geodesic*. The primary difference between vcalc and Geodesic is the manner in which the region of interest is determined. This is discussed in more detail in Section 2.2.3.4.4.

2.2.3.4.2 Previous Studies

Studies have been performed both *in vitro* and *in vivo* to determine the accuracy of PC-MRI-based flow measurements. A common *in vitro* experiment compares flow measurements derived from PC-MRI data with physical measurements using a bucket and stopwatch. Excellent correlation was found between measurements made with these two techniques for steady flow through a tube [91, 92]. Comparisons between these two methods for pulsatile flow varied. Some studies demonstrated good agreement [92, 93]. However, Sondergaard and colleagues' measurements of flow through a stenosis had accuracies of only 72-84%, depending on the degree of stenosis [94]. They found that the PC-MRI measurements tended to underestimate the flow. Other *in vitro* investigations have compared PC-MRI-derived flow measurements with quantities from a programmable flow pump [95] or from an ultrasound flow probe [96] and demonstrated good agreement.

In vivo experiments comparing PC-MRI measurements with other measurement techniques also demonstrated good agreement. Pelc, *et al.* compared measurements from PC-MRI with those from an ultrasound flow probe implanted in dogs and showed that the

two were linearly related with a slope of 1.053 and a correlation coefficient r = 0.995 [97]. Similar results were found for comparisons in abdominal aortas in 9 human subjects, where PC-MRI measurements were linearly related to Doppler ultrasound measurements with a slope of 1.11 and a correlation coefficient r = 0.99 [86]. PC-MRI flow measurements through the aorta have also compared favorably to left ventricular stroke volumes [91, 98].

Comparable experiments have been performed to investigate the accuracy of flow measurements acquired with segmented k-space PC-MRI methods. Zhang and colleagues demonstrated excellent agreement between the segmented k-space measurements and those obtained with an ultrasound flow probe, as well as with cine PC-MRI measurements [99]. Their measurements were acquired for steady and pulsatile flow through straight tubes of various diameters. In addition, they showed good agreement between cine and segmented k-space PC-MRI flow measurements in the ascending aorta of two human subjects. However, they noted that due to temporal resolution issues, the more lines per segment used, the greater the potential for inaccuracies, particularly at peak systole. This confirms the results of Poutanen and colleagues. They found that segmented k-space measurements led to time shifts and smoothing of the flow waveforms and concluded that the more lines per segment used, the more inaccurate the results, with 7 or more lines per segment producing results that are not clinically useful [100]. While Thomsen, *et al.* also observed smoothing in flow waveforms acquired with the segmented k-space method, they found no significant difference in the average flow values obtained with segmented k-space and cine PC-MRI [81]. Their studies examined flow in a straight tube, in a tube with a 90% stenosis, and in the left renal artery. Similar comparisons by Lee and colleagues demonstrated that segmented k-space techniques (2 lines per segment) led to slightly less accurate average flow values than cine PC-MRI. Comparisons of the flow waveforms acquired with the two different PC-MRI methods were reasonable, with better agreement occurring during systole than in diastole due to increased noise during diastole [101].

While it has been demonstrated that PC-MRI can measure flow very accurately, as with the velocity validation experiments, these results are dependent on the imaging

parameters and flow conditions. The conclusions from the segmented k-space investigations are a prime example, in which accuracy was found to be related to the number of lines per segment. Section 2.2.3.4.3 discusses how other imaging parameters and flow conditions can affect PC-MRI flow measurements.

2.2.3.4.3 Effects of Imaging Parameters and Flow Conditions on Accuracy

The angle of the slice plane relative to the direction of flow is important for obtaining an accurate measurement of flow. Section 2.2.3.3 described the error in velocity associated with slice plane angle. However, that error is offset by an error in the area, so that theoretically, flow is insensitive to slice plane angle. Experimentally, though, it was determined that the thicker the slice with respect to the vessel diameter, the larger the effect of the plane angle on the flow measurements. In a 6 mm diameter tube, imaged with a 10 mm thick slice, a misalignment in slice plane angle of 34^o resulted in an error of approximately 15% in flow [102]. Experiments with large slice-thickness-to-vessel-diameter ratios demonstrated that the larger the misalignment in slice plane angle, the greater the error in flow [102, 103]. While it is desirable to prescribe the slice plane to be perpendicular to the vessel axis, in some cases, this may lead to longer T_R values and affect the temporal resolution of the data acquired.

Experimental results also indicate that the higher the in-plane resolution, the more accurate the flow calculations [102, 103]. Tang, *et al.* showed that errors in flow were less than 10% if there were at least 4 pixels across the diameter [103]. Data from Wolf, *et al.* showed that at least 10 pixels across the vessel diameter were needed to achieve an error of less than 9% [102]. Their results also indicated that above a certain number of pixels per diameter, the accuracy of the flow measurements was approximately the same. Choice of the slice thickness is also critical. The thicker the slice, the larger the partial volume effects in edge voxels are and the larger the error in flow measurement, as discussed previously. This relationship has been demonstrated through both *in vitro* experiments and numerical models [102, 103].

Flow variations can also affect the accuracy of the PC-MRI measurements. Recall that PC-MRI is based on the assumption that higher-order terms, such as acceleration, can be ignored (see Section 2.2.3.1). Therefore, if fluid acceleration exists, there will be

errors in the PC-MRI data. Furthermore, flow-related enhancement of the signal can produce an overestimation of the flows, while signal loss, due to intravoxel dephasing or spin saturation which may occur during reverse or circulating flows, will result in an underestimation of the flows. Refer to "Quantitative Magnetic Resonance Flow Imaging" for further details [90].

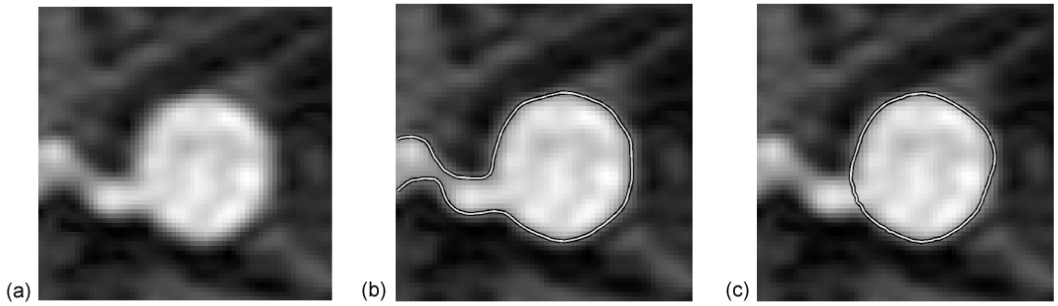


Figure 2.10: Comparison of thresholding versus the level set method for segmentation. Because the level set method is able to incorporate geometric constraints, it is more appropriate for segmentation purposes in certain situations. For example, (a) is the image of a vessel with a branch vessel. If the goal is to determine the contour of the main vessel, then thresholding would be inappropriate. (b) shows the result of thresholding this image. Note that the branch vessel is also included in the segmentation. (c) shows the segmentation generated by the level set method. *Courtesy of Kenneth C. Wang*.

2.2.3.4.4 Post-Processing Methods to Determine Regions of Interest

Because flow is directly dependent on the area of the region of interest (ROI) and on the velocities within that ROI, the manner in which the ROI is determined can be critical to the flow calculation. Since phase images generally have more artifacts due to partial volume effects than the corresponding magnitude images and will therefore produce larger errors in area, magnitude images are typically used for determining the ROI. Vcalc [90] and Geodesic [104, 105], custom software available for computing flows from PC-MRI images, employ different strategies for determining the ROI. Vcalc uses one of the most straightforward, popular methods: thresholding. Thresholding determines the ROI by including all the pixels in the image with an intensity value matching a user-defined criteria, such as being less than a certain value. To ensure that the resulting ROI is a closed region, vcalc finds the closest points surrounding a user-chosen seed point that meet the thresholding criteria and uses those points to define the ROI. Geodesic provides several different segmentation methods, including the level set method, for determining

the ROI. The level set method is a region-growing algorithm that uses intensity gradients and region curvature as stopping criteria [104]. It can be more robust than thresholding in determining ROIs, such as in the case of a vessel with a branch (Figure 2.10) in which only the main vessel is to be segmented out. The sensitivity of the flow measurements to the ROI is dependent on the flow conditions. For instance, in plug flow, where there are sharp changes in flow along the wall and larger partial volume effects, slight changes in the size of the ROI can result in relatively large changes in flow.

2.2.3.5 Precision of Velocity and Flow Measurements

Precision is a measure of reproducibility, indicating the variation of a quantity over repeated measurements. Often, the standard deviation is used as a measure of precision. Theoretically, the standard deviation for phase-contrast-measured velocities σ_v is:

$$\sigma_v = \frac{\sqrt{2}}{\pi} \cdot \frac{v_{enc}}{SNR} \tag{2.32}$$

where v_{enc} is the velocity that corresponds to a phase of 180 degrees and *SNR* is the signal-to-noise ratio of the magnitude image [106]. Note that the standard deviation does not depend directly on the value of the velocity measured. The SNR is influenced by several factors, including the flip angle, the spatial resolution and the number of measurements, or RF excitations, that are averaged together to form the final image. For example, a larger number of excitations results in a greater SNR and subsequently, a smaller standard deviation. Specifically, experiments performed on a disk rotating at 180 rpm demonstrated that the standard deviation for the velocity is inversely proportional to the square root of the number of excitations [107].

The SNR can be estimated using the following formula [108]:

$$SNR = C_{\text{interp}} \left(\frac{\mu[\text{signal ROI from frames A and B}]}{\sigma[\text{noise ROI from frame A - frame B}]/\sqrt{2}} \right) \tag{2.33}$$

where C_{interp} is a scaling factor based on the interpolation scheme used by the sequence. For both cine and segmented k-space sequences, this factor is $1/\sqrt{1.5}$. The signal is

computed by averaging together the means from the signal region of interest in the magnitude image for two frames, designated frame A and frame B in the equation above. The noise is computed as the standard deviation in the noise region of interest in the image formed from the subtraction of the magnitude image of frame B from the magnitude image of frame A. The $\sqrt{2}$ is due to this subtraction step.

The standard deviation for the flow σ_Q calculated from PC-MRI images is based on the standard deviation for velocity for the region of interest $\sigma_{\bar{v}}$:

$$\sigma_Q = \sigma_{\bar{v}} A \tag{2.34}$$

where A is the area of the region of interest. Assuming that the measurement of the area is noiseless, and that velocity is independent of spatial location and time, Equation (2.32) can be substituted into Equation (2.34):

$$\sigma_Q = \sqrt{\frac{\sigma_v^2}{N_f N_{res}}} A = \sqrt{\frac{2N_{res}}{N_f}} \frac{v_{enc} \cdot A_{res}}{\pi \cdot SNR} \tag{2.35}$$

where σ_v is the standard deviation of velocity for a single voxel, N_{res} is the number of independent resolution elements in the region of interest, A_{res} is the area of each resolution element, and N_f is the number of independent time frames in a single cycle [90]. Now, the SNR can be defined as:

$$SNR = SNR_o \cdot \Delta z \cdot A_{res} \tag{2.36}$$

where SNR_o is the SNR per unit volume of tissue, A_{res} is the area of the element, and Δz is the slice thickness. Substituting this equation into Equation (2.35) results in the following equation for the standard deviation for flow:

$$\sigma_Q = \sqrt{\frac{2N_{res}}{N_f}} \frac{v_{enc}}{\pi \cdot SNR_o \cdot \Delta z} \tag{2.37}$$

So, as with the standard deviation for velocity, the standard deviation for flow depends on the v_{enc} and SNR_o, the inherent SNR per unit volume of tissue which is independent of the spatial resolution. In addition, the standard deviation for flow is proportional to the

number of elements in the region of interest and inversely proportional to the number of frames averaged together to generate a single image. Bakker and colleagues' experiment with pulsatile flow through a 5.3 mm diameter, plastic tube confirmed the relationships described by Equation (2.37) [109]. They found that the precision of nontriggered (no gating) PC-MRI measurements improved as the number of excitations averaged together increased and as the v_{enc} decreased. The precision was also shown to vary with flip angle.

Experimentally, the precision for flow measurements with PC-MRI has been shown to be high. Preliminary results from a multi-site study found a precision of 3.5% for steady flow and 5.1% for pulsatile flow through a U-shaped tube with 2 stenoses [95]. An *in vitro* study of both steady and pulsatile flow through a model of the aorta compared flows between two consecutive measurements and found an excellent correlation between the two sets of measurements [96]. For steady flow, the relationship was $Q_1 = 1.00 \times Q_2 + 0.02$ ($r^2 = 0.999$), where Q_1 represented flow from the first measurement and Q_2 was flow from the second measurement. For pulsatile flow, the relationship was $Q_1 = 0.98 \times Q_2 + 0.72$ ($r^2 = 0.997$), where Q_1 was the temporally averaged flow based on results from the first set of measurements and Q_2 was the temporally averaged flow based on the second set of measurements.

The previously cited investigations indicate that PC-MRI is capable of accurately and precisely measuring velocities and flows. However, the accuracy and precision are strongly dependent on both the flow conditions and the sequence parameters.

2.3 Image-Based Modeling

Studies have demonstrated that arterial geometry affects local hemodynamics, such as the flow field and wall shear stress patterns [71, 110, 111], and it is hypothesized that these local changes play a role in the development of arterial disease. Because arterial geometry varies between individuals, particularly in those with disease, any blood flow simulation methods used to predict either the onset of disease or the effectiveness of a particular treatment for arterial disease require subject-specific geometric models. The

standard approach for creating these subject-specific geometric models is to acquire imaging data of an individual's vasculature and then to generate the model by segmenting the imaging data. The different model construction methods that have been used are detailed in Section 2.3.1. Section 2.3.2 then describes the mesh generation technique, which discretizes the geometric model so that finite element solver methods can operate on it. Finally, Section 2.3.3 provides details about Geodesic, custom software that is used to create image-based geometric models and to prescribe subject-specific flow data as boundary conditions for the simulations presented in this work.

2.3.1 Methods for Image-Based Geometric Models

Geometric models can be constructed from volumetric imaging data using either a two-dimensional (2D) or three-dimensional (3D) approach. The 2D approach involves generating a series of 2D profiles, which are lofted together to form a solid model. These 2D profiles are based on segmentations of the imaging data. Commonly used segmentation techniques include thresholding and edge-detection algorithms. Both of these methods rely on intensity or intensity gradient data without regard for geometric considerations. Therefore, these methods could result in segmentations that do not accurately reflect the anatomy of interest and/or are not geometrically smooth enough for discretization. On the other hand, active contour methods, also known as "snakes," do incorporate geometric constraints.

Active contour methods rely on both image intensity information and geometric constraints to deform a boundary, which is often initialized by the user. One efficient and flexible implementation of the active contour approach uses the level set method. For the level set method, the evolution of the boundary is determined by the following equation:

$$\Phi_t + v\left|\nabla\Phi\right| = 0 \tag{2.38}$$

where Φ is a scalar function representing the signed distance to the boundary, t is time, and v is a velocity function that governs how the boundary evolves. The zero level set, where Φ equals 0, defines the boundary.

The present work utilizes a two-phase level set method, described fully in [104]. In the first phase, an exponential velocity function is used to produce a boundary which is near the image edges and which maintains some geometric smoothness:

$$v_i = (\kappa_c - \kappa_i)e^{-\varepsilon|\nabla I_i|} \tag{2.39}$$

where v_i is the velocity at a given position i, κ_c is a user-specified curvature constraint value, κ_i is the curvature at the given position i, ε determines the rate of decay of the velocity function, and ∇I_i is the image gradient value for position i. The value of ε is computed as follows:

$$\varepsilon = \frac{\ln\left(\frac{\kappa_c}{v_{stop}}\right)}{mfactor \cdot \max|\nabla I|} \tag{2.40}$$

where κ_c is a user-specified curvature constraint value, v_{stop} is the stopping velocity, *mfactor* is a user-specified magnification factor, and ∇I is the image gradient. By defining ε in this manner, the velocity for a given point on the boundary begins to decrease when the image gradient associated with that boundary position exceeds the value of $mfactor \cdot \max|\nabla I|$.

The second phase of the method utilizes a velocity function that precisely determines the edge while satisfying exactly the user-defined curvature constraints:

$$v_i = \begin{cases} (\kappa_u - \kappa_i), & \kappa_i > \kappa_u \\ (\kappa_l - \kappa_i), & \kappa_i < \kappa_l \\ \beta(\nabla g_i \cdot \hat{n}_i), & \kappa_l < \kappa_i < \kappa_u \end{cases} \tag{2.41}$$

Again, v_i is the velocity and κ_i is the curvature at the given position i. g_i is equal to $|\nabla I_i|$, the absolute value of the gradient of the image intensity at position i; β controls the rate of the velocity function; and $\hat{n}_i$ is the unit normal at position i and represents the direction of maximum change. κ_u and κ_l are the user-specified upper and lower curvature constraint values, respectively. These two values define the range of acceptable

curvatures for the final boundary. Within this curvature range, the velocity function is solely dependent on the image intensity values. β is defined to be:

$$\beta = \frac{v_{stop}}{|\nabla g|_{stop}} \tag{2.42}$$

where v_{stop} is a stopping velocity, which can be different from the v_{stop} of the first stage, and $|\nabla g|_{stop}$ defines the minimum value that the absolute value of the gradient of the image intensity must be before the boundary stops evolving. Both v_{stop} and $|\nabla g|_{stop}$ are user-specified parameters, although Wang notes that in practice, the values of these two parameters do not matter much as long as they are small [104].

Many of these 2D segmentation methods have analogous 3D approaches. A 3D region-growing method, followed by either iso-surfacing or direct tessellation, has been used to obtain a geometric model from MRA data [112]. Three-dimensional versions of the active contour idea have also been implemented [113, 114], and Bekkers and Taylor have proposed a geometric model construction method that can be applied to any triangulated representation of an object, such as that obtained from an isosurface based on 3D thresholding [115]. Although not currently used as frequently as 2D methods, 3D methods have the potential to yield more accurate models, especially at branches, and will likely be used increasingly in the future.

2.3.2 Mesh Generation Techniques

Once a geometric model is created, it must be discretized into smaller pieces, called elements. The discretized model is referred to as a "mesh," and the process of discretization is called "mesh generation." Mesh generation techniques can be categorized as structured and unstructured. Structured meshes have elements that are connected in a regular pattern, whereas unstructured meshes do not display this regularity. For arbitrary geometric models, unstructured techniques are more appropriate. Numerous automated methods have been developed for generating unstructured meshes, including advancing front methods in which one element is added on at a time and

offsetting techniques based on boundary normals. See [116] for a summary of these and other methods.

The automatic mesh generation software (MeshSim, Simmetrix, Inc., Clifton Park, NY) used in this work is based on the octree method [117]. The octree method utilizes a "divide and conquer" technique, in which the geometric model is recursively subdivided into octants until user-specified size parameters are met. Resulting octants that are inside of the geometric model are divided into tetrahedral elements, while octants that are partially inside of the geometric model are trimmed to match the geometric surface and subsequently divided into tetrahedral elements. Mesh smoothing operations are then applied to generate the final mesh.

2.3.3 Geodesic

Geodesic, custom software created by Wang [104] and Wilson [105], is used to create computational models from imaging data, such as MRI, in the following experiments. Geodesic also provides the capability to map MRI velocity information onto the inlets and outlets of those objects. The model construction process is discussed in more detail in Section 2.3.3.1, while Sections 2.3.3.2 and 2.3.3.3 describe how Geodesic generates the boundary conditions used in the numerical simulations.

2.3.3.1 Geometric Model Construction

A multi-step process is currently used to construct geometric models from imaging data (Figure 2.11). The first step is to create paths along each branch of the vessel network. Two-dimensional (2D) contours, which represent the boundaries of the vessel at that point along the path, are then generated. Using the Parasolid (Unigraphics Solutions, St. Louis, MO) geometry kernel, a nonuniform rational B-spline (NURB) surface is lofted through these contours and bounded to obtain a geometric solid object representing the vessel. A geometric solid object is created for each vessel branch, and these are combined into a single object using the geometric unioning operation. The last step is to use geometric Boolean operations to trim the object so that the object inlet is at the same location as the available inlet boundary condition data.

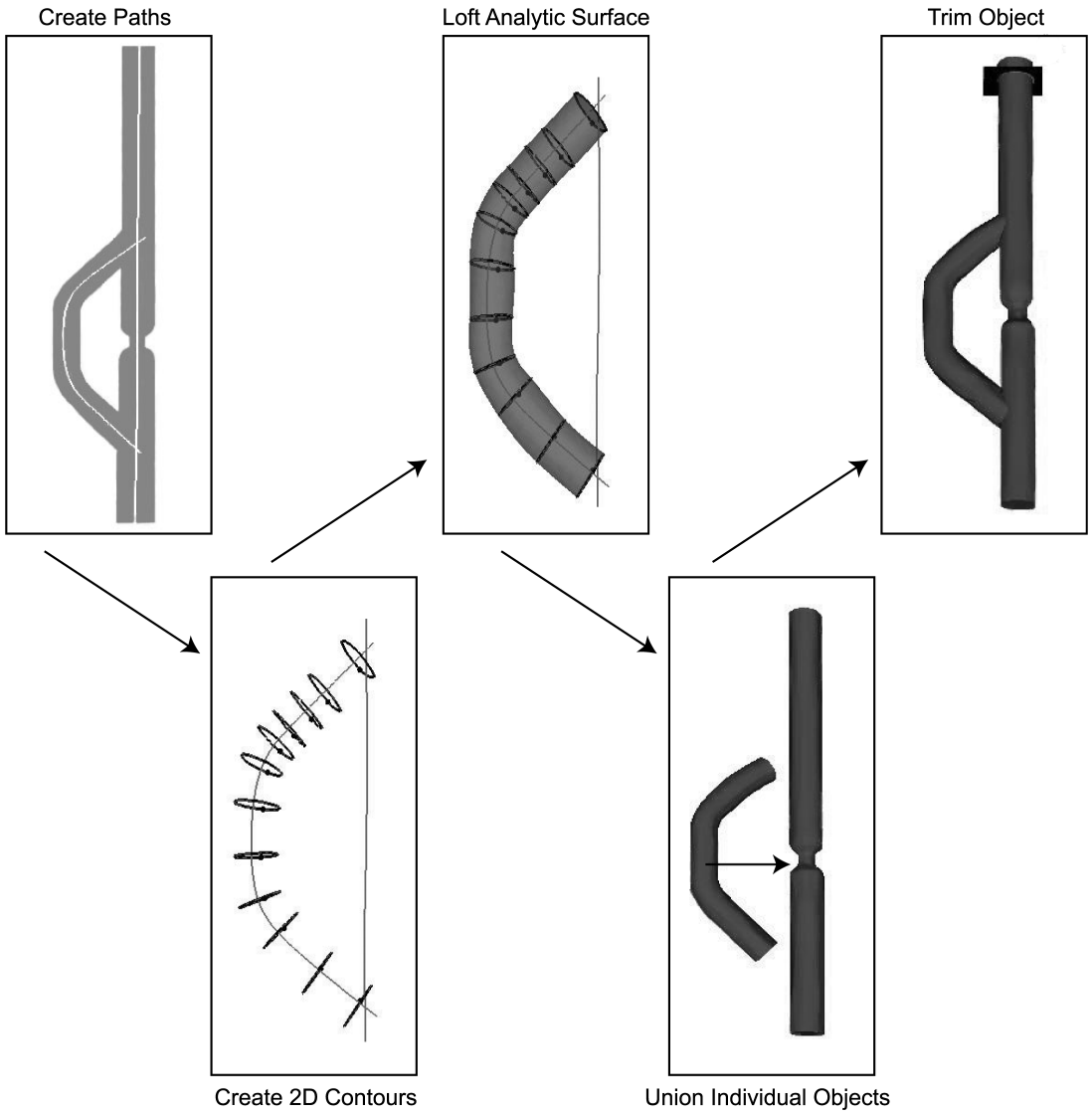


Figure 2.11: Process for creating geometric models. Using the imaging data, paths are created along each branch of the vessel network. Two-dimensional contours are then generated along each path. These contours lie in planes that are perpendicular to the path and represent the boundaries of the vessel at that point along the path. A surface can then be lofted through these contours to create a geometry representing the vessel. A geometric object is created for each vessel branch, and these are combined into a single object using geometric Boolean operations. The last step is to trim the final object so that the appropriate inlet boundary conditions can be applied to the model.

As implemented in Geodesic, the first three steps of this process—creating paths, generating 2D contours, and lofting a surface through the contours—can produce varying results, depending on parameter settings and user preferences. These differences can produce errors in the resulting solid geometry, which can significantly affect the

numerical simulations. Sections 2.3.3.1.1 to 2.3.3.1.3 discuss the effect that each of these steps can have on the final solid geometry.

2.3.3.1.1 Path Construction

The paths represent the central axes of the vessels and as such, they play an important role in defining the final shape of the geometric model. Their importance is especially apparent at junction points, where the paths determine the angles at which vessels connect. Figure 2.12 demonstrates how different paths result in different attachment angles. One path approaches the main vessel section in a straight line at approximately a 45-degree angle, while the other path curves into the main vessel and is more perpendicular to the main vessel. The manner in which the branch vessel connects to the main vessel is reflective of these path variations. Moreover, these variations affect how the branch vessel and the main vessel geometry intersect, and therefore also affect the anastomosis size and shape, which will influence the flow characteristics (Figure 2.12c).

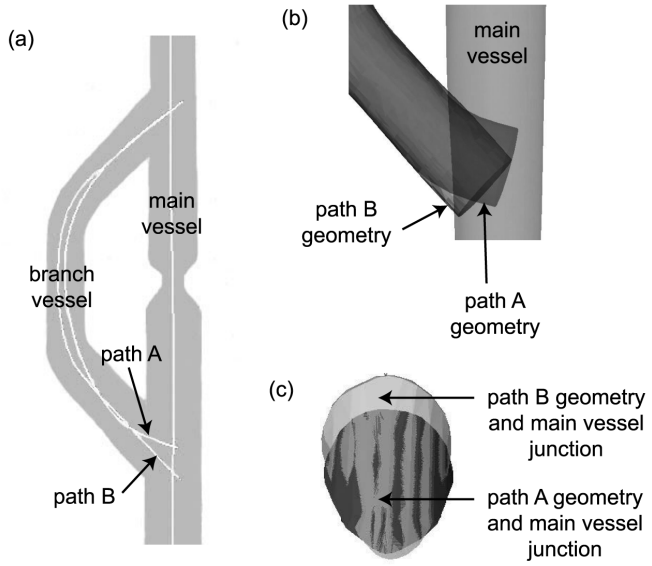


Figure 2.12: Effect of paths on geometric model of vessel junction. (a) Two different paths are prescribed through the branch vessel. Note that they intersect the main vessel path at different angles and at different locations. (b) Subsequently, the geometries constructed from these two different paths intersect the main vessel at different angles. (c) The intersection between the main vessel and the geometries representing the branch vessel also differ in shape and size.

While automated methods for constructing paths are available within Geodesic, the manual method is more robust for situations where multiple paths exist between two

points, such as with the bypass problem. The manual method requires the user to select points along the vessel. A spline is then fit through these points to produce a smooth path. Smoothness is critical for subsequent steps and is strongly dependent on the user-selected points. Points that are spaced too closely together can produce undesirable effects in the path shape that cause difficulties in subsequent steps in the process (Figure 2.13(a)). On the other hand, points that are spaced too far apart will result in paths that do not accurately follow the vessel shape, failing to capture any tortuosity or bends in a vessel (Figure 2.13(b)). In addition, the user specifies the number of points in the spline path, thus determining the minimum spacing of the two-dimensional contours that are generated in the next step of the process.

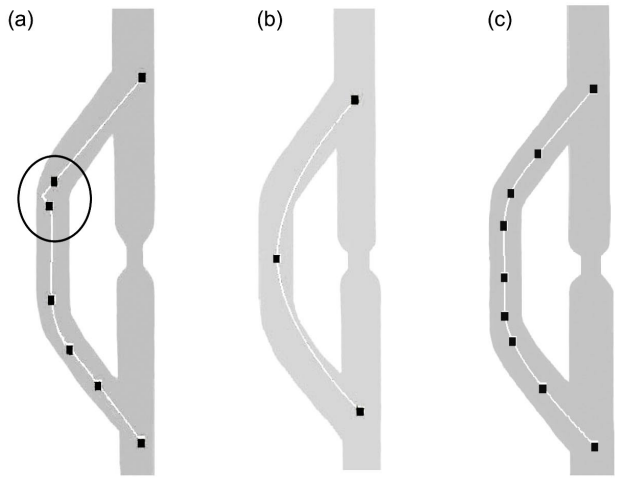


Figure 2.13: Effect of manually chosen points on resulting spline path. The squares are the manually chosen points, and the white lines connecting the squares are the spline paths. (a) Points that are spaced too closely together can result in kinks and other undesirable effects. (b) Points that are spaced too far apart do not adequately describe the vessel shape. In this case, the straight segment of the vessel is not captured by the spline path. (c) A good path.

2.3.3.1.2 Generating Two-Dimensional Contours

In generating the two-dimensional (2D) contours, both the location and shape of the contour heavily influence the final geometry that is created. Similar to the effect of the manually chosen points on the spline fit in the path construction step, the surface lofting step is dependent on the location of the contours. This is discussed further in Section 2.3.3.1.3.

Geodesic provides several methods for creating the 2D contours: analytic functions, thresholding, the level set method, and manual methods. All these methods operate on a plane that is perpendicular to the path. The analytic functions allow a user to use a circle or ellipse to represent the vessel boundary, while thresholding produces isocontours based on the image intensity values. The level set method, as implemented within Geodesic, performs segmentations based on image intensity gradients and user-specified curvature criteria [104] and is briefly described in Section 2.3.1. This approach produces a segmentation that more closely matches the lumen shape than a circular fit while still maintaining the smoothness necessary for creating a solid model. Manual methods are also available so that a user could draw the contour, a useful option in cases where the vessel is small or convoluted. For modeling blood vessels, Wilson provides guidelines as to which of these methods are most appropriate for a given vessel size [105], although ultimately, the user must decide which of the methods to use.

Each method is also subject to user variability. Both the manual method and the analytic fit method require the user to decide if the resulting contour is "good enough." For the thresholding method, the user must choose a threshold value, and for the level set method, the user decides on the acceptable curvature parameters, which will influence the final segmentation. As a result of these many user choices, several different sets of contours can represent a given vessel.

2.3.3.1.3 Surface Lofting

The analytic surface lofting process maps a non-uniform rational B-spline (NURB) surface to cover a series of 2D contours. Using the Parasolid (Unigraphics Solutions, St. Louis, MO) geometry kernel, these surfaces are then bounded to create a solid model. Within this lofting process, the user controls three parameters: the number of sample points per contour, the contour spacing, and the contour alignment method.

Prior to lofting, Geodesic obtains an analytic form for the contours by fitting a spline curve to the contours. The user specifies the number of points used in this spline curve. A smaller number of resampling points will result in smoother contours, and consequently, smoother surfaces. However, not enough resampling points will produce a distorted contour, as shown in Figure 2.14.

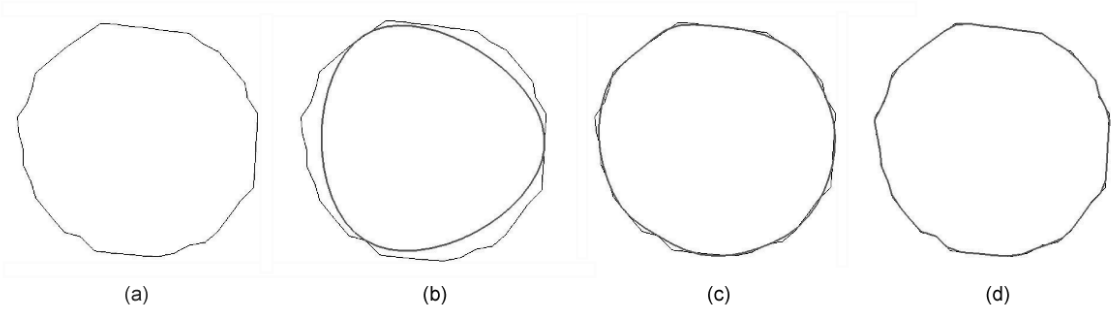


Figure 2.14: Contours resampled with different number of points. (a) is the original segmentation. Shown in dark gray are the original segmentations resampled with (b) 3 points, (c) 20 points, and (d) 60 points. These are overlaid on the original segmentation, shown in lighter gray. 3 points are not sufficient to represent the shape, while the 60-point-resampled contour does not achieve the desired smoothness. Using 20 resampling points produces a contour that is smoother than either the 60-point-resampled contour or the original segmentation, and accurately captures the original segmentation shape.

Contour spacing is a key factor in determining the shape of the geometric model. Wang addressed this issue in his thesis, indicating that contours that are spaced both too closely together or too far apart will lead to problems [104]. Obviously, contours that are too far apart will result in models that do not accurately represent the true geometry. This is an undersampling problem. Figure 2.15 is an example of geometries constructed with different contour spacings. As the contour spacing increases, the resulting model is less and less similar to the true shape.

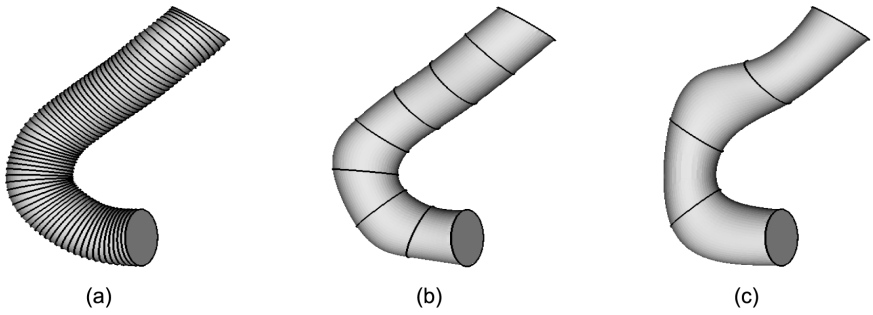


Figure 2.15: Effect of contour spacing on geometry. The geometries result from contour spacings of (a) 1 unit, (b) 9 units, and (c) 18 units. As the contour spacing increases, the resulting geometry deviates more and more from the desired geometry, shown in (a). *Courtesy of Kenneth C. Wang.*

However, contours that are placed too closely together can also produce undesirable effects. If a contour intersects another contour, a non-physical geometry is created in which the solid folds back on and intersects with itself. Even contours that are not

intersecting but happen to be close together can prove to be too restrictive for the lofting process, which must satisfy certain continuity constraints in order to maintain smoothness. The effects of these continuity constraints must be considered when constructing models with curved surfaces, such as at a bend or vessel narrowing.

In addition to poorly chosen contour spacings, bad contour alignment can also generate distorted geometries. Contour alignment determines how to join points on one contour to the points on a neighboring contour. Poor contour alignment can result in undesirable twisting in the geometric model, as shown in Figure 2.16. Within Geodesic, two methods are provided for contour alignment: alignment by vector and alignment by distance. The "alignment by vector" method finds the two points on neighboring contours that produce maximally aligned radial vectors. The "alignment by distance" method locates the two points on the neighboring contours that have the shortest distance between them. [104] describes these methods in more detail.

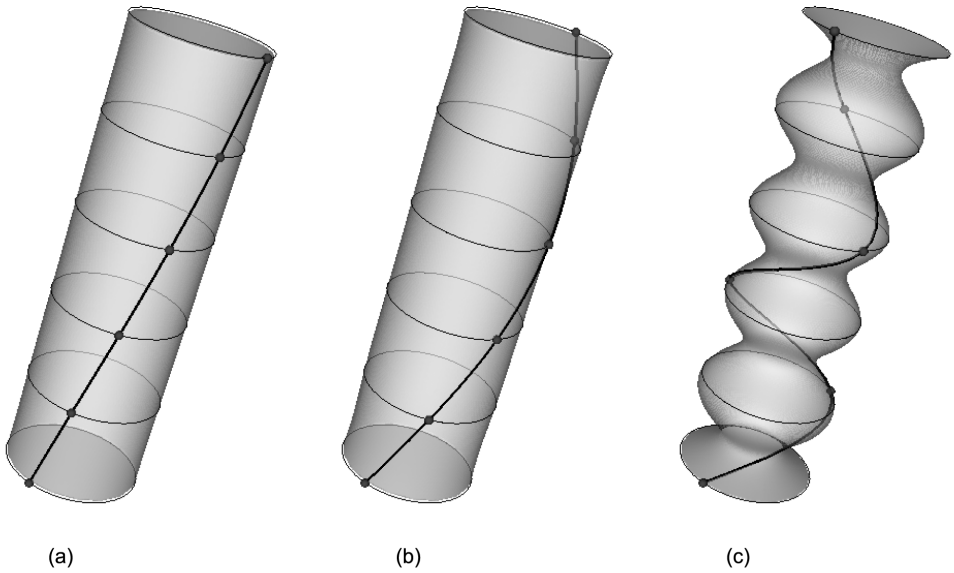


Figure 2.16: Effect of contour alignment on a solid model. These 3 solids are constructed from the same 6 contours, the only difference in the contours being how they are aligned. The small spheres connected by the darker line indicate the alignment along the axis. (a) shows a rotation of 90^o in alignment along the axis. The solid model in (b) was constructed with contours with a rotation of 180^o, while the model in (c) was constructed with contours with a rotation of 720^o. Note how the contour misalignment can produce undesirable distortions in the solid model, as shown in (c). *Courtesy of Kenneth C. Wang.*

2.3.3.2 Inlet Flow Boundary Condition

Several approaches are available within Geodesic to specify the velocities associated with the inlet of a model. The method for prescribing the analytic Womersley profile on the inlet is described in Section 2.3.3.2.1. Ideally, prescribing the measured velocities at the inlet would generate a more accurate solution, since they are presumed to more accurately reflect the true inlet conditions. Section 2.3.3.2.2 describes the method for applying the measured velocities onto the inlet. These methods are applied to a discretized version, or finite element mesh, of the geometric model.

2.3.3.2.1 Womersley

The Womersley profile represents fully developed, pulsatile flow of a Newtonian fluid in a straight, rigid cylinder and is axisymmetric [118]. By using the following formulation, the profile can be modified so that its flow matches any desired flow waveform:

$$w(r,t)=\frac{2B_0}{\pi R^2}\left[1-\left(\frac{r}{R}\right)^2\right]+\sum_{n=1}^{N}\left\{\frac{B_n}{\pi R^2}\left[\frac{1-\dfrac{J_o\left(\alpha_n\dfrac{r}{R}i^{3/2}\right)}{J_o\left(\alpha_n i^{3/2}\right)}}{1-\dfrac{2J_1\left(\alpha_n i^{3/2}\right)}{\alpha_n i^{3/2}J_o\left(\alpha_n i^{3/2}\right)}}\right]\right\}e^{in\omega t} \qquad (2.43)$$

where radius r is the radius, t is time, B_n are the Fourier coefficients of the desired flow waveform, R is the radius of the inlet, J_0 and J_1 are Bessel functions, and $\alpha_n = R\sqrt{(n\omega)/\upsilon}$ is the Womersley number where ω is the frequency in radians, and ν is the kinematic viscosity. N is the user-specified number of terms to use in computing the Womersley profile. See [119] for a derivation of this equation.

Because the inlet of the geometric model is not necessarily circular, a mapping from the circular Womersley velocity profile to the model inlet is needed. A simple mapping algorithm has been implemented within Geodesic in which the ratio of the radii at a given angle determines the value of the Womersley velocity profile that is assigned to it, as shown in Figure 2.17 and described further in [105]. The mapped velocity values

are then scaled so that the through-plane flow for the inlet mesh equals that of the desired flow waveform.

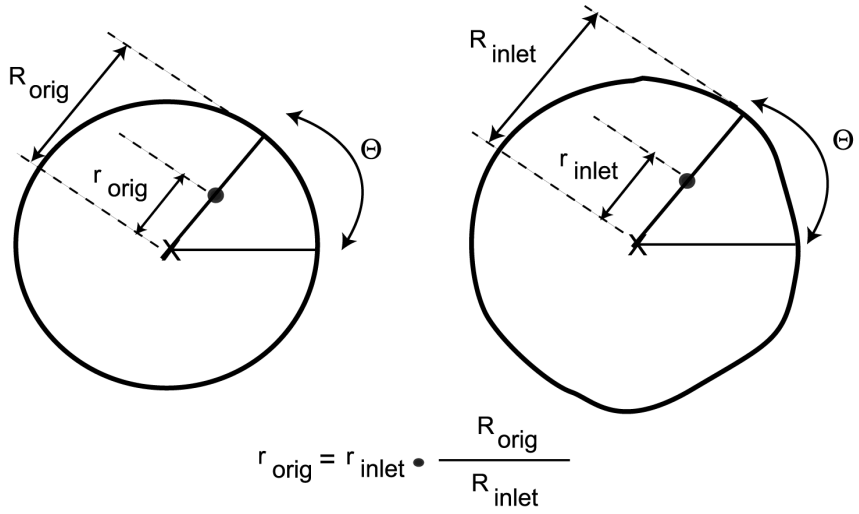


Figure 2.17: Velocity mapping algorithm. The relationship between the points on the inlet mesh (right) and those of the original data set (left) is through the radius ratio, as described in the equation above. R_{orig} and R_{inlet} are the distances from the center of the original and inlet meshes respectively to the boundary of that mesh at a given angle Θ. r_{orig} and r_{inlet} are the distances from the point of interest, marked by a solid dark circle, to the centers of the original and inlet mesh contours respectively. X marks the center of the contours, and Θ is the angle determined by the point of interest. The velocities at the point associated with r_{orig} (Θ) are assigned to the point at r_{inlet}(Θ).

2.3.3.2.2 Mapping Measured Velocities

The same method used for mapping the Womersley velocity profile onto an arbitrary inlet mesh is employed for mapping a given velocity profile onto the inlet mesh. Again, the ratio of radii determines the point in the given velocity profile to use in assigning a velocity value. For velocity data obtained from an image, the velocity data is assumed to be associated with the center of each pixel, so velocity data does not exist at all points in space. Therefore, a weighted interpolation is performed to obtain the velocity data at the desired spatial coordinates. After the mapping, the velocity values are scaled so that the through-plane flow for the inlet mesh matches that of the measured data. Finally, a Fourier-smoothing operation in time can be applied to each velocity component, if desired. See [105] for more details about this method.

2.3.3.3 Other Boundary Conditions

Just as the initial conditions must be specified at the inlet of the geometric model, they must also be provided for the outlets of the geometric model. Typically, velocity profiles or pressures are prescribed at the outlets. The velocity mapping methods described in Section 2.3.3.2 are also available to prescribe boundary conditions at the outlets of the geometric model. In addition, Geodesic provides the ability to identify outlet faces, so that pressure boundary conditions can be easily specified for numerical simulations.

2.4 Computational Hemodynamic Methods

Numerical simulations of blood flow are part of a larger field of study referred to as computational fluid dynamics (CFD). Solving CFD problems requires 1) specifying a region or geometry of interest, 2) applying initial and boundary conditions to the geometry, and 3) providing equations that describe the fluid behavior. Section 2.3 above described the process of obtaining geometric models of blood vessels and applying velocities and pressures to the vessel inlets and outlets. The following section covers the fluid simulation techniques. The basic equations used to model blood flow behavior are described in Section 2.4.1, and the general technique for solving these types of problems is described in Section 2.4.2. Lastly, Section 2.4.3 provides details about the Spectrum™ Solver, a commercial CFD solver that is used in this work.

2.4.1 Governing Equations

The following two equations are used to approximate the behavior of blood flow:

$$\nabla \bullet \vec{v} = 0 \tag{2.44}$$

$$\rho \frac{\partial \vec{v}}{\partial t} + \rho(\nabla \vec{v})\vec{v} = -\nabla p + \mu \Delta \vec{v} \tag{2.45}$$

where ρ is the density, $\vec{v}$ is the velocity, t is the time, p is the pressure, and μ is the viscosity. Equation (2.44) is the conservation of mass equation for an incompressible fluid, while Equation (2.45) is the time-dependent, three-dimensional Navier-Stokes

equation of motion for an Eulerian description of a Newtonian fluid, in which flow is observed at a fixed location in space. Only a handful of cases exist in which these equations can be solved analytically; in most situations, numerical techniques, such as the finite element method, are employed to find a solution.

2.4.2 Finite Element Methodology

The finite element methodology approximates the continuous solution space of the above equations with a finite-dimensional subset of that space. The first step involves rewriting the strong, or differential, form of the equations, such as that given above, into a weak, or integral, form. This is typically achieved by dotting the strong form of the equations with a weighting function and then integrating by parts. The semi-discrete Galerkin finite element formulation is then applied to the weak form to produce a finite-dimensional version of the weak form of the equations. The formulation approximates the weighting and solution spaces with a finite set of basis functions. The final set of equations can then be written in matrix notation. The relationship between the different forms of the equations is often shown as follows:

$$\{\mathrm{S}\} \Leftrightarrow \{\mathrm{W}\} \approx \{\mathrm{G}\} \Leftrightarrow \{\mathrm{M}\} \tag{2.46}$$

where {S} is the strong form, {W} the weak form, {G} the Galerkin form, and {M} the matrix form. Note that the only approximation occurs in going from the weak form to the Galerkin form. For a more mathematically rigorous treatment of this subject, refer to The Finite Element Method [120].

The matrix form of the equations can be written as:

$$K\vec{d} = \vec{F} \tag{2.47}$$

where K is a matrix relating the quantities of interest, $\vec{d}$ is the vector of unknown quantities that are to be determined, and $\vec{F}$ is a vector of known quantities, based on boundary and initial conditions. Solving for the vector of unknowns is straightforward if the equations are linear. In that case, inverting the matrix K produces the solution. Unfortunately, the Navier-Stokes and continuity equations result in a non-linear system

so an iterative approach must be taken in order to arrive at a solution. In the iterative method, the solution to the equations is estimated, and the quantities of interest are then evaluated based on this estimate. The difference between the computed quantities of interest and the known values of these quantities is termed the residual, which would ideally be zero. If the residual is unacceptably large, a new estimate is determined based on the residual and these steps are repeated, eventually arriving at a solution that approximates that of the non-linear equations. Different solution strategies exist for determining the residual and the new estimates.

Approximations occur at several points in the process of computing a solution to Equations (2.44) and (2.45), so it is reasonable to question the accuracy of the solutions. One way of assessing accuracy is convergence; if the solutions determined under different parameter settings are the same, then a converged solution has been found, and this converged solution is considered the best approximation to the true solution for a given solution strategy. Two important parameters that govern the convergence of the finite-element solution are the size of the elements in the model and the number of time steps used in computing the solution. The size of the elements in the model is inversely proportional to the model accuracy. Since a larger number of elements corresponds to a smaller element size, using a large number of elements results in a more accurate model and therefore, a more accurate solution. In general, increasing the number of time steps for a given time period (or decreasing the time increment) also leads to a more accurate solution. However, the numerical precision of the computer is a limiting factor, so below a certain point, decreasing the time increment fails to generate a more accurate solution. Furthermore, depending on the type of problem being solved, larger time increments can produce the desired results in less time. For a static type of problem, only the end result is of interest so it is advantageous to use large time increments to reach the final value as quickly as possible. In contrast, a time-accurate analysis is required for a dynamic problem, so smaller time increments are desirable in this case.

2.4.3 Spectrum™ Solver

The work described here utilized a commercially available stabilized finite-element application (Spectrum™ Solver, developed by Centric Engineering Systems, Inc., which is now a part of Ansys, Inc., Canonsburg, PA), which had previously been validated for blood flow simulations in a distal anastomosis model [52] and compared against analytic results for fully developed, pulsatile flow of a Newtonian fluid in a straight, rigid cylinder [105] [52].

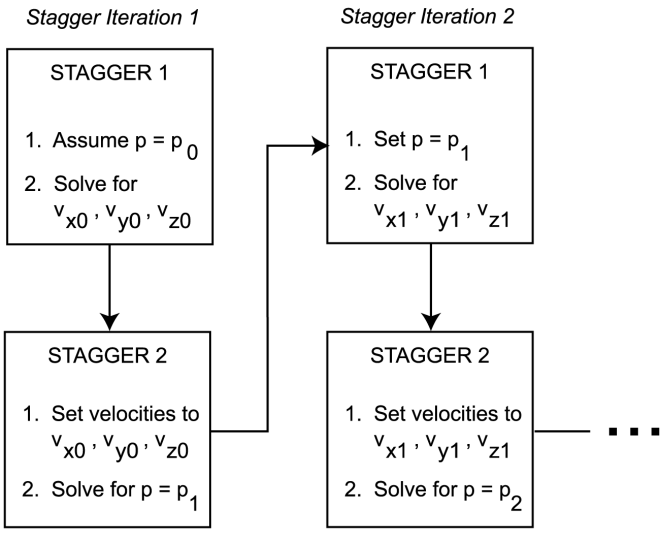


Figure 2.18: Staggered solution strategy employed by the Spectrum™ Solver. In this example, 2 staggers were defined for each iteration. One stagger solves for velocity, and the second stagger solves for pressure. In the first stagger, the pressure values p were held constant and a solution was found for the 3-components of velocity v_x, v_y, and v_z. The velocity values determined in stagger 1 were then used to initialize the velocities in stagger 2. In stagger 2, the velocities are assumed to be constant and the pressure is determined under these conditions. This new pressure value can then serve as the initialization for stagger 1 of the next iteration. Stagger iterations are run until the user-specified maximum number of iterations or the user-specified convergence criteria are met.

The Spectrum™ Solver integrates different methods to solve the Navier-Stokes equations [121]. The stabilized Galerkin finite element method is incorporated into the Spectrum™ Solver's solution strategy. Through the use of a least-squares method and a discontinuity-capturing technique, this algorithm dampens any oscillations which occur and might lead to instability in the solutions. The α-method determines how to update the variables of interest from one time step to the next [122]. The α-method used by the

Spectrum™ Solver updates some variables of interest at intermediate times to introduce numerical dissipation. This numerical dissipation provides increased stability in the solutions and is governed by the parameter α. Any value of α that is less than 1.0 results in numerical dissipation in the time integration.

The Spectrum™ Solver also incorporates an augmented Lagrangian formulation to handle the user-specified boundary conditions and other constraints. These contraints are represented by a vector $\gamma(x)$ and used to modify the system of equations as follows:

$$\bar{\Phi} \equiv \Phi + \lambda \cdot \gamma(x) + \tfrac{1}{2}\gamma(x) \cdot E\gamma(x) \tag{2.48}$$

where $\bar{\Phi}$ represents the system of equations with constraints included, Φ is the original set of equations to be solved, λ are the Lagrange multipliers, and E is a matrix of penalization factors. Through E, penalties are applied when the solution of the equations results in significant differences between the values of the constrained variables and the user-specified values.

Lastly, a multistagger approach is used to solve for both pressures and velocities in the Navier-Stokes equations. Each stagger involves the solution of an equation subsystem, the assumption being that these equation subsystems can be solved independently of each other and that the variables in the current stagger can change without affecting the value of the other variables. A stagger iteration involves solving each of the staggers one time, as shown in Figure 2.18. There are two ways to control the number of stagger iterations the Spectrum™ Solver runs. The explicit method requires the user to specify the maximum number of stagger iterations. The second method examines certain convergence criteria. One of the three measures that is examined is the degrees-of-freedom (dof) convergence, which measures the difference between the variables, such as velocities and pressures, from one iteration to the next. If the difference from one iteration to the next is zero, then it is said to be trivially converged. The residual convergence examines the residual, which is defined in Section 2.4.2 and which approaches zero as the solution converges. Lastly, the Lagrangian multipliers convergence measures the change in the value of the multipliers from one iteration to the

next. Again, these do not vary much from one iteration to the next for a converged solution.

Both direct and iterative methods are available for solving for the variables of interest in each stagger. While direct methods are robust, they can require large amounts of memory and computational power. On the other hand, iterative methods can result in non-converging solutions, but they are more memory efficient than direct methods. Moreover, within the Spectrum™ Solver, domain decomposition, which is necessary for parallel processing, is only possible when using iterative methods. Because of the large size of the problems studied in this work, iterative methods are used in the following simulations. The two different iterative methods that are available in the Spectrum™ Solver are the conjugate gradient (CG) algorithm and the generalized minimum residual (GMRES) algorithm. Both algorithms determine a solution for the linear system $A\vec{x} = \vec{b}$ by minimizing some function of the residual $\vec{r}$ where:

$$\vec{r} = \vec{b} - A\vec{x} \tag{2.49}$$

The CG method is a variation of the steepest descent technique and only applies to symmetric, positive definite systems, whereas the GMRES technique can be used for any type of linear system. Further details of how the finite element formulations are implemented and how these two iterative methods are used in the Spectrum™ Solver can be found in [52].

Chapter 3

Sensitivity of PC-MRI Measurements

No one believes the CFD [computational fluid dynamic] results except the one who performed the calculation, and everyone believes the experimental results except the one who performed the experiment. ~ Patrick Roache [123]

While experimental results are often considered a gold standard against which other techniques are compared, it is important to understand the limitations of the experimental data, for their accuracy determines how accurately the numerical simulation results can be validated. Moreover, artifacts can appear in the experimental data, so proper interpretation of the data requires knowledge of the conditions under which these artifacts occur. Towards that end, a series of experiments were conducted to examine the sensitivity and accuracy of PC-MRI-based velocity and flow measurements. Section 3.1 explores the effects of baseline correction on the PC-MRI data, while Section 3.2 discusses how imaging parameters, such as the repetition time and the angle of the plane that is prescribed, can affect the PC-MRI measurements. In Section 3.3, the effect of temporal smoothing on PC-MRI data is investigated.

3.1 Baseline Correction of PC-MRI Data

Eddy currents due to imperfections in the gradients lead to phase errors, and thus velocity errors. These errors can be minimized by using the signal in static regions of the image as a correction factor. This is referred to as "baseline correction." In the ideal case, the signal in the static region would be zero; however, due to noise and eddy currents, the signal in the static region will be non-zero. The assumption is that the signal in the static

region is representative of the errors that exist throughout the rest of the image, including in the flow regions of interest. Pelc, *et al.* have described using a linear least-squares fit model for this error [90]. This model can be extended to constant or quadratic fits. In the following investigation, two aspects of baseline correction are studied: the order of the baseline correction function and the effect of the region of interest used to determine the baseline correction function.

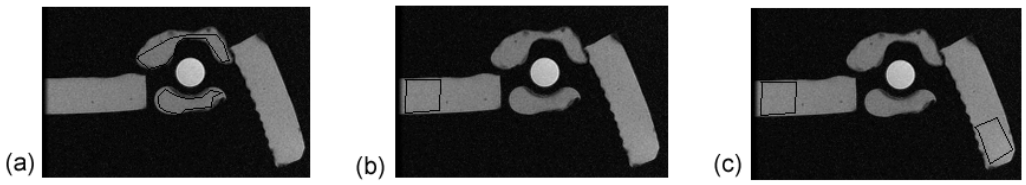


Figure 3.1: Regions used in baseline correction experiment are outlined in black in the above images. (a) Near region (b) One-sided far region (c) Far region. "In vessel" baselining used the circular region in the center of the image.

3.1.1 Method

PC-MRI images acquired during the low flow phantom experiment described in Section 4.1.1 were used to study the effects of different baseline correction functions. Briefly, this experiment consisted of a rigid model of a stenotic vessel with a bypass graft through which a mixture of distilled water, glycerol, and gadolinium was pumped using a commercially available blood flow pump. PC-MRI images perpendicular to the vessel axis were acquired with the flow pump turned on and off, with the images at the inlet of the phantom being analyzed here. It was assumed that similar noise and eddy current effects would occur in the PC-MRI image whether the flow pump was on or not. Therefore, the ideal baseline correction function could be determined by examining velocities in the flow region of interest in the PC-MRI image acquired with the flow pump off. Theoretically, these velocities should be zero. This is referred to as "in vessel" baselining, and it eliminates extrapolation or interpolation errors which may occur when computing the baseline correction function at a location other than in the flow region.

The "in vessel" region was one of the 4 regions used in computing a baseline correction function. Figure 3.1 shows the three other regions used in this comparison: a region that surrounds the tube and is relatively close to it ("near region"), a region that is approximately twice as far from the tube as compared to the "near region" and that exists both to the left and right of the tube ("far region"), and a region that is similar to the "far region" but only covers space to one side of the tube ("one-sided far region"). In evaluating the effect of the order of the correction function, constant, linear, and quadratic functions were fit to the velocity errors observed in these different regions. The custom software program, vcalc [90], was used to compute the baseline correction equations, which are functions of the pixel index, where the indices (0, 0) approximate the center of the image.

The effect of the baseline correction functions was evaluated by comparing the average flow waveforms for the tube and by examining plots of the correction function over a region that is similar in size to the tube. In this case, given the tube diameter of 19.05 mm and a pixel size of 0.78125 x 0.78125 mm^2, a region of 25 x 25 pixels was plotted. Vcalc was used to compute the average flows, and the plots of the correction function were generated using MATLAB (The MathWorks, Inc., Natick, MA). Complete analyses were performed only on measurements in the superior-inferior direction, which was the dominant direction of flow. Because the experiment was designed so that velocities in the other directions—the anterior-posterior and the right-left directions—were very small, measurements made in these two directions were likely to be dominated by noise, so it would not be possible to obtain a valid average velocity waveform from these measurements. Therefore, analysis of the baseline correction function in these directions was limited to examining the plots of the correction functions.

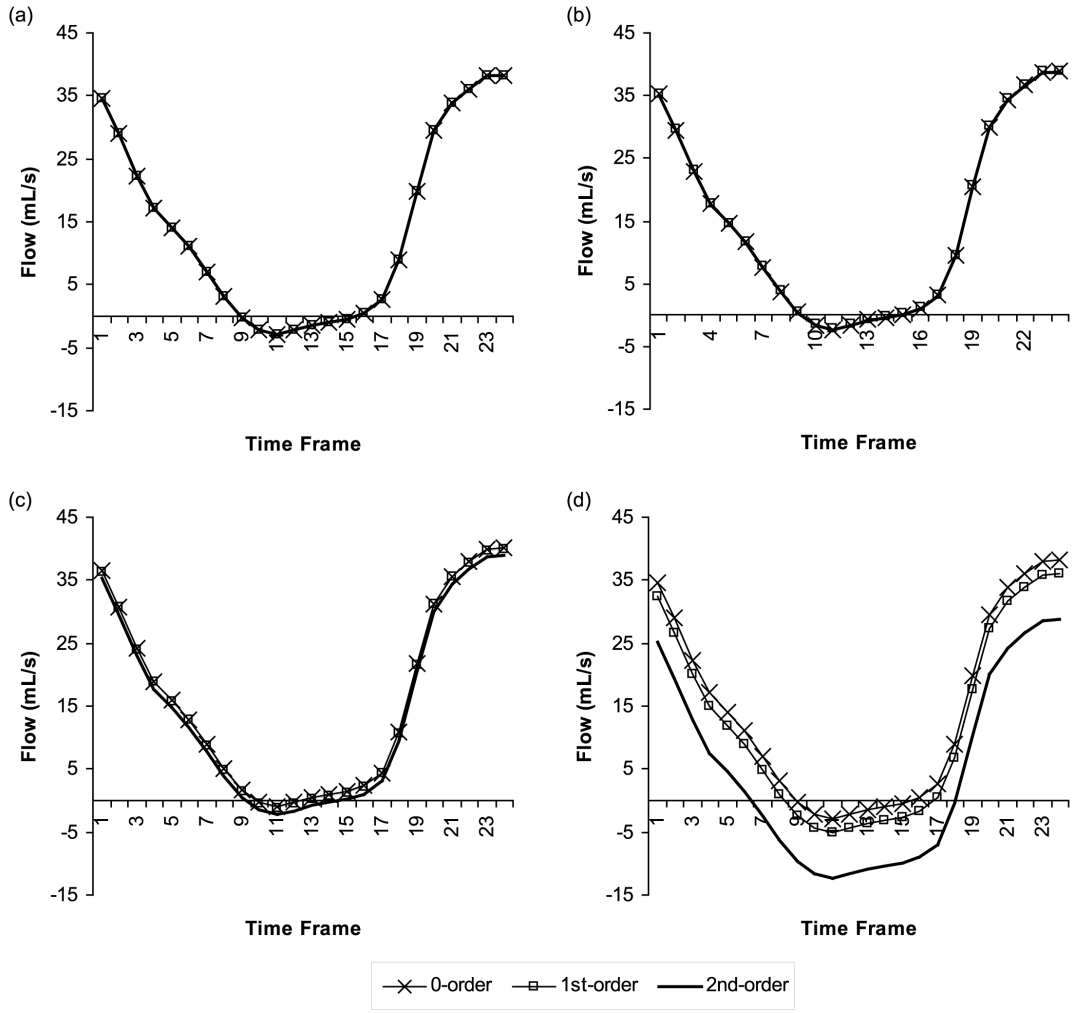


Figure 3.2: Average flow waveforms using different orders of baselining in the superior-inferior direction, which is the dominant flow direction. The region used for baselining was (a) the vessel of interest, (b) the "near region," (c) the "far region," (d) the "one-sided far region."

3.1.2 Results and Discussion

Figure 3.2 compares the effect of the order of the baseline correction function on the flow in the superior-inferior direction. Note that the baseline correction order and the region used in computing the baseline correction are interdependent and cannot be analyzed separately. While overall there is little difference in the flow waveforms due to the order of the baseline correction for the "in vessel" and "near region" baselining, more variability occurs when the "far region" or the "one-sided far region" is used. In these two regions, a noticeable difference exists between the flows computed with the second

order baseline function versus those computed with a zeroth or first order baseline function. Morever, the maximum difference between the average flows computed using a zeroth, first, and second order baseline function was much greater for the "far region" and the "one-sided far region." The differences were 0.008 mL/s, 0.20 mL/s, 1.3 mL/s, and 9.5 mL/s for the "in vessel" region, the "near region," the "far region," and the "one-sided far region," respectively.

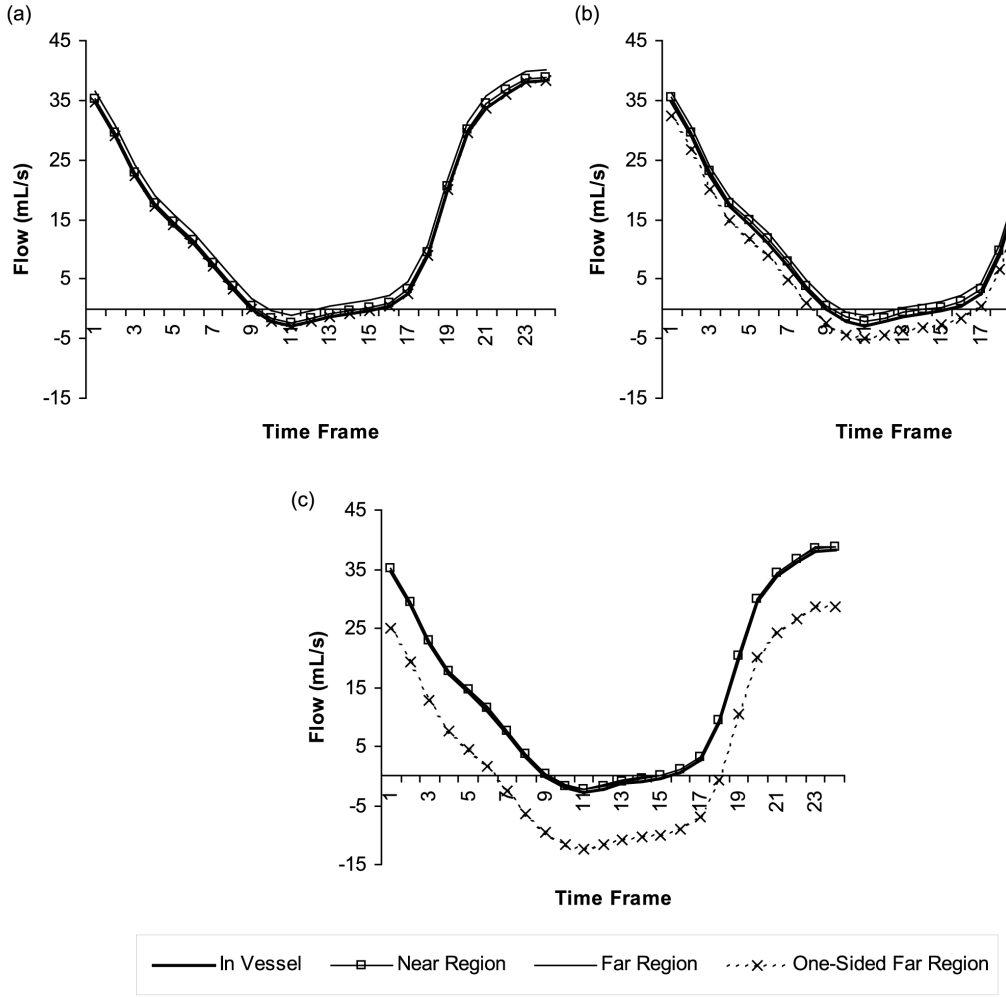


Figure 3.3: Comparison of flows in the superior-inferior direction using baseline correction functions computed using different regions. While the "in vessel" baselining and "near region" baselining produced similar results regardless of whether (a) constant, (b) linear, or (c) quadratic functions were fit to the velocity errors, flows based on the "far region" and "one-sided far region" baselining varied depending on the order of the baseline function.

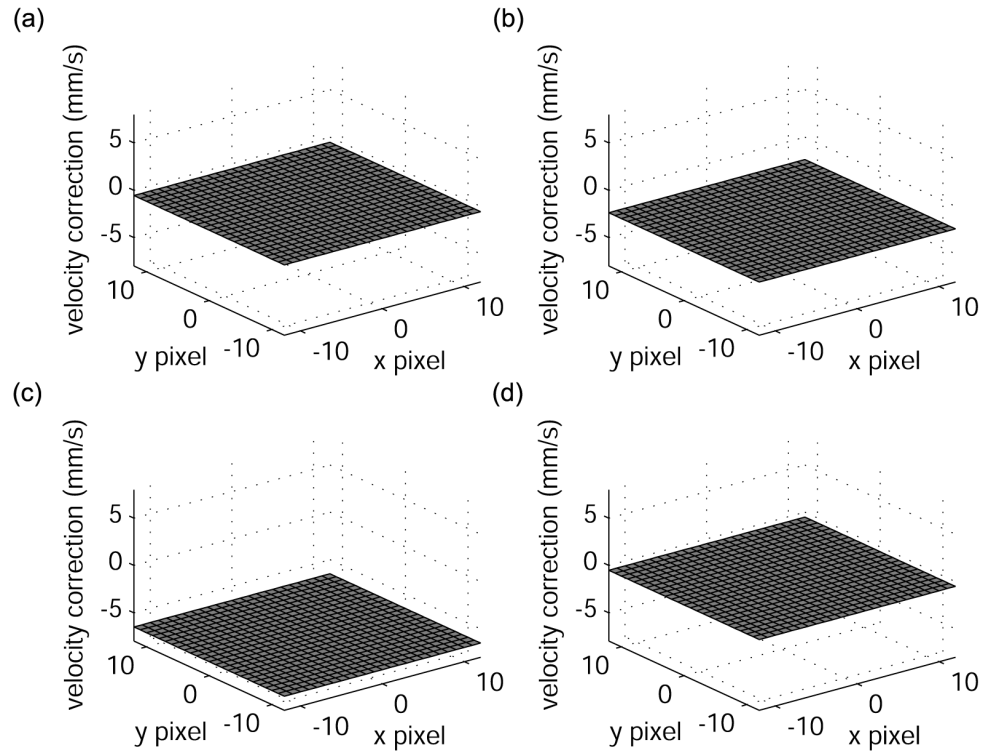


Figure 3.4: Comparison of zeroth-order velocity correction functions based on different regions of interest. Correction is for velocities measured in the superior-inferior direction using the following regions: (a) In-vessel (b) Near region (c) Far region (d) One-sided far region.

Figure 3.3 demonstrates the effect of the region used in computing the baseline correction on the flow in the superior-inferior direction. The "in vessel" baselining and "near region" baselining produced similar results regardless of whether a constant, linear, or quadratic function was fit to the velocity errors. In contrast, flow waveforms based on the "far region" and "one-sided far region" baselining differed from those produced by the "in vessel" baselining. Recall that the results based on the "in vessel" baselining are assumed to be ideal. The difference varied depending on the order of the baseline function and with no obvious pattern or trend. For the first- and second-order baselining, the "one-sided far region" produced flows that differed the most from the "in vessel" baselining results. However, for the zeroth-order baselining, the flow waveform based on the "far region" was the most different.

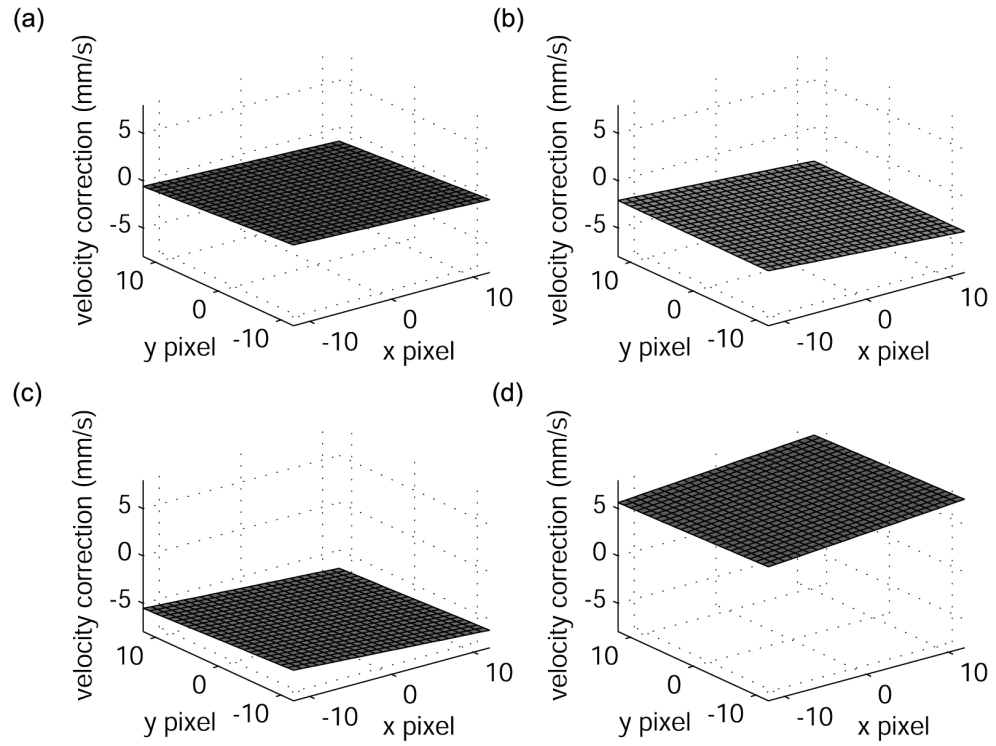


Figure 3.5: Comparison of first order velocity correction functions based on different regions of interest. Correction is for velocities measured in the superior-inferior direction using the following regions: (a) In-vessel (b) Near region (c) Far region (d) One-sided far region.

The velocity correction plots shown in Figures 3.4 to 3.6 also support the hypothesis that the "near region" baseline correction function is similar to that generated by the "in vessel" region, whereas the "far region" and "one-sided far region" baseline functions are not. The differences are primarily in magnitude, but with the second-order correction function, there is also a difference in the shape of the function. With a second-order baseline function, small errors in determining its coefficients could lead to large overall errors. Note that even with the "in vessel" baselining, there is a slight difference in the surfaces between the zeroth-order and the second-order correction function, particularly at the edges.

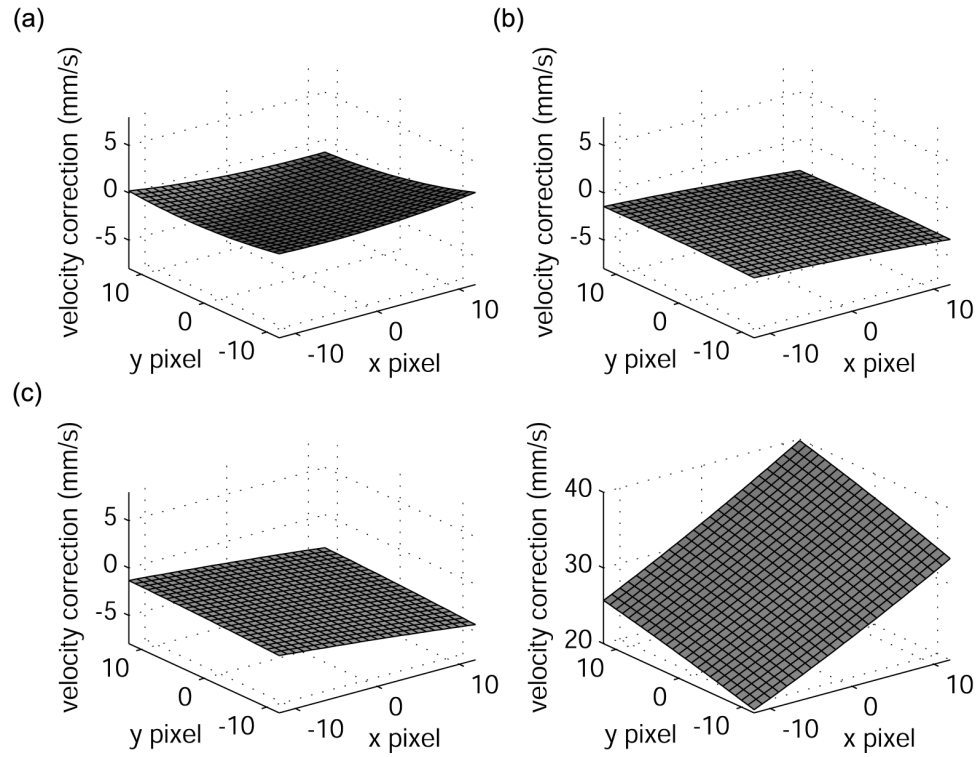


Figure 3.6: Comparison of second order velocity correction functions based on different regions of interest. Correction is for velocities measured in the superior-inferior direction using the following regions: (a) In-vessel (b) Near region (c) Far region (d) One-sided far region.

Lastly, a plot showing the first-order baseline correction function for the anterior-posterior direction is given in Figure 3.7. Again, the "far region" and "one-sided far region" produce velocity correction functions that are different from those of the "near region" and the "in vessel" region. Note also that the "one-sided far region" has positive velocity correction values over this range of pixels, compared with the negative velocity correction values generated by the other first-order baseline functions. This is a significant difference. Comparisons between the corresponding plots in Figure 3.5 and Figure 3.7 show that the baseline correction function differs depending on velocity direction. This is expected since the imaging parameters and therefore, the imaging gradients and eddy currents, may vary depending on direction.

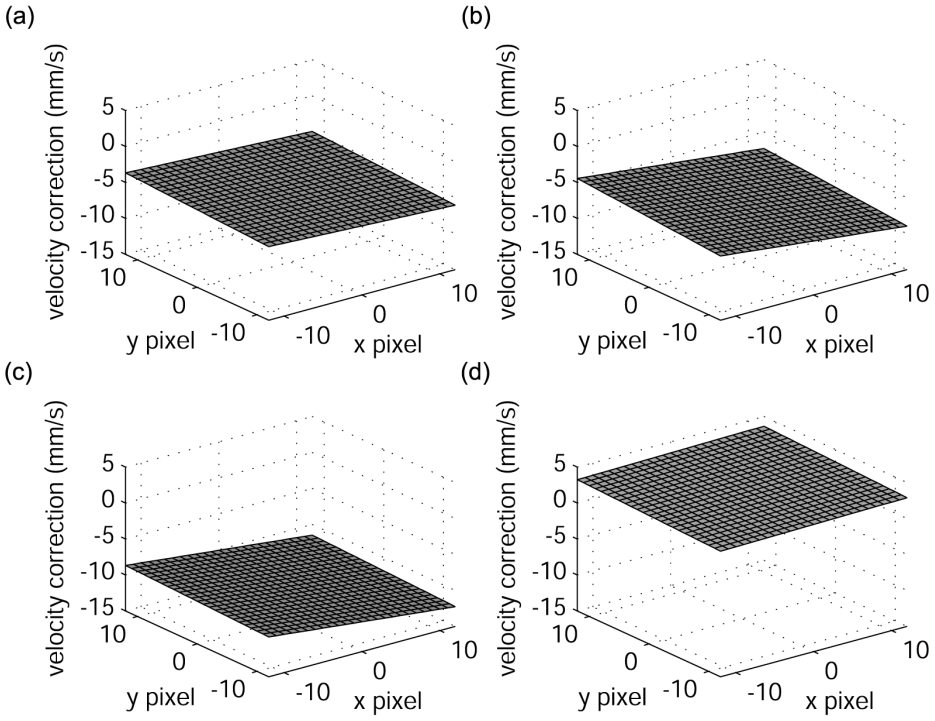


Figure 3.7: Comparison of baseline correction functions for velocities in the anterior-posterior direction using different regions of interest. The following regions were used for computing the correction function: (a) In-vessel (b) Near region (c) Far region (d) One-sided far region.

3.1.3 Conclusion

The key to accurate baseline correction is finding objects that are not moving and that have bright signal. For *in vitro* experiments, this is straightforward. The motion in the region of interest is usually controllable and can be suppressed to obtain a baseline correction image. Agar or other stationary objects could also be placed inside the magnet for baseline correction purposes. The situation is more difficult *in vivo*, depending on what locations and velocity components are of interest. The results here show that the baseline correction function differs depending on the velocity direction, so accurate velocity measurement requires finding a baseline function for each direction. This requires finding objects in the image which are stationary in each direction. Finding such objects, for example, in images of blood vessels in the chest or abdominal sections can be especially difficult. In these cases, it may be more appropriate to not apply any baseline correction.

In computing a baseline correction function, it is important to consider the region being used to generate the function and to a lesser degree, the order of the baseline function. The "near region" baseline corrections were generally better than the "far region" and the "one-sided far region" baseline corrections, and in most cases, the "far region" baselining functions produced differences that were less extreme than the "one-sided far region" baselining. The hypothesis that more accurate baseline correction functions are generated using regions which are closer to and which surround the flow region are supported by the results of this experiment. The order of the baseline function also showed differences in flows and velocity corrections. The differences were minor for the "in vessel" and "near region" cases, but were significant for the "far region" and "one-sided far region." Regardless of the region being used for baselining, though, second-order baselining is normally avoided since small errors in determining a second-order function's coefficients could lead to large overall errors. Therefore, unless significant second-order effects are expected, a linear or constant correction function is used.

3.2 Effect of Imaging Parameters on PC-MRI Measurements

Previous studies have examined the effect of imaging parameters on the accuracy of velocity and flow measurements based on PC-MRI data. Chapter 2 reviews some of these studies, which demonstrate that slice thickness, the in-plane spatial resolution, the sequence timing parameters, and the location of the object in the magnet are among the factors that can influence the PC-MRI measurements. In the following experiment, the effect of temporal resolution and the angle of the prescribed imaging plane on the PC-MRI data are examined under conditions similar to those used in the experiments described in Chapters 4 and 6.

3.2.1 Method

3.2.1.1 Experimental Set-Up

All imaging was performed in a straight, rigid polycarbonate tube, approximately 230 cm downstream of the tube entrance. A fiberglass honeycomb flow straightener was inserted at the entrance of the rigid tube to smooth and straighten out the flow. The inner diameter of the tube was 1.905 cm. Agar blocks were made out of a mixture of 95% distilled water, 4% agar, and 1% gluteraldehyde by weight and placed around the tube for error correction purposes (Figure 3.8). An abdominal phased array coil was then placed around the agar blocks. The fluid used in this system was water.

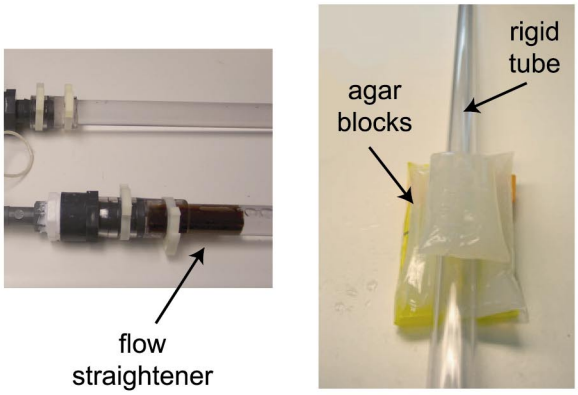


Figure 3.8: Straight rigid tube for testing effects of imaging parameters on PC-MRI measurements. Agar was placed around the tube for baseline error correction purposes and a flow straightener was placed at the entrance of the tube.

A cardiovascular flow pump (Model 1421, Harvard Apparatus, Holliston, MA) capable of producing a stroke volume from 4 to 30 mL was used to generate a pulsatile flow waveform at the tube's inlet. The trigger signal from the pump was converted to an electrocardiogram (ECG) signal to be used by the MRI system with an ECG simulator (Shelley Medical Imaging Technologies, London, Ontario, Canada). For the plane angle data, the stroke rate was set to 75 strokes per minute. For the temporal resolution experiments, the stroke rate was set to 101 strokes per minute since faster flows would make differences more evident.

A 12N in-line ultrasonic flow probe (Transonic Systems, Inc., Ithaca, NY) was placed upstream of the tube's inlet to verify the consistency of the flow pump output and to measure the flow rate. The flow probe was connected to a T101 ultrasonic blood flow meter (Transonic Systems, Inc., Ithaca, NY), which was connected to a data acquisition board (DAQPad-6020E, National Instruments, Austin, TX). The flow information was then acquired using a LabVIEW program (LabVIEW v.6 and v.6.1, National Instruments, Austin, TX) on a Dell Inspiron 8000 laptop computer (Dell Computer Corporation, Round Rock, TX) at a sample rate of at least 100 samples per second. This sytem had previously been calibrated using the bucket and stopwatch technique. A diagram of the experimental set-up is shown in Figure 3.9.

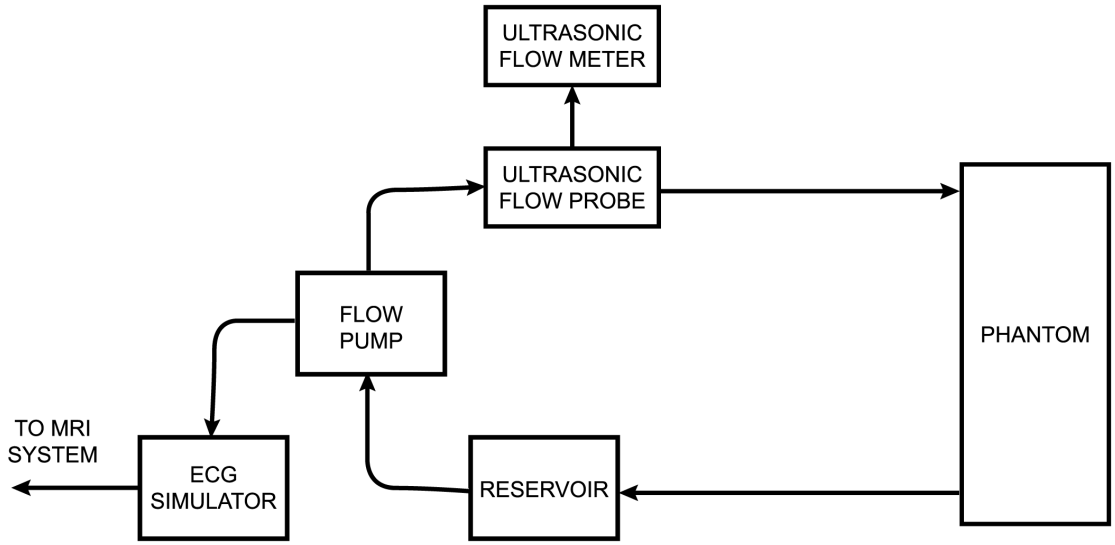


Figure 3.9: Diagram of experimental set-up for assessing the effect of imaging parameters on PC-MRI measurements.

3.2.1.2 Data Acquisition

All PC-MRI measurements were acquired on a 1.5 T MRI system (Signa, GE Medical Systems, Waukesha, WI). For all PC-MRI sequences, 24 time frames per cycle were reconstructed.

The MR images used to examine the effect of the angle of the prescribed imaging plane on cine PC-MRI [77, 78] measurements were acquired with the following

parameters: field-of-view (FOV)=24 cm, an acquisition matrix size of 256 x 256, a slice thickness of 5.0 mm, repetition time (T_R)=19.0 ms, echo time (T_E)=5.028 ms, number of excitations (NEX)=1, a flip angle of 20^o, through-plane velocity encoding of ±150 cm/s, an in-plane velocity encoding of ±50 cm/s, and a bandwidth of 16.0 kHz. Respiratory compensation and flow compensation were also used during the scan. Three image series were acquired, with only the tilt angle of the prescribed plane varying between each series. The angle of the plane was set to 0^o, 15^o, and 30^o, where 0^o describes a plane that is perpendicular to the axis of the tube.

A similar set of images were acquired to examine the effect of the angle of the prescribed plane on segmented k-space PC-MRI [79-81] measurements. The imaging parameters used for these images were FOV = 24 cm, an acquisition matrix of 256 x 192, slice thickness of 5.0 cm, 4 k-space views per segment, T_R=7.0 - 7.1 ms, T_E=3.2 - 3.3 ms, 1 NEX, a 30^o flip angle, ±150 cm/s through-plane velocity encoding, and a bandwidth of 31.25 kHz. Again, three series were acquired, each with a different tilt angle for the prescribed plane. As with the cine PC-MRI images, the plane angles were 0^o, 15^o, and 30^o, where 0^o corresponds to a plane that is perpendicular to the axis of the tube.

A third set of images was acquired to examine the effect of temporal resolution on the resulting flow measurements. Three different PC-MRI sequences were used in this comparison: a standard two-dimensional cine PC-MRI sequence, a two-dimensional segmented k-space PC-MRI sequence, and a custom cine PC-MRI sequence with improvements that could potentially shorten the T_R [124]. The standard cine PC-MRI sequence was repeated twice—measuring 3 orthogonal components of velocity and measuring just the through-plane component of velocity. For the through-plane component of velocity measurements, the imaging parameters were FOV=24 cm, an acquisition matrix size of 256 x 256, slice thickness of 5.0 mm, T_R=27 ms, T_E=5.028 ms, 1 NEX, flip angle of 20^o, through-plane velocity encoding of ±150 cm/s, respiratory compensation, and flow compensation. In measuring the 3 components of velocity, the imaging parameters were the same as for measuring the single through-plane component of velocity except that the T_R was 34 ms and an in-plane velocity encoding of ±50 cm/s was specified. The bandwidth used in these cine PC-MRI sequences was 16 kHz. The

parameters for the custom cine PC-MRI sequence were the same as that for the 3 components of velocity cine sequence; however, the resulting T_R and T_E were lower and the receiver bandwidth was higher. The T_R was 11.1 ms; the T_E was 4.004 ms; and the bandwidth was 62.5 kHz. For the segmented k-space sequence, the imaging parameters were FOV=24 cm, an acquisition matrix of 256 x 192, slice thickness of 5.0 mm, T_R=7 ms, T_E=3.3 ms, 1 NEX, flip angle of 30^o, 31.25 kHz bandwidth, and a through-plane velocity encoding of ±150 cm/s. The number of k-space views per segment was set to either 1, 2, or 4. The same imaging plane was prescribed for all sequences. These 6 scans were also performed with the flow pump turned off, so that additional information could be collected for error correction purposes. The cine sequence for 3-components of velocity was acquired 3 times and the segmented k-space sequence with 4 views per segment was repeated 5 times to assess the repeatability of the measurements. The repeatability analysis was used to determine what constituted a significant difference.

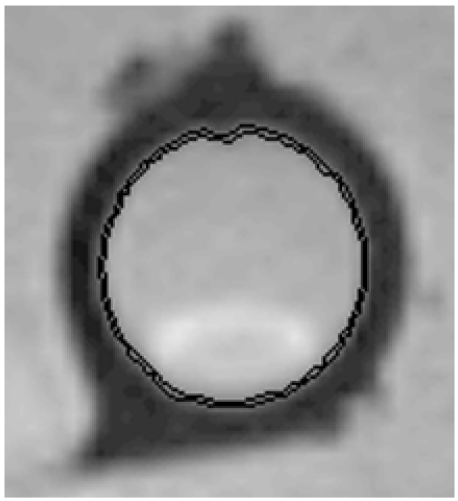


Figure 3.10: Comparison of contours obtained from thresholding. The inner contour used a thresholding value that was 10% smaller than that for the outer contour. Although there is little visual difference between the two, they produce different areas: 295 mm^2 versus 316 mm^2. These differences affect the flow value, which is a product of the area and the average velocity.

3.2.1.3 Data Processing

The custom software programs, Geodesic [104, 105] and vcalc [90], were used to process the PC-MRI data. Geodesic was used to convert the PC-MRI images into a mesh

so that the velocities could be visualized within Tecplot (Amtec Engineering, Inc., Bellevue, WA). These mesh files were also processed to examine the velocities for a single node over time.

Vcalc was used to compute the baseline error correction, the areas of the region of interest, and the average velocities of and the flows through the region of interest. All processing was performed on a version of the image that had been enlarged by a factor of 4, and a first-order baseline correction was applied in all cases (See Section 3.1 for a discussion about baseline correction). The baseline error correction was computed from the images acquired with the flow pump turned off. If those images were not available, the correction was calculated from the measurements in the agar surrounding the tube. To determine the region of interest, a threshold value that produced an average area within 1% of the theoretical area was used. This quantitative way of selecting a threshold value eliminates the variability that occurs with the standard method in which the user visually decides if the threshold value is "good enough." This can be a difficult decision, as demonstrated by the contours shown in Figure 3.10, and can affect the flow values, which are the product of area and average velocity. Therefore, a more quantitative approach was taken. For this experiment, the tube size is known to have an area of 285 mm^2. Imaging planes that are perpendicular to the tube axis should have a region of interest with an area equal to that. For tilted imaging planes, the areas will vary by a $\cos(\theta)$ factor, where θ is the tilt angle. So theoretically, for the 15^o-tilt plane, the area should be 295 mm^2, and for the 30^o-tilt plane, the area should be 329 mm^2.

In comparing data, the standard deviation for velocity and flow, as given by Equations (2.32) and (2.34) respectively, is used as a measure of variability and helps determine the significance of differences that are observed. In using Equation (2.33) to compute the signal-to-noise ratio (SNR) for these equations, frames 1 and 12 (out of a total of 24 frames) are used since they are temporally far apart and are therefore assumed to be independent of one another.

Measurements with the ultrasonic flow probe were acquired periodically throughout the imaging sessions and indicated the consistency of the flow through the tube. The measurements were converted from voltages to mL/s by multiplying the voltages by a

factor of 4.1, a quantity obtained from previous calibrations using the bucket and stopwatch technique. To obtain a single representative cycle of the flow, the trigger signal from the flow pump was also recorded and used to divide the flow signal into individual cycles. The individual cycles were then averaged together to obtain one representative cycle that would be used in the comparisons below.

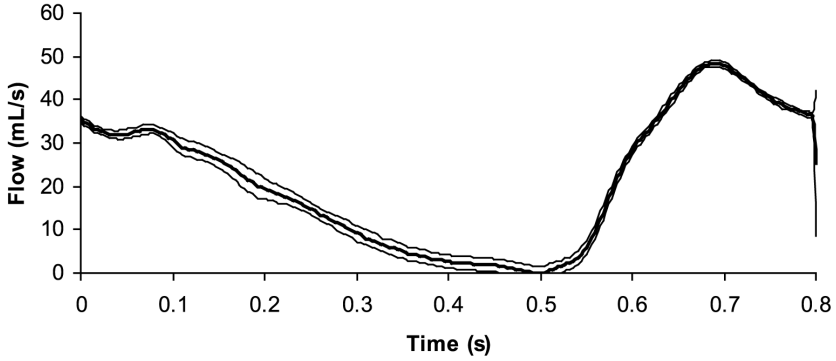


Figure 3.11: An average flow waveform based on approximately 20 cycles acquired with an ultrasonic flow probe. The dark line is the average and the lighter lines indicate plus and minus one standard deviation from the average.

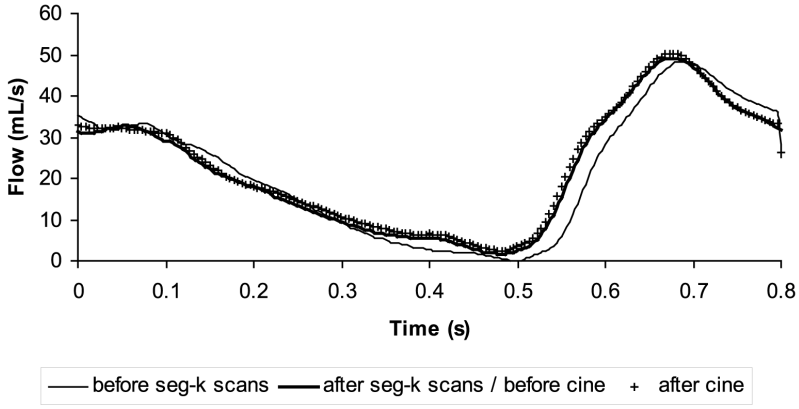


Figure 3.12: Comparison of flows at different time points during the experiment studying the effect of the plane angle on PC-MRI velocity measurements. These flow waveforms are an average of the flows measured using an ultrasonic flow probe. The segmented k-space PC-MRI measurements were acquired first, followed by the cine PC-MRI measurements. Data was acquired with the custom cine PC-MRI sequence at the end. There were some minor differences in the average flow waveforms over the course of the experiment. The dip observed in the last one or two time points of the cycle results from averaging together cycles of different lengths.

3.2.2 Results and Discussion

3.2.2.1 Flow Probe Measurements

Figure 3.11 shows the average flow waveform based on ultrasonic flow probe measurements acquired at the beginning of the experiment. The dark line is the average waveform, and the lighter lines indicate +/- one standard deviation from the average waveform. The standard deviation for each point in the cycle ranged from 0.4 to 2.7 mL/s, with larger variability occurring during deceleration. The average standard deviation was 1.4 mL/s, while the standard deviation of the average flow was 0.4 mL/s. The dip observed in the last one or two time points of the cycle resulted from averaging together cycles of different lengths. Shorter cycles had zero flow at these time points, causing the average to be lower. The differences in cycle length also explain the large standard deviations at this point in the cycle.

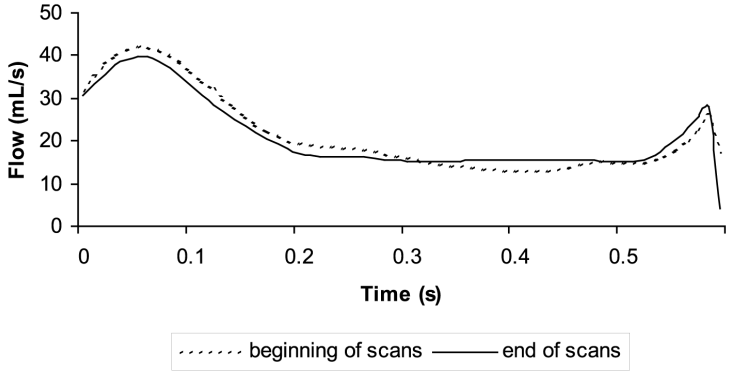


Figure 3.13: Comparison of flows at the beginning and end of the experiment studying the effect of temporal resolution on the PC-MRI flow measurements. These flow waveforms are an average of the flows measured using an ultrasonic flow probe. There were some minor differences in the average flow waveforms over the course of the experiment. The dip observed in the last one or two time points of the cycle results from averaging together cycles of different lengths.

Figure 3.12 and Figure 3.13 are comparisons of the flow measurements acquired with the ultrasonic flow probe at different times during the experiments. While there was a time shift observed between the flow waveforms in Figure 3.12, likely due to a difference

in triggering as opposed to a change in the flow, overall there was only minor variation in the flow over the course of an experiment. Ignoring the last two points in the cycle which exhibit significant deviations due to the difference in cycle lengths, the average flows during the plane angle experiment were 21.37 mL/s, 22.09 mL/s, and 23.01 mL/s at the beginning (before segmented k-space scans), middle (after the segmented k-space scans and before the cine scans), and end (after the cine scans) of the experiment, respectively. Given that the standard deviation of the average flow was 0.4 mL/s, there appeared to be some differences in flows during this part of the experiment. For the temporal resolution experiment, the average measured flow at the beginning of the scans was 21.83 mL/s. At the end of the experiment, it was 21.39 mL/s, an insignificant difference from 21.83 mL/s.

3.2.2.2 Repeatability Studies

Using Equations (2.32) and (2.33), the standard deviation in the velocity for the 5 segmented k-space acquisitions was computed to be 5.8 ± 0.8 mm/s, compared with 3.6 ± 0.5 mm/s for the 3 cine acquisitions. The theoretically calculated standard deviation was relatively small despite having a v_{enc} of 1500 mm/s because of the high SNR values. Velocities at the eight points shown in Figure 3.14 were also examined to directly compute a standard deviation for the velocity. Figure 3.15 compares the velocity waveforms measured with a segmented k-space sequence, while Figure 3.16 shows the velocities acquired with a cine sequence. The standard deviation averaged over time and the eight points for the segmented k-space sequence was 10.2 mm/s, with the range of velocities varying from –43.5 mm/s to 209 mm/s. The standard deviation varied from 7.9 to 14.4 mm/s, depending on which point was being examined. These were slightly higher than what was calculated theoretically. Notice that points associated with lower velocities, such as D, E, and H, demonstrated more variation. This relationship was not observed with the cine measurements. Overall, the cine measurements appeared to have less variability than the segmented k-space measurements, and the calculated standard deviations support this qualitative observation, the average standard deviation over time and the eight points being 6.3 mm/s for the cine acquisition versus 10.2 mm/s for the

segmented k-space sequence with 4 views per segment. The range of velocities for the cine acquisition was 36.2 mm/s to 196 mm/s. The standard deviation for the cine acquisitions ranged from 4.0 to 9.5 mm/s, which was again slightly higher than the theoretical estimate of 3.6 mm/s. Again, high SNRs produced small deviations in the velocity despite the high through-plane v_{enc} of 1500 mm/s.

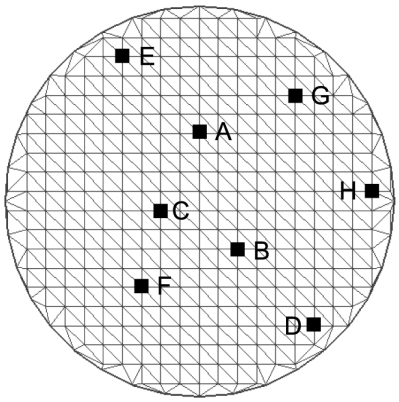


Figure 3.14: Eight points were used to examine the repeatability of velocity measurements acquired with PC-MRI. The dark squares mark these points within an axial view of the tube. Excluding points on the outer boundary, locations where two lines intersect correspond to pixel centers within a PC-MRI image.

Figure 3.17 and Figure 3.18 demonstrate how the variability in the individual velocity measurements can affect the velocity isocontours as measured with the segmented k-space and cine PC-MRI sequences, respectively. While the velocity magnitudes and the overall velocity patterns in each measurement were similar, differences were noticeable in the shapes of the isocontours. For example, the 190 mm/s contours for the peak flow plots for the segmented k-space sequence all occurred in the upper-half of the tube. However, the shapes of these contours varied from a more elliptical shape to a more triangular one. In the cine PC-MRI acquisitions, these same contours differed in extent.

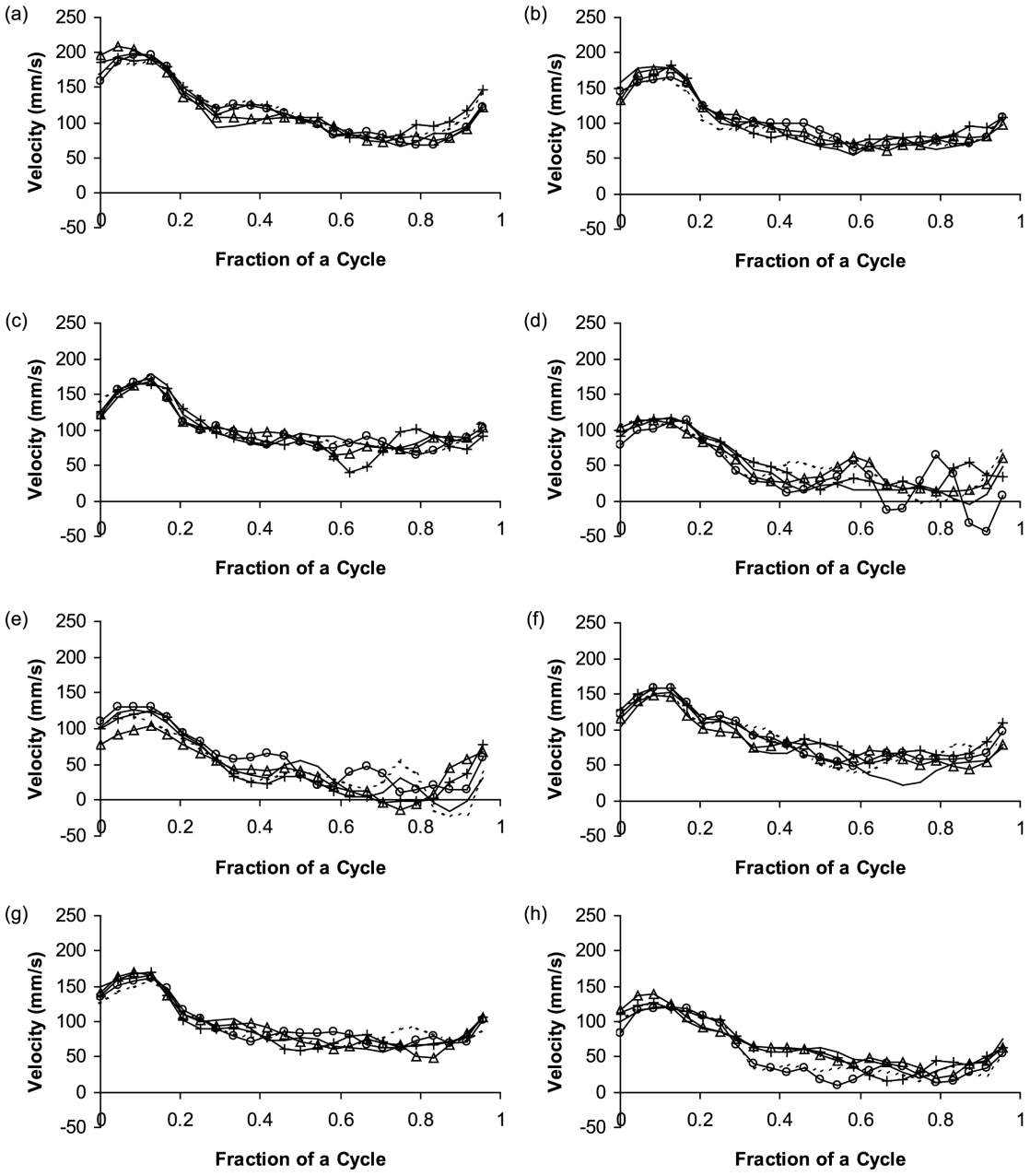


Figure 3.15: Repeated measurements of velocity using a segmented k-space sequence. The graphs show velocity measurements obtained with 5 different acquisitions at (a) point A, (b) point B, (c) point C, (d) point D, (e) point E, (f) point F, (g) point G, and (h) point H, as defined in Figure 3.14.

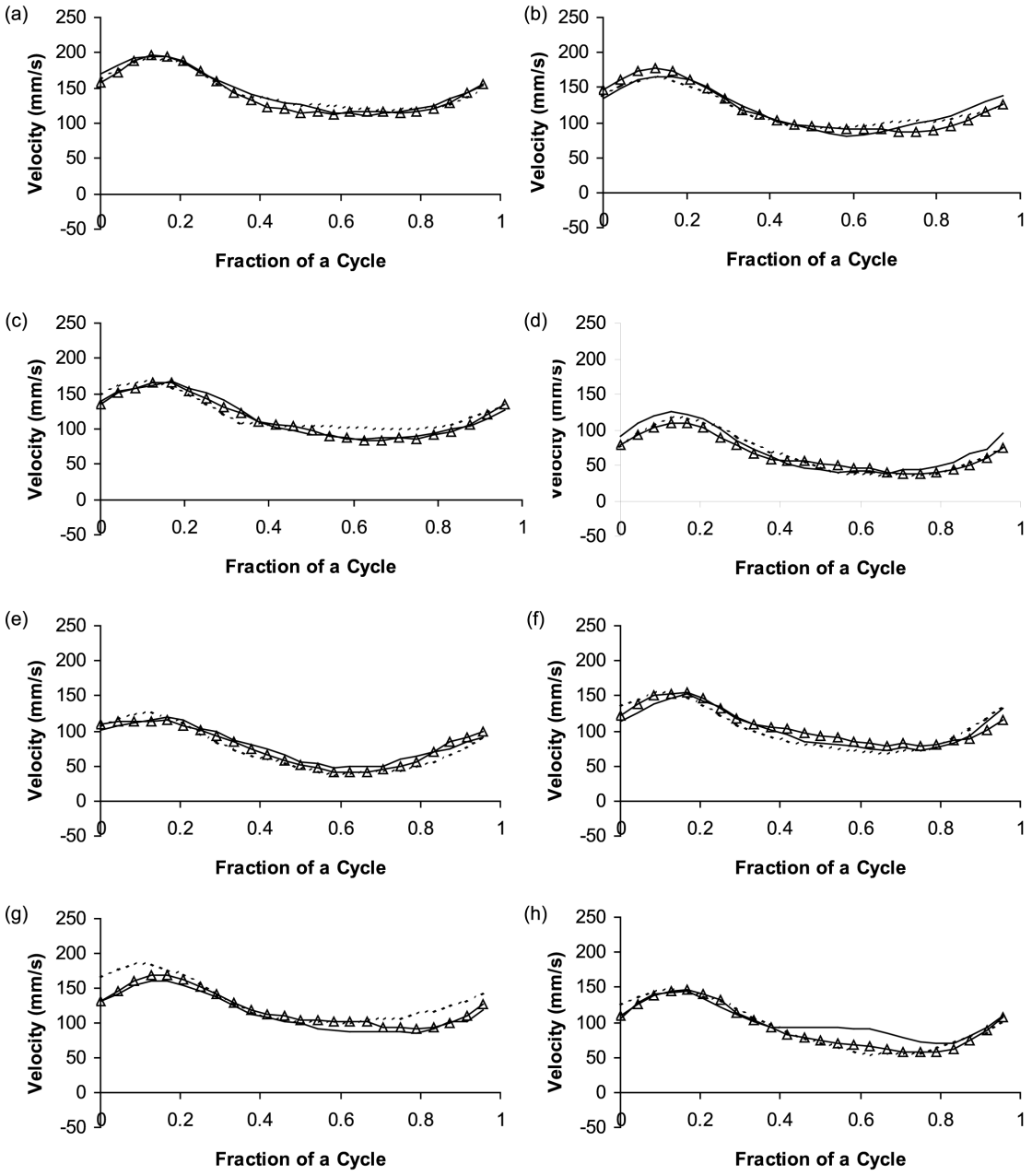


Figure 3.16: Repeated measurements of velocity using a cine sequence. The graphs show 3 velocity measurements at (a) point A, (b) point B, (c) point C, (d) point D, (e) point E, (f) point F, (g) point G, and (h) point H, as indicated in Figure 3.14.

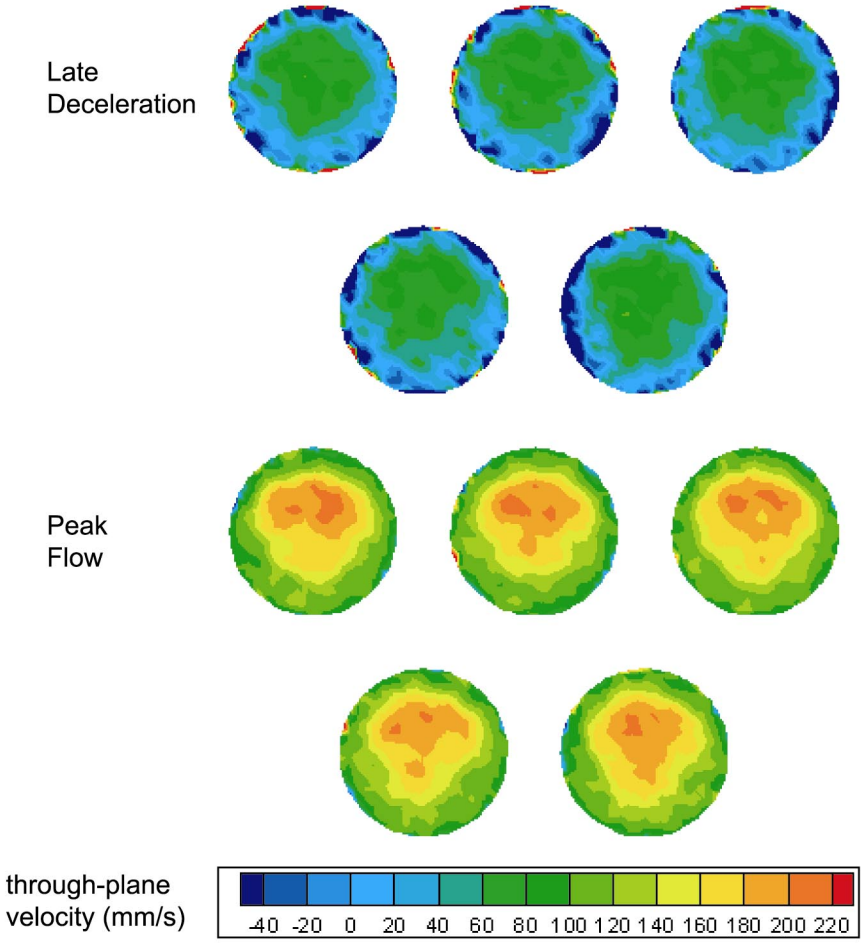


Figure 3.17: Variability in through-plane velocity contours, as measured with a segmented k-space PC-MRI sequence. Measurements were repeated five times. Isocontour plots are shown for the five measurements at two time points: late deceleration and peak flow.

Analysis of repeated flow measurements acquired with both a cine 3-components of velocity sequence and a segmented k-space sequence with 4 views per segment showed consistent results from measurement to measurement. Figure 3.19 shows the variation in flow waveforms over repeated measurements with both cine and segmented k-space sequences. The average flow was 26.3 ± 0.4 mL/s with the cine sequence and 19.8 ± 0.3 mL/s with the segmented k-space sequence. With the cine PC-MRI sequence, differences occurred predominantly at the peak and the trough, whereas the variation in the flows acquired with the segmented k-space sequence was generally limited to just the trough. The standard deviation at each time point ranged from 0.2 to 1.0 mL/s for measurements with the cine PC-MRI sequence. The average standard deviation was 0.6 mL/s. With the

segmented k-space sequence, the range was from 0.3 to 1.28 mL/s with the average being 0.7 mL/s. Although the measurements indicate similar standard deviations for flow, theoretical calculations for the standard deviation of flow for the two different sequences produced different results. For the segmented k-space sequence, the theoretical standard deviation, calculated from Equation (2.34), was 2.9 mL/s, while it was 1.8 mL/s for the cine sequence. Unlike with the velocity measurements, the theoretical standard deviation for flow was higher than that calculated from direct measurements.

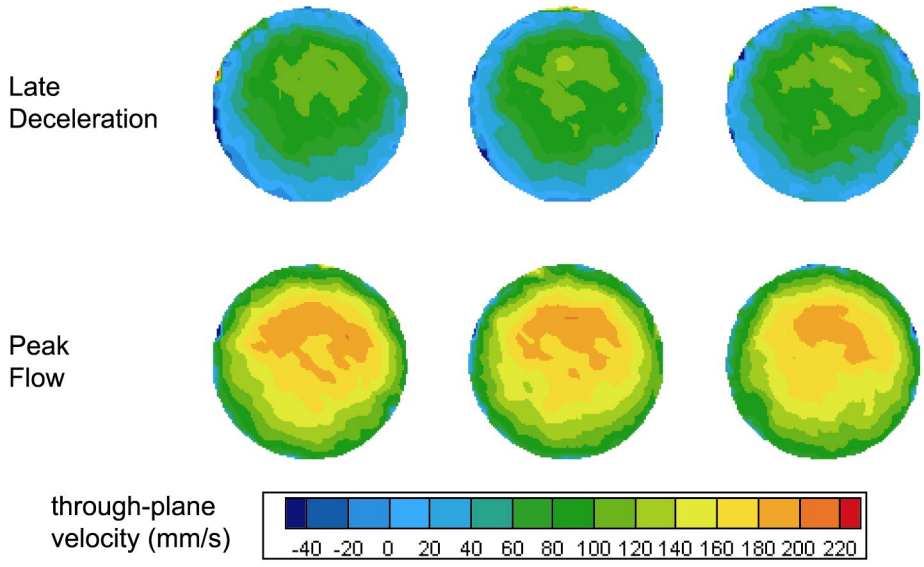


Figure 3.18: Variability in through-plane velocity contours, as measured with a cine PC-MRI sequence. Measurements were repeated three times. Isocontour plots are shown for the three measurements at two time points: late deceleration and peak flow.

Based on these analyses, the theoretical calculation for the standard deviation provides an approximate measure of the true standard deviation. For the velocity, it can be considered a lower bound on the true standard deviation, with the true standard deviation being approximately 2 to 3 times higher. For the flow, it is the same order of magnitude but tends to be an overestimation of the true standard deviation. In addition, these measurements show that the repeatability of the velocity measurements varies with location and sequence, with the segmented k-space sequence with 4 views per segment showing slightly less repeatability than the cine 3-components of velocity sequence. At higher velocities, both sequences provide repeatable velocity measurements. The deviations observed in the flow measurements are on par with the measurements made

with the flow probe, so it is reasonable to conclude that both the cine PC-MRI and the segmented k-space sequences can provide repeatable flow measurements.

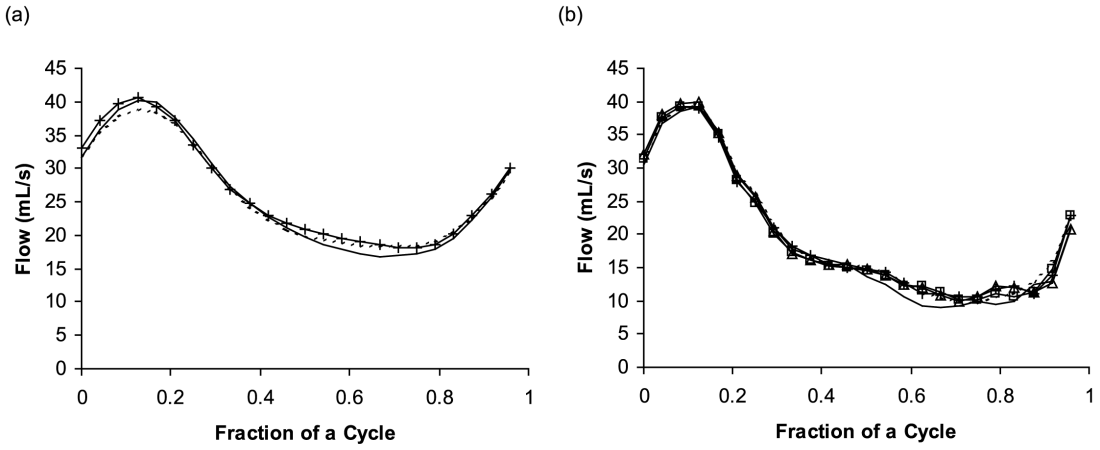


Figure 3.19: Repeatability of flow measurements acquired with different PC-MRI sequences. (a) Flow waveforms acquired 3 times using a cine 3-components of velocity sequence. (b) shows a similar graph but for measurements acquired with a segmented k-space sequence with 4 views per segment. The segmented k-space sequence was repeated 5 times.

3.2.2.3 Sensitivity to Plane Angle

Theoretically, the average velocities measured in a plane that is not perpendicular to the flow axis will underestimate the true average velocities by a factor of $\cos(\theta)$, where θ is the tilt angle. Recall that the 0^o plane is perpendicular to the tube axis. Therefore, for planes that are tilted by 15^o and 30^o from the perpendicular, the velocities would be smaller by 0.97 and 0.87 times, respectively. The experimental measurements agreed with this theory within experimental error. For the two-dimensional cine PC-MRI sequence, the average velocity, as measured with the 0^o plane, was 82.8 mm/s. With the 15^o plane, the average velocity was 85.7 mm/s, and with the 30^o plane, it was 71.0 mm/s. For the 30^o plane, the average measured through-plane velocity was similar to the theoretically calculated value of 71.7 mm/s. The theoretically computed average velocity for the 15^o plane was 80.0 mm/s, which differed from the measured value by 5.7 mm/s. Figure 3.20(b) depicts the velocities acquired with the 0^o plane against the corresponding velocities acquired with the non-perpendicular planes. A linear least-squares fit between the velocities acquired with the 0^o plane (vel_{0deg}) and those acquired with the 15^o plane

(vel_{15deg}) yielded the following equation: $vel_{15deg} = 0.953 \cdot vel_{0deg} + 6.7797$, $R^2 = 0.999$. For the 30° plane (vel_{30deg}), the relationship was $vel_{30deg} = 0.8617 \cdot vel_{0deg} - 0.3707$, $R^2 = 0.998$. The slopes of these equations indicate that the relationship between the velocities acquired with a non-perpendicular plane and those acquired with a perpendicular plane is close to that predicted by theory. Note the offset of 6.7797 mm/s in the linear fit equation for the 15° plane velocities, which suggests a possible error in the baseline correction.

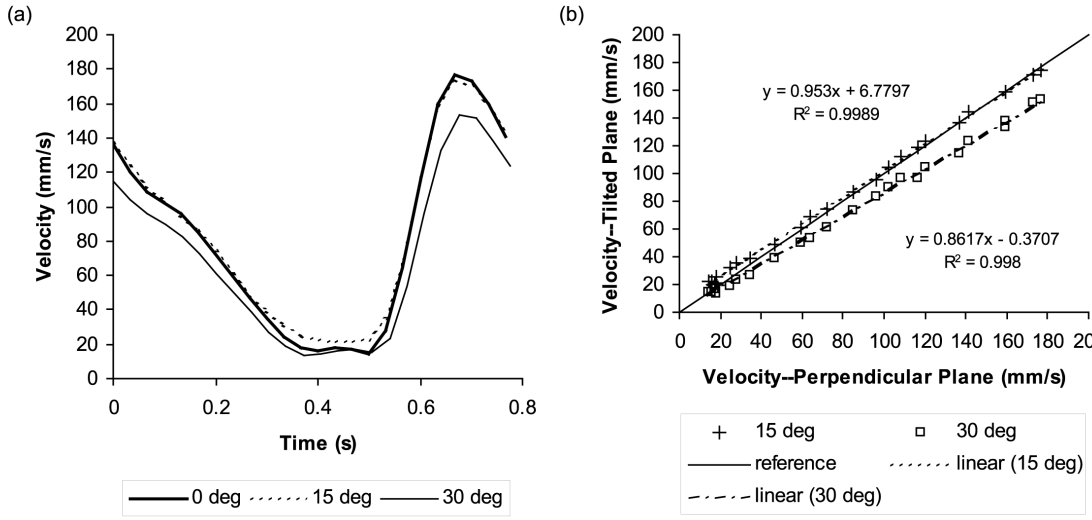


Figure 3.20: Comparison of the average through-plane velocity acquired with a two-dimensional cine PC-MRI sequence for different angles between the prescribed plane and the tube axis. "0 degrees" describes a plane that is perpendicular to the tube axis. (a) is a comparison of the average velocity waveform, and (b) displays the data as a scatter plot between velocity acquired with a non-perpendicular plane versus that acquired with a perpendicular plane. The reference line is the line of identity. The linear fit equation for the 15-degrees plane is given in the upper-left corner, while that of the 30-degrees plane is in the lower-right corner.

Similar results were observed with the segmented k-space measurements. The average velocity acquired with the 0° plane was 63.2 mm/s. From this measurement, the theoretical average velocities were 61.0 and 54.8 mm/s for the 15° and 30° planes, respectively. The measured average velocities were 65.7 and 56.3 mm/s for the 15° and 30° planes, respectively. Again, the agreement between theory and measurement was better for the 30° plane than the 15° plane. The plots in Figure 3.21 also demonstrate this. The linear least-squares fit between the velocities acquired with the 0° plane (vel_{0deg}) and those acquired with the 15° plane (vel_{15deg}) was $vel_{15deg} = 1.0058 \cdot vel_{0deg} + 2.126$, $R^2 =$

0.984. For the 30° plane (vel_{30deg}), the relationship was $vel_{30deg} = 0.897 \cdot vel_{0deg} - 0.4113$, R^2 = 0.984. Again, the equation for the 15° plane velocities has a y-intercept that is noticeably different than zero, suggesting errors with the baseline correction.

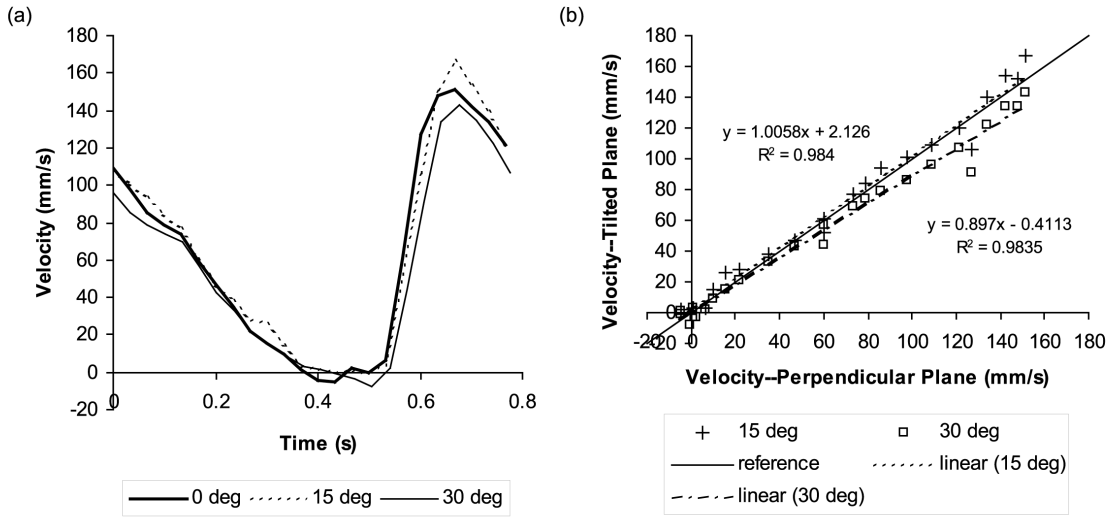


Figure 3.21: Comparison of the average through-plane velocity acquired with a segmented k-space PC-MRI sequence for different angles between the prescribed plane and the tube axis. "0 degrees" describes a plane that is perpendicular to the tube axis. (a) is a comparison of the average velocity waveforms, and (b) displays the data as a scatter plot between velocity acquired with a non-perpendicular plane versus that acquired with a perpendicular plane. The reference line is the line of identity. The linear fit equation for the 15-degrees plane is given in the upper-left corner, while that of the 30-degrees plane is in the lower-right corner.

The cos(θ) factor by which the velocities for a tilted plane are underestimated is theoretically the same factor by which the area is overestimated, so the average flow, which is the product of the average velocity and the area, should be independent of the plane angle (See Section 2.2.3.4.3). To minimize errors from the area, the contours used for these analyses were chosen to differ from the theoretical areas by less than 1.0 mm^2, so the average area over time was 284.9 mm^2 for the 0° plane (perpendicular to the tube axis), 295.0 mm^2 for the 15° plane, and 329.7 mm^2 for the 30° plane. Figure 3.22 and Figure 3.23 show that the flow measurements are similar, regardless of the plane angle, for the cine and segmented k-space acquisitions, respectively. For the cine sequence, the average flow for the 0° plane was 23.6 mL/s, while that of the 15° and 30° plane were 25.3 and 23.4 mL/s respectively. The time-averaged flows acquired with the segmented k-space sequence were 18.0 mL/s, 19.4 mL/s, and 18.6 mL/s for the 0°, 15°, and 30° planes,

respectively. Furthermore, linear fits between flows acquired with non-perpendicular planes and those acquired with a perpendicular plane have slopes in the range of 0.985 to 1.04 and, with the exception of the cine 15° plane measurements, small y-intercepts, strongly suggesting similarities in the acquired flow measurements.

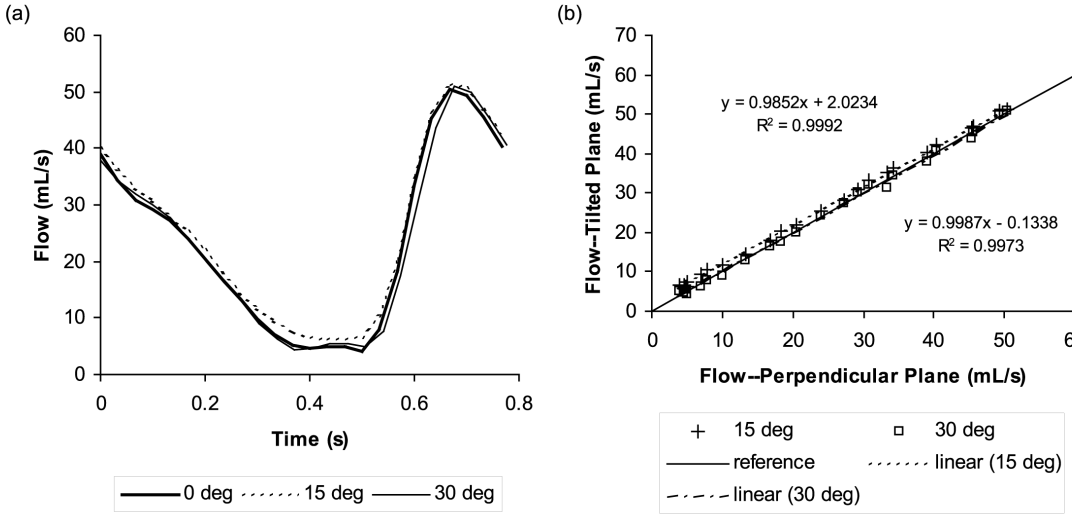


Figure 3.22: Comparison of the average flows acquired with a two-dimensional cine PC-MRI sequence for different angles between the prescribed plane and the tube axis. "0 degrees" describes a plane that is perpendicular to the tube axis. (a) is a comparison of the flow waveforms, and (b) displays the data as a scatter plot between flows acquired with a non-perpendicular plane versus that acquired with a perpendicular plane. The reference line is the line of identity. The linear fit equation for the 15-degrees plane is given in the upper-left corner, while that of the 30-degrees plane is in the lower-right corner.

These measurements used an ideal area. An inaccurate segmentation of the region of interest could have resulted in noticeable errors in the flows. Figure 3.24 shows the variation in the area of the region of interest as a function of the threshold used for segmenting the image. In the vcalc application, this threshold is specified as a percentage of the maximum intensity in a user-specified region in the magnitude image. Linear fits through these data points demonstrated a strong inverse relationship between the percent threshold and the computed area. For the standard 2D cine PC-MRI graphs, the R^2 values were 0.9994, 0.9977, and 0.9996 for the 0°, 15°, and 30° planes, respectively, and for the segmented k-space PC-MRI graphs, the R^2 values were 0.9732, 0.9952, and 0.9998 for the 0°, 15°, and 30° planes, respectively. Furthermore, the data also showed that the less perpendicular the imaging plane was relative to the vessel axis (where 0°

means that the plane is perpendicular to the vessel axis), the greater the change in the area for a given change in the percent threshold. This is the slope of the linear fit through the data. For the standard 2D cine PC-MRI data, the slopes of the linear fits were –1.2731, -1.4172, and –1.8998 for the 0^o, 15^o, and 30^o planes, respectively. Similar results were found for the segmented k-space data, where the slopes of the linear fits were –3.6467, -3.6976, and –5.6235 for the 0^o, 15^o, and 30^o planes, respectively. Also, note that for the segmented k-space data, only a small range of threshold percentages produced acceptable segmentations for the 15^o and 30^o imaging planes. Because the sensitivity of the area to the percent threshold increases with the non-perpendicularity of the imaging plane, errors in the flow measurements, which are proportional to area, are more likely with greater misalignments in the plane angle.

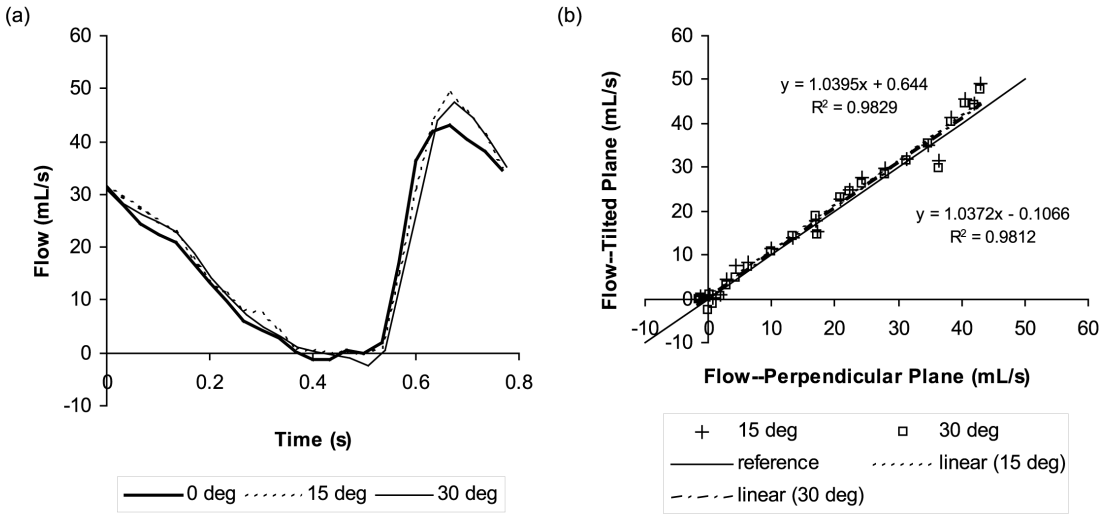


Figure 3.23: Comparison of the average flows acquired with a segmented k-space PC-MRI sequence for different angles between the prescribed plane and the tube axis. "0 degrees" describes a plane that is perpendicular to the tube axis. (a) is a comparison of the flow waveforms, and (b) displays the data as a scatter plot between flows acquired with a non-perpendicular plane versus that acquired with a perpendicular plane. The reference line is the line of identity. The linear fit equation for the 15-degrees plane is given in the upper-left corner, while that of the 30-degrees plane is in the lower-right corner.

While previous studies, as described in Section 2.2.3.4.3, have indicated that misalignments in the plane angle can result in flow measurement errors for large slice-thickness-to-vessel-diameter ratios [102, 103], it was unclear what constituted a large ratio. The current experiment had a slice-thickness-to-vessel-diameter ratio of 0.26, which is presumably small, and showed that the flow measurements were insensitive to

the plane tilt angle. This is in agreement with theoretical predictions but assumes accurate calculations of the area of the region of interest. Because measurements of area are more sensitive to the segmentation threshold value for larger plane tilt angles (planes that are more non-perpendicular to the flow axis) the non-perpendicular planes can display more errors in the flow measurements than the perpendicular planes. The average through-plane velocities for the non-perpendicular planes also varied from those of the perpendicular plane for both the cine and segmented k-space sequences. The measurements acquired with the 30° plane were much closer to the theoretically predicted values than those acquired with the 15° plane, though, possibly due to errors in the baseline correction. Also, note that the theoretical differences in velocity measurements made with a 0° plane and a 15° plane were smaller than that of the repeatability error—6.3 mm/s for cine sequences and 10.2 mm/s for segmented k-space sequences, as determined in Section 3.2.2.2—so it could be argued that differences in the through-plane velocities acquired with the 0° plane and the 15° plane were not measurable.

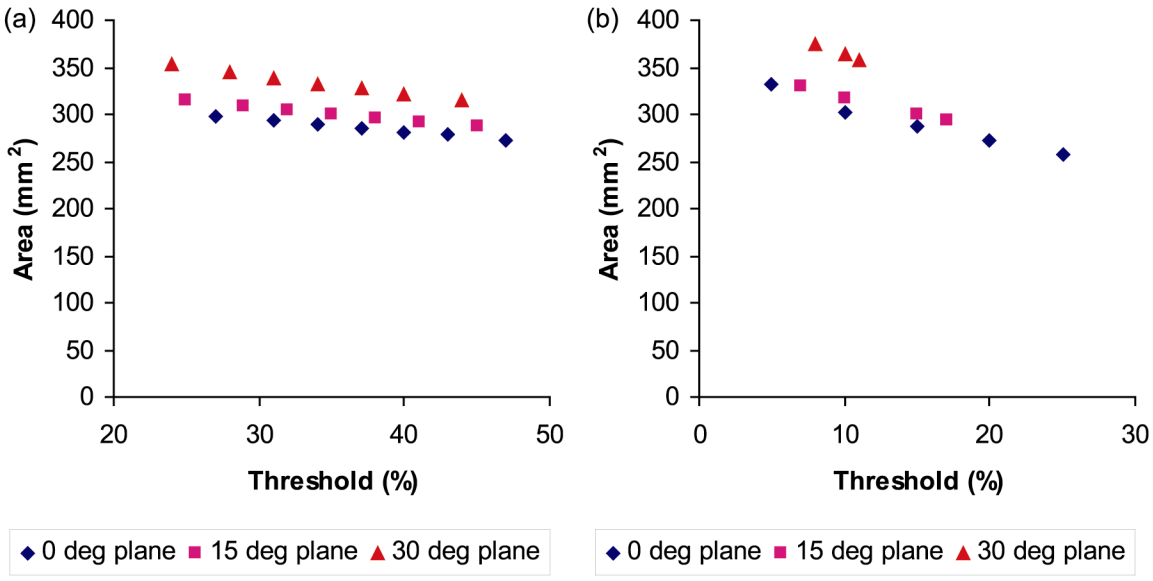


Figure 3.24: Comparison of areas of region of interest for (a) standard 2D cine PC-MRI sequences and (b) segmented k-space PC-MRI sequences for different plane angles. 0° means that the plane is perpendicular to the vessel axis. Results are plotted against the threshold percentage used in the segmentation.

3.2.2.4 Sensitivity to Temporal Resolution

In their study on how interpolation affects cine measurements, Frayne and Rutt described the interpolation process as a low-pass filter, in which the cut-off frequency is inversely proportional to the time between velocity encodings [82]. Specifically, they measured the effect of T_R on the waveform smoothing. However, T_R is only one factor that determines the time between encodings.

Recall from Section 2.2.3.2 that the number of frames per cycle acquired by PC-MRI depends on T_R and the number of velocity components acquired, and for segmented k-space PC-MRI, it also depends on the number of views per segment (vps). The actual temporal resolution can be calculated by dividing the time period by the number of frames acquired per cycle. Therefore, the effective temporal resolutions for the cine and segmented k-space PC-MRI sequences can be altered simply by changing the amount of data each sequence needs to collect within a certain time period. For the cine method, this was accomplished by choosing whether 3 components or 1 component of velocity was collected during a scan. The effective temporal resolution for the 3 components of velocity scan was 0.136 s, while that of the 1 component of velocity scan was only 0.054 s. For the segmented k-space method, changing the number of views per segment varied the effective temporal resolution. The effective temporal resolutions were 0.014, 0.028, and .056 s for 1, 2, and 4 vps respectively. In addition to these scans, a custom cine method with a significantly shorter T_R was used to acquire 3 components of velocity. The effective time resolution of this scan was 0.044 s. The period of the flow waveform was 0.59 s, and the contour used in computing the flows had an average area of 285.3 mm^2. The effect of these different temporal resolutions on the flow waveform is described below.

Comparisons of the through-plane flow waveforms acquired with the cine PC-MRI sequence for 3 components of velocity and for 1 component of velocity showed significant differences in both the shape and magnitude (Figure 3.25). Higher frequencies, apparent in the rapid changes in the flow waveform, were observed in the 1 component of velocity flow measurements because of its higher effective temporal resolution. The 3 components of velocity sequence also had a higher average flow than

the 1 component of velocity sequence—26.1 mL/s versus 20.3 mL/s—due to the asymmetrical dampening of the flow waveform. These observations were consistent with previous experiments examining the effect of T_R on the flow measurements (see Appendix A for a brief description of these results).

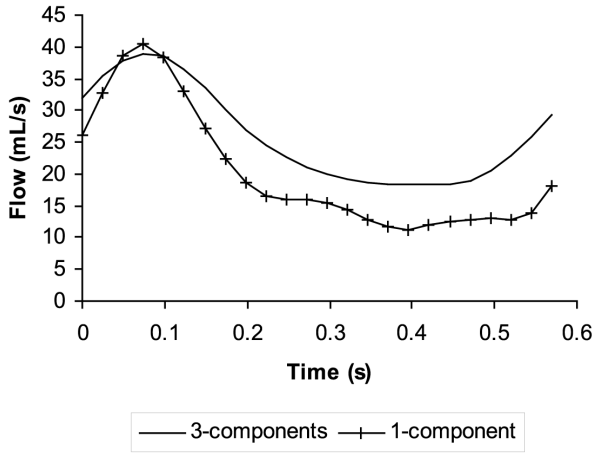


Figure 3.25: Comparison of through-plane flows acquired with a cine PC-MRI sequence for 3 components of velocity and for 1 component of velocity. These flow curves were constructed from 24 time frames. However, the actual number of frames acquired with the 3 components of velocity sequence was 4, while 14 frames were actually acquired using the 1 component of velocity sequence. Note the higher frequencies that can be observed in the 1 component of velocity flow measurements because of the improvement in the true temporal resolution.

In contrast, the flow waveforms calculated from the segmented k-space PC-MRI acquisitions showed little variation (Figure 3.26). The overall shapes were similar, although the undulations observed in the measurements acquired with the 1 and 2 vps sequence were not as apparent in the measurements acquired with the 4 vps sequence. The average flow values also reflected the insensitivity of the measurements to the number of views per segment. For the 4 vps sequence, the average flow was 20.1 mL/s, compared with 19.2 mL/s for the 2 vps method and 19.3 mL/s for the 1 vps method.

Figure 3.27 compares the flow waveforms acquired using the cine PC-MRI sequence, the segmented k-space PC-MRI sequence, the custom cine PC-MRI sequence, and the ultrasonic flow probe. All the waveforms were similar in shape and magnitude, with the exception of that obtained with the cine, 3 components of velocity PC-MRI sequence, which produced the smoothest flow waveform with the least peak-to-peak difference.

These differences are likely due to differences in the effective temporal resolution, which was significantly worse for the cine, 3 components of velocity sequence.

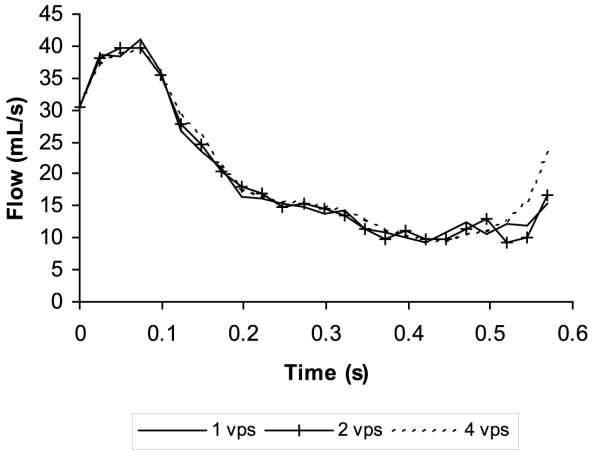


Figure 3.26: Comparison of through-plane flows measured with a segmented k-space PC-MRI sequence. The number of lines or views per segment (vps) were varied, but appeared to have little effect on the resulting flow curves.

3.2.3 Conclusion

These experiments indicate the sensitivity of the measurements made with PC-MRI. The velocity measurements were repeatable to 6.3 mm/s for a cine, 3 components of velocity sequence where the velocities ranged from 36.2 mm/s to 196 mm/s. For the segmented k-space, 4 vps sequence, the velocity measurements were repeatable to 10.2 mm/s, where the range of velocities varied from –43.5 mm/s to 209 mm/s. The average flows were from 19.8 mL/s to 26.3 mL/s and the average variation was from 0.6 to 0.7 mL/s, depending on the sequence used. The v_{enc} used in these sequences was 1500 mm/s. The theoretically computed standard deviations were smaller than the measured velocity values, but greater than the measured flow values.

Changes to the tilt angle of the prescribed imaging plane had little effect on the measured flows for this slice-thickness-to-diameter ratio, as long as the area is accurately computed. Other studies have indicated that larger slice-thickness-to-diameter ratios would result in differences in the flow measurement. This experiment also demonstrated that tilt angle does affect the measured velocities. The magnitudes of the through-plane velocities acquired with planes which were not perpendicular to the tube axis differed

from those acquired with a perpendicular plane by a cos(θ) factor, where θ is the angle between the tube axis and the perpendicular to the plane.

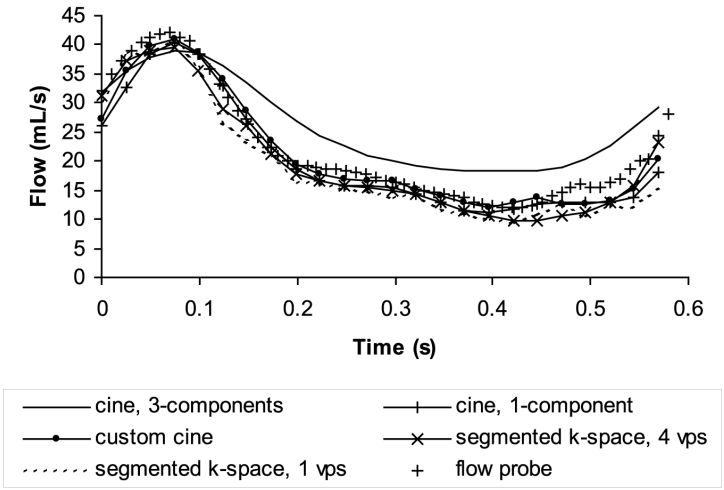


Figure 3.27: Comparison of flow waveforms acquired using different methods: a segmented k-space PC-MRI sequence with 1 and 4 views per segment (vps), a cine PC-MRI sequence for 1 and 3 components of velocity, a custom cine PC-MRI sequence for 3 components of velocity, and an ultrasonic flow probe. Note the similarity in all the waveforms acquired, with the exception of that obtained with the cine, 3 components of velocity PC-MRI sequence. This could be due to the differences in the effective sampling rate, which was significantly lower for the cine, 3 components of velocity sequence.

Lastly, the effect of temporal resolution was investigated. As with previous studies, an averaging effect was observed in flow waveforms acquired with sequences with low effective temporal resolutions. These waveforms tended to have an overall higher average flow and smaller peak-to-peak variations. While T_R is one factor that affects the temporal resolution, the number of velocity components must also be considered, and in the case of the segmented k-space sequence, the number of views per segment.

3.3 Temporal Smoothing of PC-MRI Data

Linear interpolation is applied to the acquired PC-MRI data to produce the user-specified number of time frames per cardiac cycle, as described in Section 2.2.3.2. Because linear interpolation is not a bandwidth-limited operation, information from higher frequencies

are included in the spectrum, thereby introducing variations to the time waveform. The amount of distortion that is introduced depends on the spectrum of the velocity waveform and the true sampling rate. The following analysis investigates the variability introduced by linear interpolation into PC-MRI-acquired velocity data.

3.3.1 Method

PC-MRI data acquired in the *in vitro* experiments described in Chapters 4 and 5 were used to investigate the variation in velocity waveforms due to the linear interpolation in time. Specifically, the inlet data for both the high and low flow experiments performed on a rigid phantom model of a stenotic vessel with a bypass graft were analyzed. These images were acquired using a cine, 3 component velocity sequence with T_R values of 14.0 - 18.4 ms. The period of the low Reynolds number flow was 0.7317 s, while that of the high Reynolds number flow was 0.6 s. Twenty-four time points per cycle were reconstructed.

Using Geodesic, custom software described in Section 2.3.3, each PC-MRI image was converted to a mesh file, which contained the coordinates of the pixel centers in the region of interest and their associated velocities. Velocity waveforms over one cycle were then extracted for individual mesh nodes. These waveforms were imported into MATLAB (The MathWorks, Inc., Natick, MA) for low-pass filtering, which was accomplished by taking the Fourier transform of the original waveform and setting the high frequency components to zero. The inverse Fourier transform of the filtered spectrum yielded the smoothed velocity waveform. Note that due to numerical precision, the smoothed velocity waveform was composed of both real and imaginary terms. However, the imaginary terms were on the order of 10^{-14} and were ignored.

The number of frequency components set to zero depended on the period of the cycle and the true temporal resolution. To determine the number of true frequencies n_{freq} that were measured, the following equation was used:

$$n_{freq} = \left\lfloor 0.5 \cdot \left(\frac{T}{\Delta t} \right) \right\rfloor \tag{3.1}$$

where T is the period and Δt is the true temporal resolution. The 0.5 factor comes from the Nyquist sampling theorem, which states that only frequencies less than ½ the sampling frequency can be uniquely measured. Consequently, the total number of points to set to zero n_{zero} is:

$$n_{zero} = n_{total} - \left(2 \cdot n_{freq} + 1\right) \tag{3.2}$$

where n_{total} is the total number of points in the waveform. The $2 \cdot n_{freq}$ term accounts for the positive and negative frequency terms, and an additional non-zero term is added for the DC, or zero frequency, component. Therefore, for the low Reynolds number PC-MRI images, which had a period of 0.7317 s and a temporal resolution of 0.056 s, 11 points were set to zero. In the case of the high Reynolds number, the period was 0.6 s and the temporal resolution was .0736 s, so 15 points were set to zero.

3.3.2 Results and Discussion

Figure 3.28 and Figure 3.29 compare the original velocity waveforms with the smoothed velocity waveforms for three points for the slow and high Reynolds flow conditions. There was little difference between the original and smoothed waveforms, regardless of the flow conditions. Quantitatively, the absolute differences were on the order of a few mm/s (Figure 3.30(a) and Figure 3.31(a)), an insignificant amount at most time points. Obviously, at lower velocities, such as at 0.152 s for point C of the slow Reynolds flow case, these differences will have a larger impact. The absolute difference averaged across time and the three points was 1.46 mm/s for the slow Reynolds flow and 1.55 mm/s for the high Reynolds flow, so in this case, the differences between the original and smoothed waveforms are similar, despite the differences in the period and temporal resolution for the two flow conditions.

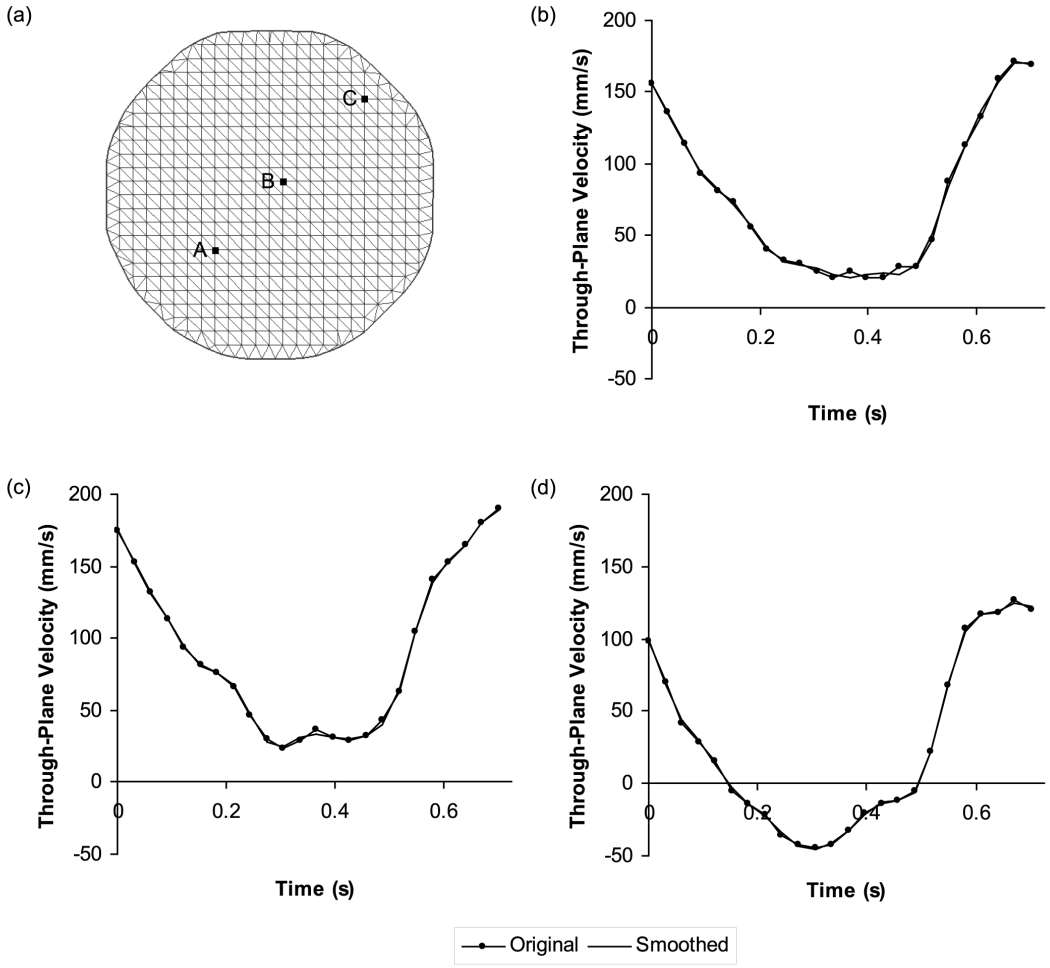


Figure 3.28: Temporal smoothing of velocities for low Reynolds flow acquired with a cine, 3 components of velocity PC-MRI sequence. The smoothed waveform was reconstructed from the DC (0 Hz) frequency plus 6 harmonics. The effect of the temporal smoothing was examined at three points in the region of interest, shown in (a). (b) compares the waveforms for point A. (c) compares them for point B, and (d) for point C. The difference between the original and the smoothed waveform is insignificant.

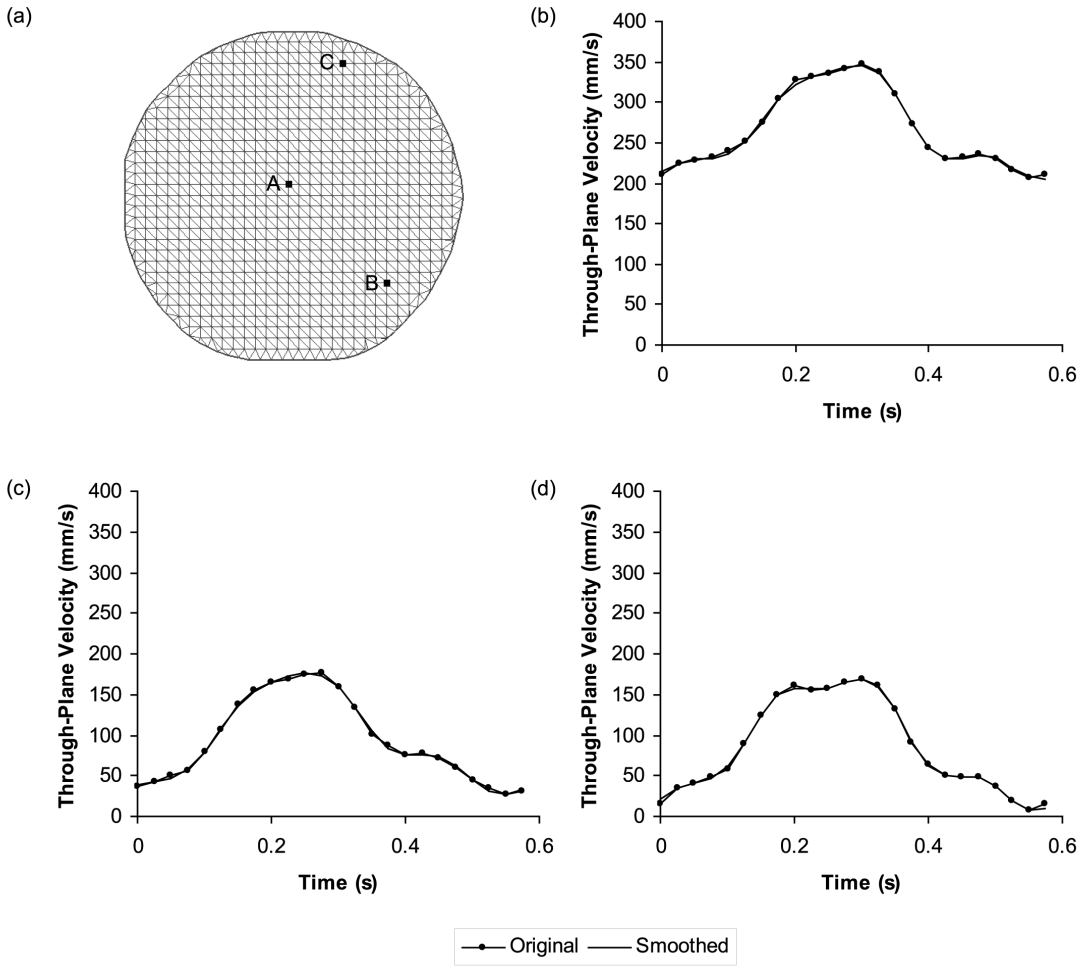


Figure 3.29: Temporal smoothing of velocities for high Reynolds flow acquired with a cine, 3 components of velocity PC-MRI sequence. The smoothed waveform was reconstructed from the DC (0 Hz) frequency plus 4 harmonics. The difference between the original and the smoothed waveform is insignificant. The effect of the temporal smoothing was examined at three points in the region of interest, shown in (a). (b) compares the waveforms for point A. (c) compares them for point B, and (d) for point C. The difference between the original and the smoothed waveform is insignificant.

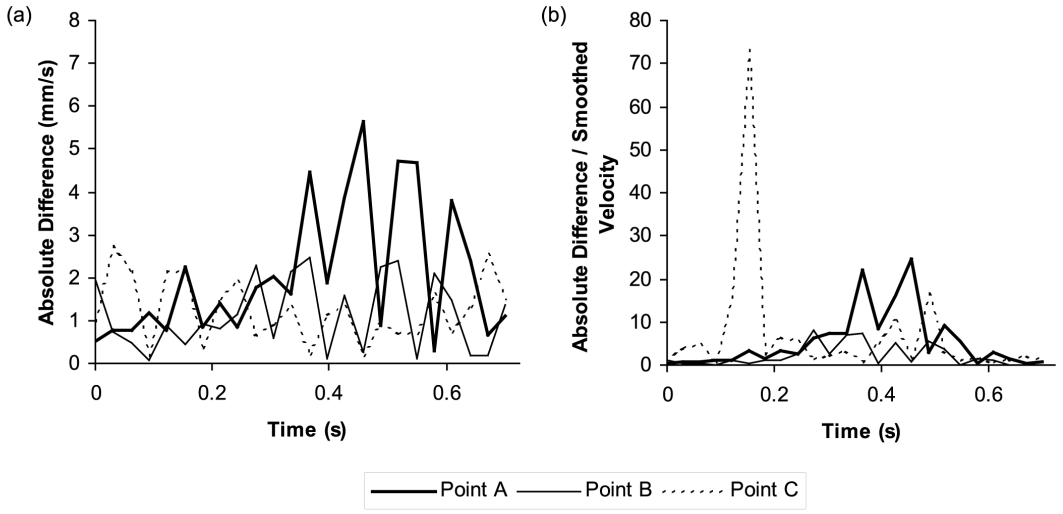


Figure 3.30: Absolute differences in the velocity waveforms due to temporal smoothing under low Reynolds conditions. The absolute differences are shown in (a), while (b) graphs the percentage of the absolute difference relative to the smoothed velocity value. The differences are small, although significant at a few time points where the velocity is small.

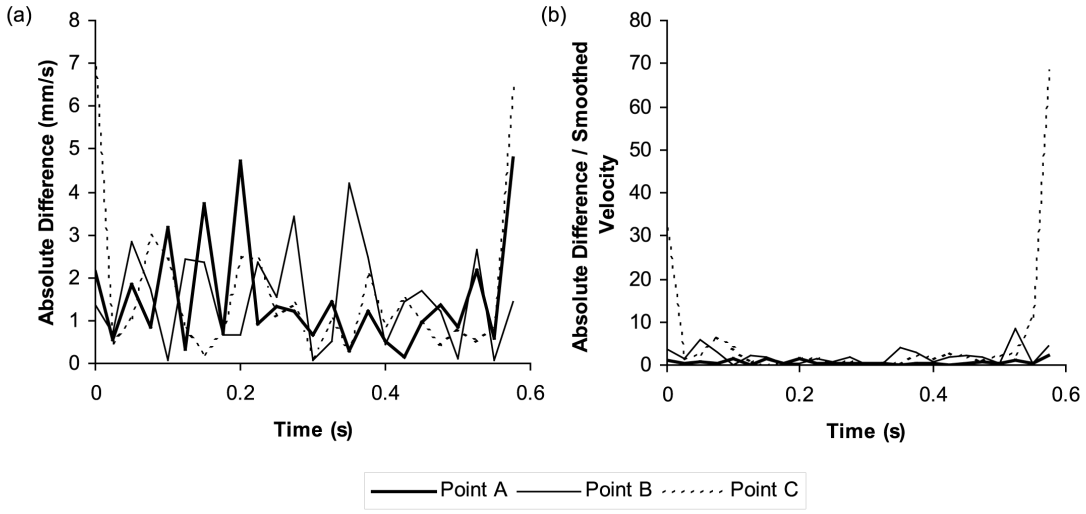


Figure 3.31: Absolute differences in the velocity waveforms due to temporal smoothing under high Reynolds conditions. The absolute differences are shown in (a), while (b) graphs the percentage of the absolute difference relative to the smoothed velocity value. The differences are small, although significant at a few time points where the velocity is small.

3.3.3 Conclusion

Temporal smoothing had little effect on the velocity waveforms in both the low and high Reynolds number cases. In fact, the average absolute difference between the smoothed

waveforms and the original waveforms was 1.4 – 1.6 mm/s, regardless of the flow conditions. This difference is obviously more significant for lower velocities, but is unlikely to notably affect the overall velocity patterns. While only three points were examined in each image, this preliminary study suggests that temporal smoothing is unnecessary for velocity waveforms acquired with a cine sequence under certain imaging and flow conditions.

Chapter 4

Low Flow *In Vitro* Experiment

If you put tomfoolery into a computer, nothing comes out of it but tomfoolery. But this tomfoolery, having passed through a very expensive machine, is somehow ennobled and no one dares criticize it. ~Pierre Gallois

With the vast improvements in computational power, it is possible to solve increasingly complex problems. However, the validity of these solutions depends upon the inputs to the computer: the program describing what the computer should do and the inputs to the program itself. In the case of computer simulations of blood flow, studies have been conducted to demonstrate their accuracy under various conditions. Previous *in vitro* experiments have compared the simulation results of blood flow to physical measurements acquired using techniques such as laser Doppler anemometry and phase-contrast MRI (PC-MRI). While the results of these comparisons have been favorable, they have been limited to simpler geometries, such as bifurcations [45, 48] or anastomotic junctions [52] [56], and used idealized geometries. To date, no studies have been conducted to compare the flow patterns predicted by numerical simulation methods in a more complex geometry, such as that of a stenotic vessel with a bypass graft, under conditions that are suitable for surgical planning purposes. Unlike many previous studies, the simulations in the following *in vitro* study assumed no *a priori* knowledge of the flow distribution between vessels and the geometric models were constructed from imaging data. Furthermore, the geometry used in this study included both the proximal and distal anastomoses, thus incorporating both diverging and converging flow situations. Section 4.1 describes the experimental set-up, the data acquisition, and the numerical

simulation parameters used in comparing PC-MRI measurements to the numerically computed results. Convergence studies for the numerical simulations are described in Section 4.2, while the methods for post-processing the numerical simulation data in order to compare them to PC-MRI measurements are explained in Section 4.3. The numerical simulation results are presented, along with the PC-MRI measurements, in Section 4.4. Section 4.5 discusses potential limitations of the experimental data, while Section 4.6 analyzes the sensitivity of the simulations to geometry and inlet velocity boundary conditions. Lastly, Section 4.7 discusses the numerical simulation results and how they compare to PC-MRI, and a summary of this experiment is presented in Section 4.8.

4.1 Experimental Protocol

4.1.1 Experimental Set-Up

A phantom model of an idealized stenotic vessel with a bypass graft [125], shown in Figure 4.1, was constructed out of a photoreactive resin using stereolithography [126]. The model was designed to be symmetric with a host vessel diameter of 1.9 cm, a graft diameter of 1.6 cm, and a 45^{o} angle between the graft and the host vessel. At its narrowest, the host vessel would be .95 cm in diameter, representing a 75% stenosis, or narrowing in the vessel's cross-sectional area. See Figure 4.2 for all model dimensions.

The fluid used in this experiment was a mixture of 39.8% glycerol, 59.7% distilled water, and 0.5% gadolinium by volume. The gadolinium was added to enhance image contrast when acquiring MRI data. The dynamic viscosity of this mixture, as measured using a size-100 Cannon-Fenske viscometer (International Research Glassware, Kenilworth, NJ), was 0.039 dynes-s/cm^2 at 22^{o} C. This was determined from 2 samples of the fluid and at least three viscosity measurements for each sample. The viscosity of the mixture depended upon that of distilled water, which was calculated according to the following empirical formula [127]:

$$\mu \approx \mu_o \cdot \exp\left\{-1.94 - 4.80\left(\frac{T_o}{T}\right) + 6.74\left(\frac{T_o}{T}\right)^2\right\} \tag{4.1}$$

where μ is the viscosity, T is the temperature in Kelvins, and μ_o is the viscosity at a temperature T_o of 273.16 K (freezing point of water). The density of the mixture was measured to be 1.1 g/mL.

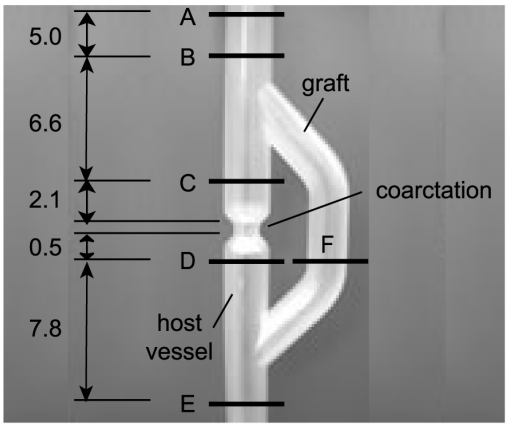


Figure 4.1: Phantom model for the *in vitro* flow experiments. Planes A-F indicate locations where PC-MRI data was acquired for the low flow experiment. Plane A is the inlet, and this information was used to prescribe the boundary condition for the numerical simulations. Flow and velocity information acquired at all other locations were used for comparison purposes. The distances between the planes relative to each other and/or relative to a distinct location on the model were estimated and are given in centimeters. Data for planes D and F were acquired with a single slice.

The phantom was placed within a flow system consisting of a blood flow pump (Harvard Apparatus, Holliston, MA), a reservoir which supplied the glycerol-water-gadolinium mixture to the pump, and two sets of tubing. The pump was connected to a set of rigid polycarbonate tubing by approximately 4.5 m of flexible, braided tubing, which allowed the pump to be placed as far as possible from the MRI system while minimizing the pressure needed to pump the fluid through the system. The 2.4 m of rigid tubing which connected the flexible tubing to the phantom provided the necessary entrance length, estimated to be 0.3 m according to Equation (2.12), to generate a parabolic flow profile at the inlet of the phantom. In addition, a honeycomb-like structure made out of fiberglass was placed at the entrance of the rigid tubing to help straighten out the flow. The trigger signal from the flow pump was connected to an electrocardiogram (ECG) simulator (Shelley Medical Imaging Technologies, London, Ontario, Canada), which generated an ECG signal to be used by the MRI system. Figure 3.9 shows a schematic of the flow system, while Figure 4.3 describes the set-up via photographs. For this experiment, the pump was set to output a pulsatile waveform at

approximately 13.5 mL/s at a rate of 82 cycles per minute. These flow settings corresponded to a Womersley number of 14.8 and an average Reynolds number of 255 at the inlet of the phantom model. The range for the Reynolds number was from 0 to 690.

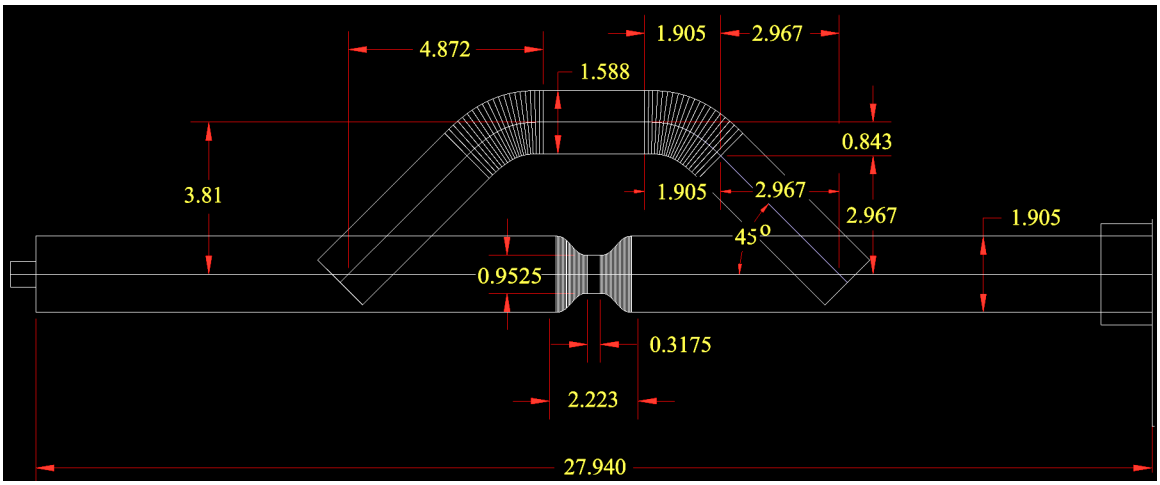


Figure 4.2: Diagram of the phantom model. Measurements are given in centimeters and are based on the original diagram, courtesy of *Gilbert Palafox*.

4.1.2 Data Acquisition

4.1.2.1 Flow Probe Measurements

As with the experiments described in Section 3.2, a 12N in-line ultrasonic flow probe (Transonic Systems, Inc., Ithaca, NY) was placed upstream of the rigid tubing to assess the periodicity of the flow and to measure the flow rate. The flow probe was connected to a T101 ultrasonic blood flow meter (Transonic Systems, Inc., Ithaca, NY), which was connected to a data acquisition board (DAQPad-6020E, National Instruments, Austin, TX), so that flow information could be acquired using a LabVIEW program (LabVIEW v.6 and v.6.1, National Instruments, Austin, TX) on a Dell Inspiron 8000 laptop computer (Dell Computer Corporation, Round Rock, TX) at a sample rate of 200 samples per second. The measurements were converted from voltages to mL/s by multiplying the voltages by a factor of 4.1, a quantity obtained from previous calibrations using the bucket and stopwatch technique. To obtain a single representative cycle of the flow, the flow signal was divided into individual cycles by identifying the minimum points of the

waveform. The individual cycles were then averaged together to obtain one representative cycle that would be used in the analysis.

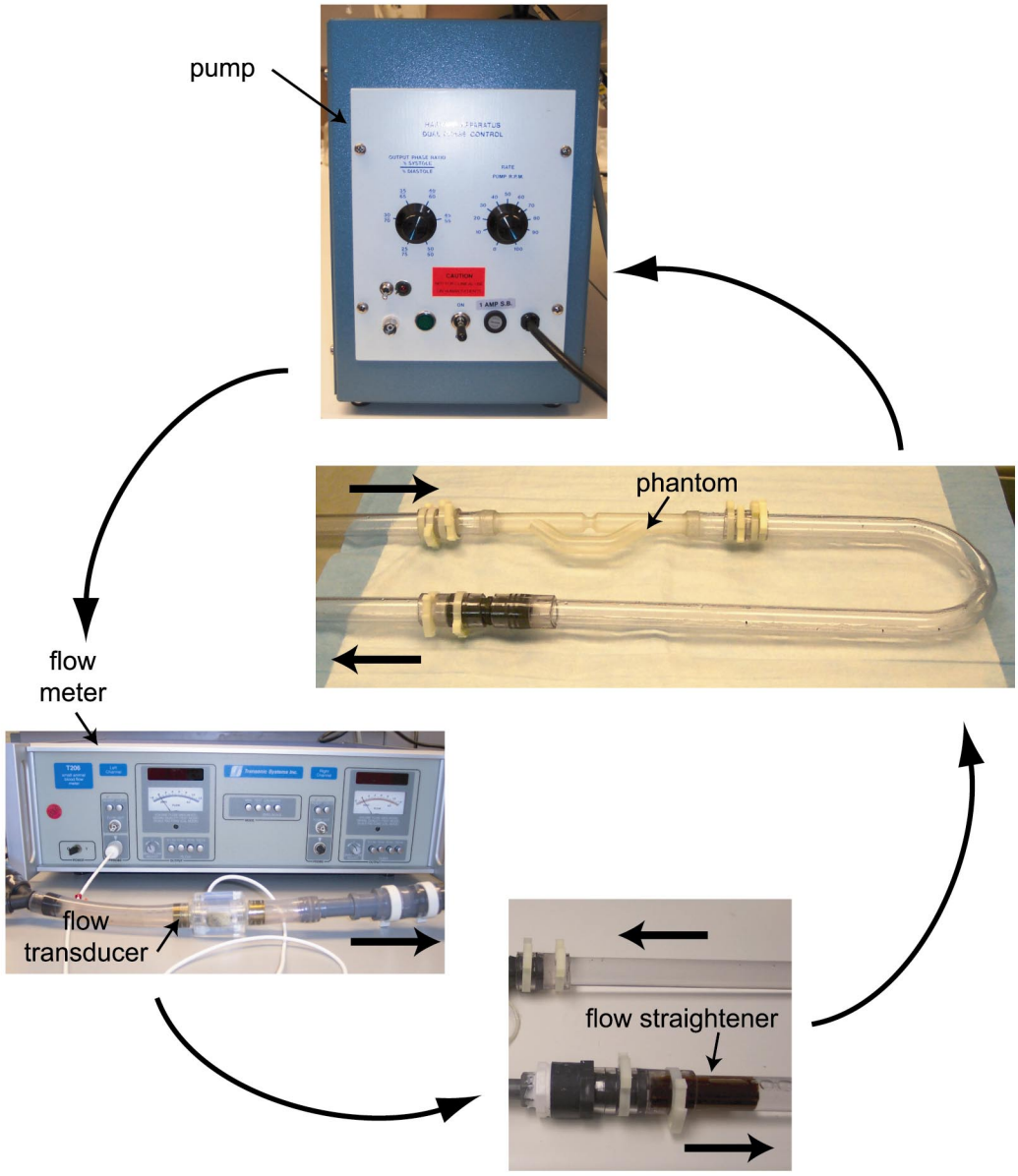


Figure 4.3: Diagram of the experimental set-up for the low flow *in vitro* flow experiment. A mixture of distilled water, glycerol, and gadolinium was pumped through the system using a blood flow pump, which generated a pulsatile flow waveform. The phantom was connected to the pump via approximately 4.5 m of flexible tubing followed by 2.4 m of rigid polycarbonate tubing. A fiberglass, honeycomb-like structure was placed at the beginning of the rigid tubing to straighten out the flow, and an ultrasonic flow transducer was placed upstream of the rigid tubing. The larger black arrows in the pictures indicate the direction of flow in the system.

4.1.2.2 MRI Data

Both geometry and flow measurements were acquired using a 1.5 T MRI system (Signa, GE Medical Systems, Waukesha, WI). The phantom was placed inside of a head coil to increase signal reception. Two-dimensional localizer images were then obtained for spatial localizations of the subsequent scans.

Contrast-enhanced magnetic resonance angiography (CE-MRA) data provided the geometric information and was obtained using a rapid, three-dimensional, gradient-recalled echo sequence [128]. The image acquisition was performed with T_R = 6.8 ms, T_E = 3.1 ms, a field of view (FOV) of 28 cm x 14 cm, a slice thickness of 1.5 mm, an acquisition matrix size of 512x256, number of excitations (NEX) = 2, and a 25-degree flip angle. 64 slices were acquired in the axial direction. Grad-warp correction was applied to the CE-MRA data prior to use.

A 2D cine phase contrast sequence [77, 78], customized to potentially shorten TR values by improving gradient heating calculations and allowing a variable bandwidth for a given spatial resolution [124], was used to acquire three orthogonal components of velocity. Oblique axial slices were acquired using parameters that resembled those used in the *in vivo* experiment described in Chapter 6: respiratory compensation, T_R = 14 to 14.5 ms, T_E = 7.4 ms, 20 cm FOV, 5 mm slice thickness, acquisition matrix of 256x256, 31.25 kHz bandwidth, NEX = 1, and a 20-degree flip angle. The through-plane velocity encoding (v_{enc}) was 30 cm/s for all locations except at the distal coarctation (plane D in Figure 4.1) and at the graft (plane F in Figure 4.1), where the through-plane encoding was 50 cm/s. The in-plane v_{enc} was 15 cm/s for all PC-MRI images acquired. For each data set, 24 time points per cycle were reconstructed, and velocity acquisitions were synchronized using the signal from the trigger-to-ECG converter.

The velocity information was acquired at 6 locations: superior to the graft (inlet, plane A), a short distance downstream of the inlet (downstream inlet, plane B), in between the proximal anastomosis and the aortic coarctation (proximal coarctation, plane C), distal to the aortic coarctation (distal coarctation, plane D), distal to the distal anastomosis (outlet, plane E), and in the graft (graft, plane F). See Figure 4.1 for the location of the planes. Velocity information for planes D and F were acquired

simultaneously. The PC-MRI data was acquired first with the flow pump turned on, and then with it turned off. When the pump was turned off, the signal from an ECG simulator (M310, Fogg System Company, Inc., Denver, CO) was used for synchronization.

A first-order baseline correction was computed from the flow-pump-off images using the custom software vcalc. This correction was applied to the PC-MRI velocity data prior to comparison. In addition, the signal-to-noise ratio and the standard deviation of the PC-MRI velocity measurements were computed for each slice plane using the method described in Section 3.2.1.3. As demonstrated by the experiments in Section 3.2.2.2, these precision calculations provide a lower bound on the repeatability of these measurements.

4.1.3 Numerical Simulations

The geometric model construction process implemented in Geodesic and described in Section 2.3.3.1 was used to generate a solid model from the grad-warp-corrected CE-MRA data. A spline-fit through five to ten manually selected points described paths through the vessels of interest. Two-dimensional slices were oriented perpendicular to these paths, and a combination of thresholding and the level set method was applied to these slices to segment out the lumen. For the slices where thresholding was applied, a threshold value of 150 was used. For the level set method, default values, including a magnification factor of 0.33, were used for all parameters except for the curvature constraints and the initial radii. For this data set, the first-phase curvature constraint and the second-phase upper curvature value were set between 0.2 and 0.4, while the second-phase lower curvature value was set to 0.0. The initial radii ranged between 3 mm and 6 mm, depending on the location of segmentation. In addition, contours could not be segmented out at the first and last positions along the bypass path, since these were located within the host vessel. However, contours were needed at these positions in order to create a bypass model that could be unioned with the model of the host vessel. Therefore, copies of contours from the next closest position along the bypass path were made and oriented at the ends of the bypass path.

The contours were resampled to 20 points per contour, and an "align by distance" method was applied to the cross-sections. Non-uniform rational B-spline (NURB) surfaces were lofted through the cross-sections and bounded to create a solid model using the Parasolid (Unigraphics Solutions, St. Louis, MO) geometry kernel. This process was used to create solid models of the host vessel and the graft, which were then joined together to construct a final geometric solid model. The PC-MRI image plane at the inlet was then used to trim the model.

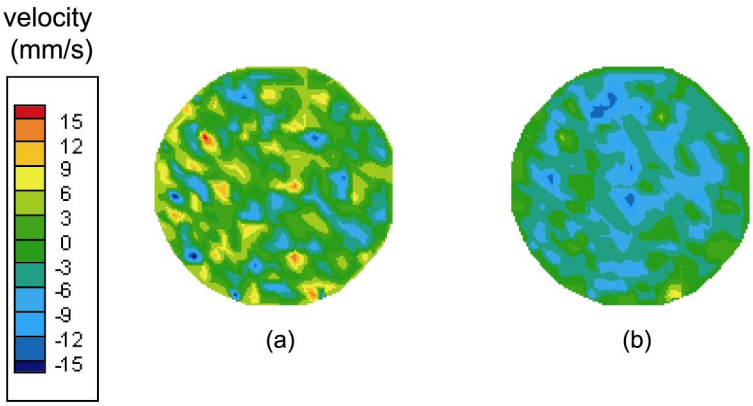


Figure 4.4: Example of the in-plane velocity components at the inlet (plane A) during peak flow. (a) Anterior-posterior velocities. (b) Right-left velocities.

Automatic mesh generation software [117] (MeshSim, Simmetrix, Inc., Clifton Park, NY) was used to discretize the model into a finite element mesh, and an inlet velocity profile based upon the PC-MRI velocity measurements was generated according to the method described in Section 2.3.3.2.2. Additional processing was performed on the inlet velocity profile, since the in-plane components were noisy due to the v_{enc} of 150 mm/s, which was high relative to the actual in-plane velocities. In this case, since the flow system was set up to produce fully developed pulsatile flow at the inlet of the phantom model, the in-plane components should be close to zero. The actual PC-MRI measurements of the in-plane velocities ranged from –17 to 15 mm/s and did not form any coherent patterns (Figure 4.4), suggesting that the measurements were primarily due to noise. Therefore, for the numerical simulations, only the through-plane component of velocity along the host vessel axis was used as an inlet boundary condition. Because the actual inlet imaging plane was not perfectly perpendicular to the host vessel axis, the

direction of the vessel axis was determined by finding the line between the centers of two contours at either end of the host vessel. This line will hereafter be referred to as the "user-defined axis." The mapped velocities were then projected onto the user-defined axis by applying the dot product operation to the vectors, and this new mapping was used as the inlet boundary condition.

Additional boundary conditions were set for the luminal surfaces of the host vessel and the graft. The velocities on these surfaces were prescribed to be zero, consistent with a no-slip condition. A zero exit pressure was also prescribed for all calculations. The simulations model the walls as rigid structures, and the blood was modeled as an incompressible Newtonian fluid with a constant density of 1.1 g/cm^3 and a constant viscosity of 0.039 dynes-s/cm^2, matching the measured values. Under these boundary conditions and assumptions, pulsatile flow was computed for 25 cycles using the Spectrum™ Solver software, described in Section 2.4.3 and previously validated for the incompressible Navier-Stokes equations [52, 105]. A sample input file for this simulation is provided in Appendix B. The simulation was run on 30 processors of a 128-processor Origin 3800 (Silicon Graphics, Inc., Mountain View, CA). Convergence studies, described in the following section, were conducted to determine the best mesh size and number of time steps per cycle to use in the simulations.

4.2 Convergence Studies

In performing the mesh convergence simulations, three different mesh sizes were examined: a 1.5-million-element mesh, a 3.3-million-element mesh, and a 4.2-million element mesh. Note that with the currently installed software, the largest mesh that can be run consists of approximately 4 million elements. The simulations were all run with 240 time steps per cycle, and the inlet boundary condition utilized the original PC-MRI velocity mapping of the three components of velocity, not the "user-defined axis" described above. For the time step convergence study, the 3.3-million-element mesh with an inlet boundary condition based upon the original velocity mapping of the three components of velocity was used. Again, three different settings were considered: 240

time steps per cycle, 480 time steps per cycle, and 960 time steps per cycle. The simulations were run for 10 cycles, and the results from cycle 9 were used to determine the mesh size and the number of time steps to use in the simulations.

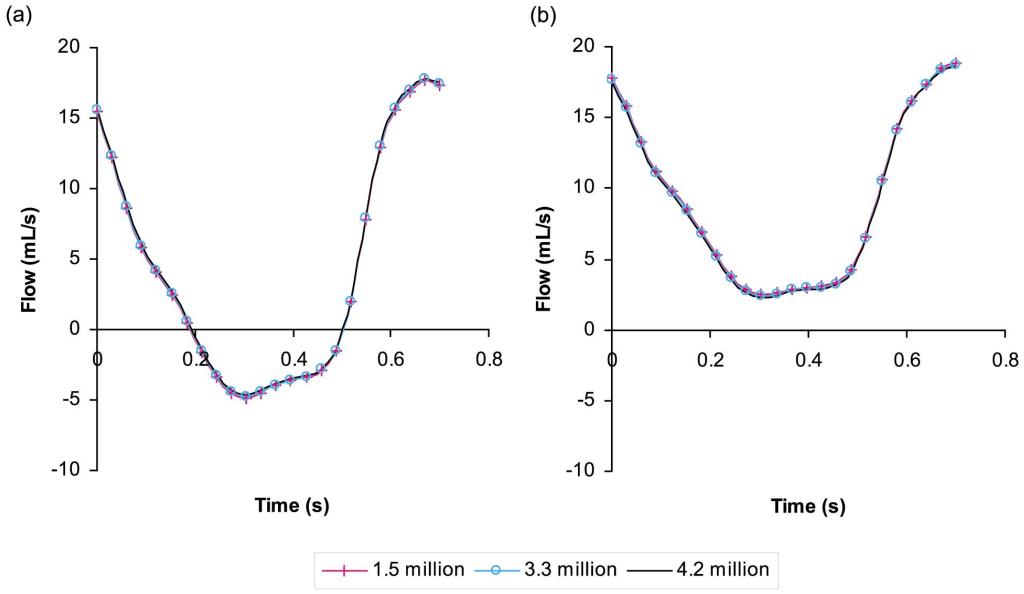


Figure 4.5: Comparison of flows through (a) the aorta (plane C) and (b) the graft (plane F) for simulations of different mesh sizes.

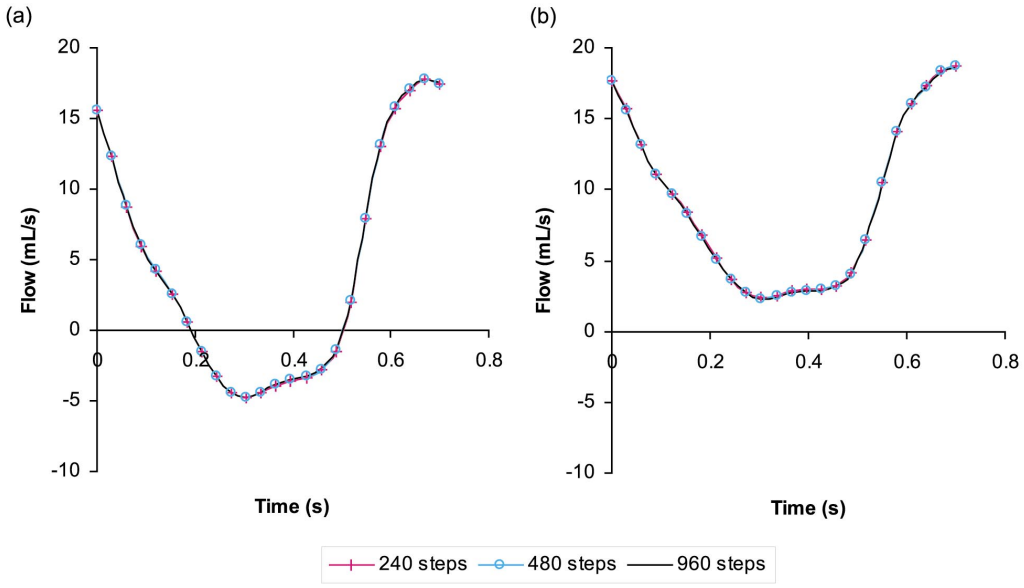


Figure 4.6: Comparison of flows through (a) the aorta (plane C) and (b) the graft (plane F) for simulations run with a different number of time steps per cycle.

A comparison of the flow waveforms from these numerical simulations indicated that the flow results have converged. Figure 4.5 and Figure 4.6 show the flows for the different mesh sizes and the different number of time steps, respectively. The waveforms in these graphs were essentially identical, regardless of the mesh size or the number of time steps used in the simulation, leading to the conclusion that the flow waveforms for the numerical simulations have converged even at the lowest mesh size and the lowest number of time steps examined here.

Examination of the through-plane velocity contours, however, revealed differences due both to mesh size and the number of time steps. Figure 4.7 through Figure 4.9 show the numerical results at 4 different time points for the 3 different mesh sizes at the level of the proximal coarctation (plane C), in the graft (plane F), and at the outlet (plane E), respectively. At both the proximal coarctation and the graft locations, there were small but noticeable shifts in the velocity contours. The general contour patterns were similar for the different mesh sizes, though. At the outlet, significant differences in the velocity contour patterns were observed for the different mesh sizes. While mesh convergence was obviously not achieved using these mesh sizes, results for the proximal coarctation and the bypass suggest that they were nearly converged at these locations. At the outlet, the differences between the results produced by the various mesh sizes suggest that notably larger meshes may be needed to achieve a converged solution for this location. As a compromise between obtaining a converged solution and obtaining a solution in a reasonable amount of time, a mesh size of 3.3-million elements was used.

A similar finding was made when comparing the results for the different number of time steps. Figure 4.10 through Figure 4.12 show the numerical results at 4 different time points for the 3 different time steps at the level of the proximal coarctation (plane), in the graft (plane F), and at the outlet (plane E), respectively. As with the mesh size comparison, little change occurred between the velocity contours for the different time steps at the proximal coarctation and at the graft slice planes, but noticeable differences existed at the outlet. At the proximal coarctation and at the graft, the velocity contours for the simulations of 480 time steps and 960 time steps were nearly identical. Therefore, all simulations used in the following comparisons utilized 480 time steps per cycle.

While these simulations may not have resulted in a converged solution at the outlet, they did produce a converged solution at the proximal coarctation and at the graft and ran in a much shorter time period than a 960-time-step simulation.

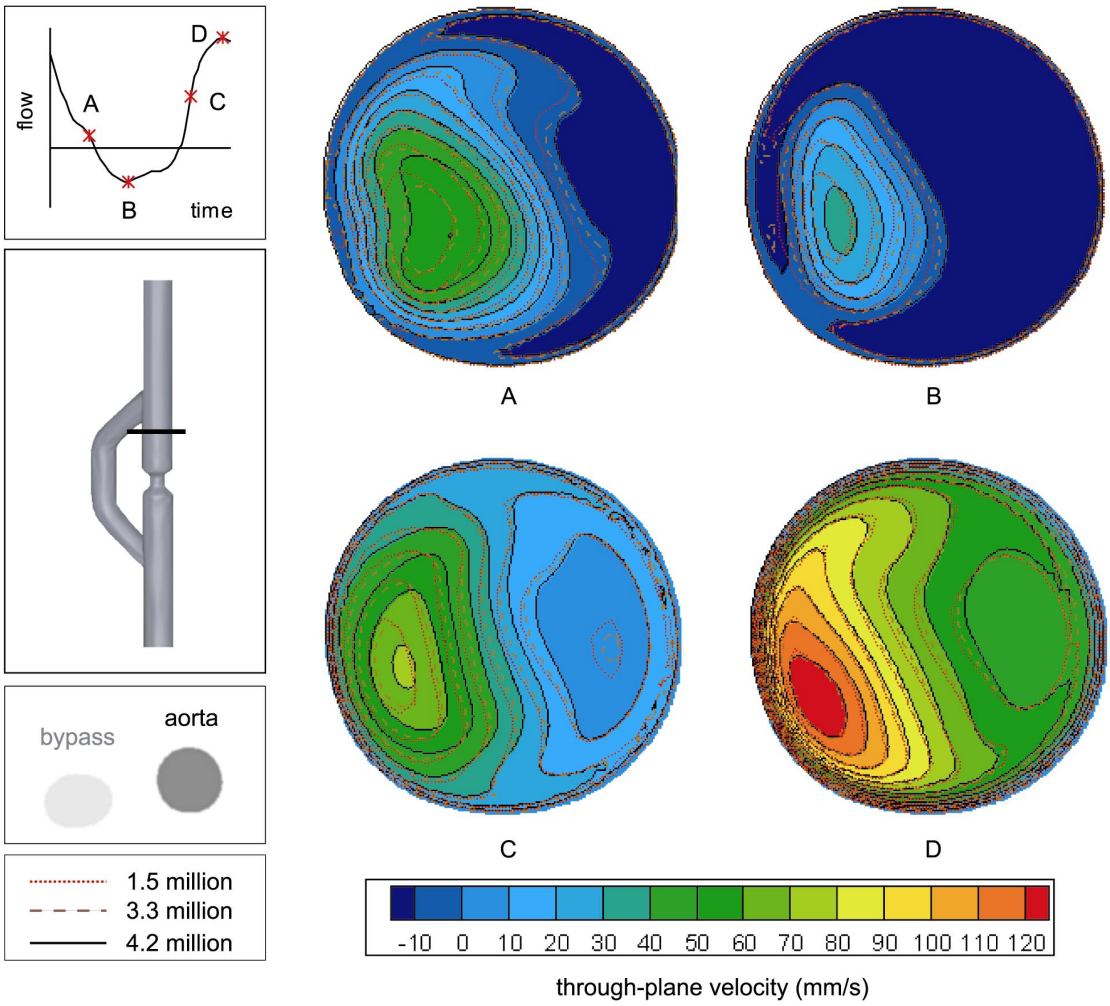


Figure 4.7: Comparison of through-plane velocity contours at the aorta proximal to the coarctation (plane C in Figure 4.1) for different mesh sizes. The color map and the solid black lines correspond to numerical simulation results for a 4.2 million element mesh. The dashed brown lines indicate contours for a 3.3 million element mesh, and the dotted red lines for a 1.5 million element mesh. Results from four different time points in the cycle are presented: mid-deceleration (A), late-deceleration (B), acceleration (C), peak flow (D).

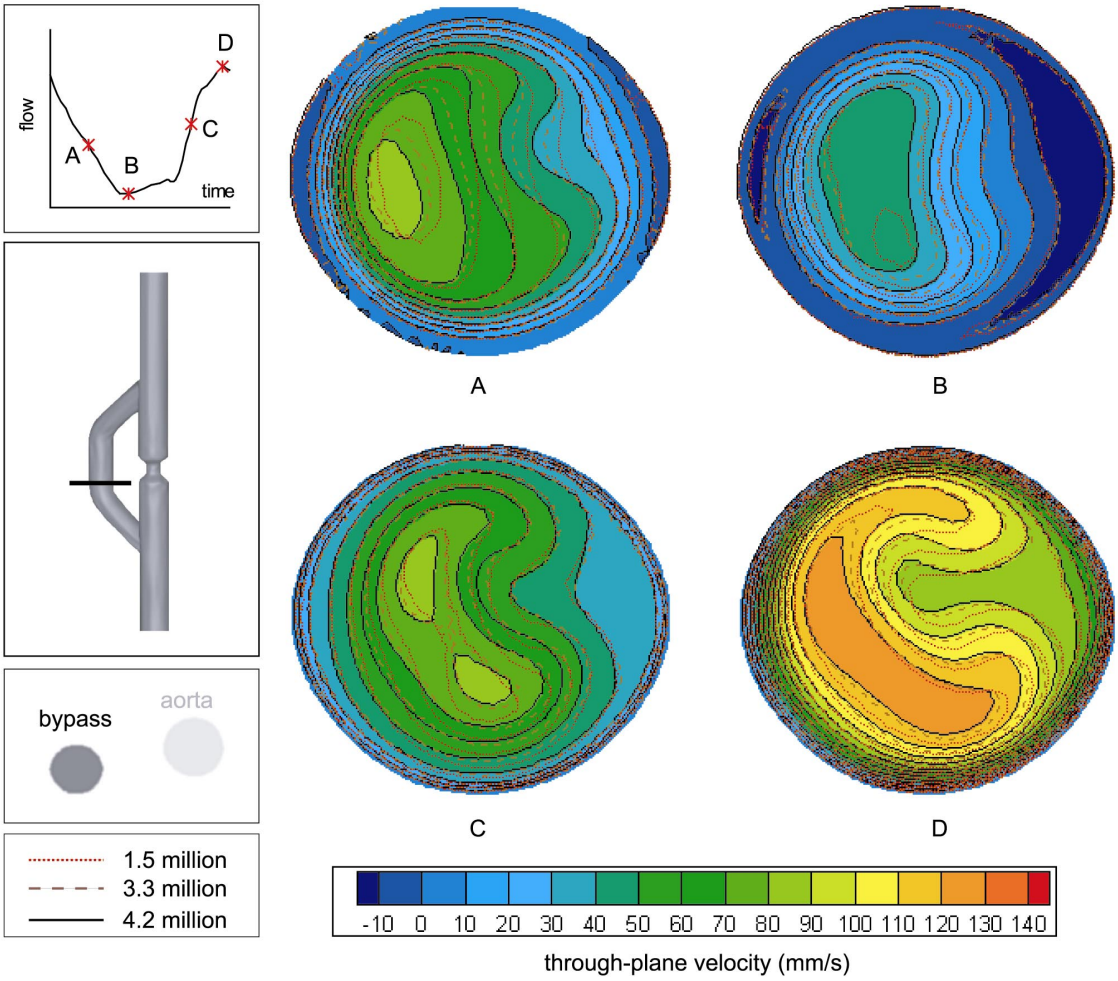


Figure 4.8: Comparison of through-plane velocity contours at the graft (plane F in Figure 4.1) for different mesh sizes. The color map and the solid black lines correspond to numerical simulation results for a 4.2 million element mesh. The dashed brown lines indicate contours for a 3.3 million element mesh, and the dotted red lines for a 1.5 million element mesh. Results from four different time points in the cycle are presented: mid-deceleration (A), late-deceleration (B), acceleration (C), peak flow (D).

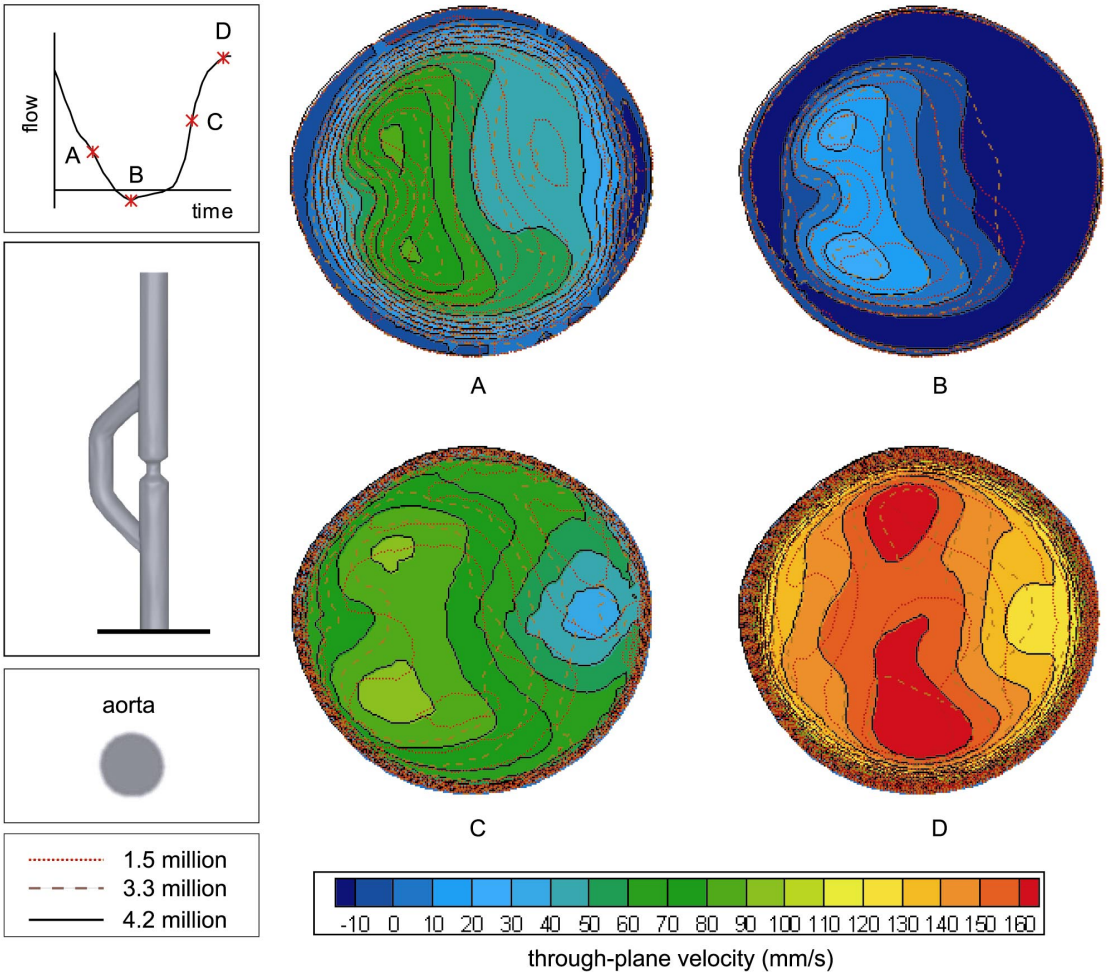


Figure 4.9: Comparison of through-plane velocity contours at the aorta distal to the bypass, also referred to as the outlet, (plane E in Figure 4.1) for different mesh sizes. The color map and the solid black lines correspond to numerical simulation results for a 4.2 million element mesh. The dashed brown lines indicate contours for a 3.3 million element mesh, and the dotted red lines for a 1.5 million element mesh. Results from four different time points in the cycle are presented: mid-deceleration (A), late-deceleration (B), acceleration (C), peak flow (D).

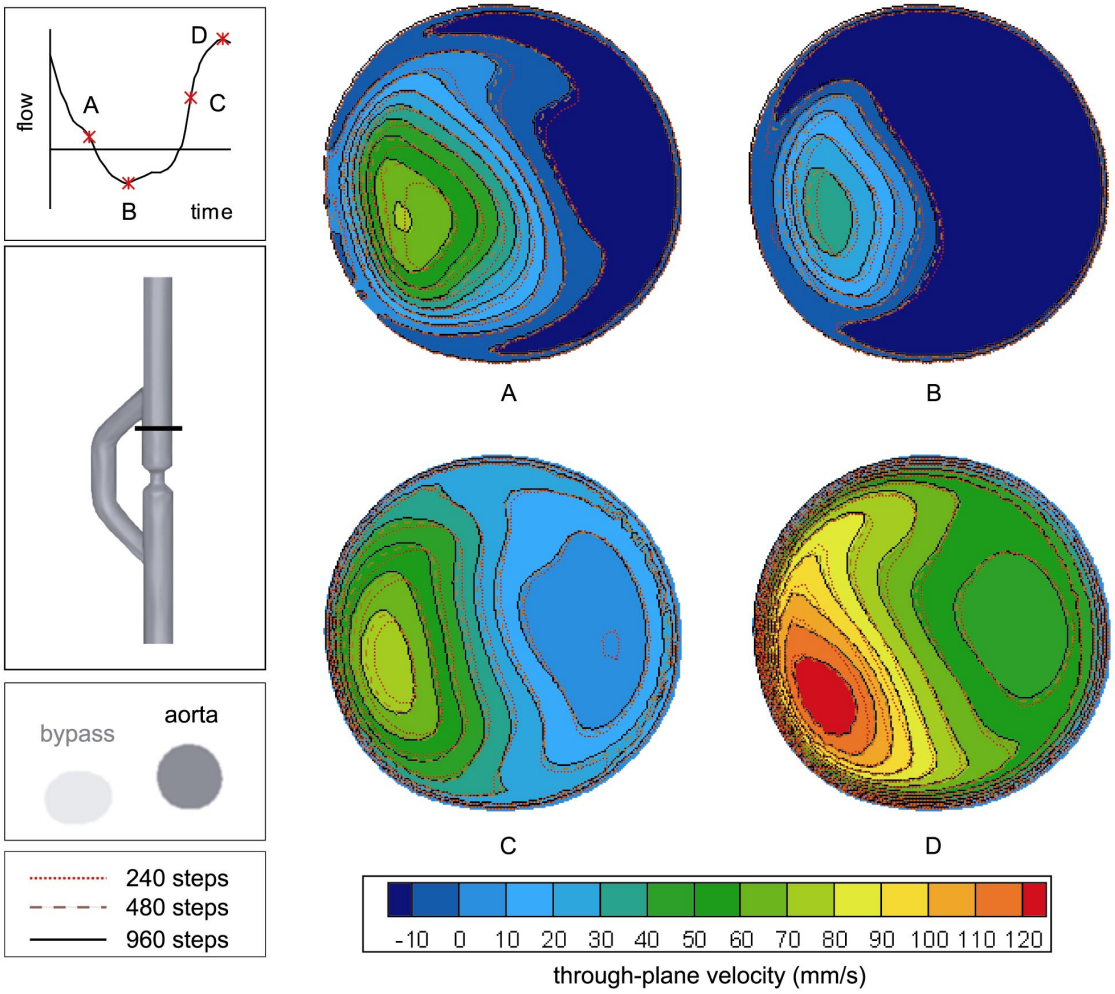


Figure 4.10: Comparison of through-plane velocity contours at the aorta proximal to the coarctation (plane C in Figure 4.1) for different number of time steps per cycle. The color map and the solid black lines correspond to numerical simulation results for 960 time steps per cycle. The dashed brown lines indicate contours for 480 time steps per cycle, and the dotted red lines for 240 time steps per cycle. Results from four different time points in the cycle are presented: mid-deceleration (A), late-deceleration (B), acceleration (C), peak flow (D).

4.3 Comparison Method

Geodesic provides the ability to extract the numerical simulation results at exactly the same locations as the planes used to acquire the PC-MRI data. In this way, velocities at the different plane locations (planes B-F) indicated in Figure 4.1 can be compared. For each plane of interest, the velocities for both the numerical simulations and for the first-order baseline-corrected PC-MRI data were written out to a file for visualization within

Tecplot (Amtec Engineering, Inc., Bellevue, WA). The mesh used for the PC-MRI data was based upon the level-set segmentation of the vessel of interest, with each node either representing the center of a pixel or a boundary point. See [105] for more details.

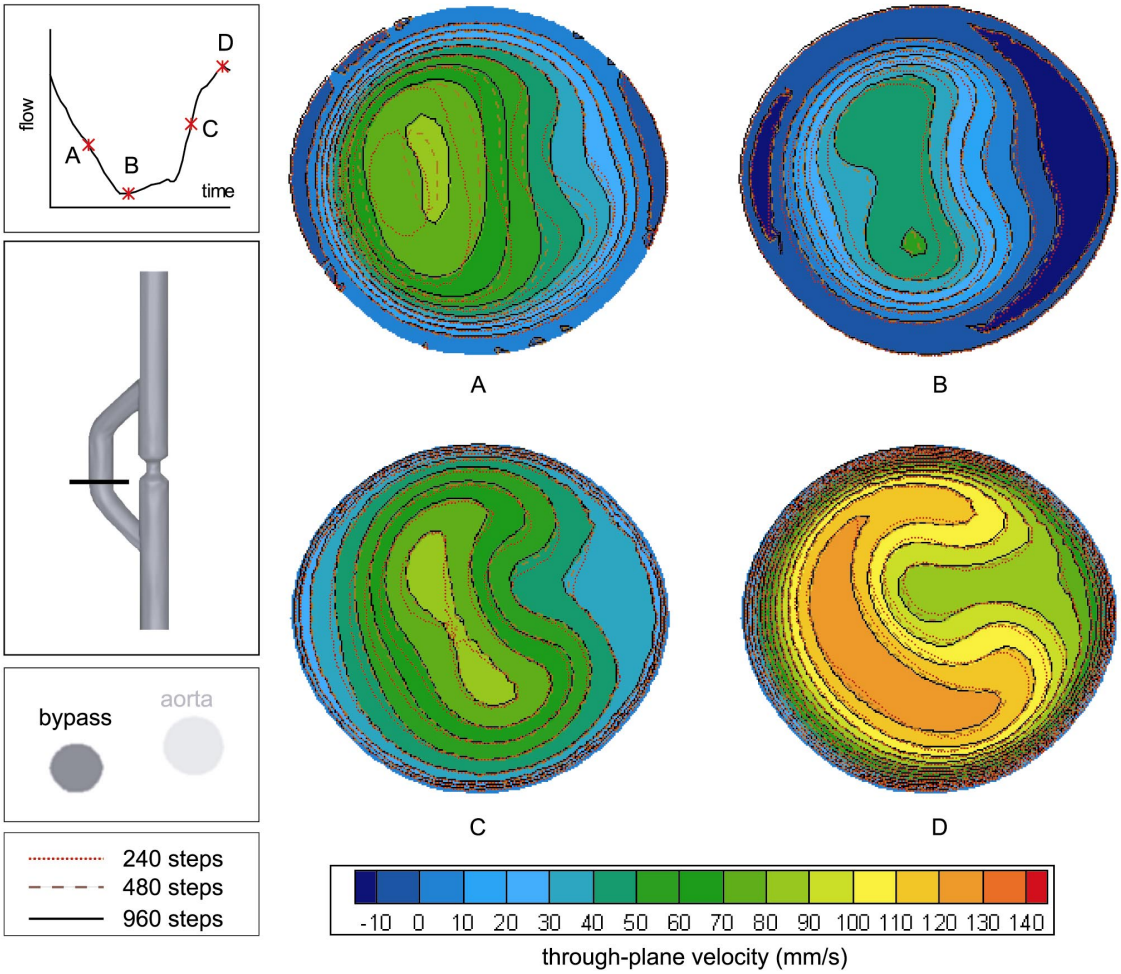


Figure 4.11: Comparison of through-plane velocity contours at the graft (plane F in Figure 4.1) for different number of time steps per cycle. The color map and the solid black lines correspond to numerical simulation results for 960 time steps per cycle. The dashed brown lines indicate contours for 480 time steps per cycle, and the dotted red lines for 240 time steps per cycle. Results from four different time points in the cycle are presented: mid-deceleration (A), late-deceleration (B), acceleration (C), peak flow (D).

With few exceptions, previous studies directly compared the numerical simulation results to the PC-MRI measurements. However, differences in the techniques suggest that additional data processing is needed in order to fairly compare the results from the two methods. With numerical simulations, velocity information can be obtained at extremely precise locations and time points. With the large mesh size and number of

time steps being utilized in these simulations, flow features may be observed in the simulations but not seen in the PC-MRI measurements, which are acquired over a finite volume in space and a finite period in time. As with the mesh convergence results, the results shown here were based upon simulations run with a 3.3 million mesh for 480 timesteps per cycle and with an inlet boundary condition based upon three components of velocity.

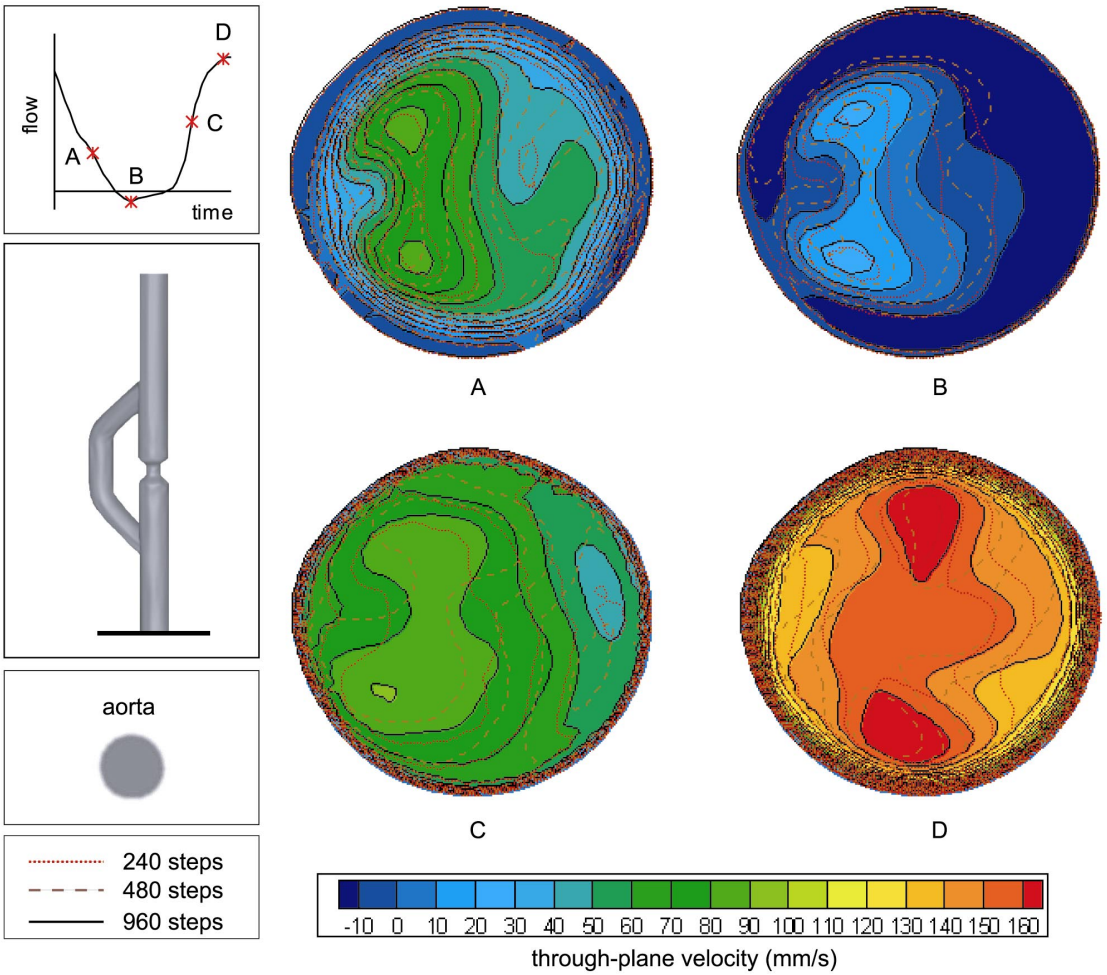


Figure 4.12: Comparison of through-plane velocity contours at the aorta distal to the bypass, also referred to as the outlet, (plane E in Figure 4.1) for different number of time steps per cycle. The color map and the solid black lines correspond to numerical simulation results for 960 time steps per cycle. The dashed brown lines indicate contours for 480 time steps per cycle, and the dotted red lines for 240 time steps per cycle. Results from four different time points in the cycle are presented: mid-deceleration (A), late-deceleration (B), acceleration (C), peak flow (D).

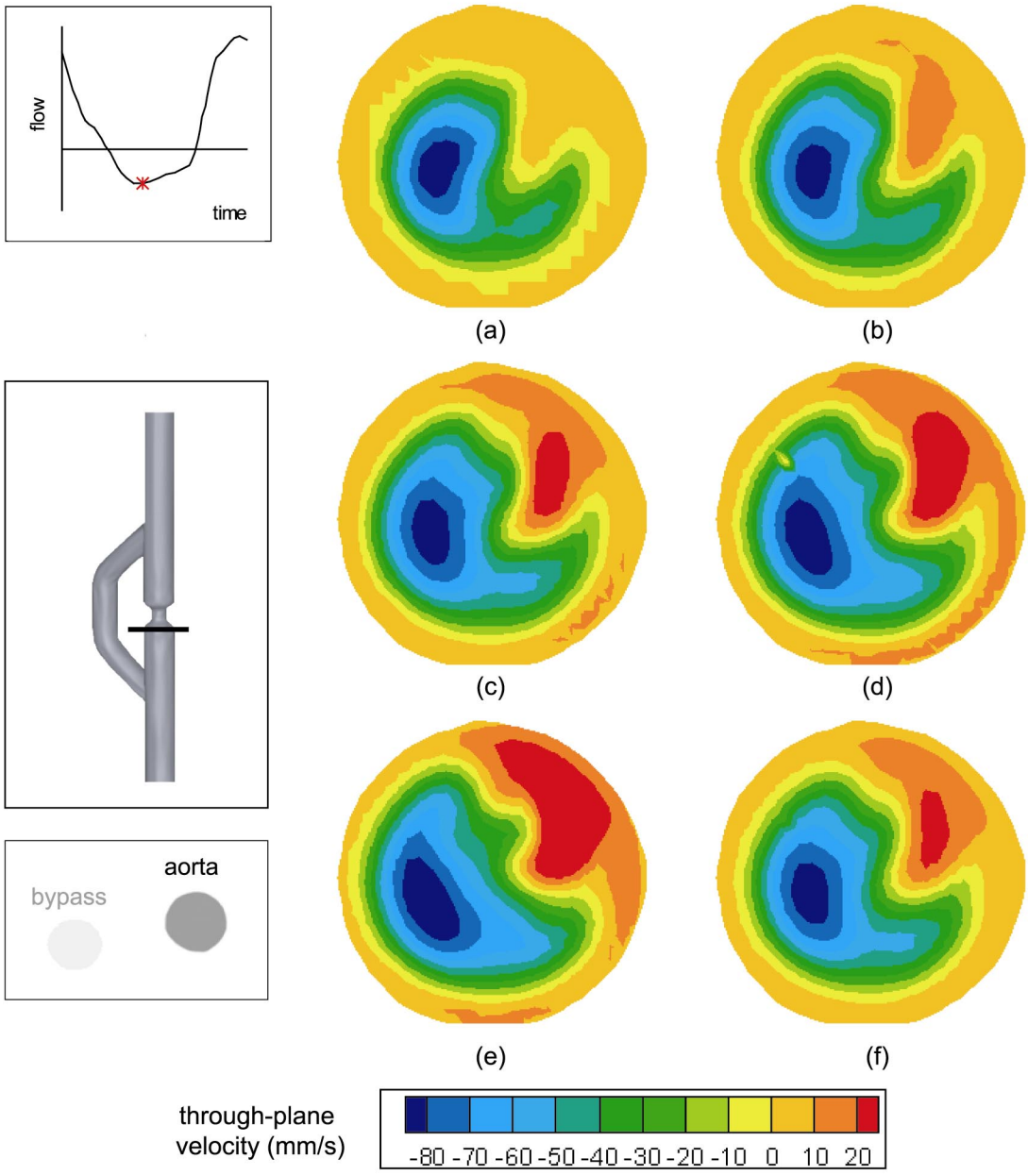


Figure 4.13: Comparison of the through-plane velocity simulation results at a given slice location versus averaged over 5 slices for the aorta distal to the coarctation (plane D) during late-deceleration. The simulation results at the given slice location are shown in (c), and the averaged results are shown in (f). (a) and (b) show the results at 2.5 mm and 1.25 mm upstream of the given slice location respectively, while (d) and (e) are the results at 1.25 mm and 2.5 mm downstream of the given slice location respectively. The jagged edges observed in (a) are because the diameter at this position is smaller than that at the given slice location.

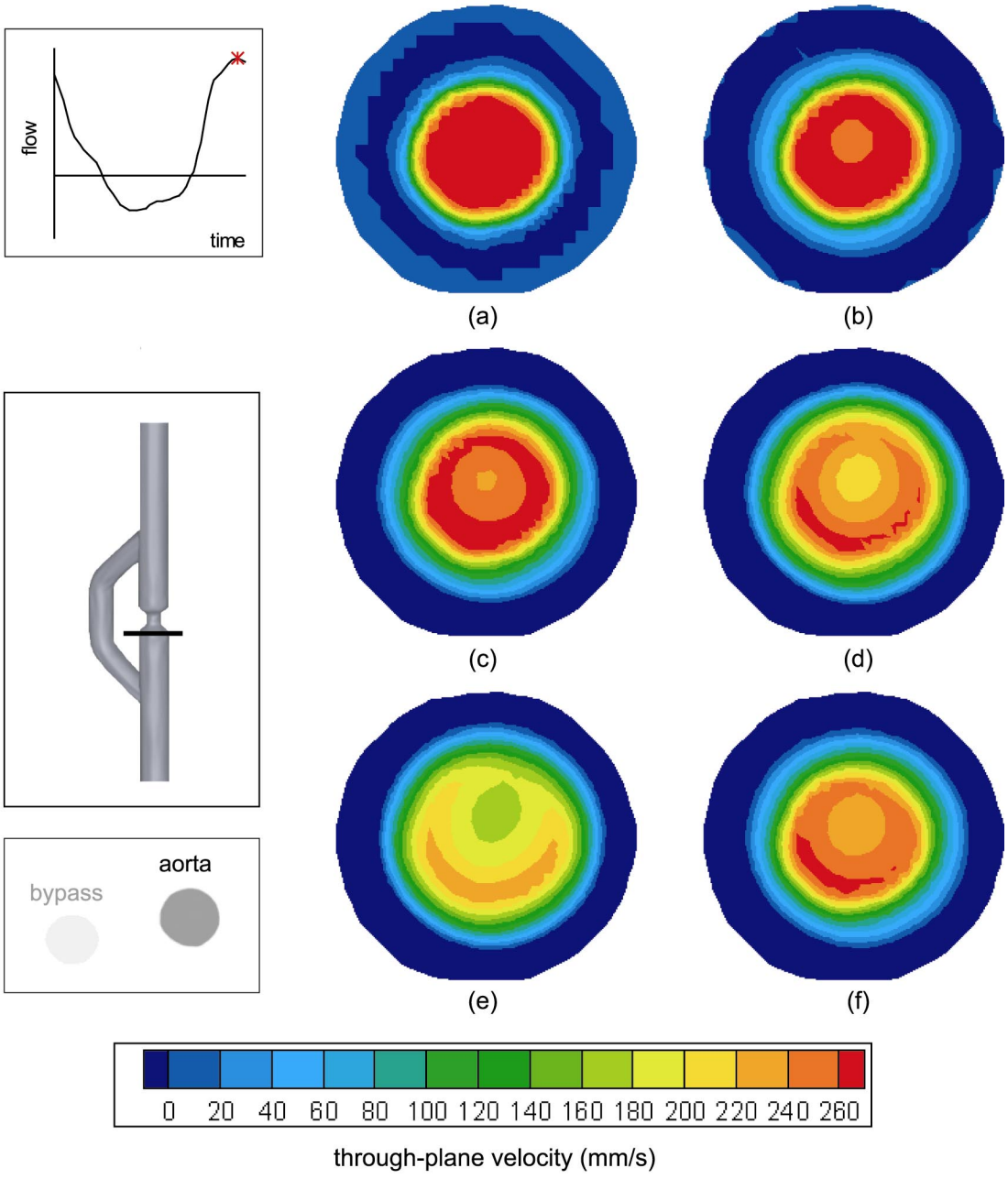


Figure 4.14: Comparison of the through-plane velocity simulation results at a given slice location versus averaged over 5 slices for the aorta distal to the coarctation (plane D) during peak flow. The simulation results at the given slice location are shown in (c), and the averaged results are shown in (f). (a) and (b) show the results at 2.5 mm and 1.25 mm upstream of the given slice location respectively, while (d) and (e) are the results at 1.25 mm and 2.5 mm downstream of the given slice location respectively. The jagged edges observed in (a) are because the diameter at this position is smaller than that at the given slice location.

4.3.1 Spatial Averaging

In their study, Botnar and colleagues [46] averaged their numerical simulation results over a slice thickness equal to that of the MR plane, and Papaharilaou, *et al.* [56] mapped both the MR and the computed results onto the same mesh prior to comparison. In general, though, comparisons between the MR measurements and the numerical simulations are made directly. Consider, though, that for this experiment, the voxel size was 0.78125 x 0.78125 x 5.0 mm^3, and that each voxel was represented by a single velocity vector, an assumption made by PC-MRI (see Section 2.2.3.1). This was coarser than the mesh used for the numerical simulations, so in order to fairly compare the numerical simulation results to the PC-MRI measurements, the computed results were mapped onto the mesh associated with the PC-MRI data using a weighted interpolation scheme. This method computed the interpolated values using the nodes of the element that contained the point of interest. The minimum distance between the interior nodes of this mesh was 0.78125 mm. To account for the slice thickness, five slices were extracted from the numerical simulation results for each plane of interest. These slices were taken at the same location as the PC-MRI slice plane, at 1.25 mm and 2.5 mm upstream of that slice plane, and at the same distances downstream of that slice plane. All the slices were oriented to have the same normal as that of the original PC-MRI slice plane. The results for these 5 slice planes were then averaged together to produce the velocities used for comparison purposes. Note that the distance covered by these 5 slices is equivalent to the slice thickness used for the PC-MRI data acquisition.

Figure 4.13 and Figure 4.14 show both the 5 individual slice planes, as well as the final averaged slice plane, at the distal coarctation location for late-deceleration and peak flow, respectively. Because the largest through-plane velocities were observed at this location, the differences between the slice plane furthest upstream and the plane furthest downstream represent the greatest changes likely to be seen in this experiment. The effect of the averaging differed depending on the time point examined. Results during late-deceleration in the averaged slice (Figure 4.13(f)) were similar to those in the original slice location (Figure 4.13(c)). Minor differences, such as a smaller 20+ mm/s velocity region and a missing crescent-shaped region in the lower-right of the vessel,

were all that distinguished the averaged slice from the original slice. In contrast, the averaged slice results (Figure 4.14(f)) during peak flow were noticeably different than those of the original slice location (Figure 4.14(c)). The averaged slice showed lower velocities overall, with a larger 230 mm/s velocity region and a much smaller region of 260+ mm/s velocities. The examples from these two time points demonstrate how spatial averaging can alter the velocity contours, both in terms of the features observed as well as in the magnitude of the velocities. Therefore, in comparing the numerical simulation results to PC-MRI measurements, which are naturally averaged over space, it is important to spatially average together the computational results. The method presented here for spatially averaging the computational results together does have some limitations, though. Namely, it would not work well if significant changes in geometry, such as a large change in diameter or a change in the vessel axis direction, existed.

4.3.2 Periodic Averaging

Another important consideration is the assumed periodicity of the PC-MRI velocity measurements in time. While the velocity measurements are for one cycle, they are actually acquired over multiple cycles, with up to several k-space lines acquired per cycle, depending on which PC-MRI sequence is used (see Section 2.2.3.2). In the case where only 1 k-space line is acquired per cycle and where the acquisition matrix is specified to be 256 k-space lines, the PC-MRI velocity measurements are based on 256 cycles. Non-periodic velocities would result in k-space data that varied over time, so the PC-MRI measurements would incorporate information from different velocity patterns. It is unclear how this would affect the final PC-MRI velocity measurements, but the non-periodic nature of the velocity patterns would not be captured.

On the other hand, the numerical simulations are able to show results over several cycles and thus can reveal any non-periodicity in the velocities and flow patterns. Therefore, in order to compare the numerical simulation results to the PC-MRI measurements, a temporal averaging was performed on the numerical computations. In this case, the velocities at each node were averaged over 8 cycles, an empirically chosen

number. This was a simple way to mimic the PC-MRI data acquisition method, which acquires data over many cycles.

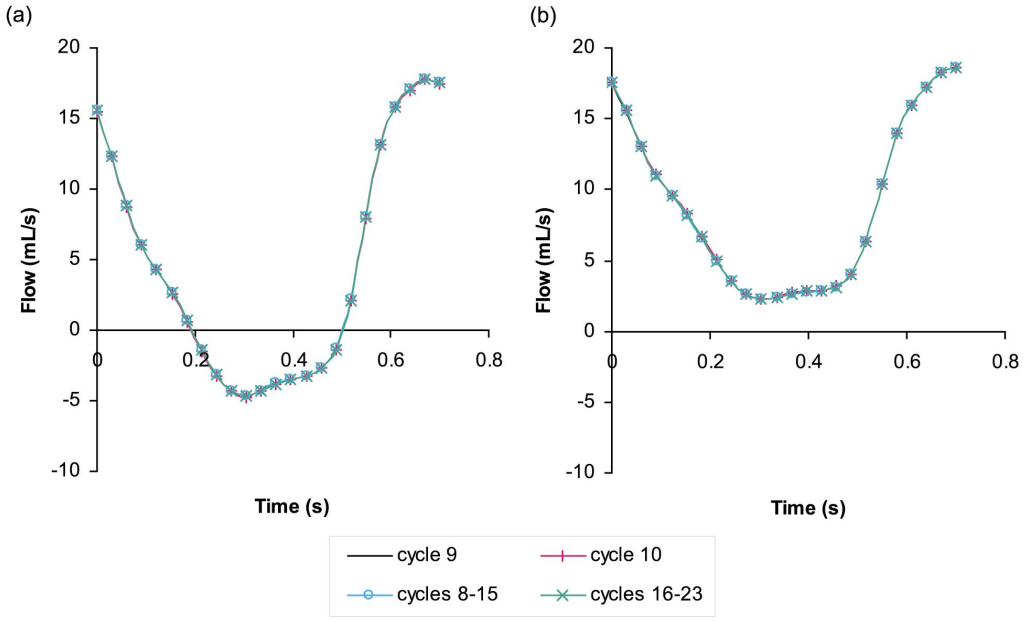


Figure 4.15: Periodicity is observed in the flow measurements through both (a) the proximal coarctation (plane C) and (b) the graft (plane F) for single cycle data, as well as for the data based on the average of 8 simulation cycles.

The temporal averaging had no effect on the flow measurements for this model. According to Figure 4.15, the flows through the coarctation and through the bypass graft were the same whether the simulation results were for an individual cycle (cycle 9, cycle 10) or for 8 cycles averaged together (cycles 8-15, cycles 16-23). The graphs also indicate that the flows were periodic in nature, since the results for cycle 9 matched those of cycle 10.

In terms of the through-plane velocity contours, the periodicity of the results depended on the location. At the proximal coarctation (plane C), the results for cycle 9, shown as the color maps in the upper row of Figure 4.16, were very similar to those for cycle 10, the black contour lines in the upper row of the same figure. Averaging together the results over 8 cycles (lower row of Figure 4.16) produced similar velocity contours as those in the single cycles. On the other hand, at the outlet (plane E), the velocity contours for cycle 9 (color maps in the upper row of Figure 4.17) were noticeably different from those of cycle 10 (black contour lines in the upper row of

Figure 4.17). The contour patterns in cycle 9 appeared to be a rotated version of those in cycle 10. The results from the averaged cycles were significantly more periodic than the single cycle results. The color map in the lower row of Figure 4.17 represents the through-plane velocity contours for cycles 8 to 15 averaged together, while the black lines in the lower row of that figure are the velocity contours for cycles 16 to 23 averaged together. There is much more similarity in the velocity contours for the averaged cycles than for the single cycles at this location.

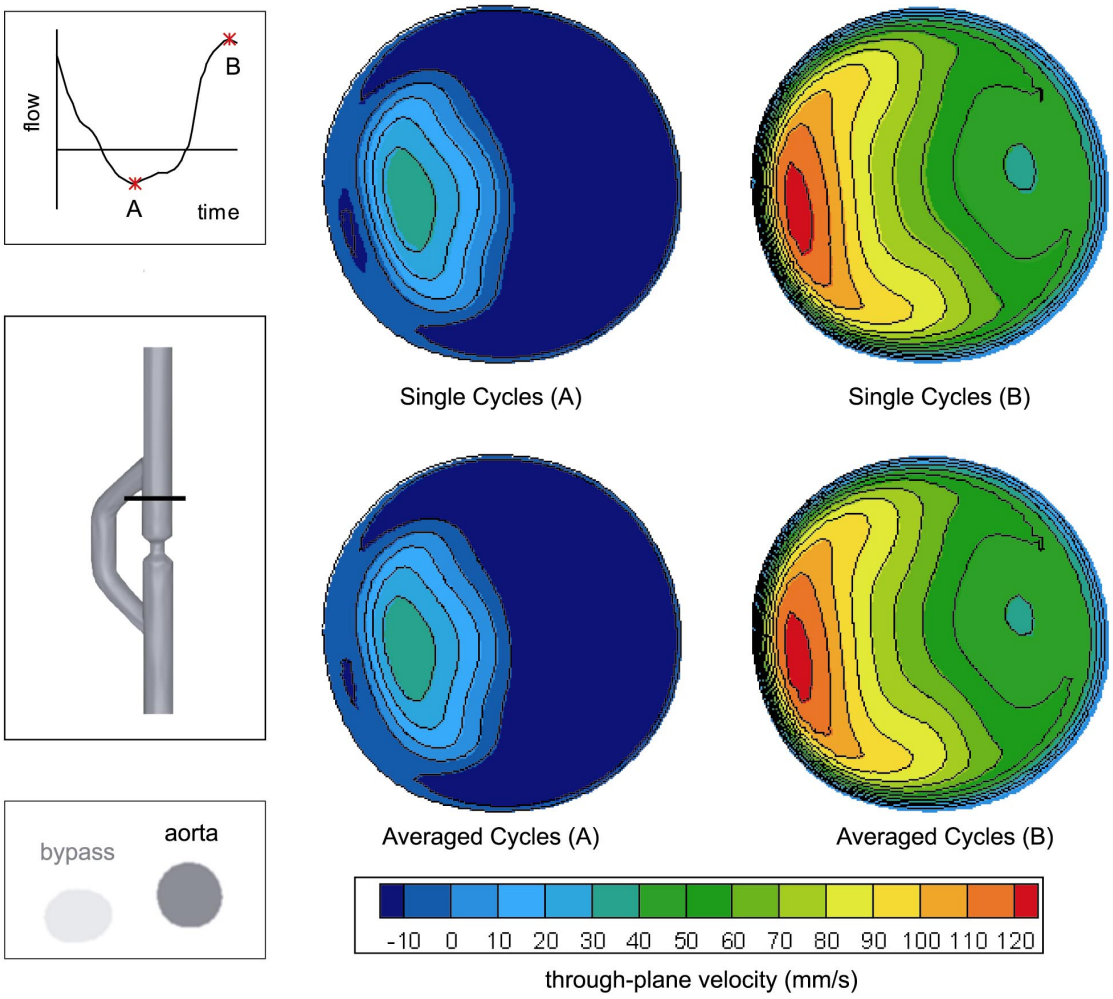


Figure 4.16: Periodicity is observed in the through-plane velocity contours in the aorta proximal to the coarctation (plane C) for both the single cycle data and for the data based on the average of 8 simulation cycles. Results from late-deceleration (A) and from peak flow (B) are presented here. The color map represents results from one data set (cycle 9 for the single cycles, average of cycles 8-15 for the averaged cycles), and the black lines are the velocity contours for the corresponding second data set (cycle 10 for the single cycles, average of cycles 16-23 for the average cycles).

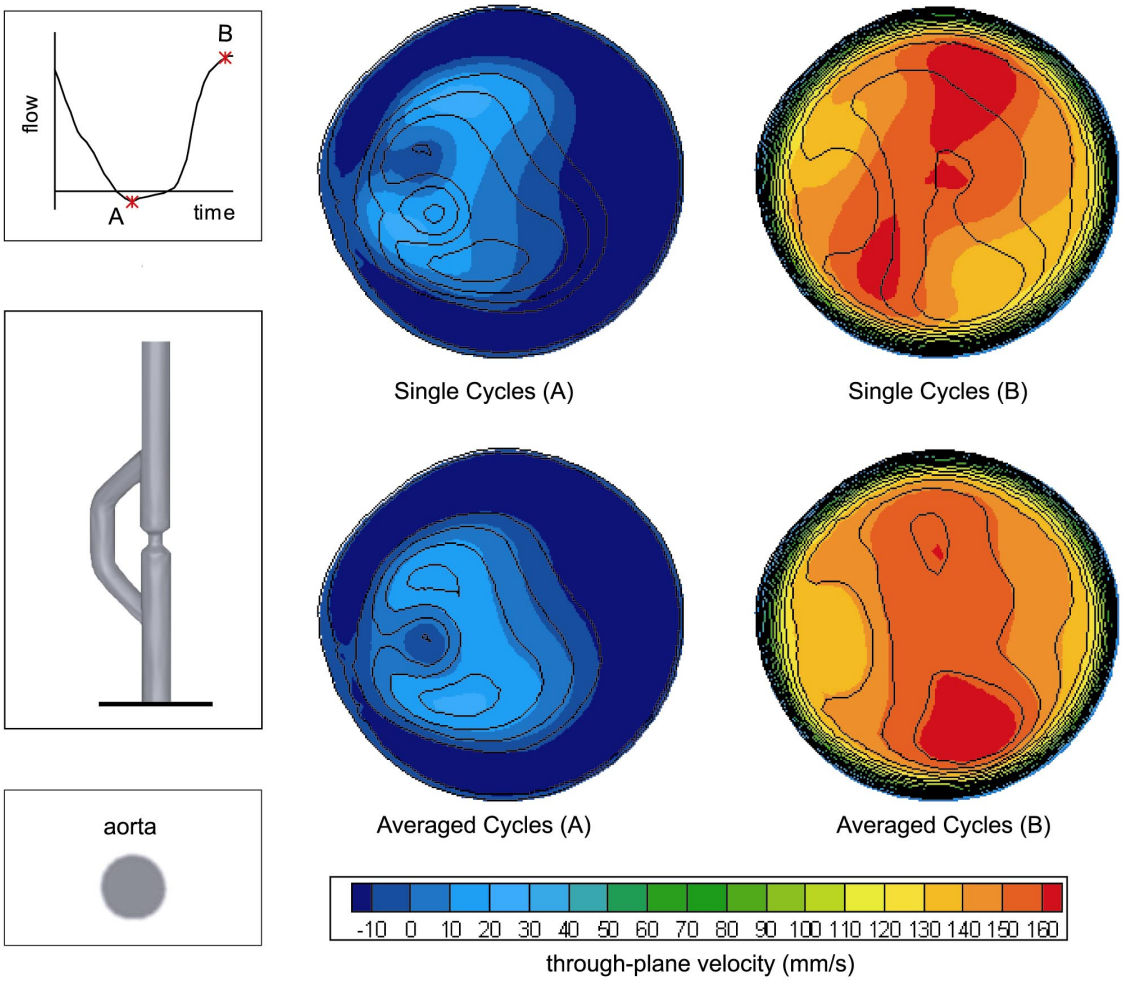


Figure 4.17: The through-plane velocities at the aorta distal to the bypass, also referred to as the outlet, (plane E) are not periodic for the single cycle data but are periodic for the data based on the average of 8 simulation cycles. The color map represents results from one data set (cycle 9 for the single cycles, average of cycles 8-15 for the averaged cycles), and the black lines are the velocity contours for the corresponding second data set (cycle 10 for the single cycles, average of cycles 16-23 for the average cycles). Results from late-deceleration (A) and from peak flow (B) are presented here.

4.3.3 Conclusions

Averaging the numerical simulation results over time and/or space do not always produce significant changes in the through-plane velocity contours. However, at locations, such as the distal coarctation, where high velocities are present, the spatial averaging can produce noticeable differences in the velocity contours. Furthermore, at locations, such as the outlet, where the results are non-periodic, temporal averaging is needed to produce more periodic results in order to compare them against the single cycle of the PC-MRI

measurements. Therefore, in the following comparisons between the numerically computed results and the PC-MRI velocity measurements, both spatial and temporal averaging of the numerical simulations are done, as described above, at all comparison planes, except at the outlet (plane E). Because the geometric model did not extend beyond the outlet slice plane, it was not possible to obtain planes downstream of the outlet slice in order to perform the spatial averaging. In fact, the model did not completely intersect the outlet slice plane, so the numerically simulated results presented for this location were simply from the outlet mesh face.

4.4 Numerical Simulation Results

Sections 4.1 to 4.3 described and motivated the methods used for generating and comparing the numerical simulation results to the PC-MRI measurements. In summary, the simulations used a 3.3-million-element mesh based on a geometric model constructed from the grad-warp-corrected MRA data and prescribed through-plane velocities based upon a user-defined vessel axis at the inlet. These were run for 480 time steps per cycle, and the results were spatially and temporally averaged. Figure 4.18 shows these results at four different time points. These results were compared to first-order baseline-corrected PC-MRI measurements.

4.4.1 Comparison to PC-MRI

Figure 4.19 compares flow waveforms measured with PC-MRI with those computed by the numerical simulations. According to the PC-MRI measurements, the average flow at the proximal coarctation (plane C) was 4.0 mL/s, versus the numerically computed 4.6 mL/s. The absolute difference in the flow waveforms at this location was 0.66 ± 0.42 mL/s. At the graft (plane F), the average flow was measured by PC-MRI to be 9.3 mL/s, compared with 8.9 mL/s as computed by the numerical simulations. The absolute difference in the flow waveforms at the graft was 0.40 ± 0.28 mL/s. Both the numerical simulations and the PC-MRI measurements had an average inlet flow of 13.5 mL/s, and the absolute difference in the flow waveforms was 0.15 ± 0.14 mL/s.

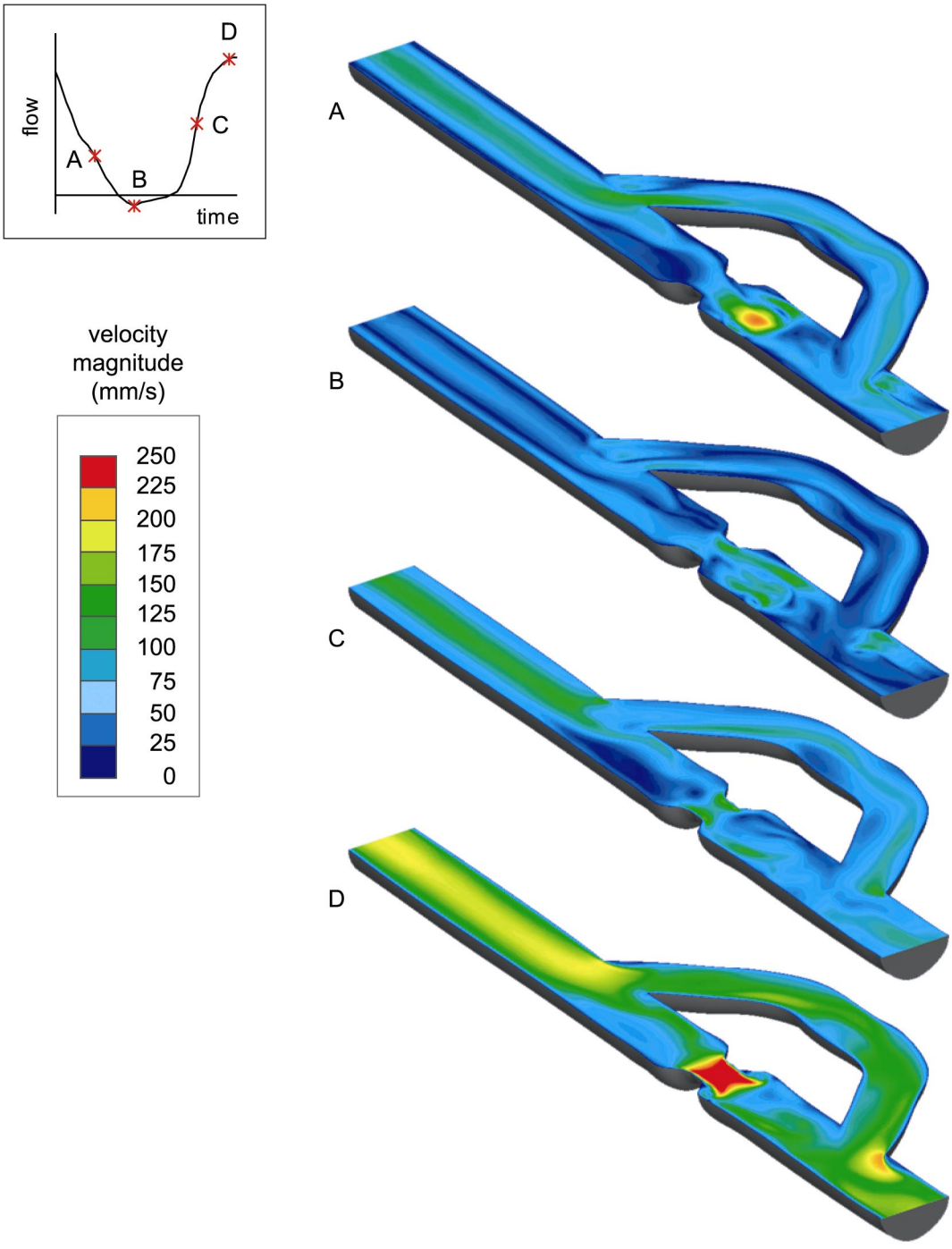


Figure 4.18: Velocity magnitudes as computed from the numerical simulations at four different time points: (A) mid-deceleration, (B) late deceleration, (C) acceleration, (D) peak flow. The velocities shown are approximately from a mid-sagittal plane. The direction of flow, as depicted here, is from the upper-left to the lower-right.

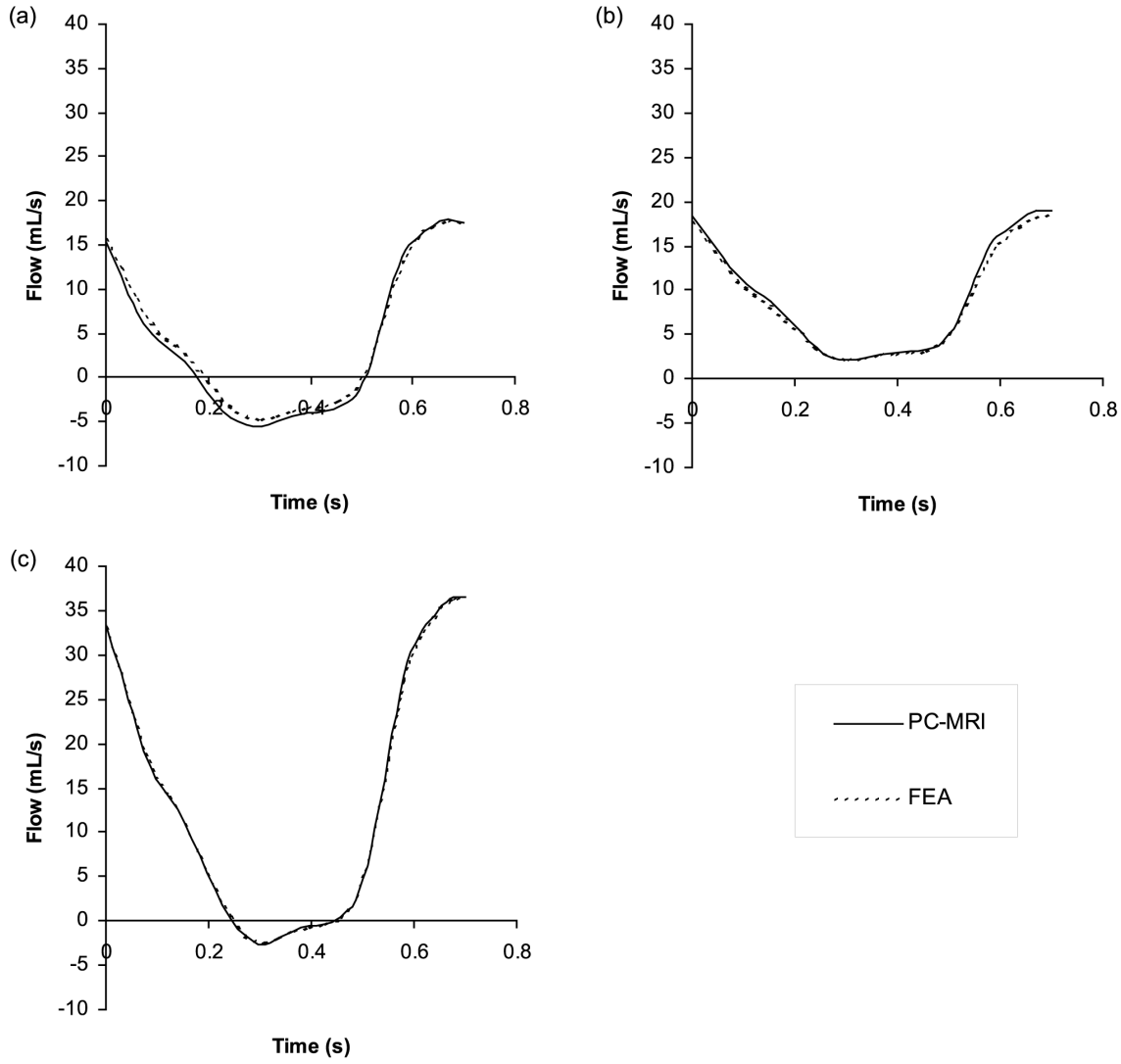


Figure 4.19: Comparison between flows from PC-MRI and the numerical simulations (finite element analysis, FEA) at the (a) proximal coarctation (plane C), (b) graft (plane F), and (c) inlet (plane A).

Figure 4.20 through Figure 4.24 use isocontour maps to compare the through-plane velocities at the five different comparison planes shown in Figure 4.1: downstream inlet (plane B), proximal coarctation (plane C), distal coarctation (plane D), graft (plane F), and outlet (plane E). Four different time points were examined: mid-deceleration, late-deceleration, acceleration, peak flow. Overall, there were similarities in both the through-plane velocity magnitudes and the resulting contour patterns. Circular symmetry was observed in both the simulations and the PC-MRI measurements at the downstream inlet location, and at the proximal coarctation level, positive velocities were observed

along the wall closest to the bypass, whereas negative velocities were noted on the opposite side of the vessel at all time points except during peak flow. There were minor differences in magnitudes, with slightly higher peak velocities observed in the simulations at all time points except peak flow, and lower minimum velocities seen in the simulations during acceleration. Comparison of the velocity contours at the graft were favorable for all time points except at peak flow, where the simulations had lower peak velocities and a more concave shape on the wall furthest from the host vessel, as compared to the PC-MRI measurements. At the distal coarctation, circular symmetry was observed in the PC-MRI measurements at all time points. This symmetry was captured by the numerical simulations at peak flow, but not during mid- or late-deceleration. However, the magnitudes of the velocities in the numerically computed results matched those of the PC-MRI measurements. At the outlet, the contour shapes for the numerical simulation results were slightly more pronounced than the PC-MRI measurements. For example, in late-deceleration, a concave shape was observed in both data sets but in the simulations, the concave shape practically resulted in a ring whereas the PC-MRI results were not as curved. At peak flow, more noticeable differences existed between the simulations and PC-MRI, with a crescent-shaped contour appearing in the PC-MRI results and a more linear pattern occurring in the simulation results.

4.4.2 Flow and Velocity Patterns

The flow patterns observed in this model confirm what would be expected theoretically. For this system, with the long, rigid, cylindrical tubing upstream, a Womersley velocity profile is expected at the inlet (plane A) and downstream inlet (plane B) locations. The circular symmetry of the velocity contours and the reversal of velocities along the tube walls correspond to velocity profiles expected with Womersley theory. The numerical simulations also show a relatively flat profile, with the maximum range of through-plane velocities at any given time point being 17.5 cm/s. Again, this agrees with Womersley theory, which would predict a relatively flat profile because of the high Womersley number of 14.8 [118].

One phenomenon observed in both the PC-MRI and the numerical simulations was the large reverse flows and velocities during late-deceleration at the proximal coarctation (plane C) location. Reverse flow at this location was larger in magnitude and longer in duration than the reverse flow at the inlet. However, there was no reverse flow through the graft. Because of flow conservation, this implies that a flow loop must have existed in which the flow through the proximal coarctation region reversed direction during deceleration and was then drawn into the bypass graft to maintain forward flow through the graft for the entire cycle. Examination of the through- plane velocity contours shows that negative velocities dominated the patterns seen at the proximal coarctation and distal coarctation locations during mid- and late-deceleration. At the proximal coarctation location, the negative velocities occurred along the wall opposite the bypass, creating a region of flow separation. A more symmetric pattern occurred at the distal coarctation slice plane, with the reverse velocities forming a large ring. A small region of reverse velocity was also observed along the walls of the graft during late-deceleration.

4.5 Limitations of Experimental Data

As discussed in Chapter 3, when performing comparisons against experimental data, it is also necessary to understand the limitations of the experimental data. Towards that end, the variability in the velocity measurements and the flow repeatability were examined. The signal-to-noise ratios (SNR) and theoretically computed standard deviations of the velocities for the PC-MRI measurements are given in Table 4.1. The SNRs ranged from 42 to 60, while the standard deviations of the velocities varied from 2.3 to 3.2 mm/s. These values were comparable to the standard deviations for the repeatability studies performed in Section 3.2.2.2. Although the techniques used in those studies do not exactly replicate the experimental set-up and imaging sequences used in this experiment, it is important to note that the repeatability study demonstrated noticeable variations in the velocity isocontour shapes from measurement to measurement despite a relatively small standard deviation in velocities. This variability needs to be considered when comparing against the PC-MRI measurements.

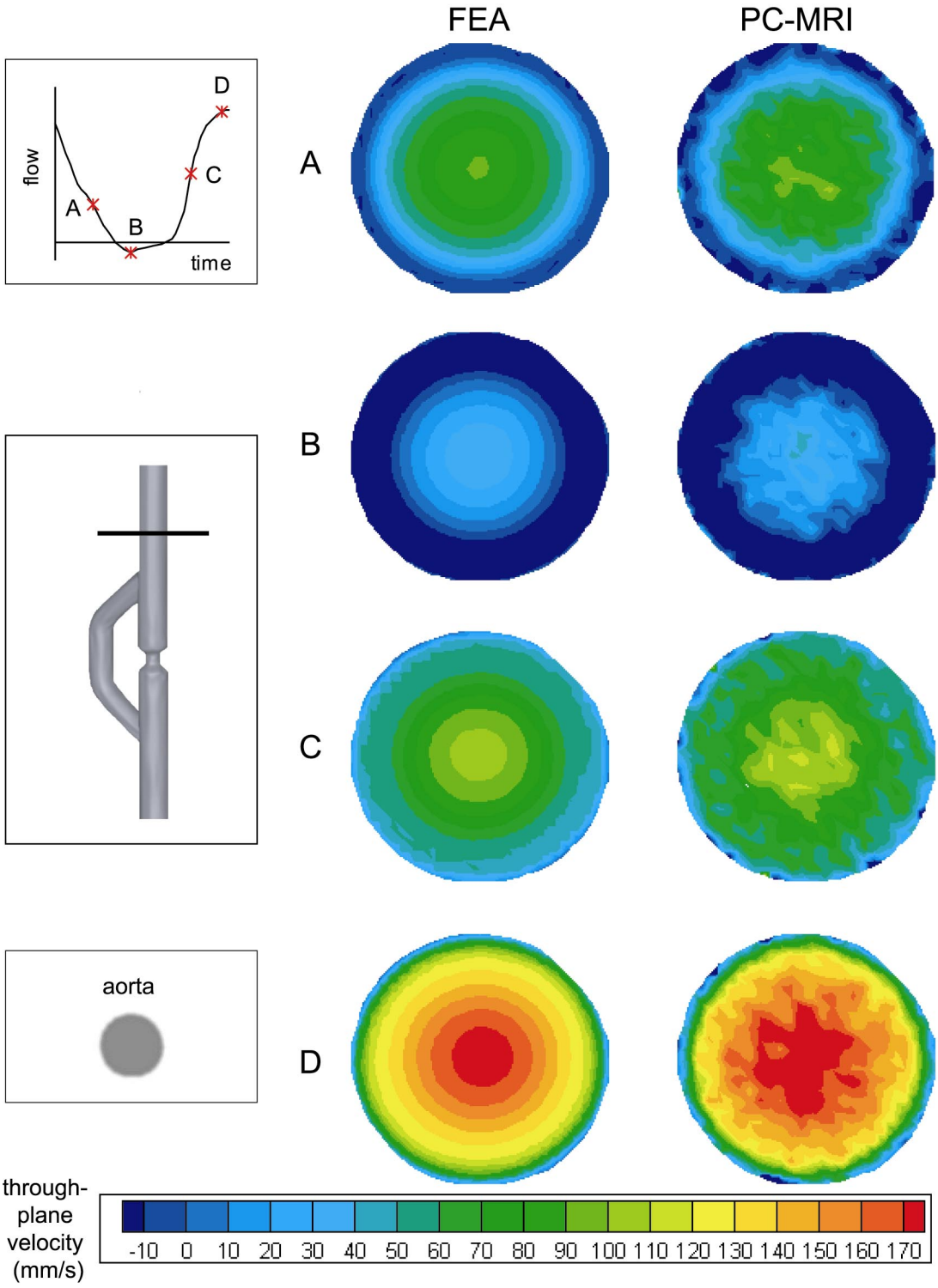


Figure 4.20: Comparisons in the aorta proximal to the bypass graft, also referred to as the downstream inlet (plane B) location, of through-plane velocities computed numerically using finite element analysis (FEA) and those acquired with PC-MRI. Four different time points are examined: mid-deceleration (A), late-deceleration (B), acceleration (C), peak flow (D).

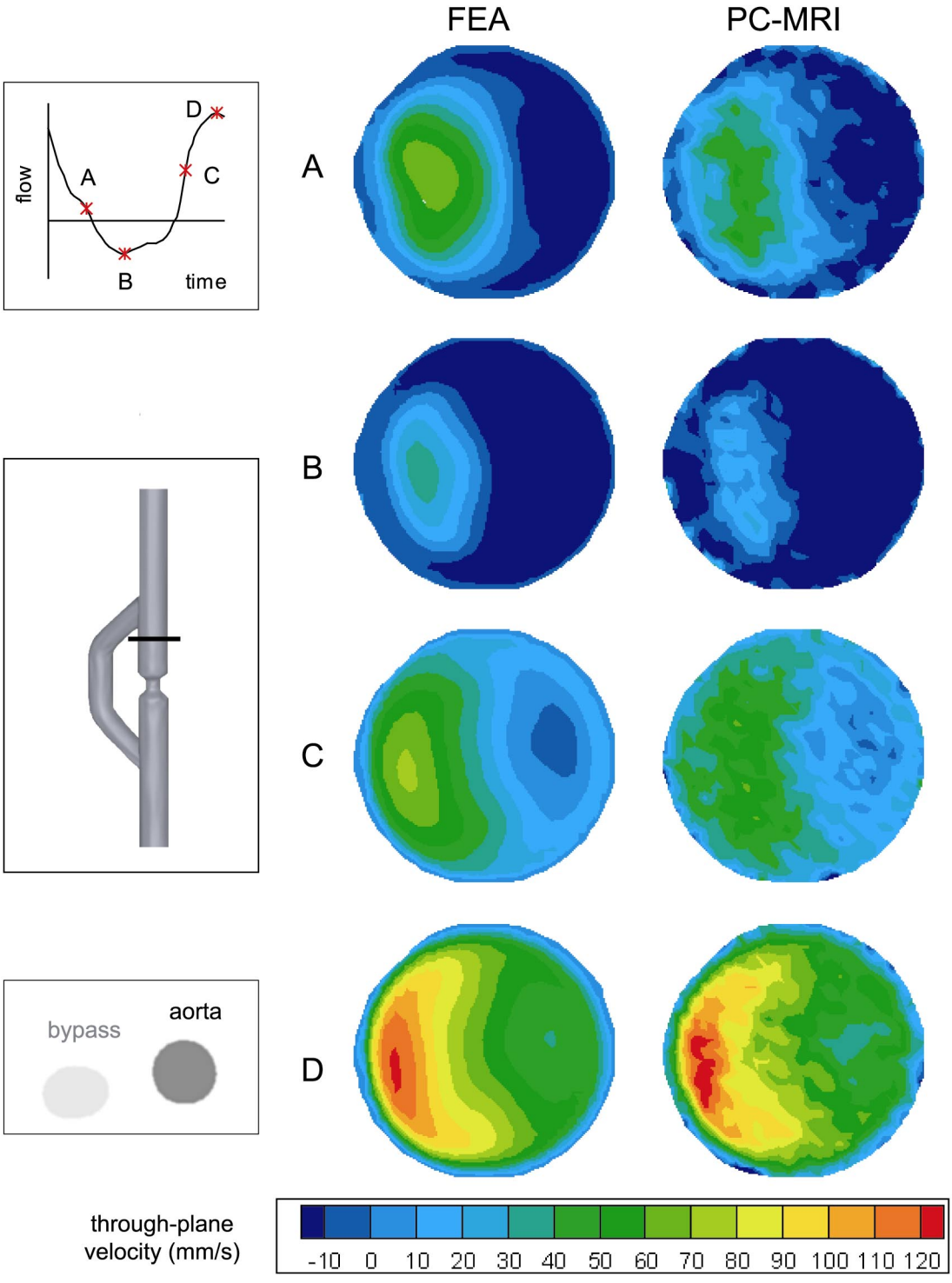


Figure 4.21: Comparisons in the aorta between the proximal anastomosis and the coarctation, also referred to as the proximal coarctation (plane C) location, of through-plane velocities computed numerically using finite element analysis (FEA) and those acquired with PC-MRI. Four different time points are examined: mid-deceleration (A), late-deceleration (B), acceleration (C), peak flow (D).

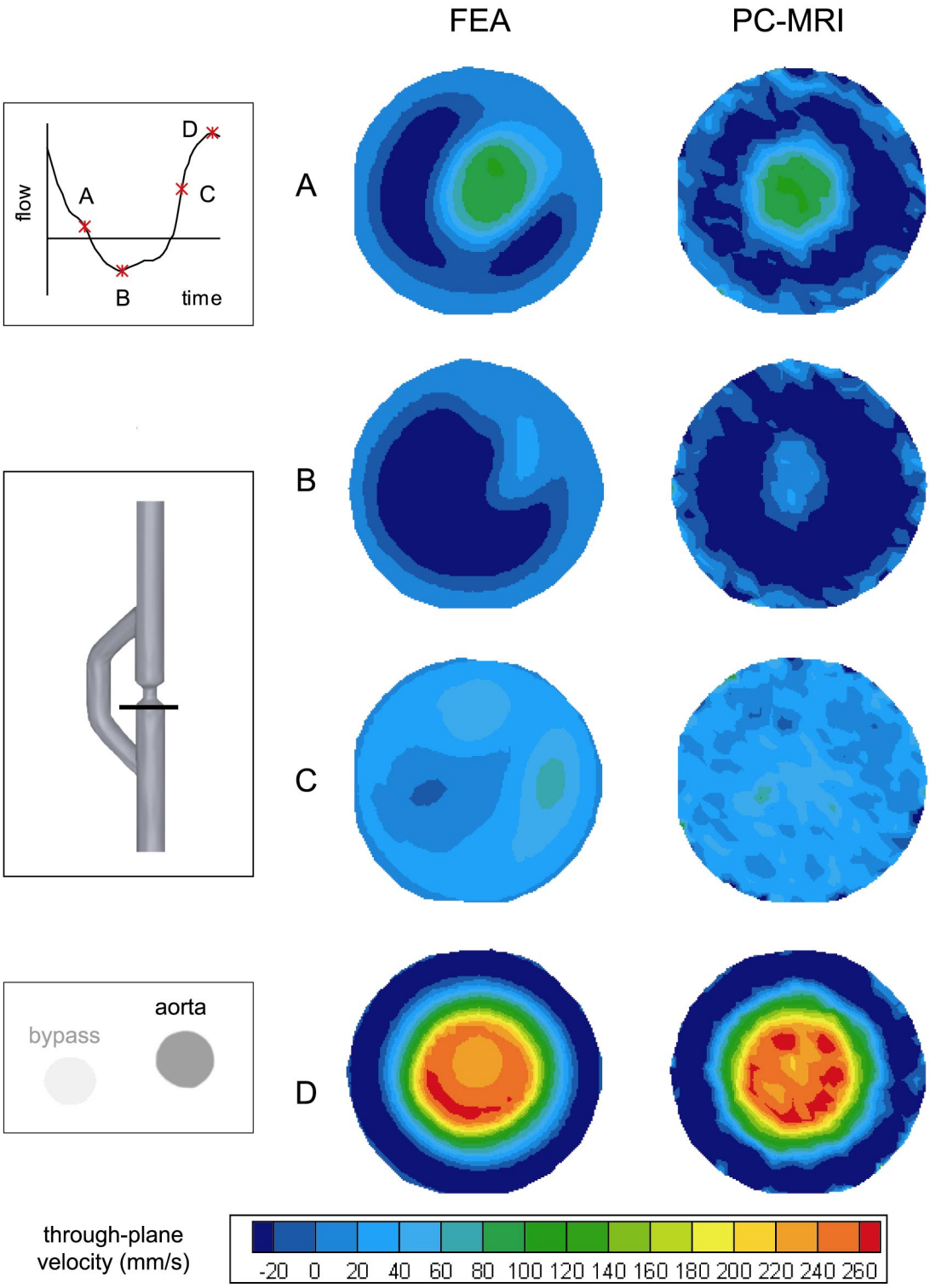


Figure 4.22: Comparisons at the distal coarctation (plane D) location of through-plane velocities computed numerically using finite element analysis (FEA) and those acquired with PC-MRI. Four different time points are examined: mid-deceleration (A), late-deceleration (B), acceleration (C), peak flow (D).

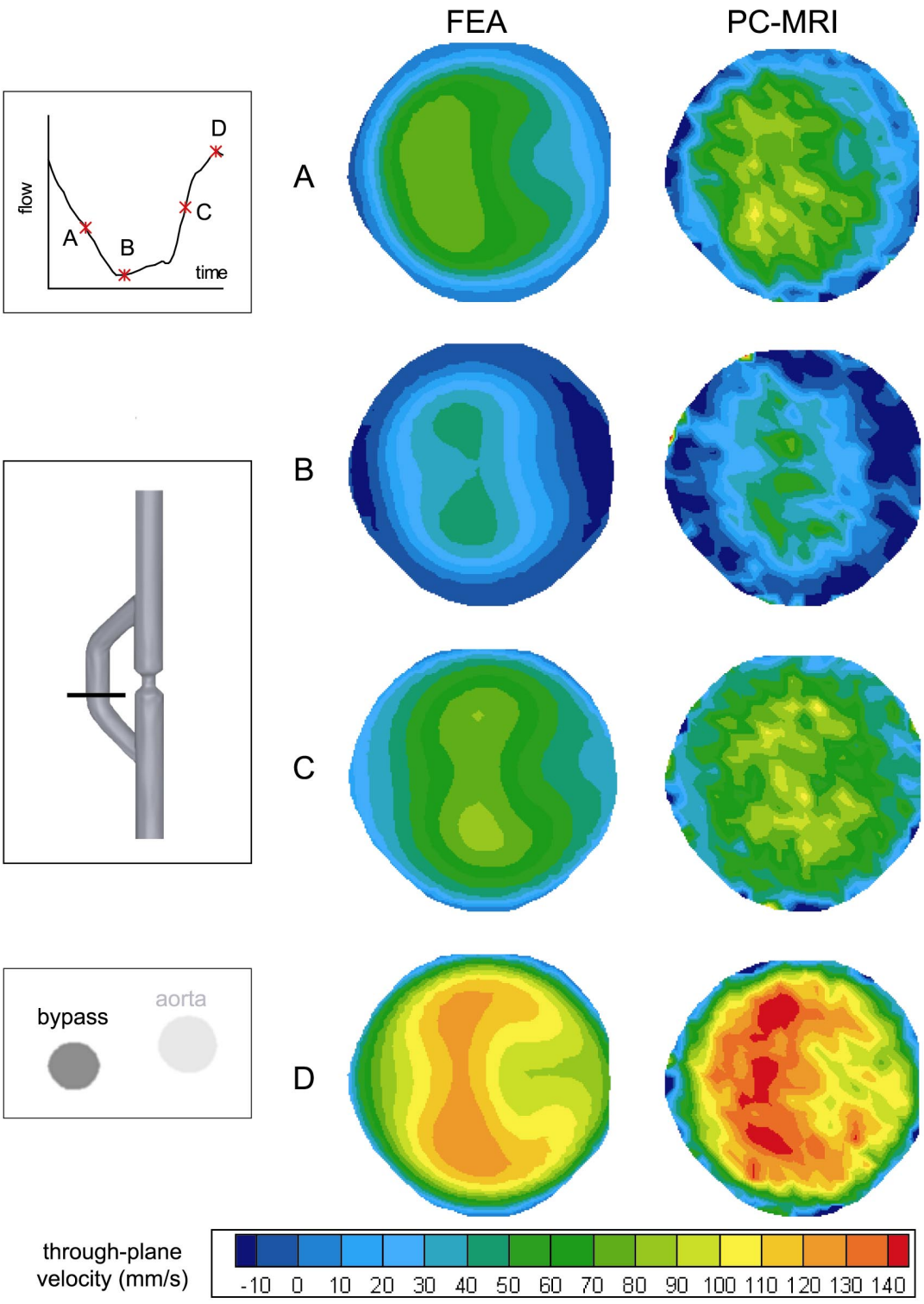


Figure 4.23: Comparisons at the bypass graft (plane F) location of through-plane velocities computed numerically using finite element analysis (FEA) and those acquired with PC-MRI. Four different time points are examined: mid-deceleration (A), late-deceleration (B), acceleration (C), peak flow (D).

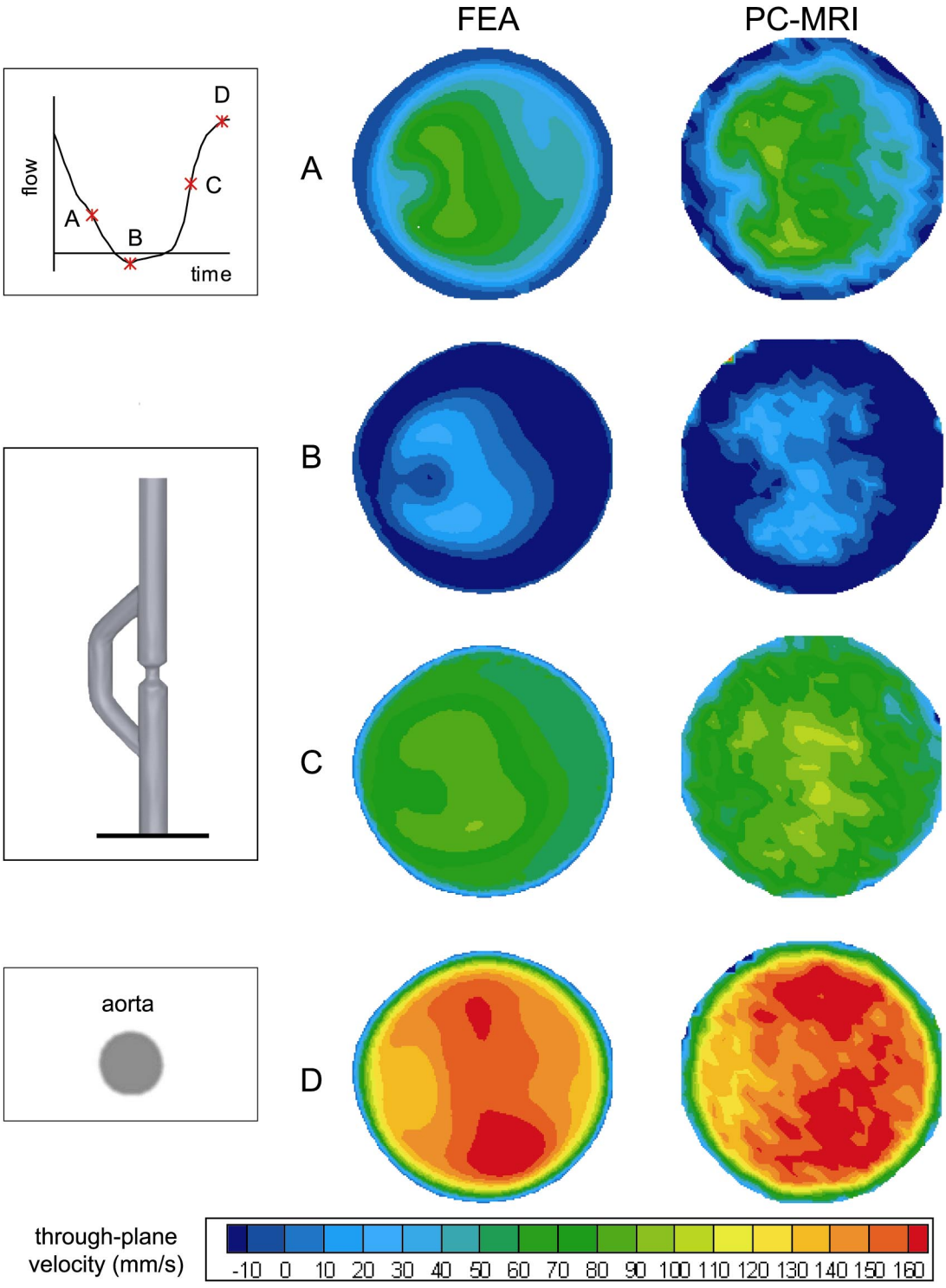


Figure 4.24: Comparisons at the distal aorta, also referred to as the outlet (plane E), of through-plane velocities computed numerically using finite element analysis (FEA) and those acquired with PC-MRI. Four different time points are examined: mid-deceleration (A), late-deceleration (B), acceleration (C), peak flow (D).

	Signal-to-Noise Ratio	Standard Deviation of Velocity Measurements (mm/s)
Plane A (inlet)	53.9	2.5
Plane B (downstream inlet)	52.3	2.6
Plane C (proximal coarctation)	59.6	2.3
Plane D (distal coarctation)	49.4	2.7
Plane E (outlet)	42.8	3.2
Plane F (graft)	51.3	2.6

Table 4.1: Signal-to-noise ratios and theoretically computed standard deviations of velocities for the PC-MRI data.

To determine the flow repeatability, measurements acquired with an ultrasonic flow transducer at two different time points during the experiment were compared (Figure 4.25(b)). The average flow waveforms at the two different time points were similar, although they differed in sharpness during peak flow and were slightly shifted from one another. The average flows for the two different time points were 15.7 mL/s and 14.5 mL/s. Figure 4.25(a) shows the cycle-to-cycle variability during the data acquisition at one time point. The largest standard deviations in the measurements were during peak flow, indicating that the individual cycles varied the most during that time in the cycle.

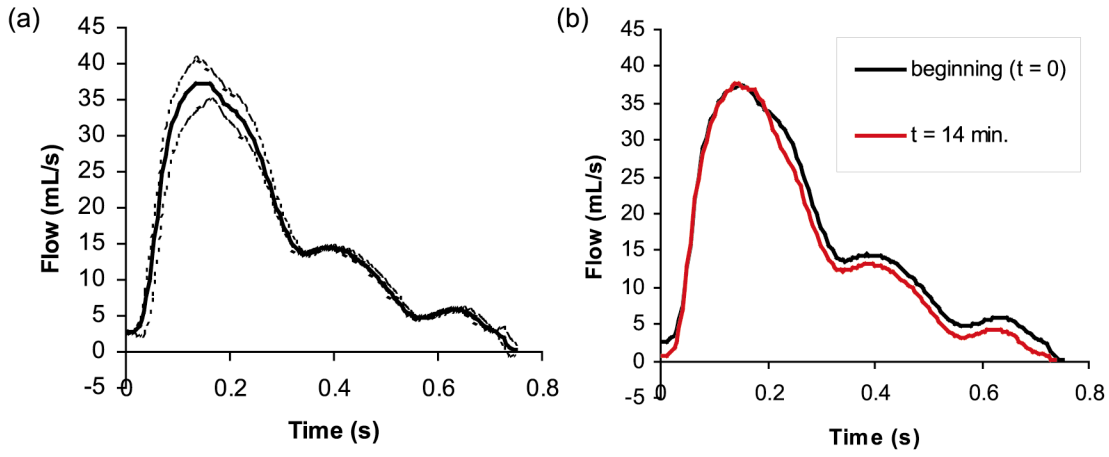


Figure 4.25: Flow measurements acquired with an ultrasonic flow probe demonstrate the repeatability of the flow that was output by the pump. (a) The dark line is the average flow over the flow cycles at the beginning of the experiment (t = 0). The dotted lines indicate ±1 standard deviation and demonstrate that more variability occurred during peak flow. (b) Comparison of the average flows at two different time points during the experiment.

4.6 Sensitivity of Numerical Simulations

Measures of the variability that can exist in the experimental set-up and the PC-MRI measurements were presented in Section 4.5 above. In the following sections, the effect of the input parameters on the numerical simulations is discussed. Section 4.6.1 examines the effect of the geometric model on the computational results, while Section 4.6.2 compares the results for different inlet velocity profiles.

4.6.1 Effect of Geometric Model on Numerical Simulations

Since the exact specifications for constructing the phantom model were known, it was possible to compare these ideal measurements to those of models constructed from the MRA data using the custom software Geodesic, which is described in Section 2.3.3.

4.6.1.1 Methods

Three models were compared. For the ideal model, the computer-aided design (CAD) drawing used to create the physical model was converted to a solid model representation and visually registered with the MRA data through simple rotations and translations. This CAD-based solid model represented the true geometry and was used as a gold standard in evaluating the MRA-based solid models. MRA-based models were constructed by two different individuals, each with at least 1.5 years of experience in using Geodesic. The only constraints imposed on the model construction process were to use 500 points in the path for the aorta and 300 points in the bypass path, thus setting the minimum distance between segmentations to be approximately 0.5 mm, and to use 20 re-sampling points and the "align by distance" option when performing the surface lofting. The individual user was free to choose all other parameters in the solid model construction process.

To compare the geometries, a model analysis tool was developed within Geodesic to extract the boundaries of a solid model along a given path (Figure 4.26). The user specifies the two endpoints of the line and the number of points along that line. At each point, the intersection of the solid model with the plane that is perpendicular to the path is determined, and the center and equivalent-circle radius of the intersection is computed.

The equivalent circle radius describes a circle with the same area as the intersecting contour. Since this tool is currently limited to examining straight segments, four segments were examined in the following comparison: the host vessel, the two 45-degree sections of the graft that attach to the host vessel, and the straight segment of the graft. The number of points was chosen so that the distance between points was approximately 0.5 mm.

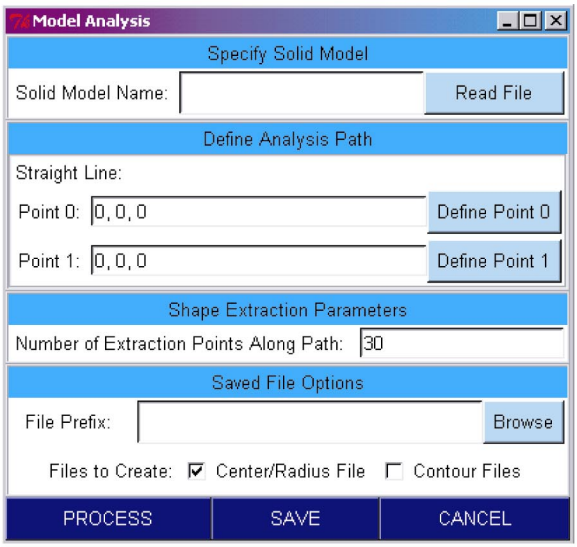


Figure 4.26: Graphical user interface for analyzing the shape of a solid model.

Numerical simulations were run on the three models using parameters similar to that described above in Section 4.1.3. The through-plane velocity components were prescribed along the direction of the user-defined axis at the inlet, and the meshes for these models were comprised of 3.2 to 3.3 million elements. The simulations were run for 480 time steps per cycle for ten cycles, and the results from a single slice plane (no spatial averaging) from cycle 9 are presented below.

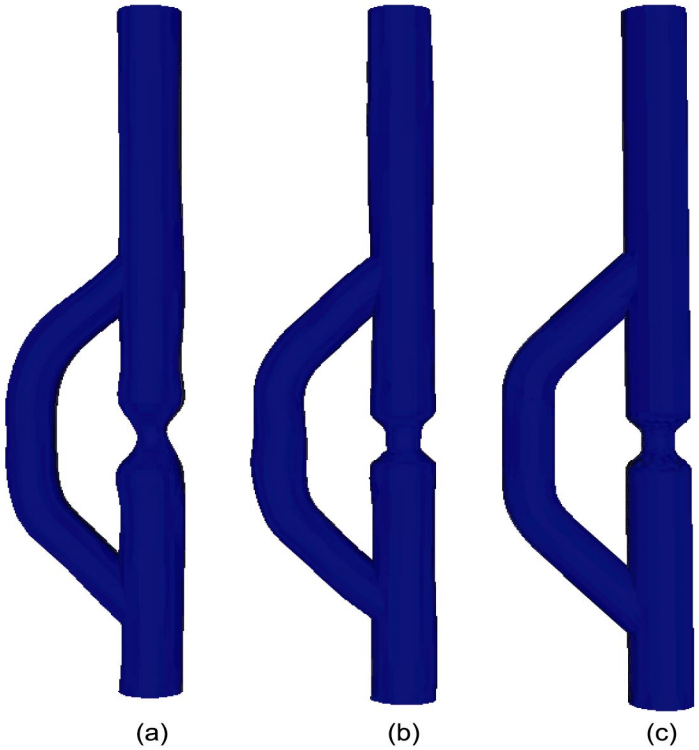


Figure 4.27: Comparison of three models of the bypass phantom. (a) and (b) were constructed from the MRA data by two different individuals using Geodesic. (a) is referred to as the user 1 model and (b) the user 2 model. (c) is the solid model based on the CAD drawing and was used as the gold standard in the geometry comparisons.

4.6.1.2 Results and Discussion

Figure 4.27 shows the three different models that were compared, while Figure 4.28 provides a quantitative comparison of the three models. Obvious differences were seen in the coarctation and bypass shapes. Quantitatively, it can be seen that immediately proximal and distal to the coarctation, the MRA-based models were larger in equivalent-circle radii than the ideal model. Differences were also found in the equivalent-circle radii at the coarctation itself (located about 130 mm along the path of the host vessel), with one of the MRA-based models having a larger coarctation radius than the ideal while the other had a smaller radius. Another region of difference was at the anastomoses. The width of these regions tended to be slightly smaller for the MRA-based models than the ideal model. This difference was more apparent at the proximal anastomosis, located about 100 mm along the path of the host vessel, than at the distal

anastomosis, located about 200 mm along the path of the host vessel. Differences also existed along straight segments of the host vessel and the graft, with fluctuations occurring in the equivalent-circle radii of the MRA-based models that did not exist in the ideal model. Figure 4.29 shows the flow waveforms through the host vessel and through the bypass graft for the three different geometric models examined in this sensitivity study, while Figure 4.30 through Figure 4.34 display the through-plane velocity contours at five different comparison planes for the three models. While the results from the simulations were similar, slight variations were observed, likely due to geometry. This agrees with previous research, which has identified a strong relationship between the observed hemodynamics and geometry [71, 110, 111, 129]. Specifically, these numerical and *in vitro* studies showed that changes in the local flow patterns and wall shear stress patterns occur with variations in geometry.

In this phantom model of a coarcted vessel with a bypass graft, not only did the local through-plane velocity patterns vary, but even the flow distribution was affected by the variations in the geometry. Figure 4.29 shows the flow waveforms through the host vessel and through the bypass graft for the three different geometric models. These waveforms all compared favorably to the PC-MRI measurements, but overall, the waveforms associated with the ideal model and the user 1 model agreed better with PC-MRI. The average flows through the host vessel were 3.9 mL/s, 4.7 mL/s, and 3.9 mL/s for the user 1, user 2, and ideal model, respectively, compared with a PC-MRI measurement of 4.0 mL/s. In the graft, the average flows were 9.5 mL/s, 8.9 mL/s, and 9.5 mL/s for user 1, user 2, and the ideal model, respectively. The PC-MRI measurement in the graft was 9.3 mL/s. These differences in the flow distribution were likely due to variations in the modeling of the coarctation region. A coarctation that is less tight, as in the case of the user 2 model versus the user 1 or the ideal model, will permit more flow through the host vessel, so less fluid will travel through the bypass graft, which is what the simulation results demonstrated.

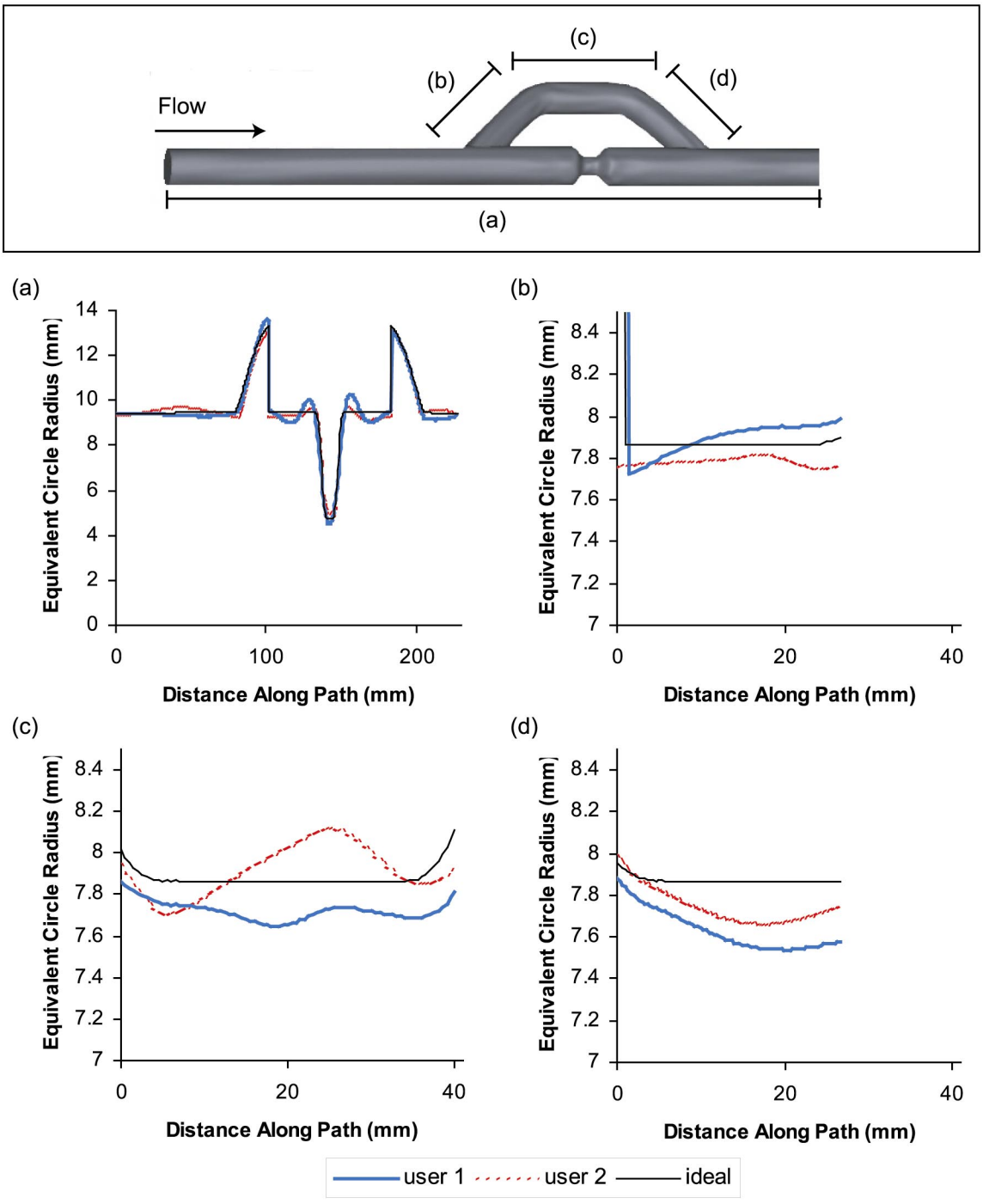


Figure 4.28: Quantitative comparison of three geometric models of the phantom. The equivalent circle radii along different segments of the model are plotted against the distance along the given segment for (a) the host vessel segment, (b) upstream graft segment, (c) straight graft segment, (d) downstream graft segment. The heavy blue lines correspond to model a (user 1 model) in Figure 4.27, while the dotted red lines are for model b (user 2 model) and the black lines for model c (ideal model) in that figure. Note that the scale for the comparisons in the graft differs from that for the host vessel segment.

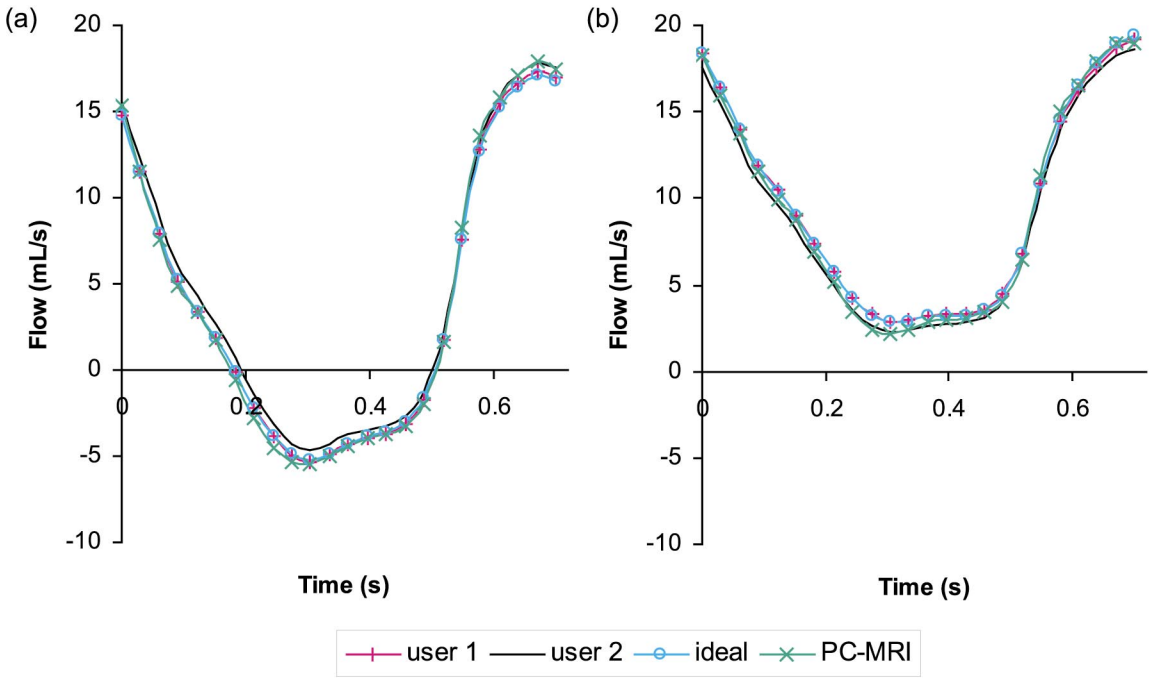


Figure 4.29: Comparison of flow waveforms for simulations based on three different geometric models. PC-MRI data is also presented as reference. (a) Flow through the host vessel (plane C) (b) Flow through the bypass graft (plane F).

Understanding how the geometric variations affected the through-plane velocity contours is a more difficult task. Sometimes the differences occurred during late-deceleration, as seen in the host vessel at plane D (distal coarctation), while at other locations, such as at plane B (downstream inlet), the variations existed primarily at peak flow. In all cases, though, the through-plane velocities observed in the simulation with the ideal model compared most favorably to those measured by PC-MRI. This was most evident at the distal coarctation location, where the simulation based on the ideal model displayed symmetry in the velocity patterns during late-deceleration. This symmetry was also seen in the PC-MRI measurements, but not in the simulations with the MRA-based models. Recall that both of the MRA-based models bulged immediately downstream of the coarctation, probably causing the asymmetry. At peak flow, though, this asymmetric effect was diminished, since the velocity contours were strongly influenced by the high velocities of the fluid exiting the coarctation during this time.

More subtle variations in the velocity contours were observed at other locations. Downstream of the inlet, the area of highest velocity varied at peak flow, with the user 2

simulation showing the smallest area, and the user 1 simulation showing the largest area. This could correspond inversely to the equivalent-circle radii, which was largest for the user 2 model and smallest for the user 1 model at this location. At plane C (proximal coarctation), both the MRA-based model simulations showed a slightly sharper peak in the velocity contours than either the ideal model simulation or the PC-MRI data. However, it is unclear which MRA-based model produced velocity patterns that more closely resembled the PC-MRI and ideal case. During late-deceleration, the user 2 simulation captured the small negative velocity region along the wall closest to the bypass, but the contours of the user 1 simulation were more similar in shape to the ideal and PC-MRI contours. During peak flow, though, the user 2 velocity contours more closely resembled those of the ideal model. While the equivalent-circle radii for the MRA-based models differed from that of the ideal at this location, it would be simplistic to identify that single parameter as the cause of these differences. More likely variations in the modeling of the proximal anastomosis combined with deviations in the host vessel produced the minor differences seen in the velocity contours at this location.

Differences also existed during both late-deceleration and peak flow at planes E (outlet) and F (graft). While the velocity magnitudes at the outlet were similar, the contours differed. At this location, the flows exiting the graft and the coarctation interact, so the geometric variation may have less influence on the velocity patterns than the flow conditions upstream, particularly during peak flow. Note that the contour patterns of the three models during late-deceleration appeared to be rotated versions of one another, while the contours during peak flow were different in shape. Furthermore, in the simulation based on the ideal model, negative velocities were observed at all points along the wall, whereas the simulations based on the MRA-based models did not display such a large extent of negative velocities. In the graft, the main difference occurred in the peak velocities during peak flow, where the velocity contours associated with the user 2 model appeared flatter than those of the user 1 or the ideal model, both of which were slightly flatter than the PC-MRI data. Again, it is difficult to pinpoint a specific geometric variation that might account for the changes in the velocity contour patterns.

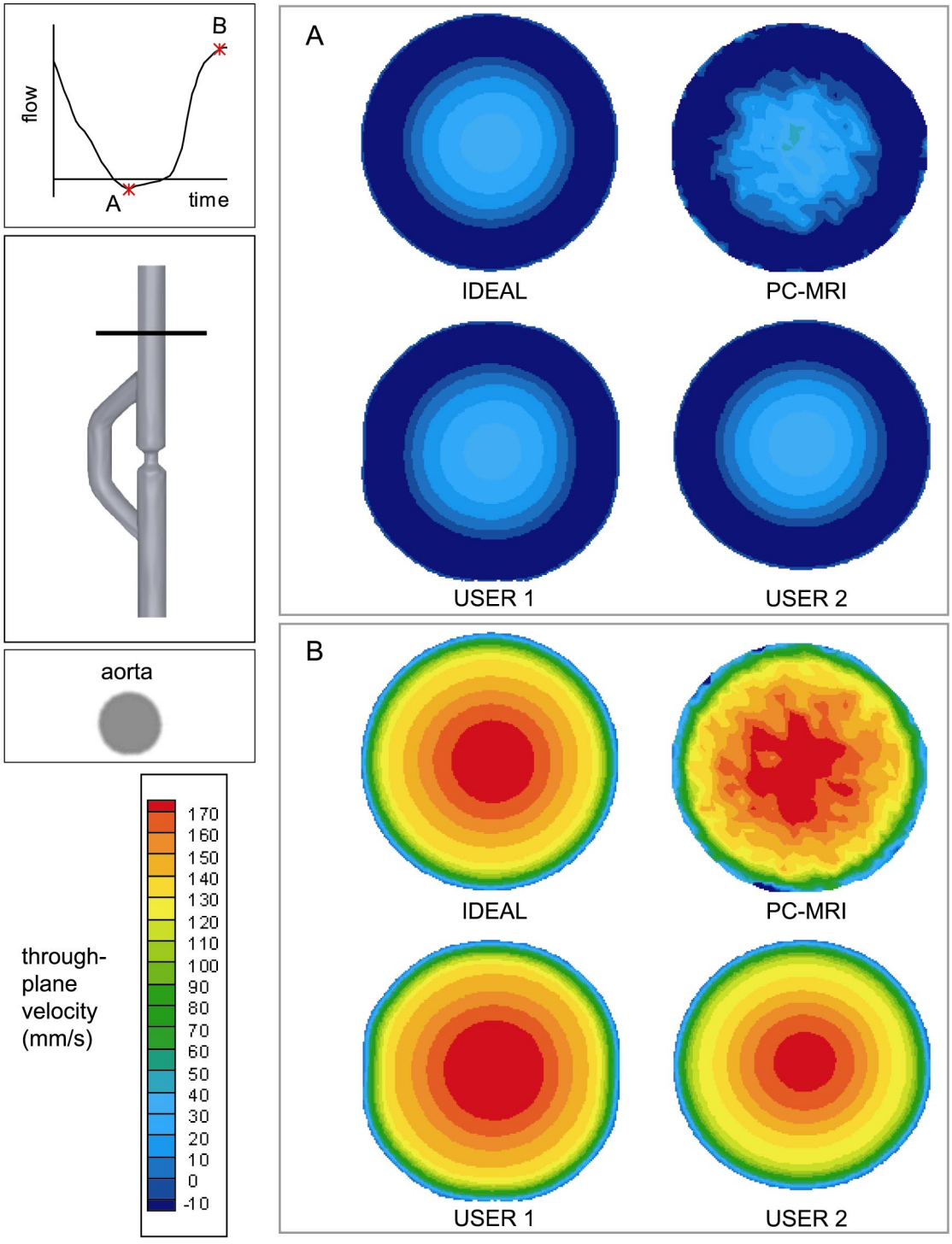


Figure 4.30: Comparison of through-plane velocity contours in the aorta proximal to the bypass, also referred to as the downstream inlet (plane B), for three geometric models of the phantom: an ideal model based on the CAD drawings of the phantom and two user models constructed from the MRA data. PC-MRI data is also presented for reference purposes. Results from two time points are shown: late-deceleration (A) and peak flow (B).

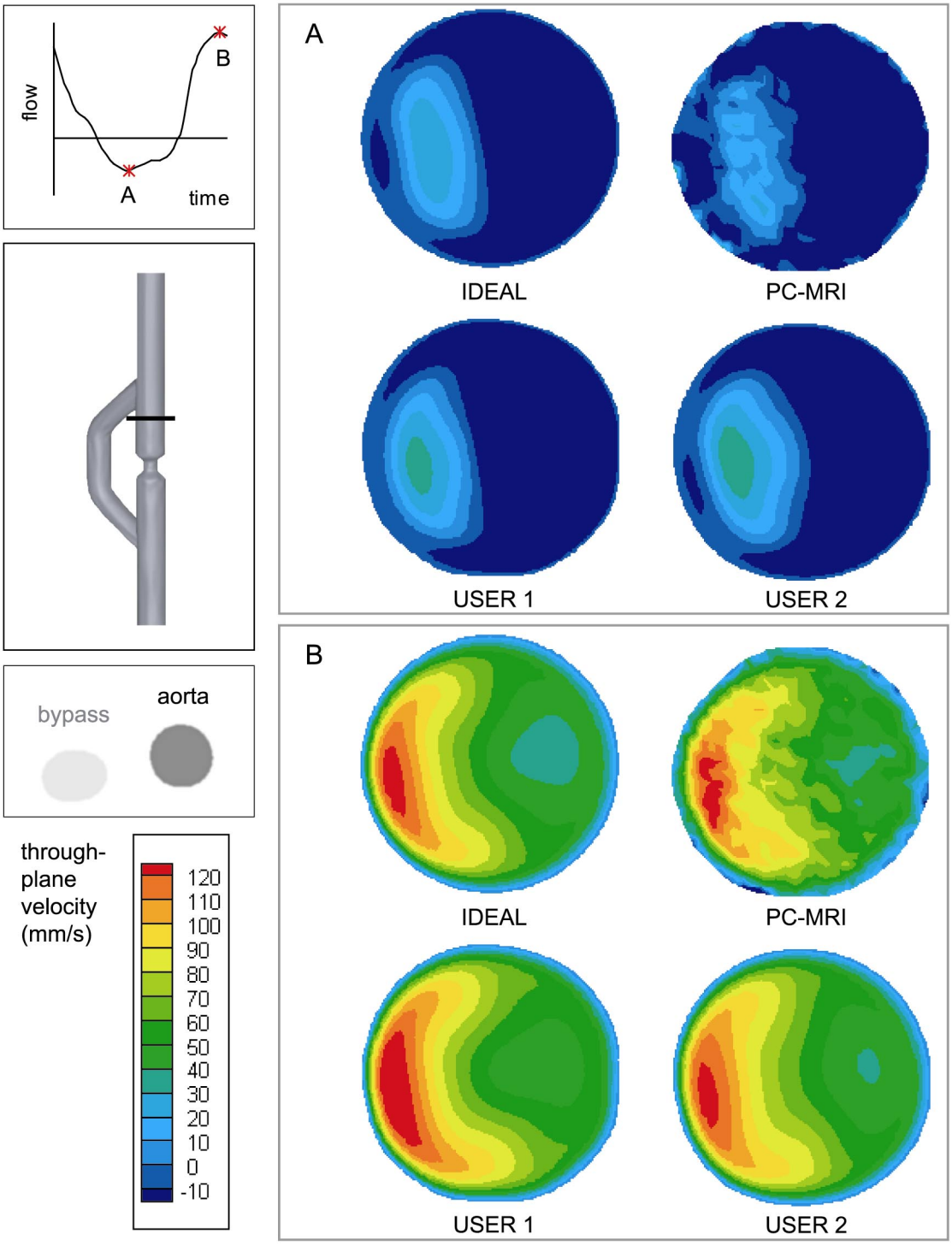


Figure 4.31: Comparison of through-plane velocity contours at the aorta proximal to the coarctation but distal to the bypass (plane C) for three geometric models of the phantom: an ideal model based on the CAD drawings of the phantom and two user models constructed from the MRA data. PC-MRI data is also presented for reference purposes. Results from two time points are shown: late-deceleration (A) and peak flow (B).

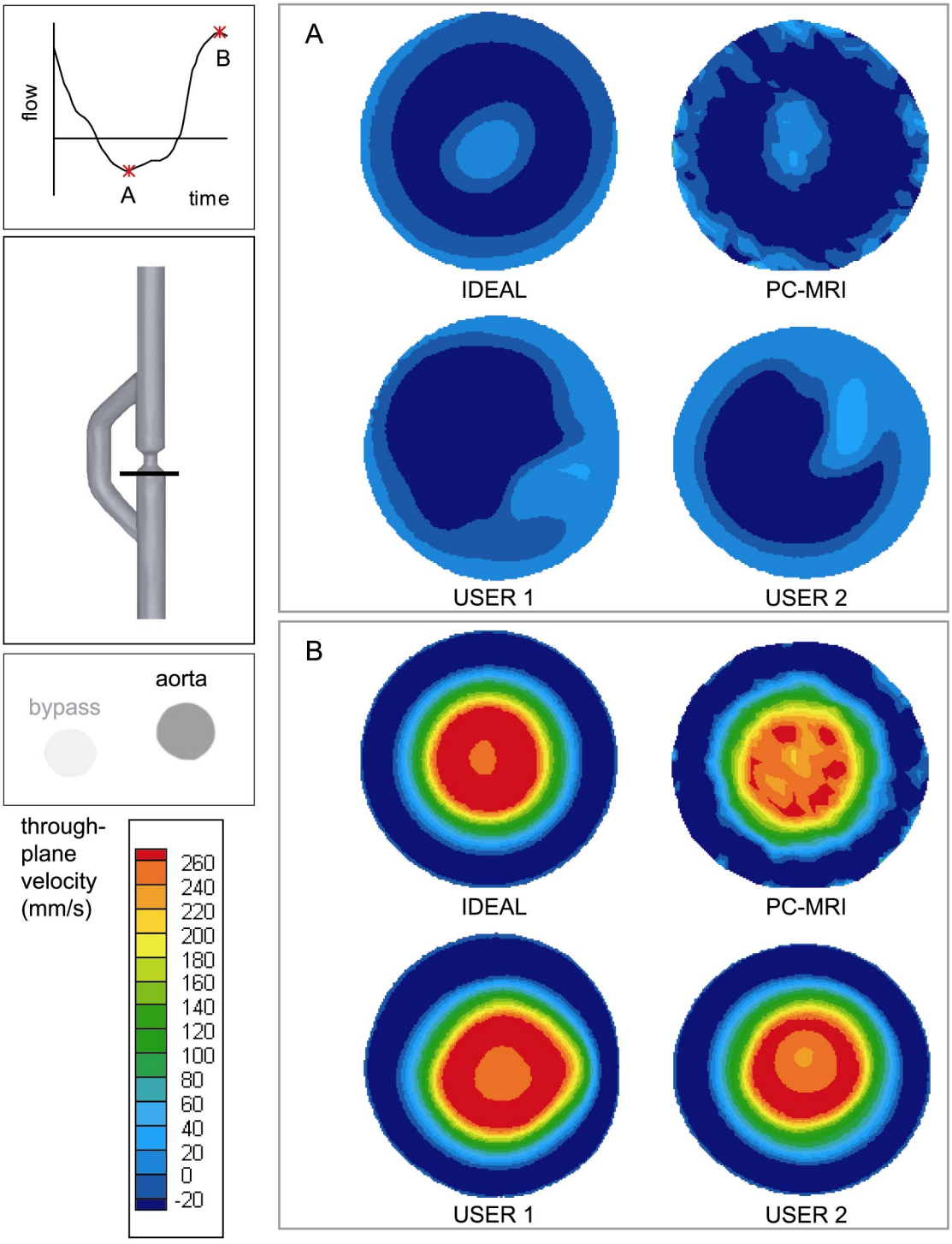


Figure 4.32: Comparison of through-plane velocity contours in the aorta distal to the coarctation (plane D) for three geometric models of the phantom: an ideal model based on the CAD drawings of the phantom and two user models constructed from the MRA data. PC-MRI data is also presented for reference purposes. Results from two time points are shown: late-deceleration (A) and peak flow (B).

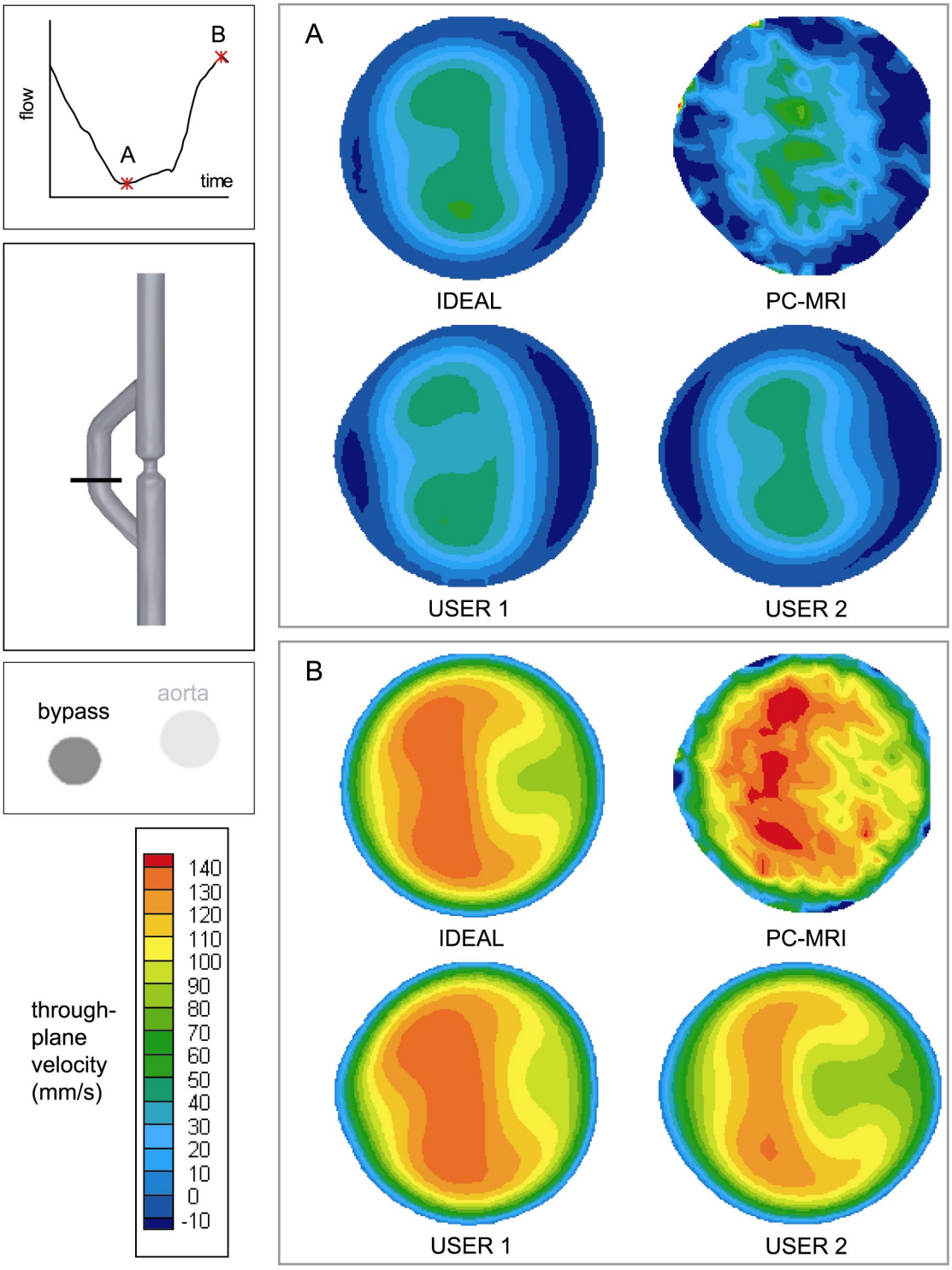


Figure 4.33: Comparison of through-plane velocity contours in the bypass graft (plane F) for three geometric models of the phantom: an ideal model based on the CAD drawings of the phantom and two user models constructed from the MRA data. PC-MRI data is also presented for reference purposes. Results from two time points are shown: late-deceleration (A) and peak flow (B).

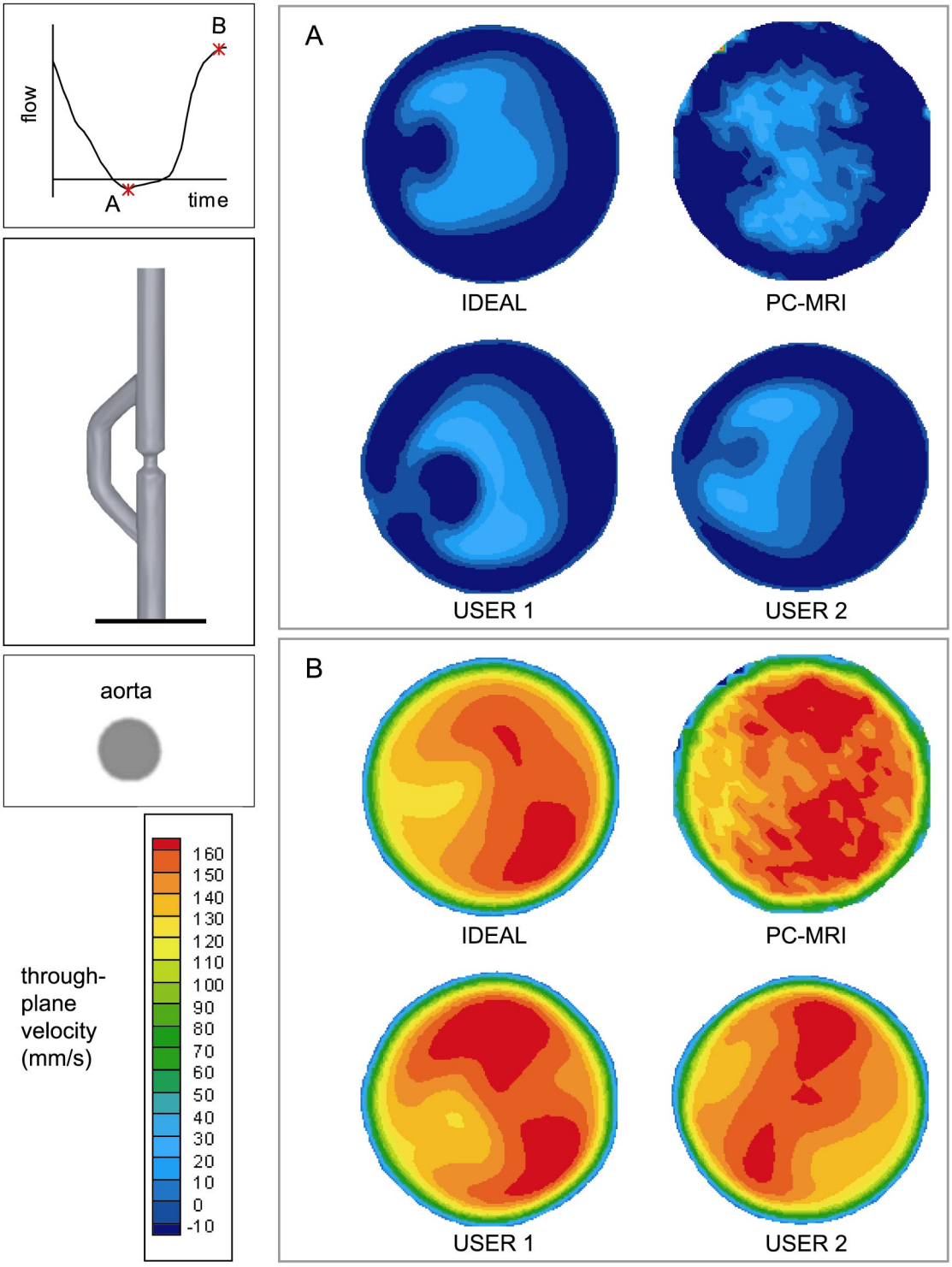


Figure 4.34: Comparison of through-plane velocity contours in the aorta distal to the graft, also referred to as the outlet (plane E), for three geometric models of the phantom: an ideal model based on the CAD drawings of the phantom and two user models constructed from the MRA data. PC-MRI data is also presented for reference purposes. Results are shown for late-deceleration (A) and peak flow (B).

Rather, it is important to emphasize that the MRA-based models do display differences in geometry, as compared with the ideal model. These geometric differences can cause changes in both flow distribution and through-plane velocity contours, and at certain locations, such as distal to the coarctation, the variations can be important. Certain geometric features, such as branches and curves, are particularly difficult to capture accurately using the 2D approach implemented within Geodesic. Since the lofting operation involves fitting a spline through the 2D level set contours, relatively abrupt changes in the shape of neighboring contours or in the path direction result in errors, as described in Section 2.3.3.1. In this model, these discrepancies were noticeable at the anastomosis, the bends in the bypass graft, and regions proximal and distal to the coarctation. In the case of the distal coarctation region, the variation in velocity contour patterns can be directly attributed to the differences in the local geometry. The differences in the flow distributions predicted by the simulations based on the MRA-based models were likely due to differences in the area of the coarctation. Limitations in the imaging resolution, combined with the difficulties in segmenting small regions, are possible causes for the inaccuracies in the geometric modeling at this small but vital region. Future work involving 3D segmentation algorithms could resolve many of these issues.

4.6.2 Effect of Inlet Velocities on Numerical Simulations

The velocities that are prescribed at the inlet of the geometric model can also strongly influence the results of the numerical simulations [36, 130]. As described in the Experimental Protocol section (Section 4.1.3), only the through-plane velocity component was prescribed for the numerical simulations. In the simulations presented above, the direction of that component was defined to be along the axis of the host vessel (user-defined axis). Another possibility is to set the through-plane velocity direction to be along the normal to the inlet plane. The results of using these two different directions to prescribe the inlet velocities are compared below. The numerical simulations were run with a 3.3-million element mesh for 480 time steps per cycle, and the results from a single slice plane (no spatial averaging) from cycle 9 were compared.

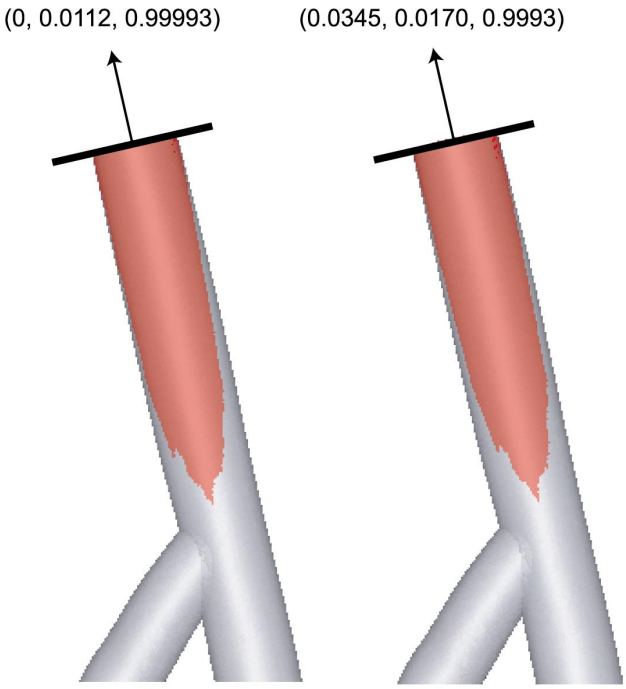


Figure 4.35: Comparison of two different inlet velocity profiles at peak flow. For this experiment, only the velocity component along the vessel axis was prescribed at the inlet. On the left is the velocity profile that was prescribed when the normal to the inlet plane was assumed to be in the direction of the vessel axis. On the right is the profile when a user-defined vessel axis was used. The velocity profiles are shown at a scale 4 times greater than that of the geometric model to emphasize the differences between them, and the coordinates at the top indicate the direction of the vessel axis used in prescribing the inlet velocities.

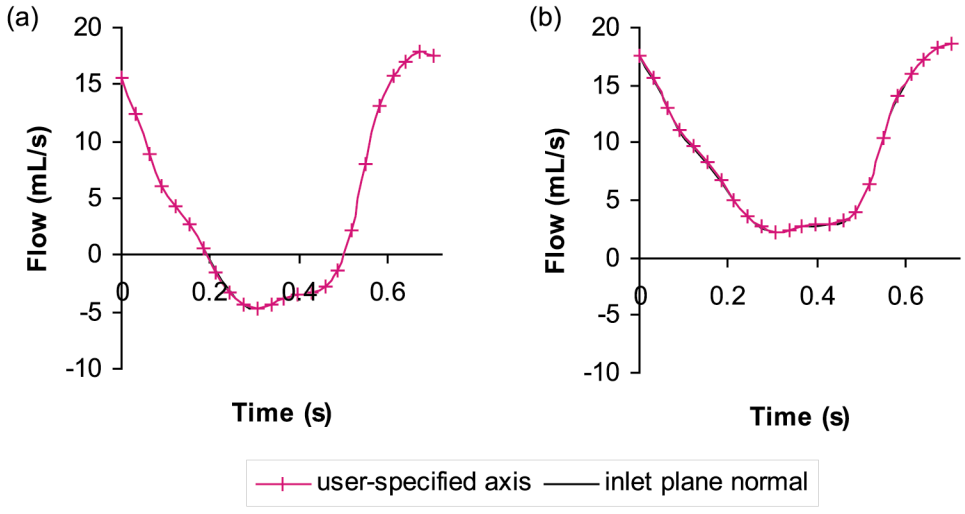


Figure 4.36: Comparison of flow waveforms for simulations run with two different inlet velocity profiles. In one, the prescribed velocities were in the direction of a user-specified vessel axis. The other case prescribed velocities along the normal to the inlet plane. (a) Flow through the host vessel. (b) Flow through the bypass graft.

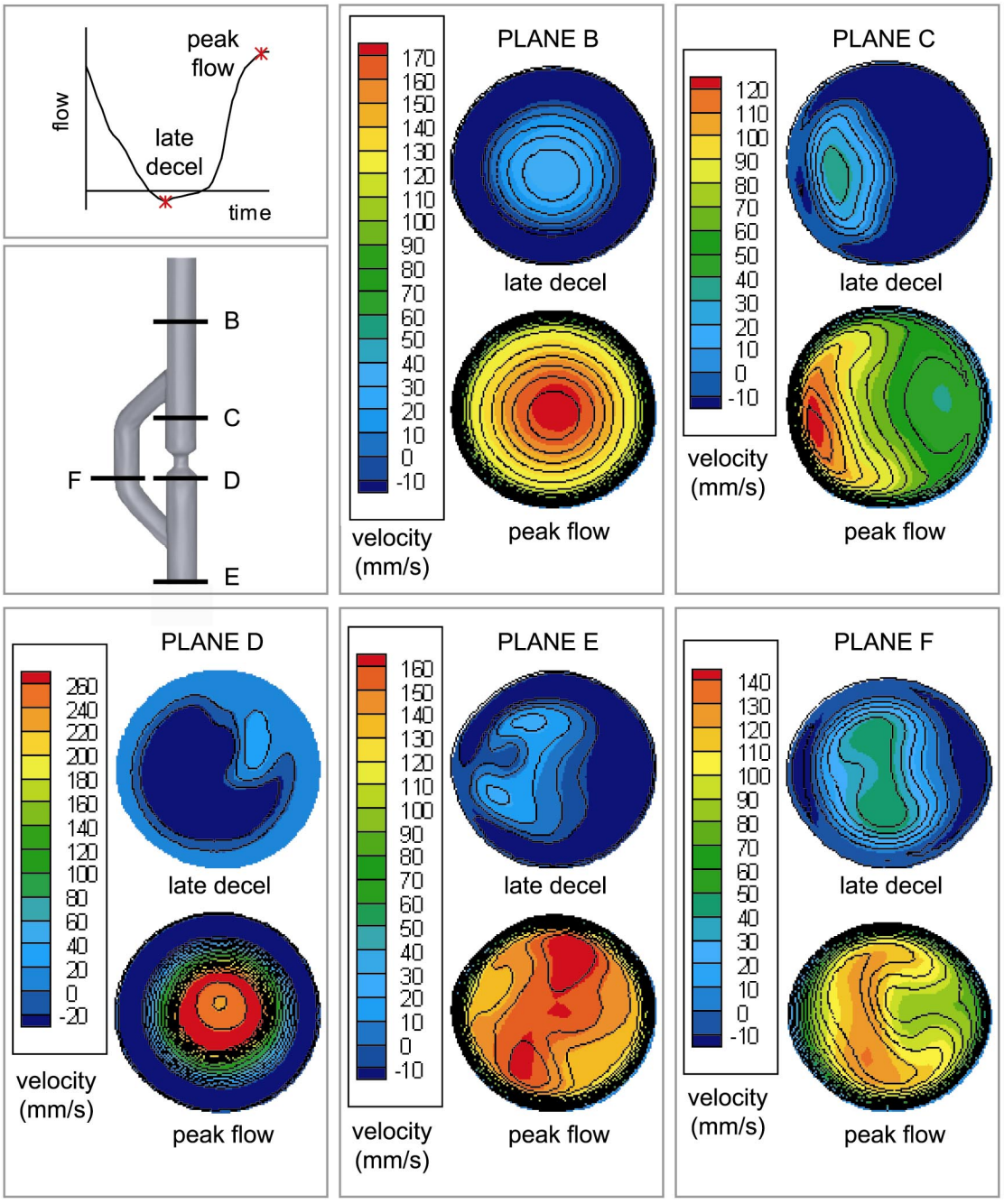


Figure 4.37: Comparison of through-plane velocity contours at five different locations for different inlet velocity boundary conditions. Results are shown during both late deceleration (late decel) and peak flow. The color maps correspond to simulation results where a user-defined vessel axis was used to prescribe the inlet velocities, while the black contour lines were from a simulation where the inlet velocities were prescribed using the normal to the inlet plane. Note that the color scales are different at each location.

The direction of the normal to the inlet plane was (0, 0.0112, 0.99993), while that of the user-defined axis was (0.0345, 0.0170, 0.9993). The difference between these two

directions was small, corresponding to a change in angle of 0.034 radians, or 1.9°. Examination of the inlet velocity profiles shows a minor shift that only became visually detectable when the profiles were magnified (Figure 4.35).

In terms of the flow distribution, this change in the direction of the inlet velocities was insignificant. Figure 4.36 demonstrates the similarities in the flow waveforms generated by the two different simulations. With the user-defined axis, the mean flow was 4.56 mL/s through the host vessel and 8.89 mL/s through the bypass graft. Using the normal to the inlet plane, the simulation results predicted an average flow of 4.55 mL/s through the host vessel and 8.95 through the bypass graft. The slight differences in the flows corresponded to slight differences in the inlet flows: 13.51 mL/s for the simulation using the normal to the inlet plane versus 13.46 mL/s for the simulation using the user-defined axis. The ratio of the flows remained the same in both cases, though: 34% through the host vessel and 66% through the bypass graft.

Differences in the numerical simulation results were more apparent when comparing the velocity contours, particularly at the proximal coarctation slice plane and in the bypass graft. Figure 4.37 shows the through-plane velocity contours for the two different simulations at five different locations for two different time points. At the distal coarctation (plane D) and the outlet (plane E), the results for the simulations were extremely similar. At the other locations, noticeable differences were observed in the velocity contours, especially during peak flow. During peak flow, at the proximal coarctation (plane C) and the bypass graft (plane F), the simulation results using the user-defined axis were rotated versions of the results using the normal to the inlet plane. A shift in the velocity contours also occurred at the downstream inlet (plane B) location, with the peak velocities being more off-center for the simulations run with the inlet plane normal. These variations were reasonable. Since the normal to the inlet plane was not exactly in the direction of the host vessel axis, the inlet velocity profile was asymmetric relative to the host vessel, and that non-symmetry translated into shifts in the downstream velocity profiles. Note that the differences in the inlet velocity profiles did not have much impact on velocity isocontours at the distal coarctation and outlet planes, corroborating previous research which found that the effect of the inlet velocity profile

shape on the downstream flow patterns was limited to a short distance [130-133]. It is also interesting that the bypass graft and the distal coarctation planes were approximately the same distance from the inlet, but variations only occurred in the bypass graft location. A likely explanation for this is that the geometry of the coarctation is a stronger influence on the flow behavior than the geometry of the bypass graft, so changes in the inlet velocity profile would only propagate down and affect velocity contours in the bypass graft.

While the effect of the inlet velocity profile on the flow simulation results is limited, very minor changes in the inlet velocities can produce these variations. In this case, a change of 1.9^{o} in the direction in which the through-plane velocity components were prescribed caused a noticeable shift and/or rotation in the velocity isocontours at some locations. Therefore, if only the through-plane component of the velocity is to be prescribed at the inlet, it is crucial that the direction of that velocity component be accurately determined. This criteria is less important if all three components of velocity are prescribed at the inlet, since presumably, the in-plane components would adjust the inlet velocities to be in the correct direction.

4.7 Discussion

The primary goal of this experiment was to assess the ability of finite-element-based numerical methods to accurately model flow distributions and velocity profiles using only MR-based geometry and velocity information. These results were compared against PC-MRI measurements. Because of the spatial and temporal averaging effects that occur with PC-MRI, it was determined that a fair comparison would require a similar spatial and temporal averaging of the numerical simulation results, a post-processing step not done in previous studies. The effect of this averaging on the computational results varied, depending on the location of interest. For instance, averaging slices along the vessel axis made a difference at the distal coarctation, a location of high through-plane velocities, but not at the proximal coarctation plane, where the peak through-plane velocities were less than half that at the distal coarctation. Similarly, temporal averaging

was more important at the outlet plane, where non-periodic flow patterns existed, than at the proximal coarctation location. In fact, without the temporal averaging, which produced relatively periodic results at the outlet, it was unclear which cycle of the simulation to compare against the PC-MRI measurements. However, this averaging had no impact on the flow waveforms.

Good agreement was found between these spatially and temporally averaged numerical simulation results, whose geometry and inlet boundary conditions were based upon MRI data, and the PC-MRI measurements at the five different slice plane locations and four different time points that were examined. Because of the geometry used in this experiment, both diverging and converging flow patterns were simultaneously examined, a flow situation that has not previously been studied. The coarctation is an additional complexity that has been observed to produce non-periodic flow behavior [134] and further complicates the flow patterns. The complex nature of this problem provided the opportunity to more rigorously test the ability of the finite-element-based numerical simulations to accurately predict blood flow patterns.

In terms of flow distributions, the flows predicted by the numerical simulations were similar to those measured with PC-MRI. The PC-MRI-measured mean flow rates were 4.0 mL/s and 9.3 mL/s through the host vessel and bypass graft, respectively, compared with the numerical predictions of 4.6 mL/s and 8.9 mL/s through the host vessel and bypass graft, respectively. In addition, the predicted flow rates compared favorably with the measured flow rates over the entire cycle. The through-plane velocity isocontours were also comparable, with regions of high and low velocities occurring in similar locations. The magnitudes and shapes of the velocity isocontours were most similar at the downstream inlet location, while the most noticeable discrepancies occurred at the outlet and distal coarctation slice planes.

Because neither PC-MRI nor the numerical simulations are considered a gold standard, these discrepancies could be due to errors in either the PC-MRI or the numerical simulations or both. In terms of the PC-MRI measurements, it has been found that the velocity measurements were less accurate in regions of complex flow, such as that observed downstream of a coarctation or at an anastomosis [87, 88] (see Section

2.2.3.3). The PC-MRI measurements for this experiment also appeared to be rather noisy, although the theoretically computed standard deviation for the through-plane velocities was only on the order of 2 to 3 mm/s, a best-case value according to the sensitivity studies described in Section 3.2.2.2. The in-plane components were also observed to be noisy, though fairly small in magnitude. Results from the repeatability studies also demonstrated that the exact velocity isocontour shapes varied from measurement to measurement, despite a low theoretically computed standard deviation. Furthermore, some differences were observed in the repeatability of the flow pump output. This experimental variability suggests that it would be unreasonable to require exact agreement when comparing with PC-MRI-measured velocity contours, although the general velocity patterns should be similar.

Increases in the signal-to-noise ratio, possible through increased averaging, combined with lower velocity encoding (v_{enc}) values could decrease the variability and improve the comparisons. Note that in this experiment, the through-plane v_{enc} was approximately twice that of the maximum measured velocity, and during late deceleration, the contrast was even greater. The difference between the in-plane v_{enc} and the maximum velocity component measured in-plane was even larger, approximately a factor of 10. New techniques, such as the phase-unfolding technique used by Papaharilaou, *et al.* [56] in their comparisons between PC-MRI measurements and numerical simulation results, would permit a much lower v_{enc} to be set and could prove to be useful here.

The numerical simulations were also sensitive to input parameters. Specifically, the effect of geometry and the direction of the inlet velocity profiles were analyzed. As has been shown in previous studies, the velocity isocontours varied depending on the local geometry. Results from the simulations run with an ideal model showed better agreement with the PC-MRI measurements than those run with an MRA-based model. Compared with the simulations using the MRA-based model, the ideal model simulation showed more symmetric velocity contours distal to the coarctation. Proximal to the coarctation, the velocity profiles were slightly flatter, and at the outlet, the contours were more crescent-shaped and agreed better with the PC-MRI measurements. The numerically computed velocities from the simulations using the two different MRA-based models

also showed marked differences. In some cases, the differences in geometries produced differences in the flow distribution, probably because of variations in the modeling of the coarctation. Analysis of the three geometric models showed that aside from the coarctation, geometric differences occurred immediately proximal and distal to the coarctation, at the anastomoses, and near the bends in the bypass graft. Many of these differences can be attributed to the 2D nature of the current model construction process and could potentially be reduced by using a 3D segmentation algorithm.

The direction in which the through-plane velocities are prescribed at the inlet was also found to affect the velocity contours, primarily at locations upstream of the coarctation. Comparisons between simulations run using two different directions for the through-plane velocity component demonstrated that even a relatively minor shift of 1.9^{o} caused noticeable shifts in the velocity contours. Simulations run with the normal to the inlet plane, which was not along the host vessel axis, showed a peak velocity that was shifted towards the wall at the downstream inlet location and a rotation in the velocity patterns at the proximal coarctation and the bypass graft locations, relative to the patterns observed in the simulations with the user-defined axis, which was in the direction of the host vessel axis. The simulations based upon the user-defined axis were better matched to the PC-MRI measurements. While the numerical simulation results appear to be extremely sensitive to the inlet velocities and seem to require either a precise orientation of the inlet plane or some manual intervention, it is presumed that this degree of accuracy would not be required if three components of velocity were prescribed at the inlet, assuming that accurate in-plane velocity components could be obtained which would automatically adjust the inlet velocities to be along the correct direction.

A source of error that is unique to the outlet is the fact that mesh-independent solutions were not obtained at this location. It is unclear how much the velocity contours would change if a mesh-independent solution were used in the comparisons. Nonetheless, the agreement between the numerical simulations and the PC-MRI measurements for both flow distributions and through-plane velocity contours was very good, despite the limitations of the measurement technique and the sensitivity of the numerical computations.

4.8 Summary

Although the eventual application of these numerical simulation techniques is to patient cases, *in vitro* studies, such as this, help determine the accuracy, and ultimately, the usefulness of these methods for predicting blood flow distributions and patterns. While the model used in this experiment was more complex than that used in previous comparison studies, the comparisons between the temporally and spatially averaged numerically computed results still agreed well with the PC-MRI measurements. Further improvements in the comparisons could be obtained by improving the quality of the PC-MRI measurements, as well as utilizing more accurate geometric model construction methods.

Chapter 5

High Flow *In Vitro* Experiment

The important thing is not to stop questioning.
~Albert Einstein

While the simulation results from the low flow *in vitro* experiment described in Chapter 4 agreed quite well with the PC-MRI measured velocities, the flow conditions in the experiment are simple relative to conditions found *in vivo*. *In vivo* the Reynolds number is estimated to be between 3600 and 5800 in the ascending aorta, between 1200 and 1500 in the descending aorta, and between 110 and 850 in the large arteries [66]. The low flow *in vitro* experiment had a mean Reynolds number of 255, and other studies have been limited to mean Reynolds numbers of less than 490 with most of them in the 200 to 300 range [36, 46-48, 52, 53, 56, 57]. To conduct a more rigorous comparison between the flow simulation results and the PC-MRI measurements, the *in vitro* experiment from Chapter 4 was repeated with higher mean flows, and consequently, higher mean Reynolds numbers. Section 5.1 reviews the methods, identifying slight modifications to the experiment, while Section 5.2 presents the results of the comparison between the numerical simulations and PC-MRI measurements. Sections 5.3 and 5.4 examine the sensitivity of the comparisons to the experimental data and the numerical results, respectively. Finally, the findings are discussed in Section 5.5, and a summary of the *in vitro* studies is given in Section 5.6.

5.1 Methods

5.1.1 Experimental Set-Up

A set-up similar to that used for the low flow *in vitro* experiment, detailed in Chapter 4, was employed for this experiment. Briefly, this experiment involved pumping a mixture of 39.8% glycerol, 59.7% distilled water, and 0.5% gadolinium through a rigid phantom model of a vessel with a 75% area coarctation and with a bypass graft. The fluid was measured to have a dynamic viscosity of 0.036 dynes-s/cm^2 at 23^o C and a density of 1.1 g/mL. As with the low flow experiment, the phantom was connected to a pulsatile pump via approximately 4.5 m of flexible, braided tubing and 2.4 m of rigid tubing, a length which exceeds the estimated entrance length of 0.88 m required for parabolic flow at the inlet of the phantom (See Equation (2.12)). Again, a flow straightener and ECG simulator (Shelley Medical Imaging Technologies, London, Ontario, Canada), which converted the pump's trigger signal into a simulated ECG signal, were used.

Improvements to the experiment included the use of adjustable stopcock valves to provide fluid resistance and a glass bottle with a column of air above the fluid to model system capacitance, as shown in Figure 5.1. The handle of each stopcock valve could be turned to vary the fluid resistance and the height of the air column adjusted to vary system capacitance. A stopcock valve and glass bottle were placed right before the flow entered the reservoir, and a second glass bottle was placed just downstream of the flow pump, as shown in Figure 5.2. Adjustment of the resistances and capacitances modified the shape of the flow waveform and helped maintain a reasonable pressure in the system. In addition, a custom pulsatile pump, which generated high flow waveforms that were more periodic than that of the Harvard Apparatus pump in the low flow experiment, was used. The displacement of the flow pump piston was controlled using a triangular waveform, which produced a sinusoidal-like flow waveform at a rate of 100 cycles per minute. The average flow was 38.6 mL/s, as measured with PC-MRI (see Section 5.1.2.2). These flow settings corresponded to a Womersley number of 17.0 and an average Reynolds number of 766 at the inlet of the phantom model. The range for the Reynolds number was from 502 to 1156.

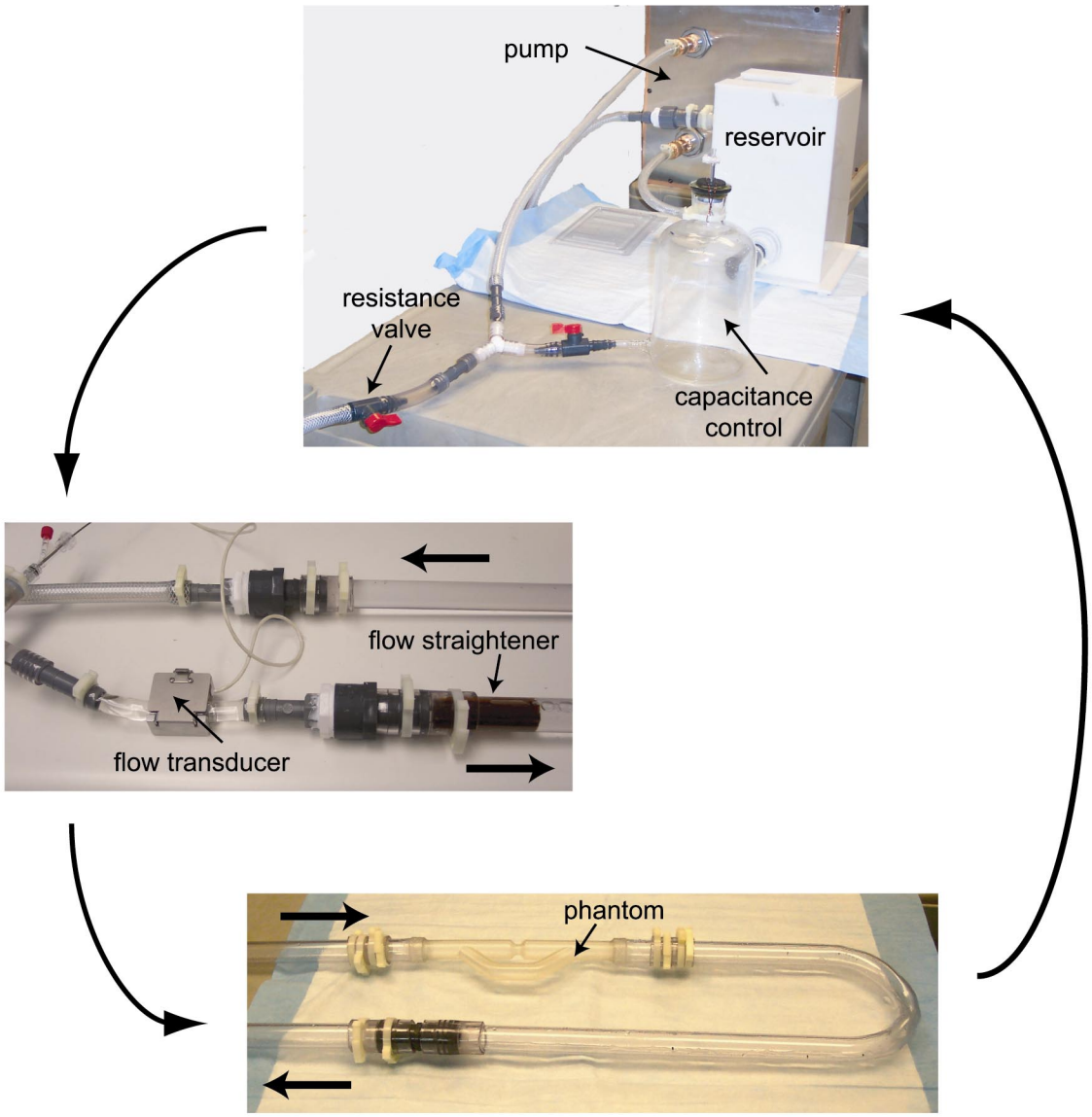


Figure 5.1: Set-up for the high flow *in vitro* experiment. A custom pulsatile flow pump was used to pump a mixture of glycerol, distilled water, and gadolinium through a rigid bypass phantom. A set of flexible tubing followed by 2.4 m of rigid tubing connected the pump to the phantom. An ultrasonic flow transducer was placed immediately upstream of the rigid tubing, and valves and glass bottles were used to provide resistance and capacitance, respectively, to the flow system. The larger arrows in the photos indicate the direction of flow through the system.

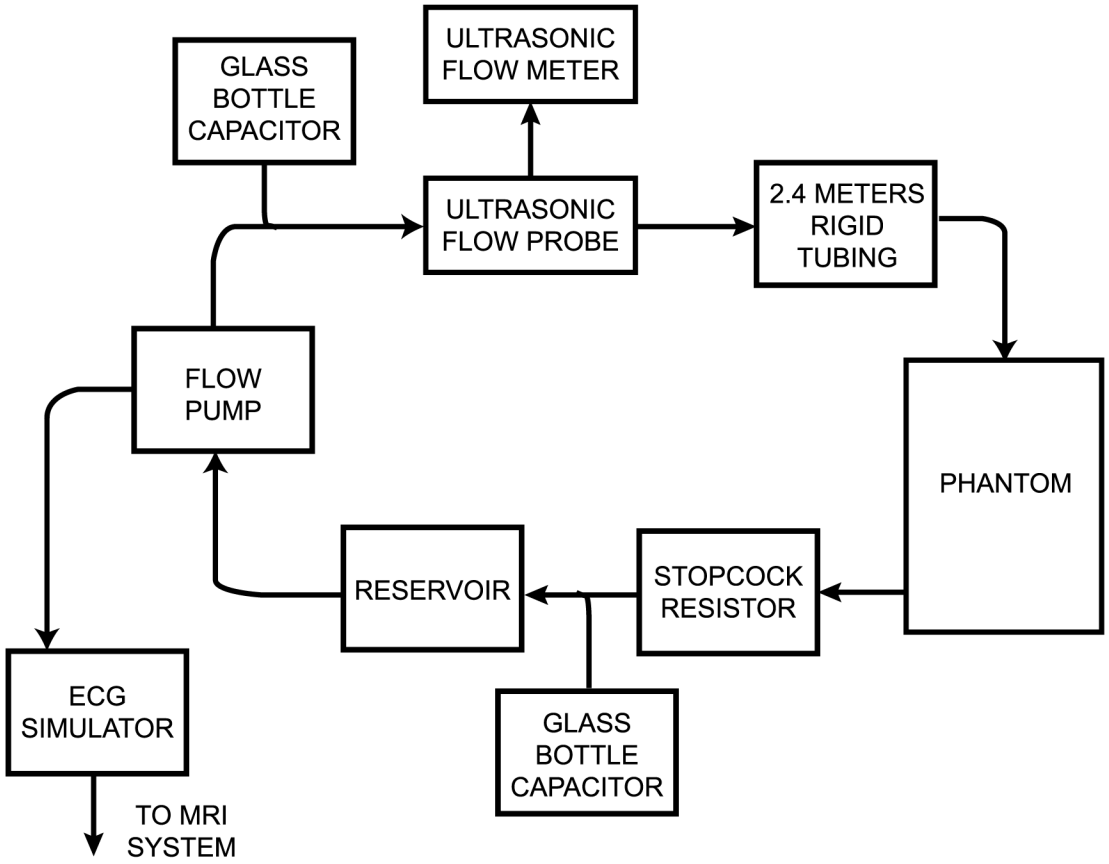


Figure 5.2: Diagram of the experimental set-up for the high flow *in vitro* study. The glass bottles added capacitance to the system, while the stopcock was used to control resistance.

5.1.2 Data Acquisition

5.1.2.1 Flow Probe Measurements

A 14C externally clamped ultrasonic flow probe (Transonic Systems, Inc., Ithaca, NY) was placed upstream of the rigid tubing to assess the periodicity of the flow and to measure the flow rate. The flow probe was placed around Tygon tubing R3603, and lubricating jelly was used to improve the coupling between the tubing and the flow probe. The signal from the probe was sent to a T206 small animal blood flow meter (Transonic Systems, Inc., Ithaca, NY). The data from the flow meter was recorded at a sample rate of 200 samples per second using a data acquisition board (DAQPad-6020E, National Instruments, Austin, TX) and a LabVIEW program (LabVIEW v.6 and v.6.1, National Instruments, Austin, TX) running on a Dell Inspiron 8000 laptop computer (Dell

Computer Corporation, Round Rock, TX). The measurements were converted from voltages to flow using the following equation:

$$Q = V \cdot 4.7553 - 0.0155 \tag{5.1}$$

where Q is the flow in L/min and V is the voltage in volts. This equation was obtained from a linear fit of voltage plotted against flow measurements acquired using the bucket and stopwatch technique for steady flow at 4 different rates. To obtain a single representative cycle of the flow, the flow signal was divided into individual cycles using a trigger signal generated by the pump. The individual cycles were then averaged together to obtain one representative cycle that would be used in the analysis (see Figure 5.3).

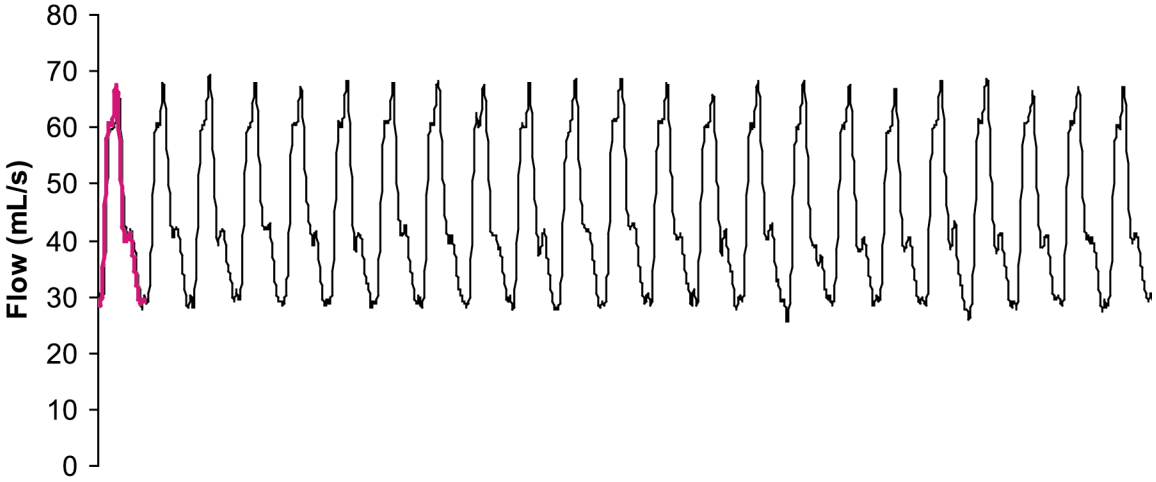


Figure 5.3: Example of measurements of flow acquired with the ultrasonic flow probe. The average of the measurements is the first cycle, plotted in pink.

5.1.2.2 MRI Data

The MRI data acquisition for the high flow *in vitro* experiment was similar to that of the low flow experiment. Geometry and flow measurements were acquired using a 1.5 T MRI system (Signa, GE Medical Systems, Waukesha, WI) and a head coil. The first scans were two-dimensional localizer images, which provided information for spatial localization of the subsequent scans. Geometric information was obtained from contrast-enhanced magnetic resonance angiography (CE-MRA) data acquired with a rapid, three-

dimensional, gradient-recalled echo sequence [128], and the custom 2D cine phase contrast sequence described in Section 4.1.2.2 was used to measure the three orthogonal components of velocity.

The specific imaging parameters for the CE-MRA were: T_R = 3.4 ms, T_E = 1.3 ms, a field of view (FOV) of 28 cm x 28 cm, a slice thickness of 2.0 mm zero-filled to produce 1.0 mm between slice centers, an acquisition matrix size of 256x192, number of excitations (NEX) = 1, and a 20-degree flip angle. 64 slices were acquired in the axial direction, and a three-dimensional grad-warp correction was applied to the data prior to use.

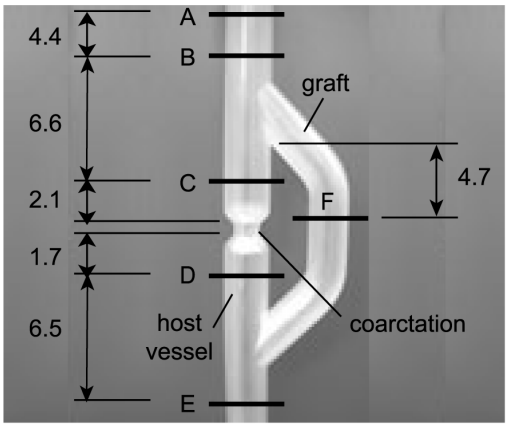


Figure 5.4: Phantom model for the *in vitro* flow experiments. Planes A-F indicate locations where PC-MRI data was acquired for the high flow experiment. Plane A is the inlet, and this information was used to prescribe the boundary condition for the numerical simulations. Flow and velocity information acquired at all other locations were used for comparison purposes. The distances between the planes relative to each other and/or relative to a distinct location on the model were estimated and are given in centimeters.

As with the low flow *in vitro* experiment, the velocity information was acquired at 6 locations with the flow pump turned both on and off. These locations are shown in Figure 5.4: at the inlet of the phantom (inlet, plane A), a short distance downstream of the inlet (downstream inlet, plane B), in between the proximal anastomosis and the aortic coarctation (proximal coarctation, plane C), distal to the aortic coarctation (distal coarctation, plane D), distal to the distal anastomosis (outlet, plane E), and in the graft (graft, plane F). Oblique axial slices were acquired using the following parameters: respiratory compensation, flow compensation, T_R = 18.5 ms, T_E = 9.3 to 10.0 ms, 24 cm FOV, 5 mm slice thickness, acquisition matrix of 256x256, 15.63 kHz bandwidth, NEX =

1, and a 20-degree flip angle. The through-plane velocity encoding (v_{enc}) was 40 cm/s for all locations except at the distal coarctation (plane D in Figure 5.4) and at the graft (plane F in Figure 5.4), where the through-plane encoding was 80 cm/s and 60 cm/s, respectively. The in-plane v_{enc} was 10 cm/s for all acquisitions, except for the distal coarctation plane and the outlet plane, where the v_{enc} was 20 cm/s. For each data set, 24 time points per cycle were reconstructed, and velocity acquisitions were synchronized using the signal from the trigger-to-ECG converter.

A first-order baseline correction was computed from the flow-pump-off images using the custom software vcalc and applied to the PC-MRI velocity. The signal-to-noise ratio and the standard deviation of the PC-MRI velocity measurements were also computed for each slice plane using the method described in Section 3.2.1.3, providing an estimation of the repeatability of these measurements.

5.1.3 Numerical Simulations

The process used to generate the geometric model and boundary conditions needed by the numerical simulation methods was the same as that used in the low flow *in vitro* experiment. From the grad-warp-corrected CE-MRA data, a geometric model was constructed using manual path-planning methods and the level set segmentation algorithm. Default values, including an initial radius of 4.0, a first-stage curvature threshold value of 0.4, and a second-stage upper curvature constraint also of 0.4, were used for the level set segmentation. For the bypass, copies of contours from the positions closest to the ends of the path were made and oriented at those locations. See Section 4.1.3 for more information, including the motivation behind this approach. These contours were used to construct a geometric solid model, which was then discretized. Again, Section 4.1.3 describes these processes in more detail.

The inlet boundary conditions were also determined as in the low flow *in vitro* experiment, with only the PC-MRI velocity component in the direction of a user-defined axis being used. The user-defined axis was used because it was closer in direction to the axis of the host vessel than the normal to the inlet plane was. In this case, the user-defined axis was in the direction (-0.0236, 0.0075, 0.9997), compared with the normal to

the inlet plane, which was in the direction (0, 0.0207, 0.9998)—a 1.5° or .026 radian difference. As the sensitivity study performed in Section 4.6.2 showed, small changes in the through-plane velocity direction at the inlet affects the resulting velocity patterns, particularly in those locations closer to the inlet. Furthermore, the higher Reynolds number at the inlet means that flow effects will propagate further than in lower Reynolds number problems, therefore making the correction of the axis direction even more critical. As with the low flow experiment, in-plane velocity components were not used because they were considered to be in the noise range of the acquisitions. The values of the in-plane components varied from –13.2 mm/s to 24.5 mm/s and as Figure 5.5 shows, they were fairly close to zero and appeared to be random, not forming any discernable patterns.

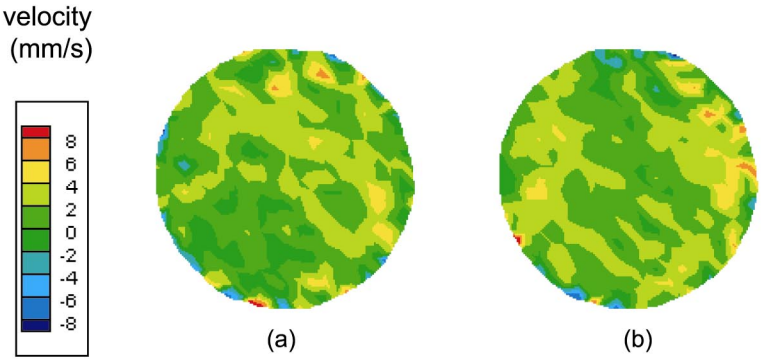


Figure 5.5: In-plane velocity components at the inlet (plane A) during peak flow. (a) Anterior-posterior velocities. (b) Right-left velocities.

The numerical simulations were performed using the exact same assumptions as for the low flow experiment: a rigid model, no-slip condition, zero pressure at the outlet, an incompressible Newtonian fluid with a density of 1.1 g/cm^3. The only change was in the viscosity, which was set to 0.036 dynes-s/cm^2 to match the measured value. A 4.3 million element mesh and 480 time steps per cycle were used for this problem. Although this mesh size and number of time steps most likely did not result in mesh-independent and time step-independent solutions, technical and time constraints did not permit larger problems to be run. As before, the Spectrum™ Solver was used to compute the solutions to this problem for 25 cycles of pulsatile flow on 30 processors of a 128-processor Origin 3800 (Silicon Graphics, Inc., Mountain View, CA), taking approximately 8 days to run.

5.1.4 Post-Processing of the Numerical Simulations

The numerical simulation results were spatially and temporally averaged, as described in Section 4.3. Spatially, the numerical simulation results were interpolated onto a Cartesian grid with the same in-plane resolution as the PC-MRI data, and because the PC-MRI slice thickness was 5.0 mm, 5 slices from the simulations were spatially averaged together. These five slices were taken at the following locations: at the same location as the PC-MRI slice, ±1.25 mm from the PC-MRI slice location, and ±2.5 mm from the PC-MRI slice location. Temporally, results from the corresponding time points in 8 different cycles were averaged together. The results presented here come from averaging together the simulation from cycles 16 to 23.

5.2 Comparison of Numerical Simulation Results to PC-MRI

The results of the numerical simulations using the MRA-based geometric model are compared against first-order baseline-corrected PC-MRI data. Section 5.2.1 examines the flows, while the velocity patterns are studied in Section 5.2.2.

5.2.1 Comparison of Flows

The average flow rates computed from the numerical simulations were similar to those measured with PC-MRI. Through the host vessel, the average flow was measured to be 17.8 mL/s, while the computed flow was 16.7 mL/s. Assuming the PC-MRI measurement to be correct, the simulation underestimated the flow by 6.2%. On the other hand, the numerical simulation slightly overestimated the flow through the bypass graft as compared with that measured with PC-MRI: 21.8 mL/s versus 21.4 mL/s. Again, assuming the PC-MRI measurement to be correct, the discrepancy is 1.8%. Note that the sum of the PC-MRI-measured average flow through the host vessel and through the bypass graft, 39.6 mL/s, does not equal the average flow at the inlet, which was 38.6 mL/s. The lack of conservation of flow indicates some error in the PC-MRI measurements.

The slight discrepancy in the average flows is also reflected in the flow waveform comparisons, shown in Figure 5.6. Little difference is seen in the flow waveforms

through the bypass graft. However, the PC-MRI measurements were higher than that of the computed results during peak flow through the host vessel, though the overall shapes of the flow waveform were similar.

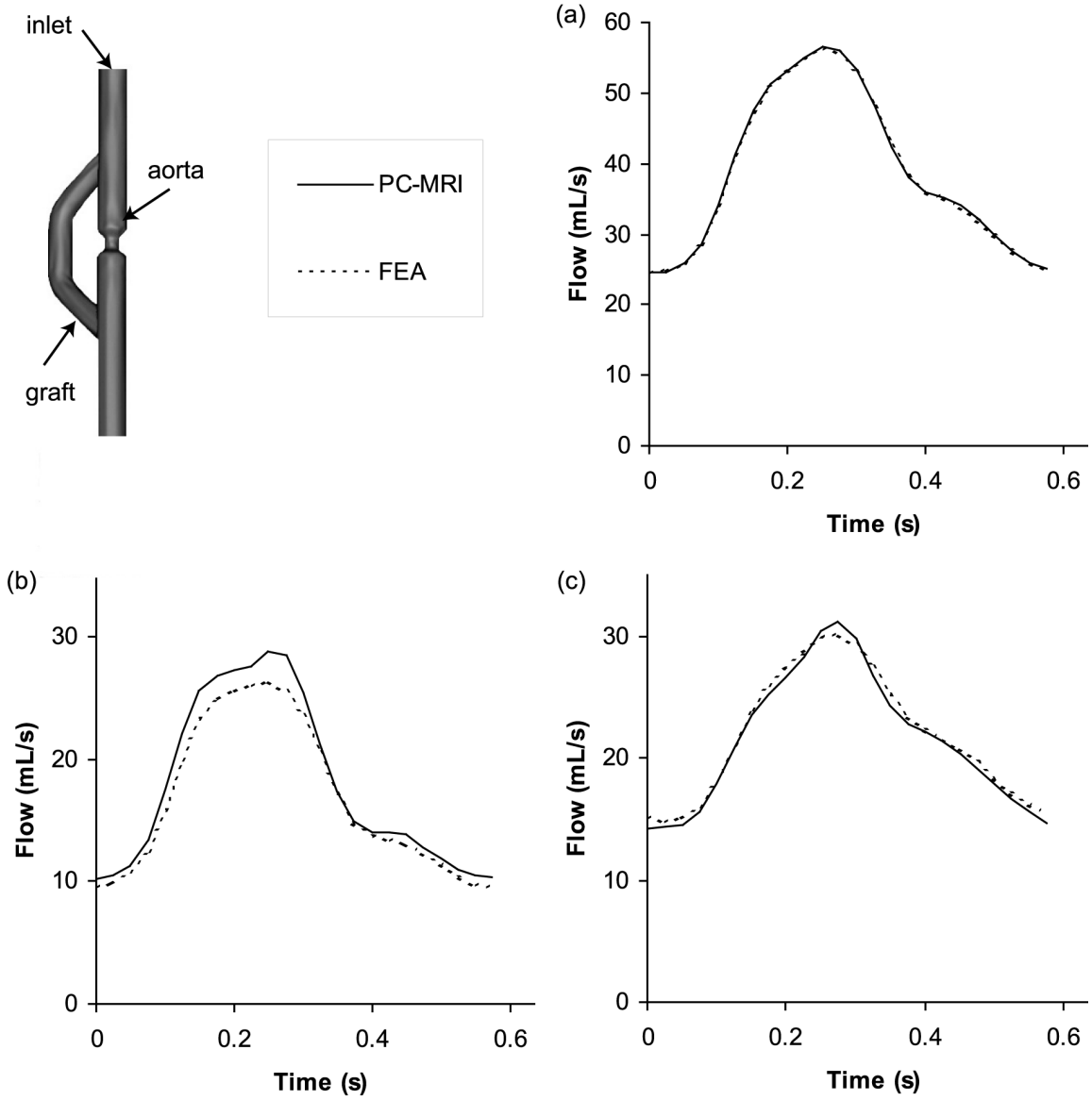


Figure 5.6: Comparison of flow waveforms measured with PC-MRI and those from the numerical simulations. (a) PC-MRI-measured flow at the inlet compared with prescribed flow at the inlet of the simulation. (b) Flow through the host vessel. (c) Flow through the bypass graft.

5.2.2 Comparison of Velocity Patterns

With the higher Reynolds number, the flow features are more complex and propagate further downstream than in the lower Reynolds number problem described in Chapter 4. Figure 5.7 shows the velocity magnitudes from the higher Reynolds number problem along a slice plane approximating the plane of symmetry. Note that the jet from the stenosis extends further downstream than in the lower Reynolds number problem. In addition, vortices are shed downstream of the stenosis, a phenomenon not observed in the lower Reynolds number problem.

The complexity of the flows created in this experiment presented challenges to both the numerical simulation and the PC-MRI acquisition. Figure 5.8 to Figure 5.12 show the comparisons at the five different planes indicated in Figure 5.4: downstream inlet (plane B), proximal coarctation (plane C), distal coarctation (plane D), graft (plane F), and outlet (plane E). Isocontour maps display the through-plane velocities for four different time points: acceleration, peak flow, mid-deceleration, and late-deceleration. Note that the color scales differ for each location.

The patterns and velocity magnitudes from the numerical simulations were similar to those acquired with PC-MRI, although the degree of similarity depended on location. At the downstream inlet (plane B) location, where flow remained laminar, there was excellent agreement between the PC-MRI measurements and the numerical simulation results. A circular pattern whose center was shifted slightly towards the upper wall was observed in both cases. Similarly, good agreement was found at the proximal coarctation (plane C) location, with higher velocities forming a crescent shape along the wall closest to the bypass graft and low or negative velocities appearing at the opposite wall.

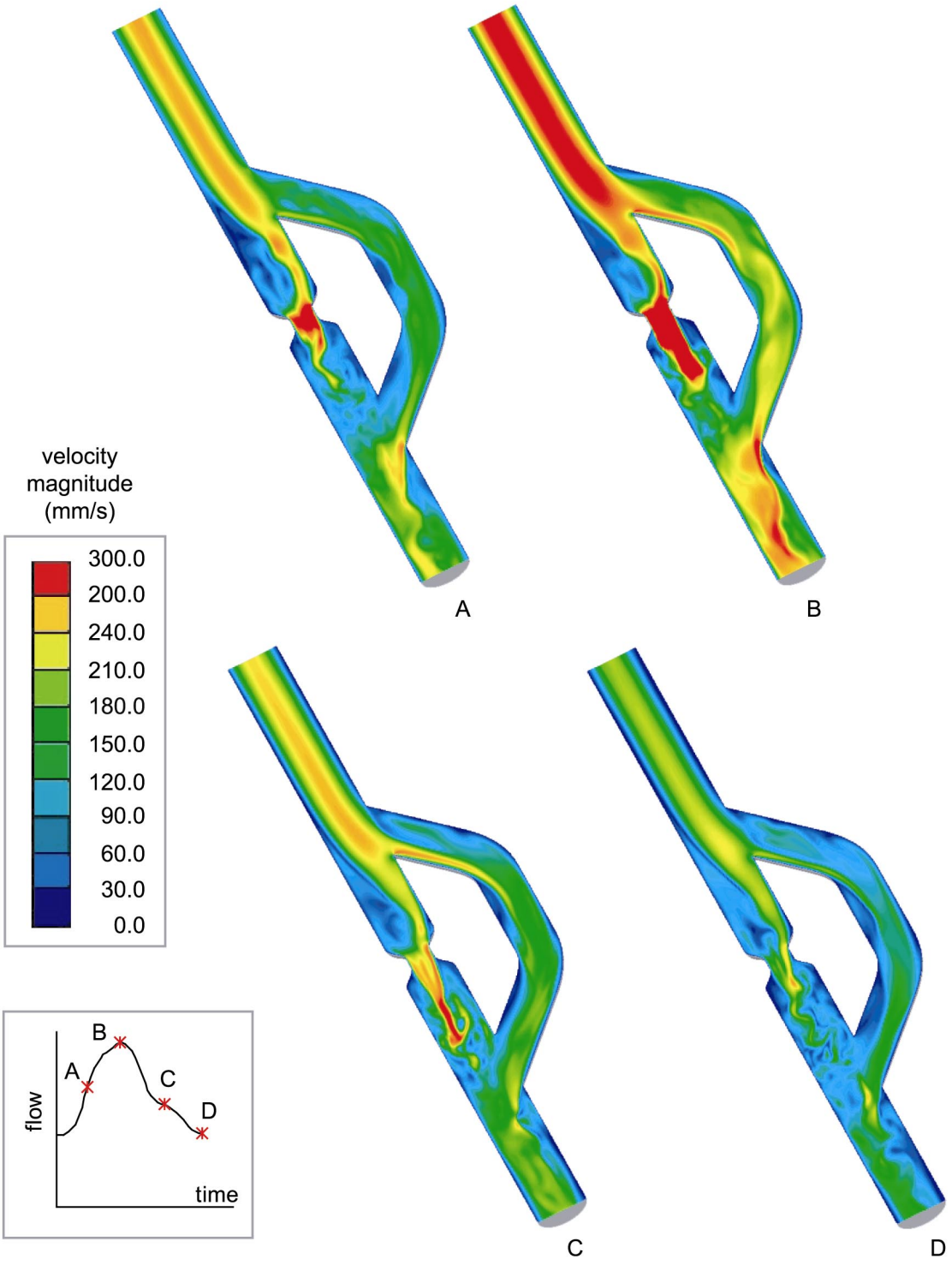


Figure 5.7: Velocity magnitudes as computed from the numerical simulations for cycle 9 at four different time points: (A) acceleration, (B) peak flow, (C) mid-deceleration, (D) late-deceleration. Velocities are shown at approximately the mid-sagittal plane, and the direction of flow, as depicted here, is from the upper-left to the lower-right.

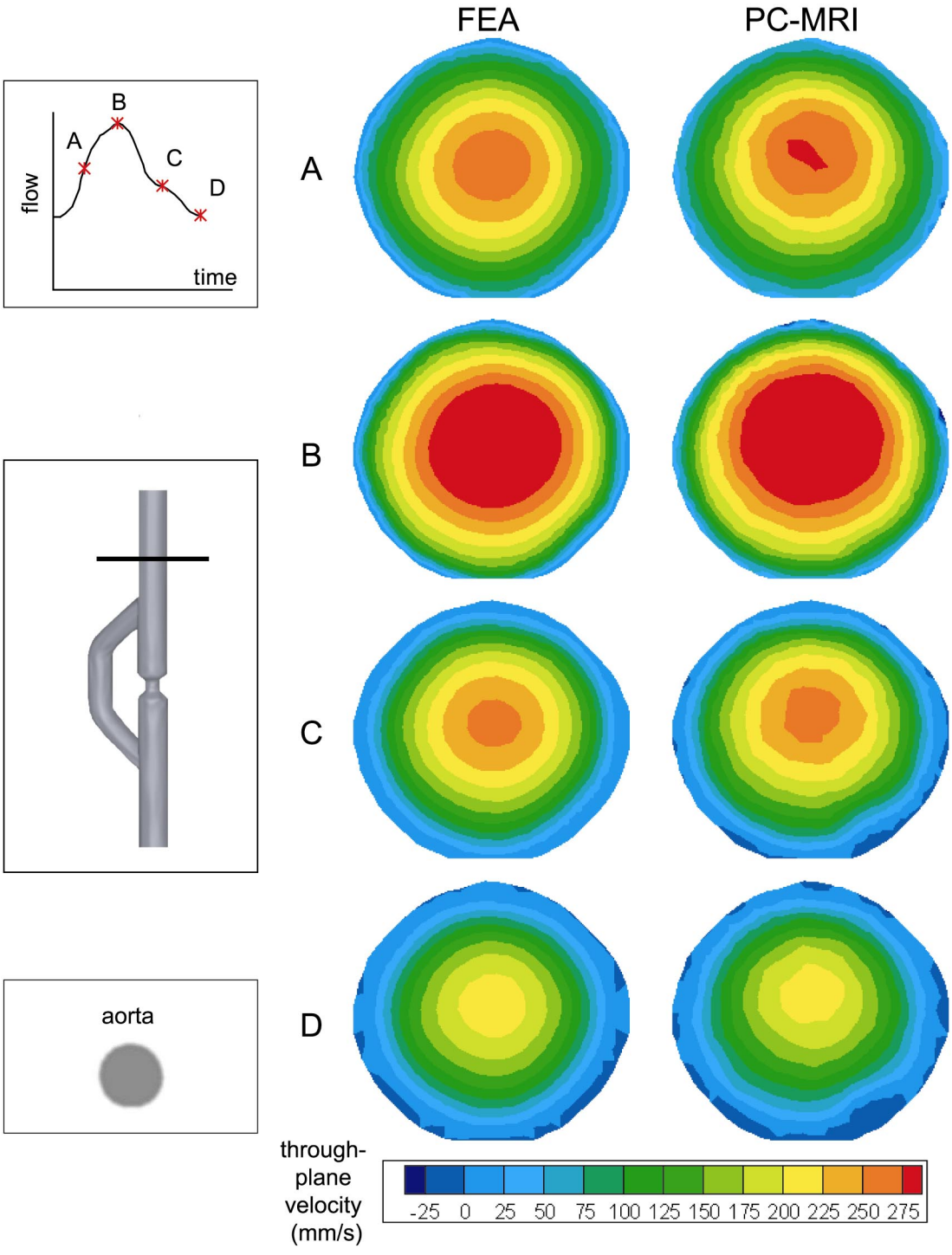


Figure 5.8: Comparisons in the aorta proximal to the bypass graft, also referred to as the downstream inlet (plane B) location, of through-plane velocities computed numerically using finite element analysis (FEA) and those acquired with PC-MRI. Four different time points are examined: acceleration (A), peak flow (B), mid-deceleration (C), late-deceleration (D).

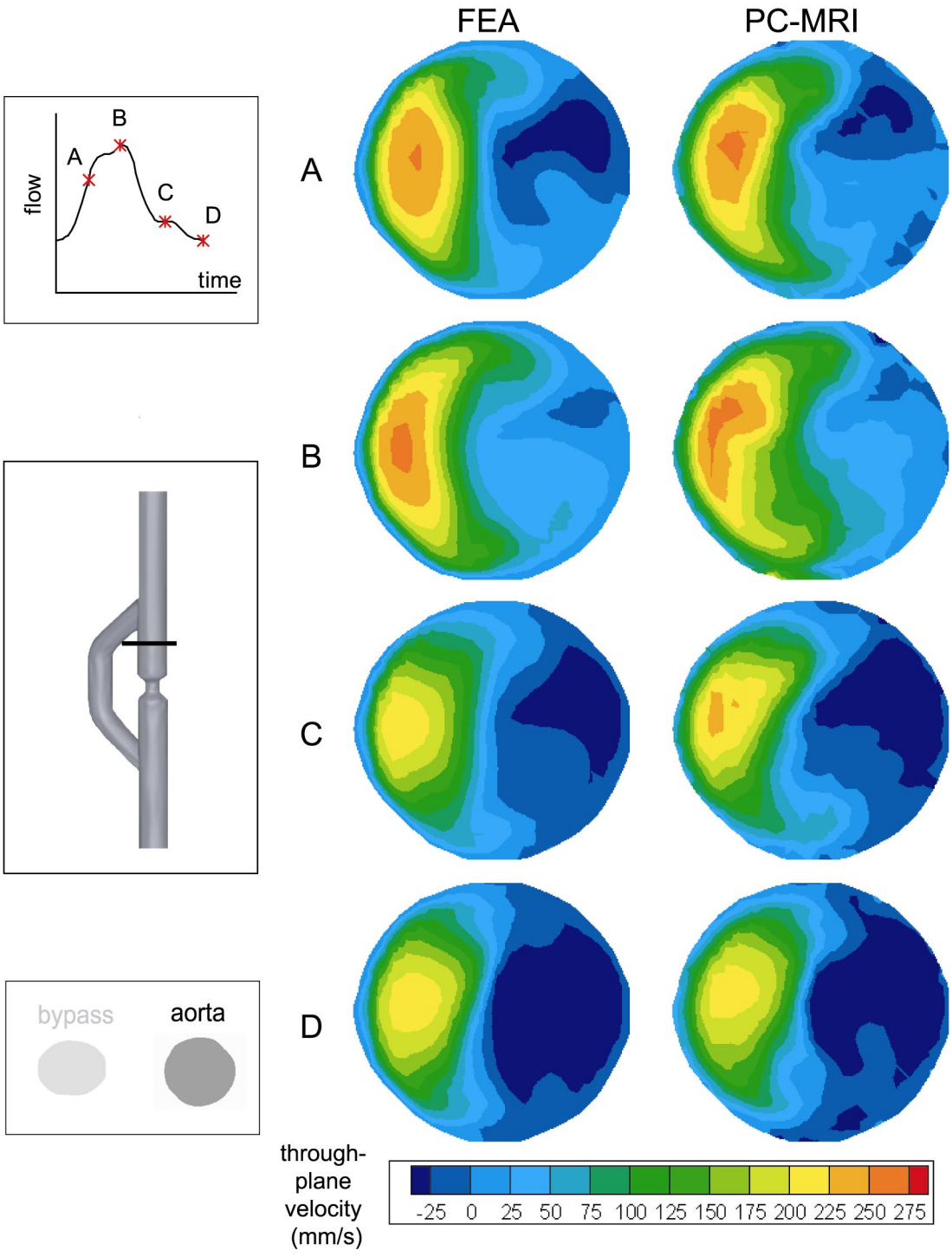


Figure 5.9: Comparisons in the aorta proximal to the coarctation (plane C) of through-plane velocities computed numerically using finite element analysis (FEA) and those acquired with PC-MRI. Four different time points are examined: acceleration (A), peak flow (B), mid-deceleration (C), late-deceleration (D).

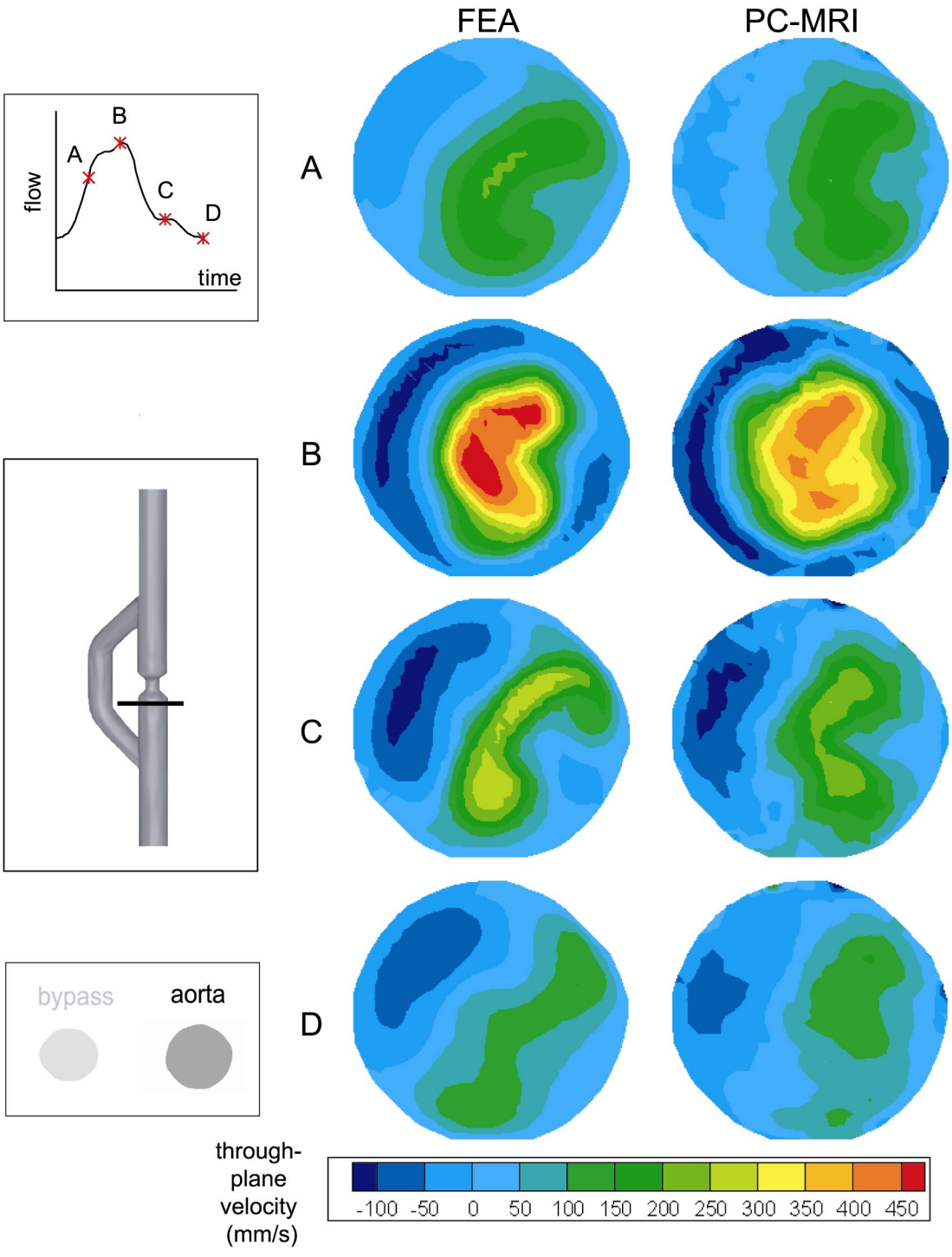


Figure 5.10: Comparisons in the aorta distal to the coarctation (plane D) of through-plane velocities computed numerically using finite element analysis (FEA) and those acquired with PC-MRI. Four different time points are examined: acceleration (A), peak flow (B), mid-deceleration (C), late-deceleration (D).

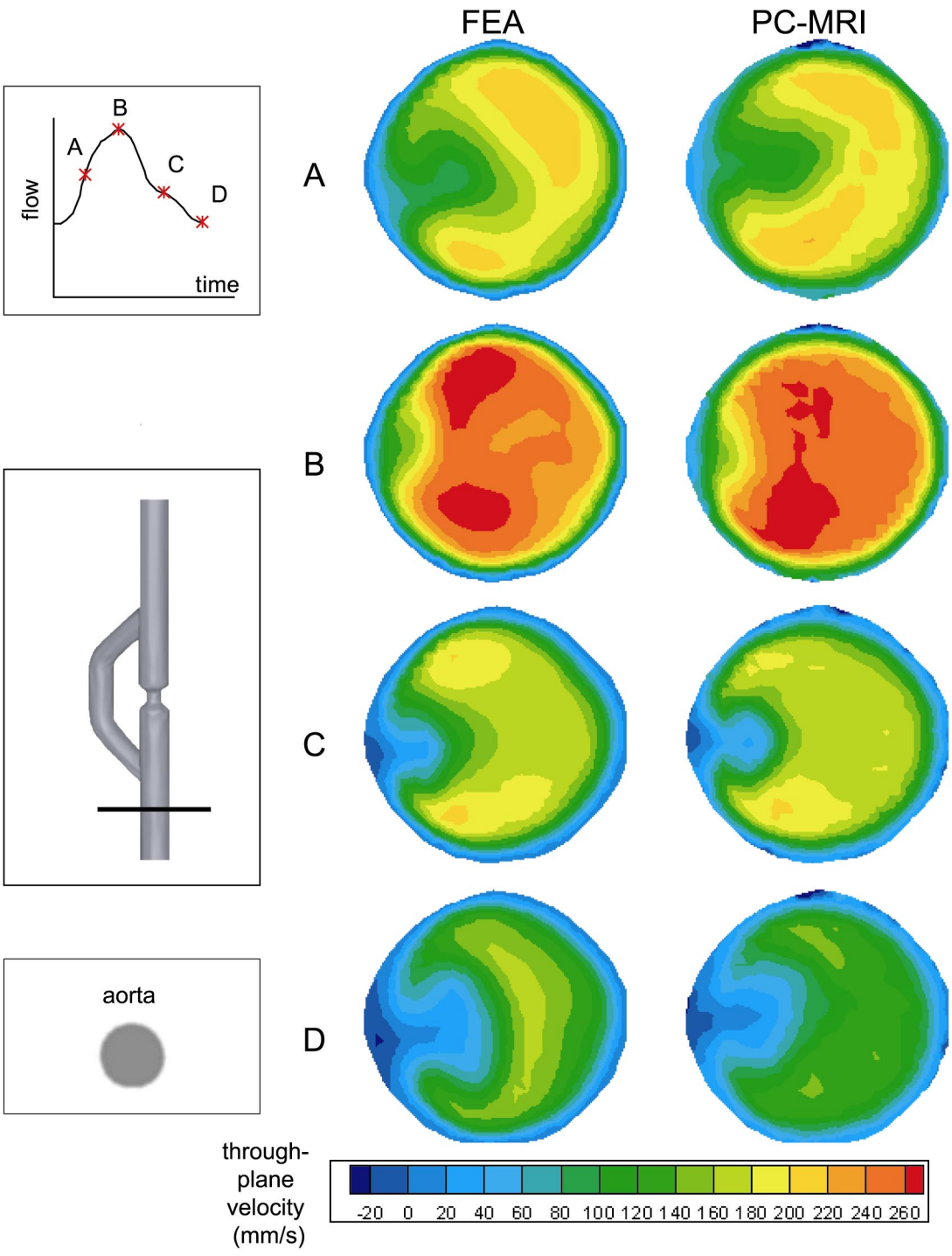


Figure 5.11: Comparisons in the aorta distal to the bypass graft, also referred to as the outlet (plane E), of through-plane velocities computed numerically using finite element analysis (FEA) and those acquired with PC-MRI. Four different time points are examined: acceleration (A), peak flow (B), mid-deceleration (C), late-deceleration (D).

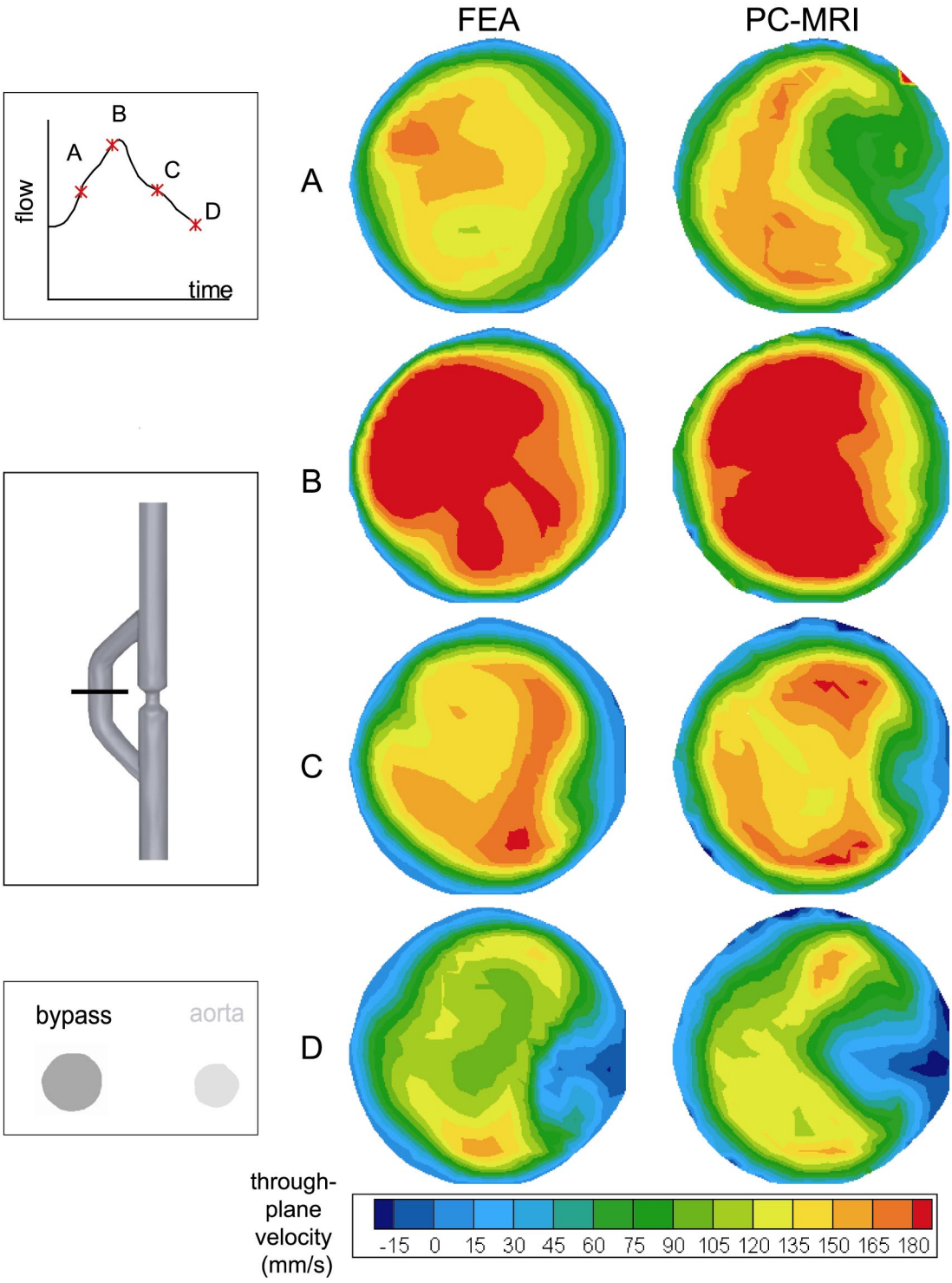


Figure 5.12: Comparisons in the bypass graft (plane F) of through-plane velocities computed numerically using finite element analysis (FEA) and those acquired with PC-MRI. Four different time points are examined: acceleration (A), peak flow (B), mid-deceleration (C), late-deceleration (D).

Even at locations with complex flows, such as at the distal coarctation (plane D) and at the outlet (plane E), there were similarities in the overall velocity patterns and magnitudes although minor discrepancies were seen. Examination of the velocities during peak flow at the distal coarctation plane showed that the patterns were more complicated and without the symmetry observed at this location in the lower Reynolds number experiment. Nonetheless, the patterns measured with PC-MRI and computed with the numerical simulations compared favorably: a thin crescent-shaped region of negative velocities along the wall closest to the bypass graft, a small region of negative velocities along the opposite wall, and a peak in velocities near the center of the vessel, though the peak velocities were slightly higher in the simulation results than in the PC-MRI measurements. Likewise, at the outlet, the differences between the simulation results and the PC-MRI measurements were minor: the isocontour for the 240 to 260 mm/s range at peak flow extended closer to the wall for the PC-MRI measurements versus that for the simulation results, and the peak velocities during late-deceleration were greater in the simulation results than in the PC-MRI measurements.

The location that showed the largest differences was the bypass graft (plane F), where the velocity magnitudes were similar but noticeable variation in the isocontour shapes occurred at several time points. For instance, during acceleration the simulation results for velocity isocontours in the 75 to 120 mm/s range were oblong, whereas the corresponding isocontours from the PC-MRI measurements were crescent-shaped. During late-deceleration, the simulation results predicted a valley, corresponding to a small decrease in the through-plane velocities, at the center of the vessel. This feature was not observed in the PC-MRI data.

5.3 Sensitivity of Experimental Data

The differences observed between the simulations and the PC-MRI measurements could be due to either errors in the experimental data or in the numerical simulations. In this section, the potential errors in the experimental measurements and set-up are discussed.

One measure of the precision of the velocity measurements is the standard deviation, presented in Table 5.1. The standard deviation and the signal-to-noise ratio (SNR) needed to compute the standard deviation were calculated using Equations (2.32) and (2.33), respectively. The SNRs ranged from 76 to 163, which were significantly higher than those for the lower Reynolds number experiment and probably due to the use of a narrower receive bandwidth, larger voxels, and more appropriate velocity encoding (v_{enc}) values. Consequently, the standard deviations of the velocity measurements were generally lower than in the lower Reynolds number experiment. The standard deviation ranged from 1.1 to 4.7 mm/s, although all locations except the outlet had standard deviations of 2.1 mm/s or less. The actual standard deviation may be slightly higher than the theoretically computed standard deviations, as seen in Section 3.2.2.2. While these errors could lead to variations in the isocontour patterns, the differences would be minor, particularly given the relatively large values of the velocities being measured.

	Signal-to-Noise Ratio	Standard Deviation of Velocity Measurements (mm/s)
Plane A (inlet)	84.9	2.1
Plane B (downstream inlet)	162.2	1.1
Plane C (proximal coarctation)	108.6	1.7
Plane D (distal coarctation)	128.3	2.1
Plane E (outlet)	76.2	4.7
Plane F (graft)	121.2	1.5

Table 5.1: Signal-to-noise ratios and theoretically computed standard deviations of velocities for the PC-MRI data.

The repeatability of the flows generated by the pump was also investigated. Measurements were acquired with the ultrasonic flow probe at three different time points during the experiment, and an average flow waveform was computed for each time point. There was little variation in the flow waveforms from cycle to cycle, as demonstrated by Figure 5.13(a). Furthermore, the measurements indicated that the pump output was fairly consistent over time. The average flows were 44.7 mL/s, 44.5 mL/s, and 44.5 mL/s for time t = 0, t = 18 minutes, and t = 33 minutes, respectively. Figure 5.13(b) shows that the

average flow waveforms were nearly identical in shape. A time shift existed between the flow waveforms due to the trigger occurring at a different point in the flow cycle for time t = 0 as compared to the other times. This time shift did not appear in the PC-MRI-measured flow waveforms, though. However, the peaks of the flow waveforms at t = 18 minutes and t = 33 minutes were 0.8 mL/s higher than that at t = 0, and this difference was reflected in the PC-MRI measurements. Figure 5.14 compares the flows acquired at the different times. The inlet, downstream inlet, and proximal stenosis measurements were acquired between t = 0 and t = 18 minutes, while the remaining three locations—the distal stenosis, bypass, and outlet—were acquired between t = 18 minutes and t = 33 minutes. While the flow waveform at the outlet and the sum of the flows through the host vessel and the graft were similar, they both differed from that at the inlet. The peak flows were 58.9 mL/s, 59.6 mL/s, and 56.6 mL/s for the outlet, the sum of the host vessel and graft, and for the inlet, respectively. These differences were likely due to the changes in the flow pump output and could affect the comparisons between the numerical simulations, which used the inlet data as a boundary condition, and the PC-MRI measurements at locations such as the bypass graft and the outlet, which were acquired after the change in the flow pump output occurred.

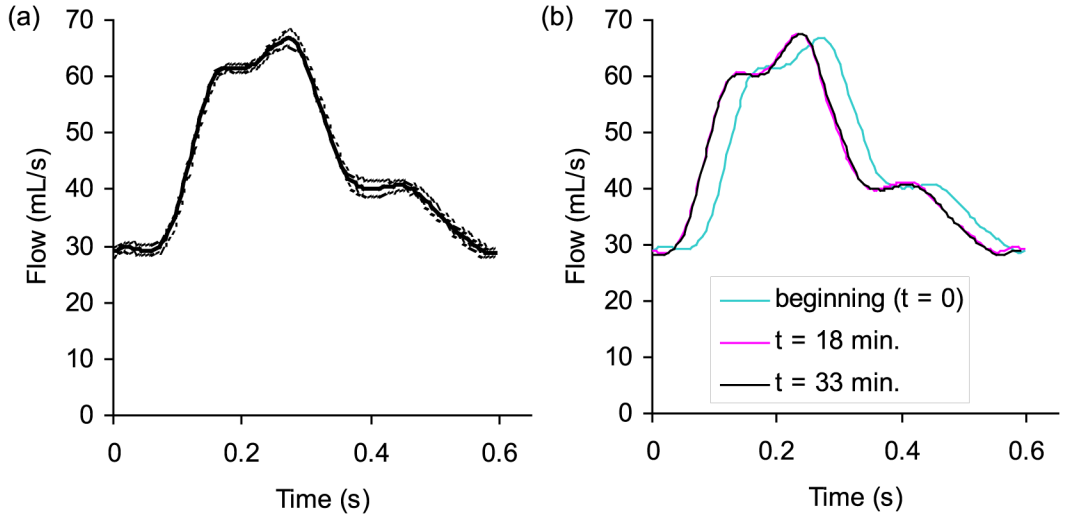


Figure 5.13: Repeatability of output from flow pump, as measured with the ultrasonic flow probe. (a) The heavy black line is the average flow acquired at the beginning of the data acquisition, and the dotted lines represent ±1 standard deviation. (b) The average flows measured at three different time points during the experiment.

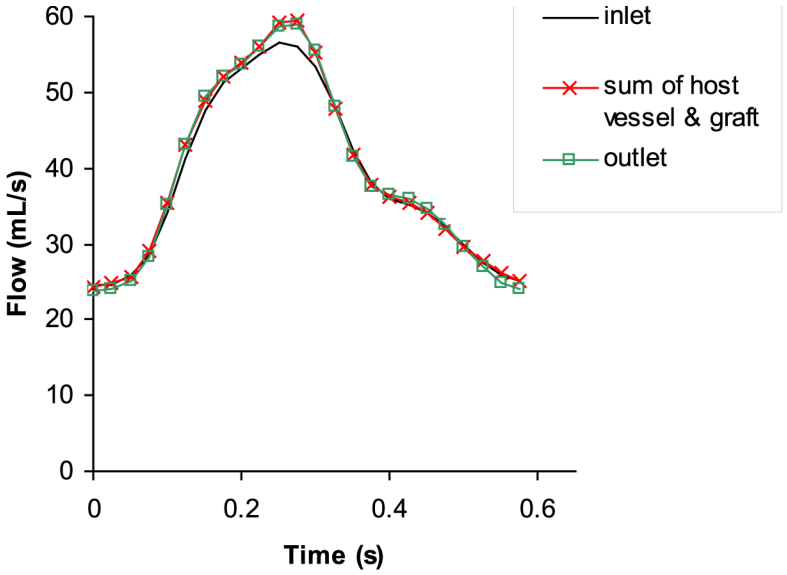


Figure 5.14: Comparison of PC-MRI measurements. The sum of the flows through the host vessel and through the graft should equal the flow at the inlet and the flow at the outlet.

5.4 Sensitivity of Numerical Simulations

As demonstrated in Section 4.6, variation in the inputs to the numerical simulations, such as the geometry or the inlet velocity boundary condition, can noticeably affect the simulation results. In Section 5.4.1, the differences in the numerical simulation results due to geometric variation are again assessed. The primary purpose of this comparison is not to determine whether or not significant changes in the velocity patterns will occur due to geometric variations—a question that was explored earlier in this thesis—but rather to discover how the simulation results would compare to the PC-MRI measurements under ideal circumstances. Section 5.4.2 then examines the role of the temporal and spatial averaging for this higher Reynolds number problem.

5.4.1 Effect of Geometry on Numerical Simulations

Figure 5.15 shows the two geometric models used in the numerical simulations. One was constructed from the MRA data using Geodesic, while the other model was based on the CAD drawing used to construct the physical model. The simulation run using the CAD-

based model was considered the gold standard. Quantitative comparisons of the two models were made using the model analysis tool described in Section 4.6.1.1, in which the equivalent circle radii were computed at 0.5 mm increments along different segments of the model. The results of this comparison, shown in Figure 5.16, indicate that the two models were very similar, more so than in the lower Reynolds number case. The radii of the coarctation, a key geometric feature, varied by only 0.13 mm on average, and there was only a slight variation in the radius upstream and downstream of the coarctation. Differences were apparent at the anastomotic junctions, and the radii of the bypass graft in the MRA-based model were smaller than those of the ideal CAD-based model.

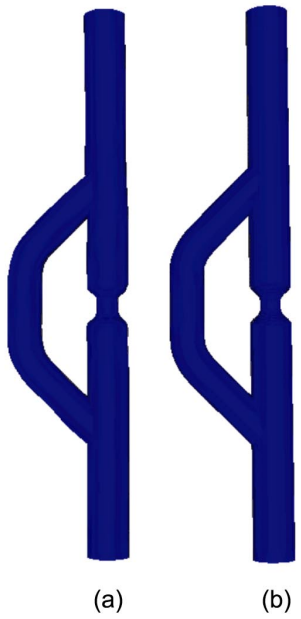


Figure 5.15: Comparison of geometric models (a) constructed from MRA data and (b) based on the CAD drawing. The CAD-drawing-based model is used as the gold standard in these comparisons.

The numerical simulation for the MRA-based model was run according to the procedure described in Section 5.1.3. For the ideal model, similar parameters were used: through-plane velocities along the direction of the user-defined axis were prescribed at the inlet; no-slip condition; zero pressure at the outlet; a rigid model; an incompressible Newtonian fluid with a density of 1.1 g/cm^3 and a viscosity of 0.036 dynes-s/cm^2; 480 time steps per cycle. The mesh size was 4.0 million elements, though, versus the 4.3 million elements for the simulation with the MRA-based model. The spatial and temporal averaging was the same for both simulations and was described in Section 5.1.4.

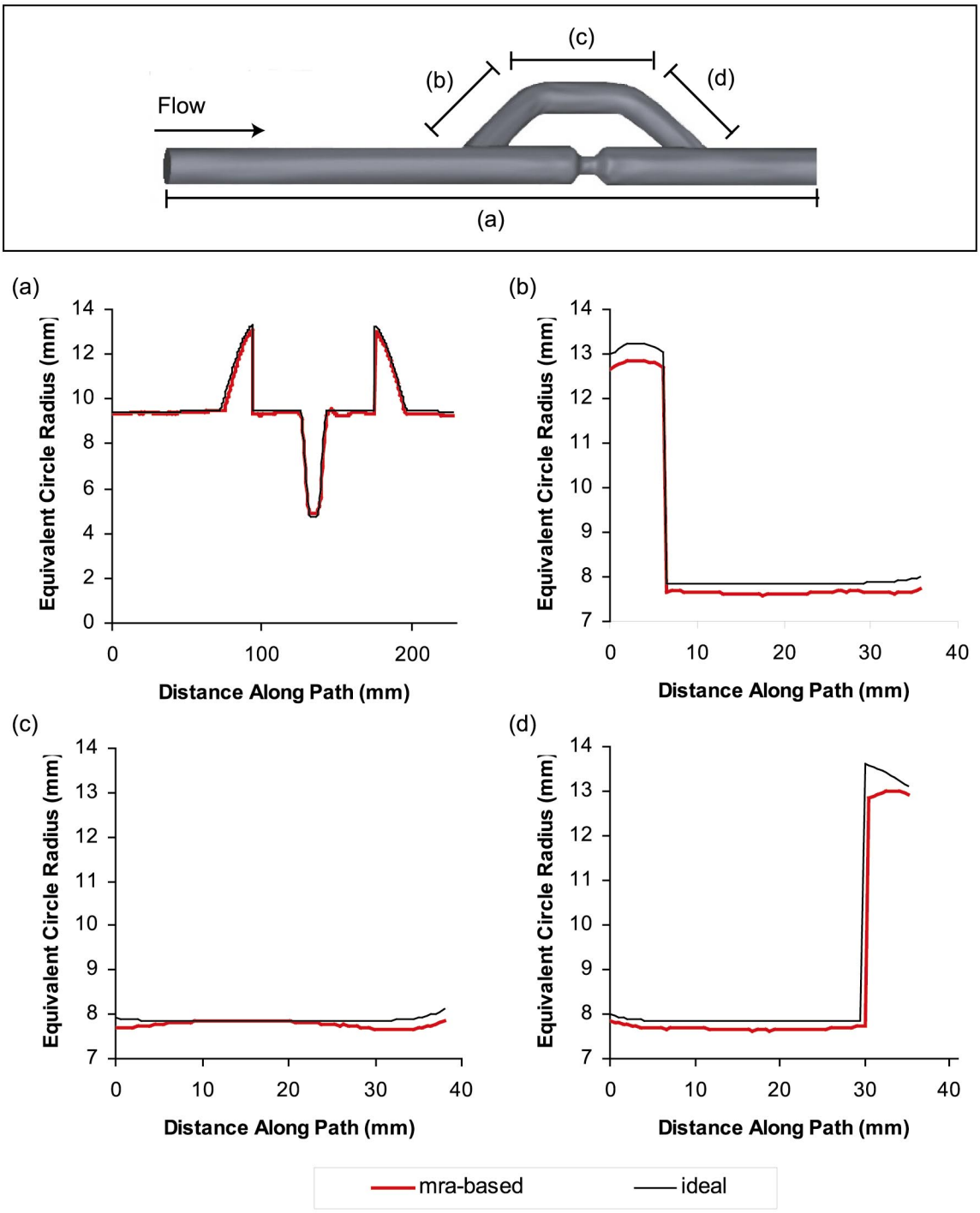


Figure 5.16: Quantitative comparison of two geometric models of the phantom. The equivalent circle radii along different segments of the model are plotted against the distance along the given segment for (a) the host vessel segment, (b) upstream graft segment, (c) straight graft segment, (d) downstream graft segment. The heavy red lines correspond to model (a), the MRA-based model, in Figure 5.15, while the black lines are from model (b), the CAD-based/ideal model, in that figure.

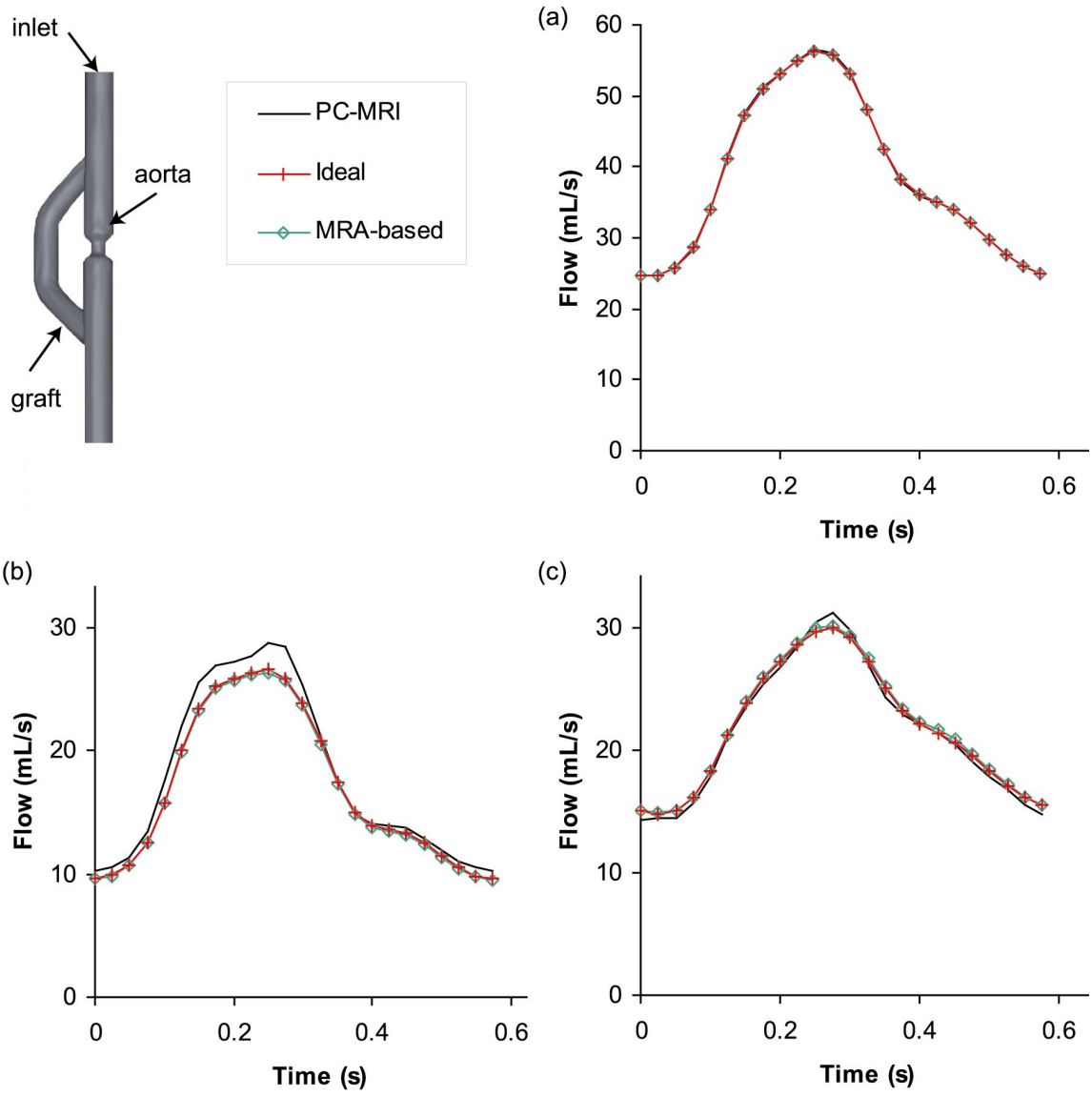


Figure 5.17: Comparison of flow waveforms measured with PC-MRI and those from the numerical simulations. The numerical simulations used either a CAD-based geometric model (ideal) or an MRA-based geometric model. (a) PC-MRI-measured flow at the inlet compared with prescribed flow at the inlet of the simulation. (b) Flow through the host vessel. (c) Flow through the bypass graft.

The similarity in the two geometric models was reflected in the flow distribution results, as seen in Figure 5.17. The flow waveforms computed from the numerical simulation results for the ideal model and for the MRA-based model were nearly identical, although they both differed from the PC-MRI measurements. In terms of average flow, the simulation using the MRA-based model predicted 16.7 mL/s through the host vessel and 21.8 mL/s through the bypass graft. The simulation using the ideal

model predicted 16.8 mL/s through the host vessel and 21.7 mL/s through the bypass graft. In contrast, the PC-MRI measurements of average flow were 17.8 mL/s through the host vessel and 21.4 mL/s through the bypass graft. So, the differences in the geometries produced no significant differences in terms of flow distribution.

On the other hand, minor differences do occur in the through-plane velocity patterns (see Figure 5.18 to Figure 5.22), depending on the geometric model used for the numerical simulations. However, the numerical simulations run with the ideal geometric model did not necessarily produce better agreement with the PC-MRI measurements than those run with the MRA-based model, as might be expected and as was found for the lower Reynolds number case. In fact, the comparisons varied. In some instances, such as during acceleration at the distal coarctation location or during peak flow at the bypass graft location, it could be argued that the isocontours based on the numerical simulations using the ideal geometry compared more favorably with the PC-MRI measurements than the numerical simulations using the MRA-based geometry. However, during acceleration and mid-deceleration at the outlet location, the converse could be argued, and during late-deceleration at the proximal coarctation location, there were no significant differences between the velocity patterns from the two simulations.

One of the more noticeable differences between the velocity patterns for the simulation based on the ideal geometry versus that based on the MRA data was at the downstream inlet and at the proximal coarctation locations, where the regions of peak velocity were smaller in area or non-existent for the ideal-geometry simulation. This was directly related to the method used to map the velocities onto the inlet mesh. In this case, the area of the inlet of the MRA model was 278.9 mm^2 and the area for the inlet of the ideal model was 285.0 mm^2. Since the segmentation for the PC-MRI data had an area of 274.6 mm^2 and the mapped velocities were scaled to produce a flow through the mesh that was equivalent to the PC-MRI computed flows, the mapped velocities for the ideal model were appreciably smaller than those for the MRA model. This difference in the inlet velocity pattern propagated downstream and could account for the lower peak velocities and/or smaller peak velocity areas for the ideal-geometry simulation. Therefore, while the overall geometry of the MRA-based model was a fairly accurate

representation of the phantom, resulting in velocity patterns similar to that of the simulations based on the ideal geometry, differences in the inlet area affected the magnitude of the velocities prescribed at the inlet and subsequently, the regions of peak velocities at slice locations near the inlet.

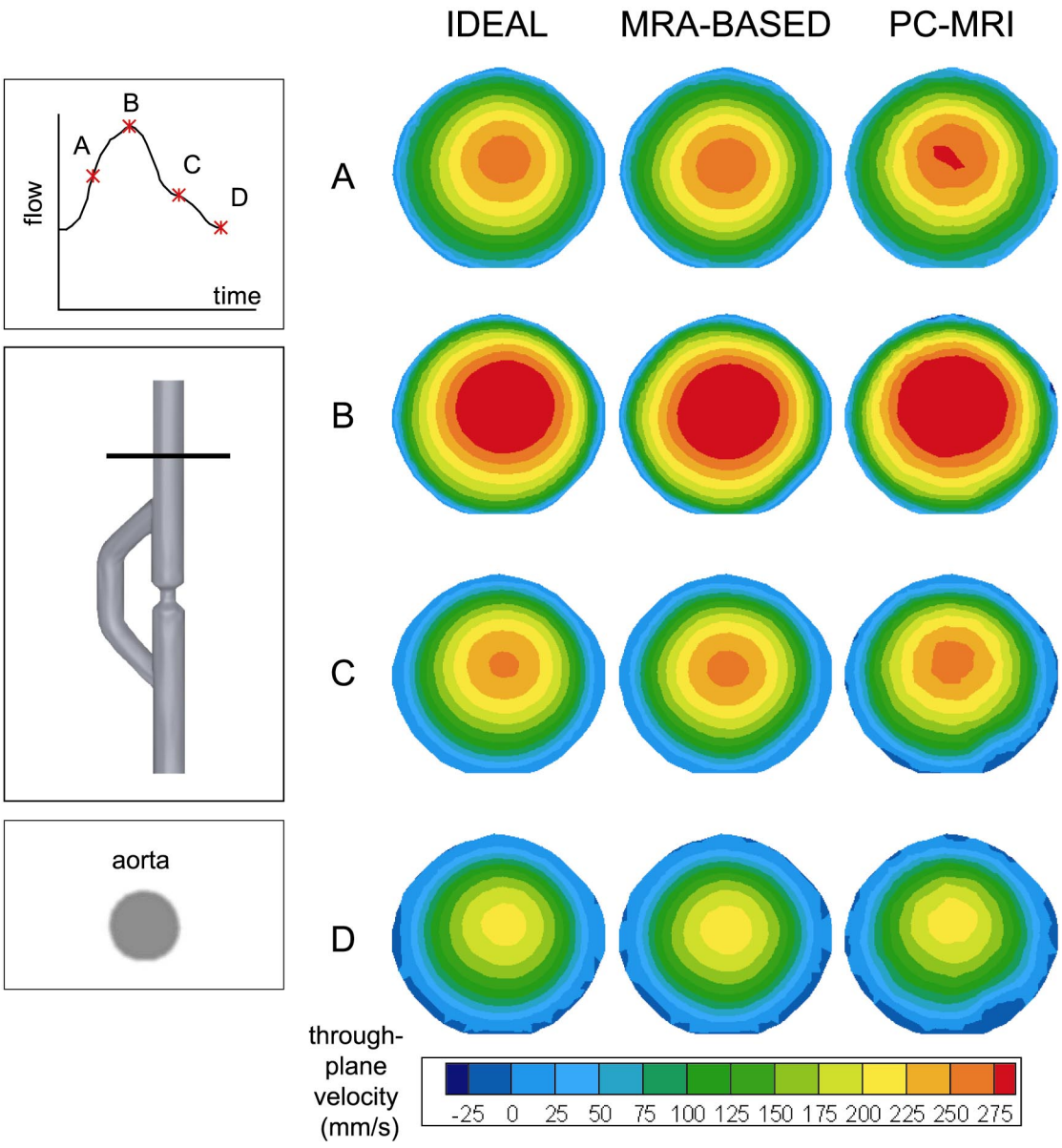


Figure 5.18: Comparison of through-plane velocity contours in the aorta proximal to the bypass graft, also referred to as the downstream inlet location (plane B), for two geometric models of the phantom: an ideal model based on the CAD drawings of the phantom and a model constructed from the MRA data. PC-MRI data is also presented for reference purposes. Results from four time points are shown: acceleration (A), peak flow (B), mid-deceleration (C), late-deceleration (D).

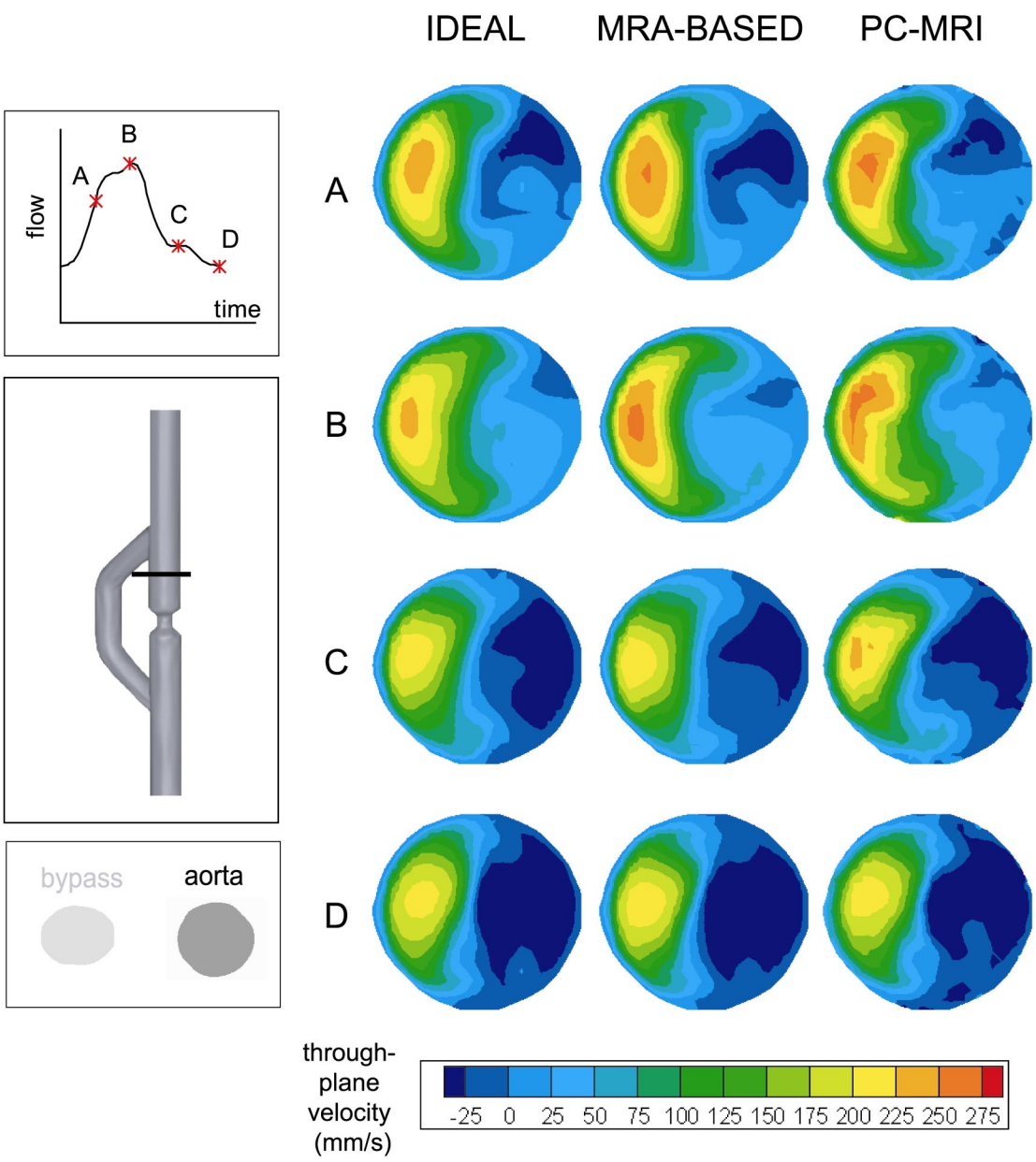


Figure 5.19: Comparison of through-plane velocity contours in the aorta proximal to the coarctation (plane C) for two geometric models of the phantom: an ideal model based on the CAD drawings of the phantom and a model constructed from the MRA data. PC-MRI data is also presented for reference purposes. Results from four time points are shown: acceleration (A), peak flow (B), mid-deceleration (C), late-deceleration (D).

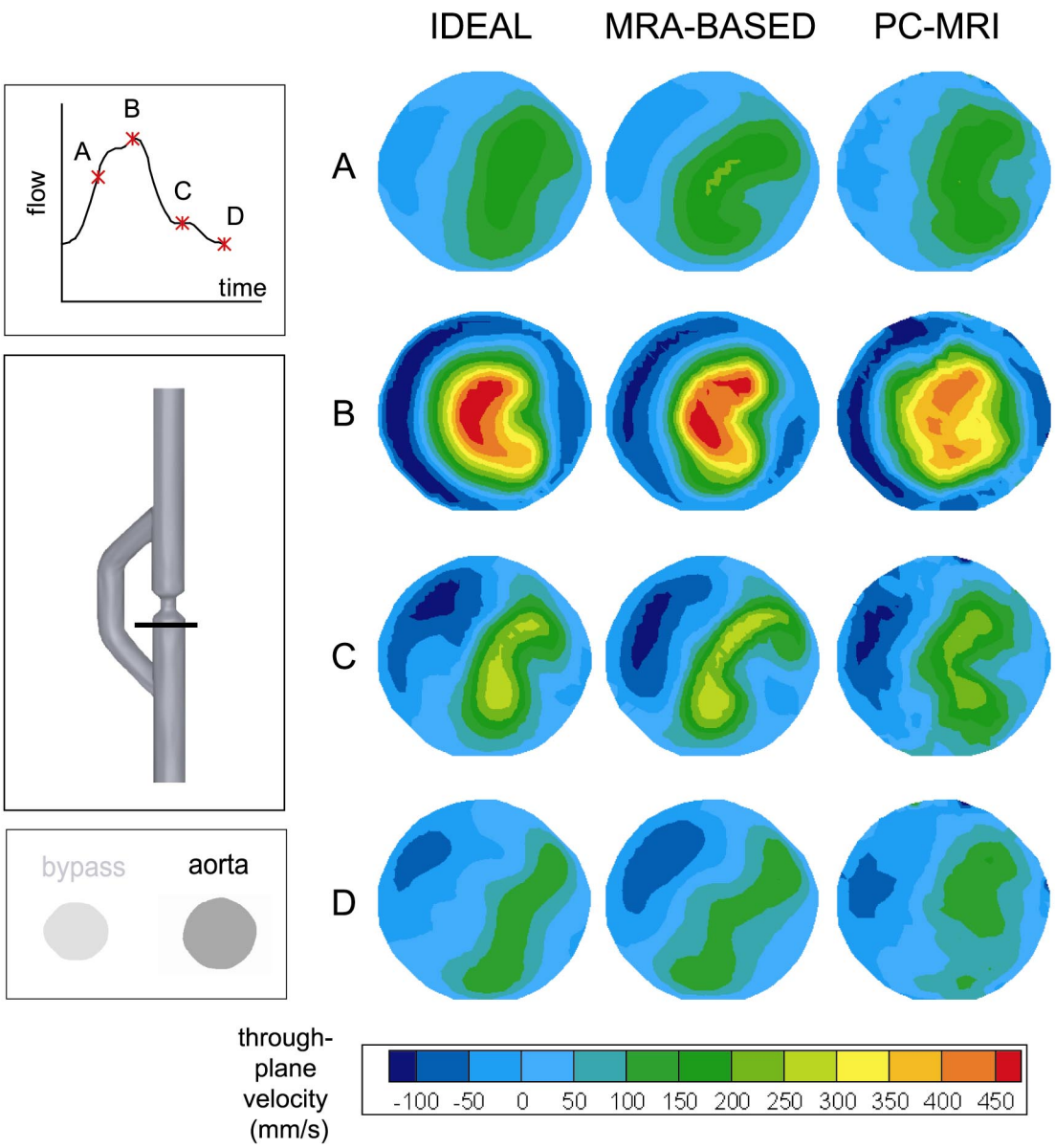


Figure 5.20: Comparison of through-plane velocity contours in the aorta distal to the coarctation (plane D) for two geometric models of the phantom: an ideal model based on the CAD drawings of the phantom and a model constructed from the MRA data. PC-MRI data is also presented for reference purposes. Results from four time points are shown: acceleration (A), peak flow (B), mid-deceleration (C), late-deceleration (D).

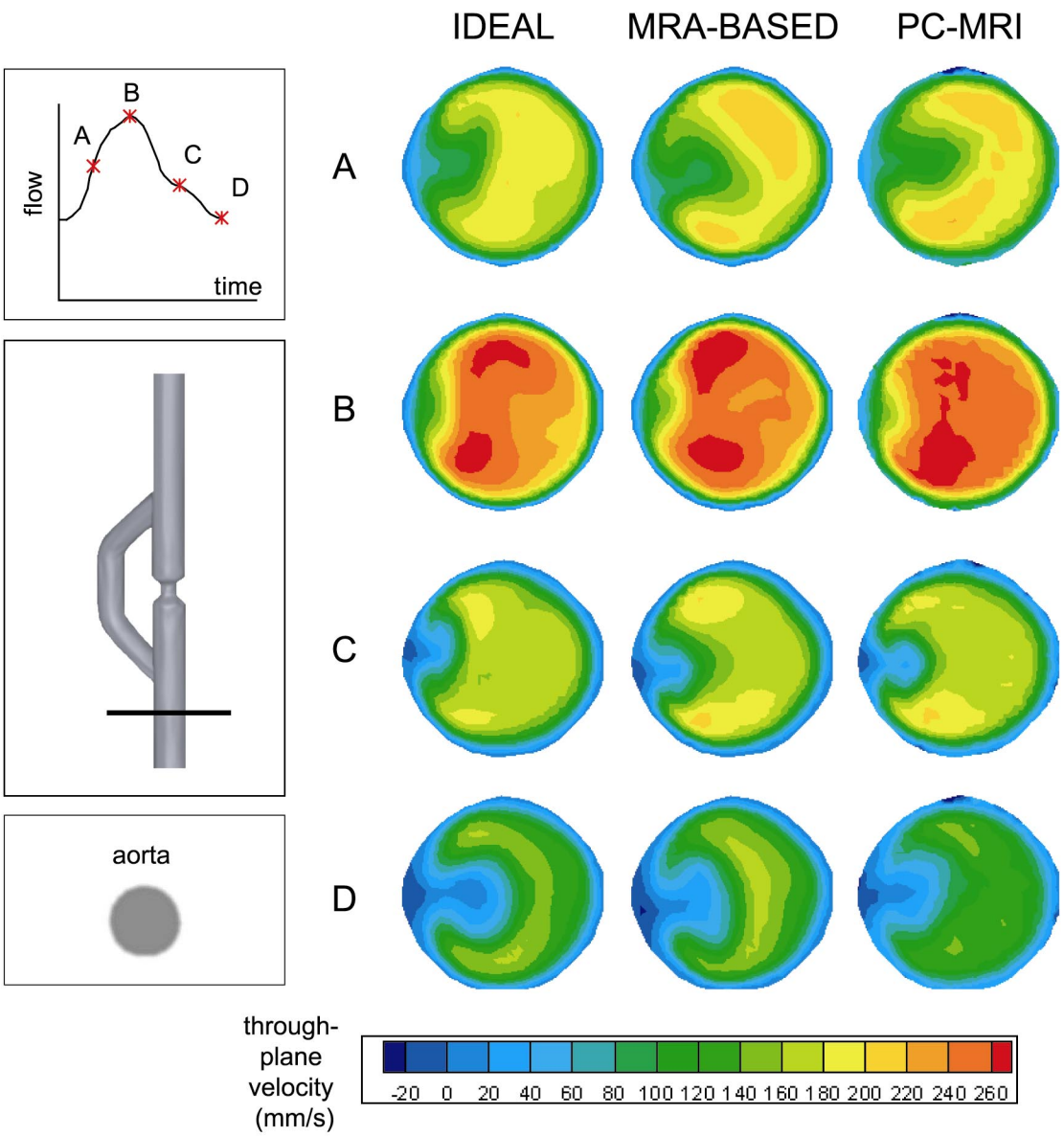


Figure 5.21: Comparison of through-plane velocity contours in the aorta distal to the bypass, also referred to as the outlet (plane E), for two geometric models of the phantom: an ideal model based on the CAD drawings of the phantom and a model constructed from the MRA data. PC-MRI data is also presented for reference purposes. Results from four time points are shown: acceleration (A), peak flow (B), mid-deceleration (C), late-deceleration (D).

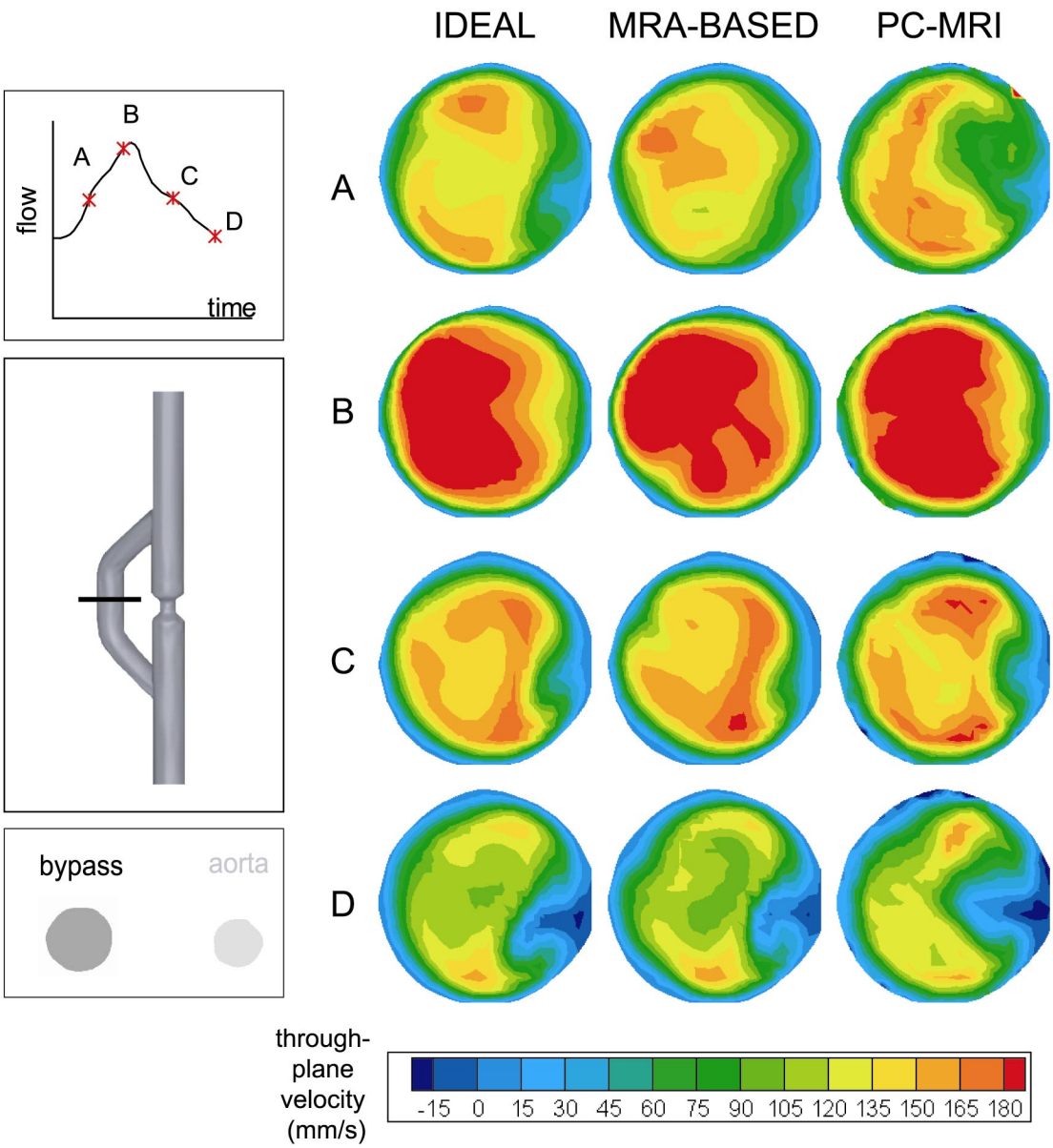


Figure 5.22: Comparison of through-plane velocity contours in the bypass graft (plane F) for two geometric models of the phantom: an ideal model based on the CAD drawings of the phantom and a model constructed from the MRA data. PC-MRI data is also presented for reference purposes. Results from four time points are shown: acceleration (A), peak flow (B), mid-deceleration (C), late-deceleration (D).

5.4.2 Post-Processing Effects on the Numerical Simulations

Because of the higher velocities and more complex velocity patterns that existed in this experiment, as compared to that described in Chapter 4, the spatial and temporal

averaging affected a larger number of the slice locations. The following comparisons use the simulation results described in Section 5.4.1 for the ideal, CAD-based model to examine specifically how these post-processing steps altered the through-plane velocity patterns.

Figure 5.23 illustrates the effect of spatial averaging. The through-plane velocity patterns are shown at the different locations for simulation results that have been temporally averaged over cycles 16 to 23. The black contour lines represent velocity isocontours from an average of 5 different slices: at the location of interest, 1.25 mm upstream and downstream of the location of interest, and 2.5 mm upstream and downstream of the location of interest. The color map shows results from a single slice at the location of interest. There was little difference between the color map and the black contour lines at most slice locations. As with the lower Reynolds number problem, some variation occurred at the distal coarctation slice location. This was expected, given that this location had the highest velocities observed in the model and therefore, the velocity patterns upstream and downstream of the location of interest would vary significantly. The spatial averaging also produced minor changes at the proximal coarctation and at the outlet locations, but the differences in the velocity patterns were not significant at any of these locations.

In contrast, the temporal averaging had a noticeable effect on the velocity patterns and their periodicity. Figure 5.24 compares the results of numerical simulations that have been averaged over eight cycles versus the results for a single cycle. Through-plane velocity isocontours are shown for 5 different slice locations during peak flow and late deceleration. These results were not spatially averaged but were taken from a single slice location. Two consecutive "periods" were plotted to assess the periodicity of the results. For the "single cycle" results, the color map represents velocities from cycle 9 and the black contour lines are velocities from cycle 10. For the "averaged cycle" results, the color map used velocities averaged over cycles 8 to 15, and the black contour lines were from the average of cycles 16 to 23.

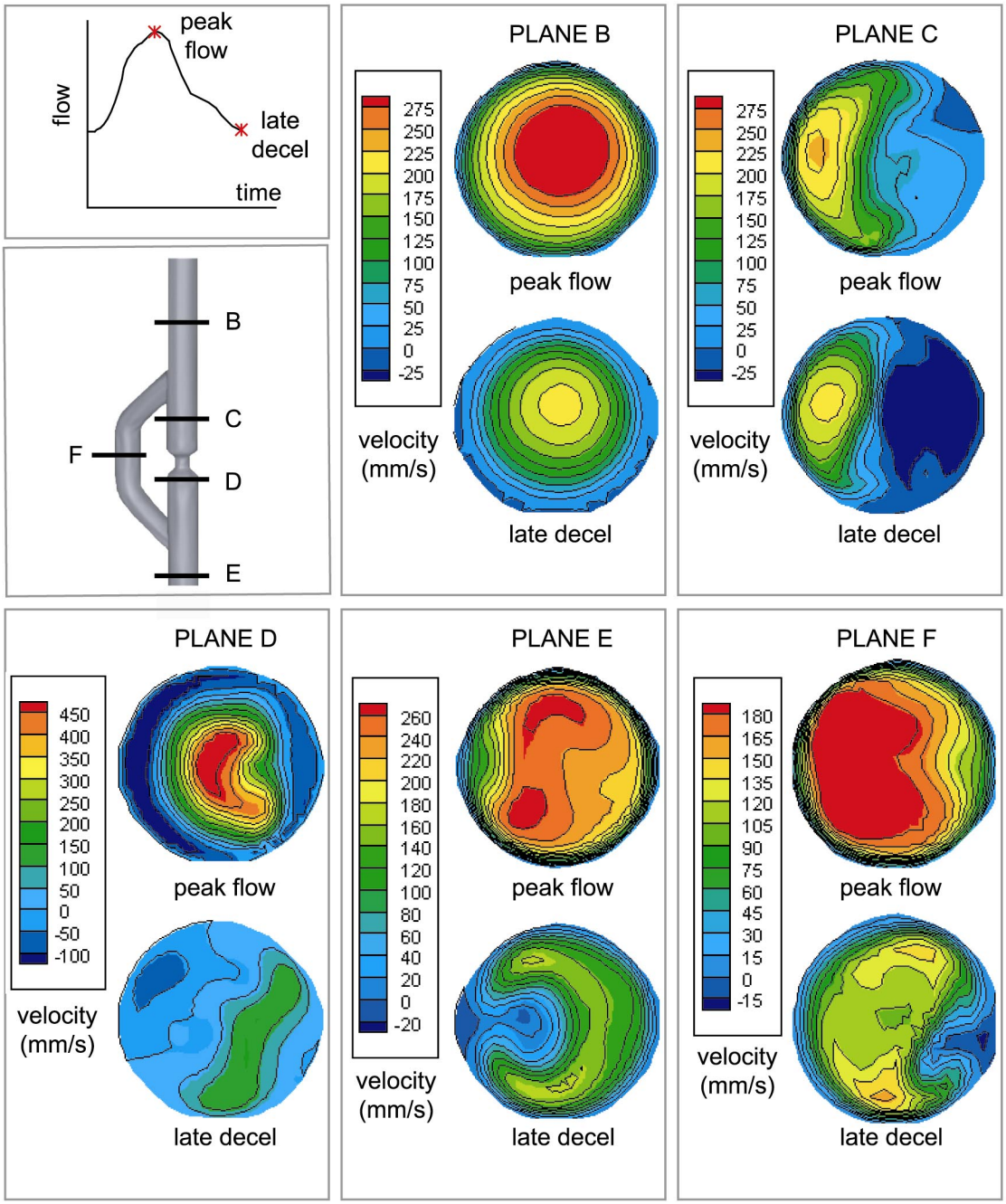


Figure 5.23: Comparison of through-plane velocity isocontour patterns with and without spatial averaging. Results are shown for peak flow and late deceleration (late decel) at 5 locations: downstream inlet (plane B), proximal coarctation (plane C), distal coarctation (plane D), outlet (plane E), and the bypass graft (plane F). The color maps are the results from a single individual slice, while the black contour lines are the velocity isocontours from an average of 5 different slices taken at the location of interest, 1.25 mm upstream and downstream of the location of interest, and 2.5 mm upstream and downstream of the location of interest.

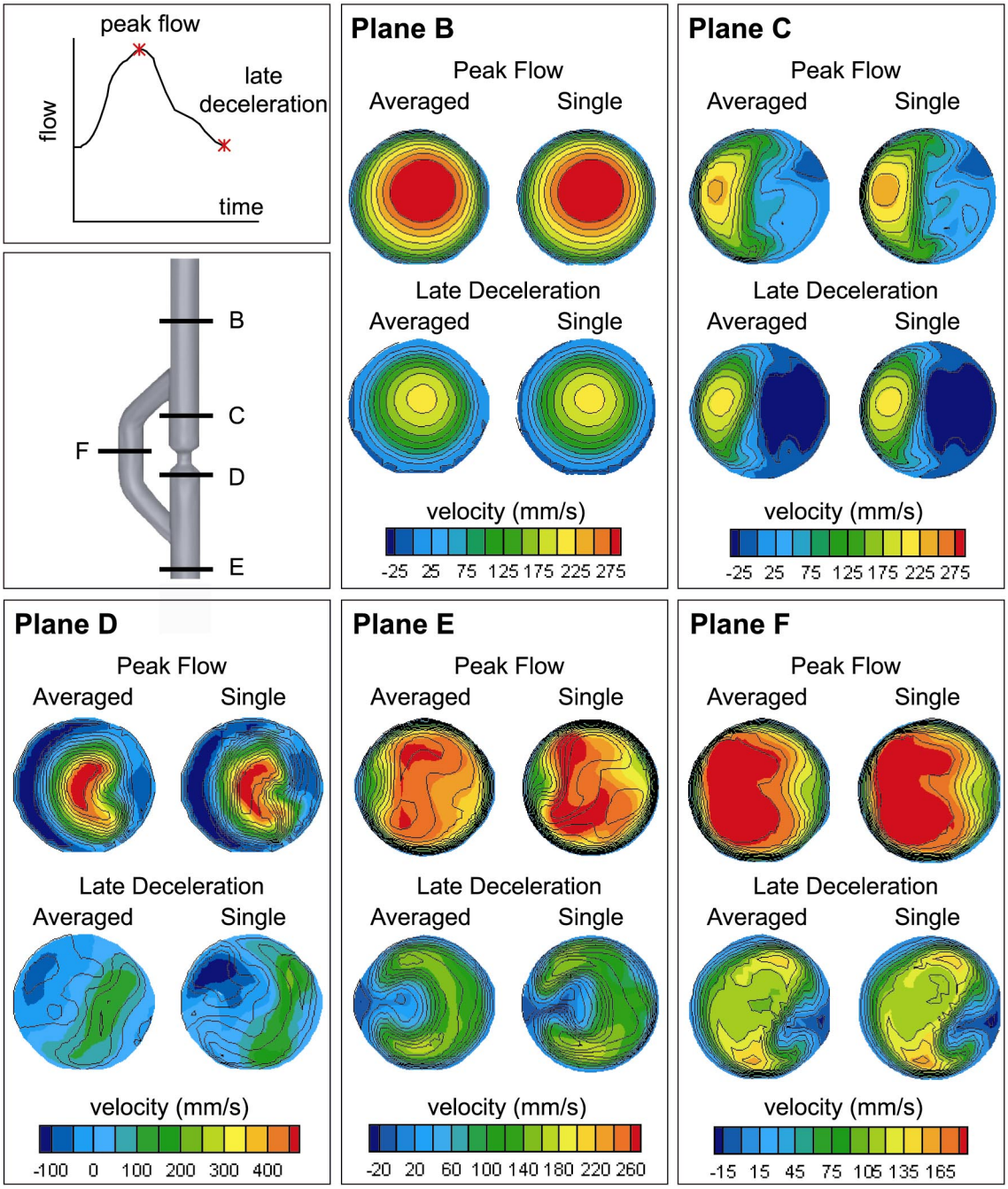


Figure 5.24: Effect of temporal averaging on the numerical simulation results. Through-plane velocity isocontours are shown for 5 different slice locations at peak flow and late deceleration. The "averaged" results represent velocities that have been averaged over 8 cycles, the color map showing results from the average of cycles 8 to 15 and the black contour lines showing results from the average of cycles 16 to 23. The "single" results are taken from one cycle of the simulation, with the color map being from cycle 9 and the black contour lines from cycle 10.

Unlike the lower Reynolds number case, the "single cycle" simulation results for all locations except for the downstream inlet (plane B) location were non-periodic. With temporal averaging, subtle changes were observed in the velocity patterns at the proximal coarctation (plane C) and at the bypass graft (plane F) locations, and the results were slightly more periodic than in the "single cycle" case. The changes were more dramatic at the distal coarctation (plane D) and at the outlet (plane E) locations. At these locations, the "single cycle" velocities displayed more non-periodicity than at the other locations. The temporal averaging significantly improved the periodicity of the velocity patterns at these locations, with the results from the average of cycles 8 to 15 and the results from the average of cycles 16 to 23 agreeing much more closely. However, some differences between the two sets of velocity patterns were still noticeable. Increasing the number of cycles that were averaged together and/or changing the starting cycle for the averaging could possibly further improve the periodicity of the velocity patterns.

5.5 Discussion

In Chapter 4, excellent agreement was found between the flow distributions and velocity patterns predicted using numerical simulations and those measured with PC-MRI. However, the average Reynolds number at the inlet of that experiment was only 255, on the lower end of the Reynolds numbers observed *in vivo* in the arterial system. The higher Reynolds number experiment described in this chapter had an average inlet Reynolds number of 766, thereby extending the range of *in vivo* conditions studied. Because of the higher Reynolds number flows, the velocity patterns observed in this experiment were much more complex than those of the lower Reynolds number problem, particularly distal to the coarctation where vortex shedding occurred. In general, the results were less periodic and less symmetric than in the lower Reynolds number case.

Nevertheless, there was still good agreement between the numerical simulation and the PC-MRI measurements. In terms of flow distributions, the difference between the numerical calculations and the PC-MRI measurements was 0.9 mL/s in the host vessel (where the measured flow was 17.8 mL/s) and 0.4 mL/s in the bypass graft (where the

measured flow was 21.4 mL/s). Comparisons of the flow waveforms showed that the largest differences occurred during peak flow. This could be due to changes in the flow pump output, causing the measured flow at the inlet to not match the measured flow at the outlet or the sum of the flows through the host vessel and the bypass graft. Flow enhancement effects, mentioned in Section 2.2.3.4.3, could also account for some of the differences.

The velocity pattern comparisons further demonstrated the ability of the numerical methods to produce results that match the PC-MRI measurements. At all five locations that were examined, the general through-plane velocity patterns were similar. Even in the regions where the flows were most complex, such as at the outlet and at the distal coarctation, there was remarkable agreement between the numerical simulations and the PC-MRI data. The region with the largest discrepancies was the bypass graft. It is unclear why this region would show the greatest mismatch, particularly since it was one of the locations least sensitive to the temporal and spatial averaging, indicating more stable velocity patterns. One possible explanation for the differences could be the change in the flow pump output, so that the velocity patterns acquired at the bypass graft differed from those that existed there when the inlet velocity profiles, which were prescribed at the inlet of the numerical simulations, were acquired. Another factor could be the curvature in this region, a geometric feature not observed elsewhere in this model. Lastly, recall that mesh independence and time step independence have not been established for these numerical simulations due to technical and resource limitations, so these results may not resemble the converged solution.

As with the lower Reynolds number problem, it was necessary to spatially and temporally average together the numerical simulation results in order to fairly compare them against the PC-MRI measurements. The effect of the spatial averaging was small, but the temporal averaging produced significant differences in the velocity patterns. Note that the original simulation results were non-periodic at all locations except the downstream inlet, making the temporal averaging more critical than in the lower Reynolds number problem where most locations were periodic. The non-periodicity for the higher Reynolds number problem was particularly evident at locations downstream of

the coarctation (e.g. the distal coarctation and the outlet locations), where instabilities in the shear layer can result in transitional and turbulent flow [134]. The temporal averaging did not achieve perfectly periodic velocity patterns, though, and changes in the number of cycles averaged together and/or the start cycle for the averaging could improve the periodicity of the velocity patterns.

Geometric sensitivity studies were also conducted for this experiment. However, in this case, the MRA-based and the ideal, CAD-based geometric models were similar, so no differences were observed in the flow distributions. In terms of the through-plane velocity patterns, the only appreciable difference was in the peak velocities for the locations closer to the inlet. This discrepancy was related to the method used to map the PC-MRI-measured velocities onto the inlet of the model. Differences between the areas of the PC-MRI data and the inlet mesh result in a scaling of the velocities mapped onto the inlet mesh. Therefore, inaccurate segmentation of the PC-MRI images and/or an inaccurate inlet geometry will produce errors in the prescribed inlet boundary condition.

5.6 Summary

The *in vitro* experiments described in Chapters 4 and 5 have addressed questions of what post-processing steps, if any, are needed to compare numerical simulation results to PC-MRI measurements, how sensitive the comparisons are to different input parameters, and, of most interest, how well the numerically computed results compare with the PC-MRI measured velocities under various flow conditions. The complex geometry, with the coarctation and the loop formed by the bypass and the host vessel, combined with the lower and higher inlet flows provided a more rigorous test of the numerical simulations than had previously been done. Moreover, these conditions encompassed a larger range of *in vivo* conditions than had been studied in the past.

Unlike an *in vivo* experiment, an *in vitro* experiment has limited or no exposure to errors due to physiologic variations and invalid assumptions, such as a rigid-walled vessel. Thus, it is easier to determine what other, more controllable factors affect the comparisons between the numerical simulations and PC-MRI. One critical realization

was the need for spatial and temporal averaging of the numerical simulation results in order to fairly compare them with PC-MRI measurements, which are acquired over a finite volume and multiple periods. Variations in the geometric model also affected the velocity patterns generated by the numerical simulations, with minor changes in the coarctation affecting the flow distribution, as well. Many of the differences observed in the geometric models could be attributed to the geometric reconstruction method of lofting together 2D segmentations. The numerical simulations were also sensitive to the prescribed inlet velocities. Inaccurate inlet velocities, whether due to noisy measurements or incorrect areas for the PC-MRI inlet and/or the inlet of the geometric model, altered the velocity patterns of regions near the inlet.

When conducting these *in vitro* experiments, careful attention to the set-up and data acquisition is key. Ideally, the input flow for these experiments is perfectly periodic, so that measurements taken from one time point are consistent with those taken from another time point. For the experiments described in Chapters 4 and 5, the pump output varied slightly during the course of the experiment, possibly accounting for some of the differences observed between the numerical simulations and the PC-MRI measurements. Differences in PC-MRI parameters, such as the field of view, the receive bandwidth, and v_{enc} can affect the SNR, and subsequently the quality of the images, while changes in T_R determine the temporal resolution.

By paying attention to all these factors, it was possible to achieve good agreement between the numerical simulations and the PC-MRI measurements in terms of both flow distribution and through-plane velocity patterns. This was demonstrated through comparisons under two different inlet conditions at five different locations in the model, each with distinct flow characteristics, thus providing a comprehensive assessment of the accuracy of the numerical simulation results. The results of these experiments suggest that numerical methods can be used to accurately model blood flow distributions and velocity patterns *in vivo*. Studies which incorporated more physiologically accurate components, such as a compliant vessel, a non-Newtonian fluid, and significant in-plane velocities at the inlet, could further strengthen this idea, as would comparisons against techniques that provided instantaneous velocity measurements.

Chapter 6

In Vivo Experiment

Under the most rigorously controlled conditions of pressure, temperature, volume, humidity, and other variables, the organism will do as it damn well pleases. ~Harvard Law

In vitro experiments are suitable for the initial validation of a new method, but *in vivo* validation studies are needed in order to fully assess the usefulness of a new method. While the experiments described in Chapters 4 and 5 demonstrated that numerical simulation methods can accurately predict both flow rates and velocity profiles in a complex geometry, such as that of a stenotic vessel with a bypass, they did not replicate the compliant nature of blood vessels or the non-Newtonian shear-thinning behavior of blood. Moreover, conditions could be controlled in the *in vitro* experiment, so that there was minimal variation in parameters, such as the flow periodicity. In animals, conditions are much more complex and variable, prompting the need for *in vivo* experiments. In this chapter, the results of a series of porcine studies designed to test the accuracy of the numerical simulation methods for an arterial bypass graft in the thoracic aorta are described. Section 6.1 explains the experimental protocol, while Section 6.2 compares the flow and velocity measurements acquired with PC-MRI to those generated by the numerical simulation. Lastly, Section 6.3 investigates physiologic differences that exist, depending on whether the bypass is open or closed, situations which simulate post-operative and pre-operative conditions, respectively.

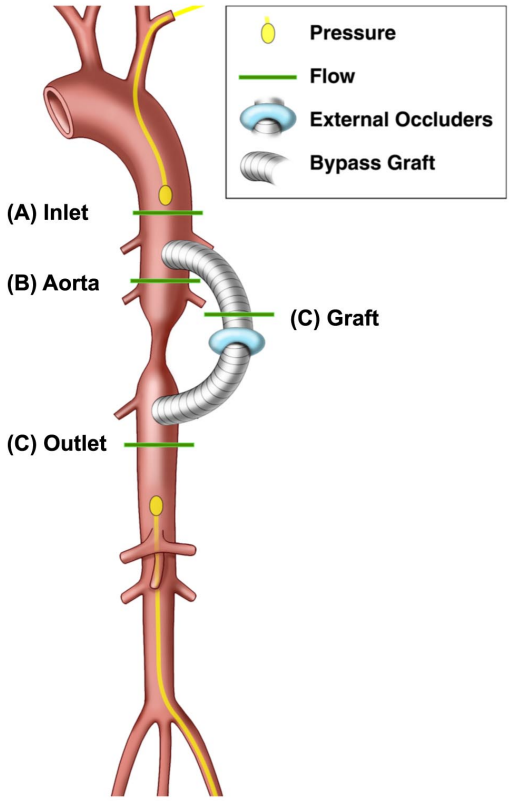


Figure 6.1: Diagram of the *in vivo* experiment protocol. A thoraco-thoraco aortic bypass procedure was performed to bypass an 80-95% constriction of the descending thoracic aorta in the pig. An external occluder was placed around the bypass and could be inflated to constrict the bypass to simulate pre-operative conditions. Pressure catheters were placed both upstream and downstream of all imaging locations. Flow measurements were acquired using phase contrast magnetic resonance imaging at the four locations indicated. The inlet flow measurements were used as boundary conditions for the numerical simulations, while the flow rates at the other locations were used for validation of the numerical simulations.

6.1 Experimental Protocol

Pigs were chosen for this experiment because they resemble humans in terms of cardiovascular anatomy and hemodynamics [135]. Fifteen Yorkshire cross pigs were used in this investigation, of which the results from eight of the pigs (36.5 to 48 kg) are presented here. Two of the pigs died during surgery: one due to a slow leak in the intubation tube [136] and one due to pulmonary atelectasis, likely due to over-hydration with fluid therapy [137]. A third pig was physiologically unstable with heart rates up to 140 bpm, and data under only one of the two desired conditions was acquired for one of

the pigs due to a broken occluder [136]. Issues such as poor gating, RF noise, and bugs from software changes produced unusable imaging data in three of the experiments.

All animal procedures were approved by and performed in accordance with the policies set by the Institutional Animal Care and Use Committee. In each of the pigs, an aortic coarctation was created, and a graft was anastomosed to the thoracic aorta proximally and distally to bypass the coarctation (Figure 6.1). This model resembles surgical bypasses of severe stenoses in patients using proximal and distal end-to-side anastomoses. Section 6.1.1 describes the surgical procedure, while Section 6.1.2 explains how the velocity data was acquired and Section 6.1.3 explains the measurement techniques used for acquiring the pressure data.

6.1.1 Surgical Procedure

Each animal was pre-anesthetized with telazol (5 – 7 mg/kg, IM) mixed with atropine (0.05 mg/kg) prior to endotracheal intubation. Animals were anesthetized with isoflurane (1 – 4 %) during the entire procedure, and ventilation was mechanically controlled. With the animal in a supine position, a longitudinal midline incision in the neck was used to isolate the internal jugular vein and common carotid artery. Arterial and venous access was obtained with 7F sheaths for monitoring purposes. A longitudinal incision in the right groin was used to isolate the common femoral artery that was accessed with a 7F sheath. A left anterolateral thoracotomy was performed and the descending thoracic aorta from the azygos vein to the diaphragmatic hiatus was exposed. Beginning with the fourth experiment, the paralytic pancuronium bromide (0.11 mg/kg) was administered prior to the thoracotomy. A 150 to 300 IU/kg intravenous bolus of heparin sulfate was given to achieve an activated clotting time (ACT) greater than 250 seconds. The ACT was monitored every 30 minutes, and additional heparin was given as needed to maintain the ACT greater than 250 seconds. A side-biting vascular clamp was used to partially occlude the proximal thoracic aorta. An end-to-side anastomosis between the aorta and an 8-10 mm-diameter polyester fabric (Dacron) vascular graft was performed with a fine-running monofilament suture. The distal end of the graft was anastomosed to the distal descending thoracic aorta in a similar fashion. A polyester (Dacron) umbilical tape was

tied around the thoracic aorta midway between the two anastomoses to create an 80 – 95% stenosis. Also, for the experiments C through H, any noticeable intercostal arteries in the surgical region were ligated using suture material to try to maintain flow conservation between the inlet and outlet imaging regions.

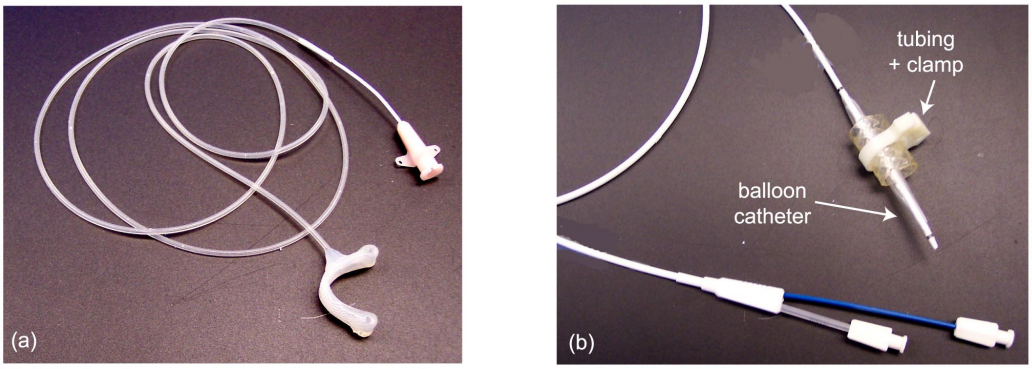


Figure 6.2: External occluders used to control whether the bypass graft was open or closed. (a) A commerically available occluder. (b) A custom occluder which used a balloon catheter inside of tubing and a snap-grip hose clamp to control the occlusion of the graft.

An external occluder was placed around the bypass graft to control whether the graft was open or closed. Injection of water caused the occluder to inflate and close off the Dacron graft, simulating a pre-operative situation in which blood can only flow through the native, stenosed aorta, while withdrawing water from the occluder caused it to deflate and allow blood to flow through the open graft, thus mimicking a post-operative situation. Two different methods were used to occlude the graft. Of the eight experiments with usuable data, two of them (pigs A and B) utilized a commercially available vascular occluder (Harvard Apparatus, Inc., Holliston, MA), depicted in Figure 6.2(a), which was placed around the graft; however, these had a tendency to burst. As a result, in the other six experiments, a custom occluder composed of a balloon catheter, rigid tubing, and a snap-grip hose clamp was used (Figure 6.2(b)). The rigid ring, composed of the tubing and clamp, secured the balloon catheter against the Dacron graft and was slipped onto the bypass graft prior to attaching the distal end of the graft to the descending thoracic aorta. The thoracotomy incision was then sutured closed.

Pressure catheters (Model SPC-350, Part Number 800-4019, Millar Instruments, Inc., Houston, TX), described further in Section 6.1.3, were inserted through the 7F sheaths in

the common femoral artery and the carotid artery and positioned in the thoracic aorta, distal and proximal to the bypass, respectively. Fluoroscopy was used to ensure correct positioning of the catheters. The animal was then transported to the MRI suite while still monitored and ventilated under general anesthesia. Throughout both the surgery and the imaging, epinephrine and fluids were administered to maintain the pig in a stable condition.

6.1.2 Magnetic Resonance Imaging

Both vascular geometry and blood flow measurements were acquired using a 1.5 T MRI system (Signa, GE Medical Systems, Waukesha, WI). A wrap-around phased array coil was placed around the animal's abdomen for signal reception, and a respiratory sensor was wrapped around the animal's chest for monitoring respiration. The animal was placed in the magnet in the right decubitus position. Two-dimensional localizer images were obtained for spatial localizations of the subsequent scans.

	BYPASS OPEN T_R (in ms) / T_E (in ms) / v_{enc} (in cm/s)				BYPASS CLOSED T_R (in ms) / T_E (in ms) / v_{enc} (in cm/s)		
	Inlet	Aorta	Graft	Outlet	Inlet	Aorta	Outlet
A	7.7/3.3/150	8/3.5/150	8/3.4/150		7.7/3.3/200	8/3.5/200	8/3.5/500
B	7.9/3.5/150	8/3.5/150	7.9/3.5/200	8/3.5/350	7.9/3.5/150	8/3.5/150	8/3.5/350
C							
D	7.3/3.3/150	7.3/3.3/150	7.4/3.3/250	7.3/3.3/250	7.3/3.3/150	7.2/3.2/250	7.3/3.3/350
E	7.5/3.4/150	7.4/3.4/150	7.3/3.3/250	7.5/3.5/200	7.5/3.4/150	7.4/3.4/150	7.5/3.5/250
F	7.5/3.5/150	7.4/3.4/150	7.2/3.2/250	7.5/3.5/250	7.5/3.5/150	7.4/3.4/150	7.5/3.5/300
G	7.5/3.5/150	7.5/3.4/150	7.5/3.4/200	7.5/3.5/150	7.5/3.5/150	7.5/3.4/150	7.5/3.5/350
H	7/3.2/150	7.1/3.3/150	7.1/3.3/250	7.1/3.3/250	7/3.2/150	7.1/3.3/150	7/3.3/250

Table 6.1: Imaging parameters for segmented k-space PC-MRI data. The left-most column specifies the animal. The middle columns provide the imaging parameters for data collected at the four different locations with the bypass open. The right columns are the imaging parameters for data collected at three locations with the bypass closed. Each entry lists 3 numbers: T_R (in ms) / T_E (in ms) / v_{enc} (in cm/s). Blank entries indicate that segmented k-space data was not collected for that animal at that imaging location.

	BYPASS OPEN T_R (in ms) / T_E (in ms) / NEX				BYPASS CLOSED T_R (in ms) / T_E (in ms) / NEX		
	Inlet	Aorta	Graft	Outlet	Inlet	Aorta	Outlet
A							
B					30/6.34/2		
C	34/4.25/1	34/4.25/1	25/3.96/1	34/4.25/1	34/4.25/2	38/5.79/2	34/4.25/1
D	19/9/2	19/8.77/1		19/8.62/1	19/9/2	19/8.62/1	19/8.58/1
E	25/8.77/2				25/8.58/2		
F	30/8.77/2				30/8.77/2	30/8.77/2	30/8.77/2
G	30/5.03/2	30/5.03/1	30/4.94/1		30/5.03/2	30/5.03/1	
H	30/5.03/2	30/5.03/2	30/5.03/2	30/5.03/2	30/5.03/2	30/5.03/2	30/4.94/2

Table 6.2: Imaging parameters for 2D cine PC-MRI data. The left-most column specifies the animal. The middle columns provide the imaging parameters for data collected at the four different locations with the bypass open. The right columns are the imaging parameters for data collected at three locations with the bypass closed. Each entry lists 3 numbers: T_R (in ms) / T_E (in ms) / NEX. Blank entries indicate that 2D cine data was not collected for that animal at that imaging location.

	BYPASS OPEN in-plane v_{enc} (cm/s) / through-plane v_{enc} (cm/s)				BYPASS CLOSED in-plane v_{enc} (cm/s) / through-plane v_{enc} (cm/s)		
	Inlet	Aorta	Graft	Outlet	Inlet	Aorta	Outlet
A							
B					50/150		
C	50/150	50/150	100/250	50/250	50/150	100/150	50/450
D	30/150	50/150		80/250	30/150	80/250	100/250
E	50/150				100/150		
F	50/150				50/150	50/150	50/150
G	50/150	100/150	100/250		50/150	50/150	
H	50/150	50/150	50/150	50/150	50/150	50/150	50/250

Table 6.3: Velocity encodings for the 2D cine PC-MRI data. The left-most column specifies the animal. The middle columns provide the imaging parameters for data collected at the four different locations with the bypass open. The right columns are the imaging parameters for data collected at three locations with the bypass closed. Each entry lists 2 numbers: in-plane v_{enc} (cm/s) / through-plane v_{enc} (cm/s). Blank entries indicate that 2D cine PC-MRI was not collected for that animal at that imaging location.

Anatomic and physiologic data were acquired first with the bypass graft open. The bypass graft was then occluded, and a second set of images was acquired. The contrast-enhanced magnetic resonance angiography (CE-MRA) data was obtained using a rapid, three-dimensional, gradient-recalled echo sequence [128]. A 0.2 mmol/kg dose of Magnevist (Berlex Laboratories, Wayne, NJ), a gadolinium-based contrast agent, was injected into the animal via the 7F sheath in the internal jugular vein at a rate of 2.5 to 3 cc/s. A pre-timing scan was performed to ensure that the acquisition occurred during maximum concentration of contrast in the thoracic aorta. The image acquisition was performed during suspended respiration with T_R = 3.76 to 4.9 ms depending on the field of view (FOV= 24 to 32 cm), T_E = 0.90 to 1.07 ms, a maximum slice thickness of 3.0 mm zero-filled to produce 1.5 mm between slice centers, an acquisition matrix size of 512x192, and a 25-degree flip angle. Between 80 and 100 slices were acquired in the axial direction.

Two methods were used to acquire the velocity information: a 2D cine phase contrast sequence [77, 78] which was used to acquire three orthogonal components of velocity and a 2D segmented k-space sequence [79-81] with a higher temporal resolution and shorter total scan time. The segmented k-space sequence was acquired with T_R = 7 to 8 ms, T_E = 3.2 to 3.5 ms, FOV=24 cm, 5 mm slice thickness, 256x192 acquisition matrix, 4 k-space lines per cardiac cycle, NEX (number of excitations) = 1, 30 degree flip angle, and a 31.25 kHz bandwidth. For images acquired with the bypass open, the flow encoding used to acquire the velocity component along the vessel axis ranged from ±150 cm/s to ±350 cm/s. In the bypass-closed state, the flow encoding varied from ±150 cm/s to ±550 cm/s. Respiration was suspended during these scans. The parameters for the 2D cine phase contrast sequence were: respiratory compensation, oversampling to prevent spatial aliasing (no phase wrap), T_R = 19 to 38 ms, T_E = 4.0 to 9.0 ms, 24 cm FOV, 5 mm slice thickness, acquisition matrix of 256x256 (except for Pig E which used an acquisition matrix of 256x192), 16 kHz bandwidth, NEX = 1 or 2, and a 20-degree flip angle. The through-plane velocity encoding was between ±150 cm/s and ±250 cm/s for the bypass-open state and between ±150 cm/s and ±450 cm/s for the bypass-closed state. For the in-plane velocity encoding (v_{enc}) [138], values were between 50 cm/s and 100

cm/s for images acquired with the bypass open, while they varied between 30 cm/s and 100 cm/s for images acquired with the bypass closed. For both methods, 24 time points per cardiac cycle were reconstructed, and velocity acquisitions were synchronized using the signal from a photoplethysmograph attached to the animal.

For the bypass-open state, velocity information was acquired at four locations: superior to the graft (inlet), between the proximal anastomosis and the aortic coarctation (aorta), in the graft (graft), and distal to the graft (outlet) (Figure 6.1). Data was also acquired at the inlet, aorta, and outlet for the bypass-closed state. A segmented k-space acquisition was used to acquire this data for all of the animals, except for Pig C, for which only the 2D cine PC-MRI data was usuable. Time permitting, 2D cine PC-MRI data was also collected, in addition to the segmented k-space data. Table 6.1 through Table 6.3 indicate which imaging planes were acquired for each experiment and provide details about the imaging parameters that were used.

6.1.3 Pressure Measurements

6.1.3.1 Set Up and Data Acquisition

A strain-gauge-based manometer, the Millar Mikro-tip 5F, 120 cm long catheter pressure transducer (Model SPC-350, Part Number 800-4019, Millar Instruments, Inc., Houston, TX), was utilized to acquire pressure measurements for the experiments presented here. In this catheter pressure transducer, the pressure sensor is mounted on the side of the catheter tip, thus measuring lateral pressure, instead of end-on pressure, which is subject to errors from the kinetic energy of the fluid [70]. This transducer is capable of measuring pressures in the range of –50-300 mmHg, has a nominal sensitivity of 5 μV/V/mmHg, and has a flat frequency response up to 10 kHz, so that it can accurately sample pressures at rates as low as 0.1 ms/sample [139].

The pressure transducers were connected to a control unit box, which output a voltage corresponding to the pressure. The output of the control unit boxes were connected through a control panel in the MR scanner room to a data acquisition (DAQ) module (DAQPad-6020E, National Instruments, Austin, TX) located in the MR control room.

The voltages were sampled at a rate of 100 samples/second and with 12-bits of resolution. A LabVIEW program (LabVIEW v.6 and v.6.1, National Instruments, Austin, TX) running on a Dell Inspiron 8000 laptop computer (Dell Computer Corporation, Round Rock, TX) was used to record the data (Figure 6.3).

Pressure data was acquired periodically throughout both the surgery and imaging portions of the experiment. For each experiment, at least four data sets were acquired: at the beginning and end of the PC-MRI imaging with the bypass open, and at the beginning and end of the PC-MRI imaging with the bypass closed.

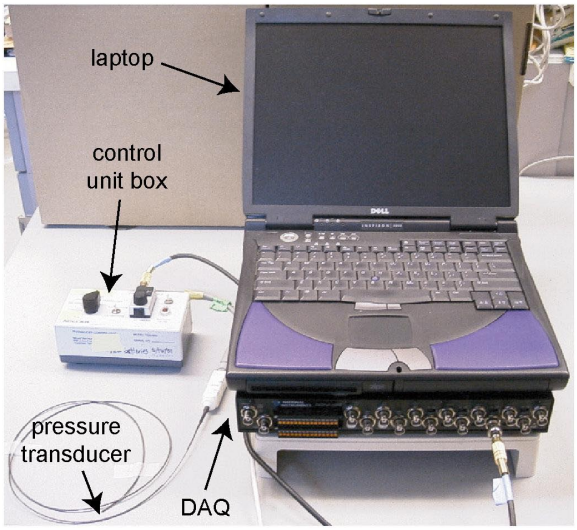


Figure 6.3: Equipment set-up for acquiring pressure measurements. The catheter pressure transducer is placed in the vessel of interest. The measured pressure signal is converted to a voltage by the control unit box. The DAQ board samples the voltage from the control unit box and sends the resulting waveform to the laptop to be viewed and/or saved to a file.

6.1.3.2 Calibration

Both the control unit boxes and the catheter pressure transducers were calibrated prior to use. The control unit box was calibrated by setting it for a conversion factor of 1 volt/100 mmHg. After putting the control unit box in STANDBY 0 mode, the mean voltage reading was recorded using the LabVIEW program. The transducer balance was then adjusted so that the mean measured value was 0. As an additional check, the control unit box was set to 20 mmHg and 100 mmHg. The corresponding readings in LabVIEW should be 0.200 and 1.00 volts, respectively.

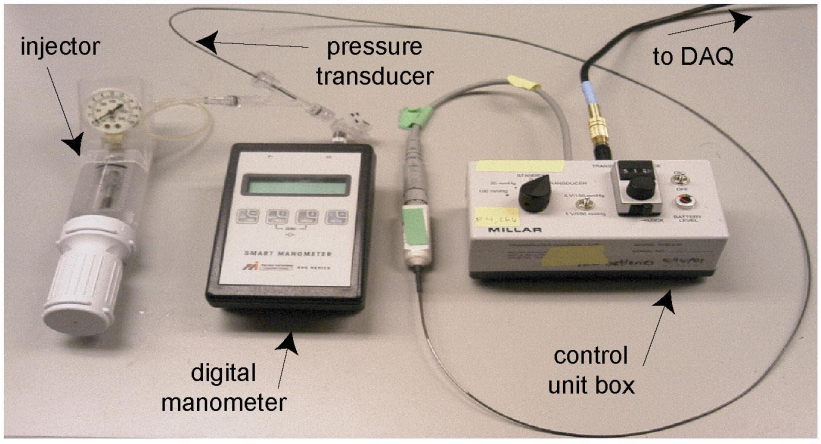


Figure 6.4: Set-up for pressure transducer calibration. Pressure measurements were made with the pressure transducer and compared against the corresponding measurements taken with the digital manometer. A handheld injector was used to change the pressure being measured.

Before calibrating the pressure transducers, they were soaked in de-ionized water at room temperature for 30 minutes to minimize drift. Simultaneous pressure measurements were acquired with both the pressure transducer and an independent digital manometer (350 Smart Manometer, Meriam Instrument, Cleveland, OH). The digital manometer has an accuracy of 0.05% of full scale [140] and was zeroed at atmospheric pressure. A handheld injector was used to manually adjust the pressure values from 0 to 100 mmHg (Figure 6.4). To capture potential hysteresis effects, pressure measurements were made in the 0 to 100 mmHg direction, as well as in the 100 to 0 mmHg direction. The pressure transducer voltages were plotted against the digital manometer measurements and a linear fit was determined. The coefficients of the linear fit were then used to convert the subsequent pressure transducer voltage measurements into units of mmHg. This calibration was performed prior to each experiment that used the pressure transducer.

6.2 Validation of Numerical Simulation Methods

Two sets of simulation results based on the bypass-open data were evaluated: one to predict flow rates and flow distributions, and one to analyze velocity patterns. Section 6.2.1 discusses the eight simulations that were analyzed for flow rate and flow

distribution predictions, while Section 6.2.2 focuses on initial results evaluating the numerically computed velocity patterns.

6.2.1 Predicting Flow Rates and Flow Distributions

6.2.1.1 Methods

In the following simulations and comparisons, the segmented k-space data was used for all pigs except for pig C, for which only 2D cine PC-MRI data was available.

6.2.1.1.1 Numerical Simulations

The process for generating the numerical flow solutions is depicted in Figure 6.5. Using the CE-MRA data, geometric models of the thoracic aorta and the bypass graft were constructed with Geodesic, as described in Section 2.3.3.1. A spline-fit through five to ten manually selected points described paths through the vessels of interest. Two-dimensional slices were oriented perpendicular to these paths, and the level set method was applied to each of these slices to segment out the vessel lumen. Non-uniform rational B-spline (NURB) surfaces were lofted through the cross-sections and bounded to create a solid model using the Parasolid (Unigraphics Solutions, St. Louis, MO) geometry kernel. This process was used to create solid models of the aorta and the bypass, which were then joined together to construct a final geometric solid model. The PC-MRI image plane at the inlet was then used to trim the model.

Automatic mesh generation software [117] (MeshSim, Simmetrix, Inc., Clifton Park, NY) was used to discretize these models into finite element meshes needed to compute the flow solutions. The inlet flow was described by an axisymmetric, fully developed, pulsatile flow (Womersley) velocity profile that was based upon the PC-MRI through-plane flow rate data at the inlet. Since blood is incompressible, the walls were assumed to be rigid, the model had only one outlet, and velocity was prescribed at the inlet, the choice of exit pressure did not affect the velocity fields. A zero exit pressure was prescribed for all calculations. Velocities along the luminal surface of the aorta and the graft were prescribed to be zero, consistent with a no-slip condition. Blood was modeled as a Newtonian fluid with a constant density of 1.06 g/cm^3 and a constant viscosity of

0.04 dynes-s/cm^2. Under these boundary conditions and assumptions, pulsatile flow was computed for 5 cardiac cycles using the Spectrum™ Solver software, described in Section 2.4.3 and previously validated for the incompressible Navier-Stokes equations [52, 105]. The parameters used by the Spectrum™ Solver include residual control being on (adding discontinuity capturing to increase the stability of the numerical simulations), a maximum of two stagger iterations, a GMRES iteration for solving the velocities using 30 Krylov vectors, a maximum of 10 cycles, and a convergence tolerance of 0.02, and a conjugate-gradient iteration for solving for pressures using 10 projection vectors, a maximum of 1394 iterations, and a convergence tolerance of 0.1.

Convergence studies were conducted on Pig D to determine the mesh size and the time increment to use in computing the flow solutions for these models. Comparisons were made of the flow solutions for meshes of 151,000 elements, 548,000 elements, and 1.24 million elements against results for a mesh with 1.85 million elements (Figure 6.6). The flow rates in the native aorta for the 151,000 element mesh showed an average absolute difference of 27%, while those of the 548,000 element mesh showed an average absolute difference of 13%. The average absolute difference was 5% for the 1.24 million element mesh. In the bypass, the flow rates were much higher, so the differences in flow due to mesh size were less significant. For the bypass flow rates, the average absolute difference was 7% in the 151,000 element mesh, 3% in the 548,000 element mesh, and 1% in the 1.24 million element mesh. In order to obtain an accurate result in a reasonable amount of time, the experiments were run with meshes of approximately 550,000 elements. The actual mesh sizes varied from 546,000 to 764,000 linear tetrahedral elements. The number of time steps per cardiac cycle was also varied for the flow solution of the 548,000 element mesh for Pig D, as shown in Figure 6.7. The average absolute difference in flow rates for calculations performed for 240 versus 480 time steps per cardiac cycle was 2%, or 0.15 ± 0.12 cc/s, in the native aorta and 0.4%, or 0.16 ± 0.13 cc/s, in the bypass graft. Therefore, to reduce computation time, 240 time steps were used per cardiac cycle.

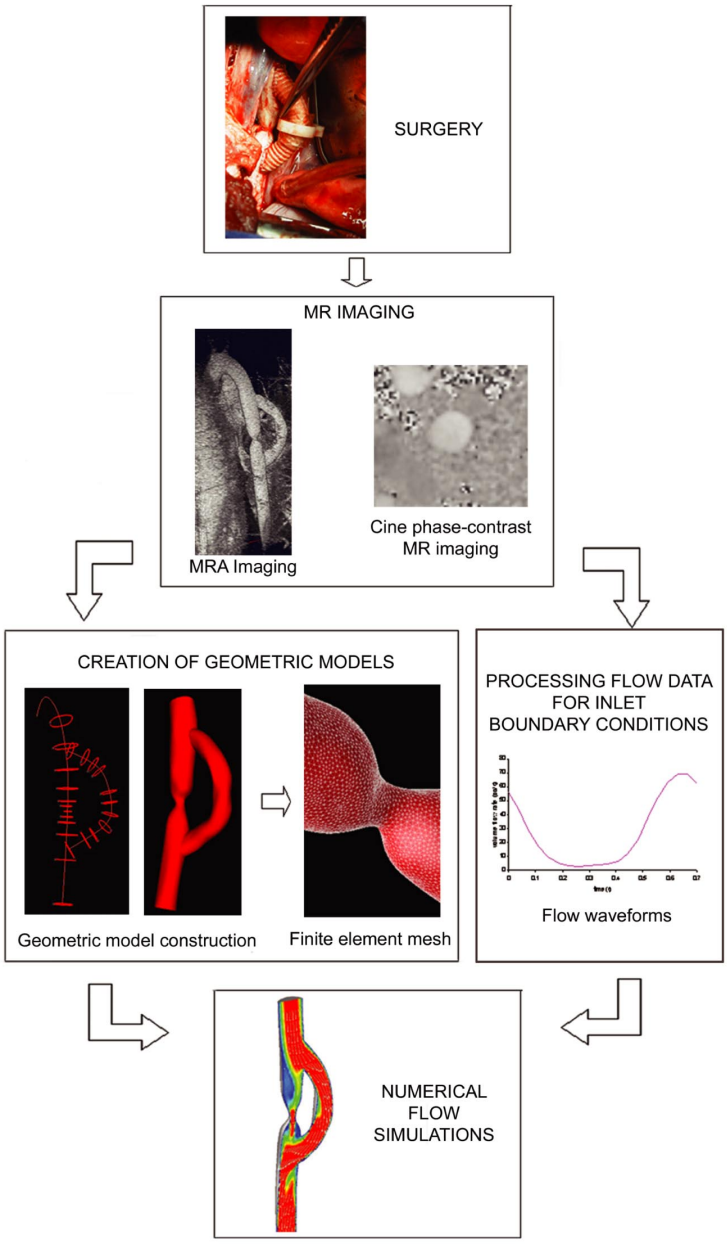


Figure 6.5: Process for generating the numerical simulation results. Magnetic resonance angiography (MRA) provided anatomic information from which a geometric model was constructed. The phase contrast imaging plane at the inlet was used to trim the geometric model. Automatic mesh generation software converted the solid geometric model to a finite-element mesh, which was used in the numerical simulation. The numerical simulation also required boundary conditions. The inlet flow velocity was acquired using phase contrast magnetic resonance imaging (PC-MRI) and integrated over the cross section to compute a flow rate, which in conjuction with pulsatile flow (Womersley) theory, was utilized as a boundary condition for these simulations.

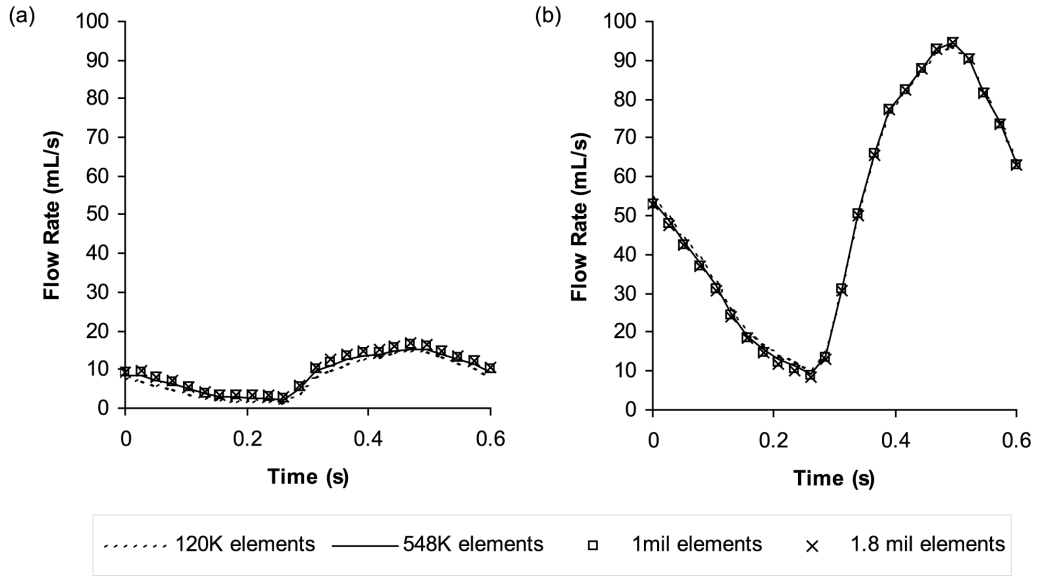


Figure 6.6: Comparison of flow results from simulations using 240 time steps per cycle and different mesh sizes: 120,000 elements, 548,000 elements, 1 million elements, and 1.8 million elements. (a) shows the flows through the aorta of pig D at these different mesh resolutions, while (b) shows the flows through the bypass. The differences in flow rate between these mesh sizes are small.

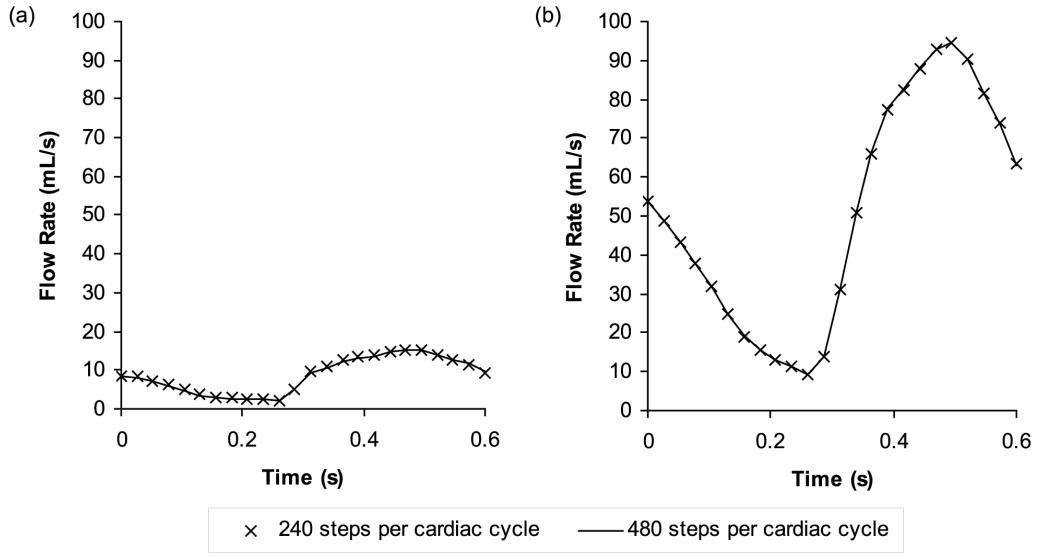


Figure 6.7: Comparison of flow results from simulations using a different number of time steps per cardiac cycle and a 548,000 element mesh. (a) shows the flows through the aorta of pig D at these different time resolutions, while (b) shows the flows through the bypass. The differences between using 240 steps versus 480 steps per cycle are small.

Additional models were created to examine the sensitivity of the simulated flow results to variations in the degree of coarctation. Since the cross-sectional area of the coarctation has the largest effect on the pressure drop, the lumen boundary acquired using the level-set method for this region was scaled up and down for one pig (Pig E) and changes in flow distribution were quantified. An equivalent-circle radius was defined as the radius of a circle with the same cross-sectional area as the segmented contour. The scale factor was determined by increasing and decreasing the equivalent circle radius up to an amount equal to the pixel resolution of the MRA data acquired for that pig. The mesh and flow solutions for these modified models were produced using the same methods and under the same conditions as for the original model.

6.2.1.1.2 Data Analysis

To verify the accuracy of these simulation methods, custom visualization software based upon the Spectrum™ Visualizer was used to calculate the blood flow rates from the computed velocity fields in the native aorta and in the bypass graft. The program calculated the through-plane flow at each time point in the simulation using a user-specified plane through the region of interest.

Vcalc was used to determine the flows measured with PC-MRI. The segmented k-space data was used in all cases, except in Pig C, for which only the 2D cine PC-MRI data was available. Volume flow rates for each slice location were computed by multiplying the average through-plane velocity by the cross-sectional area of the region of interest. A second-order baseline correction, computed from the fatty and muscular regions in the image, was applied to the flow computations to account for eddy currents and thresholding was used to segment out the region of interest from the magnitude images.

In addition, both the signal-to-noise ratio (SNR) and a theoretical calculation of the standard deviation of the flow measurements based on the SNR were calculated using the method described in Section 2.2.3.5. For this calculation, the first and twelfth frames (out of 24 reconstructed frames) were used to compute the SNR, and the area used to compute the standard deviation was the average area of the region of interest over the 24 time frames.

Pig	Inlet Correction (mL/min)	Aorta Correction (mL/min)	Graft Correction (mL/min)	Outlet Correction (mL/min)
A	-11.24	-10.50	11.74	--
B	22.34	-19.41	3.73	277.43
C	36.19	35.18	-32.56	55.32
D	35.13	72.04	69.56	269.59
E	-59.15	-47.19	-36.71	23.80
F	-103.89	15.43	28.16	47.30
G	-119.65	-44.19	-95.08	3.37
H	-93.05	-154.23	-89.61	-47.39

Table 6.4: Average baseline corrections applied to the PC-MRI images for the 4 different slice planes for the eight experiments.

6.2.1.2 Results

The computational flow results were compared to the PC-MRI measurements for all eight animals, as shown in Figure 6.8. The average baseline corrections applied to the PC-MRI measurements are given in Table 6.4, and the Reynolds number at the inlet are given in Table 6.5. Volume blood flow through the thoraco-thoraco bypass graft was significantly greater than through the constricted thoracic aorta. This is consistent with theoretical predictions and was demonstrated by both PC-MRI flow measurements and computational results. The PC-MRI data showed that, on average, 3.2 mL/s to 18.3 mL/s of blood flowed through the native aorta, depending on the tightness of the surgically created coarctation. This was only 10% to 35% of the blood that entered the descending thoracic aorta. The numerical solutions predicted similar results, differing from the PC-MRI-measured aorta-to-inlet blood flow ratios by –10.6% to 8.9%, as shown in Figure 6.9(a). The mean absolute difference in flow ratios was 6.0 ± 3.3%. Good agreement between the PC-MRI measurements and the numerical solutions was also observed for the blood flow through the bypass grafts, with the difference in the bypass-to-inlet blood flow ratios ranging from –9.7% to 3.6%. These differences are depicted in Figure 6.9(b). The mean absolute difference was 5.4 ± 2.8%. The difference in flow rates between *in*

vivo measurements and simulation results ranged from –3.8 to 4.6 mL/s in the native aorta and from –5.1 to 2.0 mL/s in the bypass graft. The average absolute difference was 2.7 ± 1.4 mL/s in the native aorta. In the bypass, the average absolute difference was 2.3 ± 1.2 mL/s. The theoretically calculated standard deviations of flow are presented in Table 6.6. The standard deviations vary from a minimum of 1.4 mL/s to a maximum of 7.8 mL/s, with the average value being 3.5 mL/s.

	Pig A	Pig B	Pig C	Pig D	Pig E	Pig F	Pig G	Pig H
Average Re	1246	1778	850	1374	1191	995	757	869
Min Re	140	361	27	267	300	126	79	201
Max Re	2374	3038	2171	2518	2225	2351	1751	1698

Table 6.5: Inlet Reynolds numbers (Re) for the 8 pigs.

The PC-MRI-measured and numerically computed flow rate waveforms appeared to have similar shapes and amplitudes (Figure 6.10). Qualitatively, minor differences existed between the MRI measurements and the numerical solutions. For instance, the PC-MRI measurements showed a small amount of reverse flow in the aorta for four of the animals and in the bypass for one of the animals. However, this phenomenon was not observed in the corresponding numerical measurements. There was also a small time delay between the PC-MRI-derived flow waveforms and the numerically computed flow waveforms in the native aorta and the bypass for pigs A, B, E, and F.

Figure 6.11 shows the flow distributions for pig E for different coarctation contours. As predicted theoretically, a tighter coarctation, which corresponds to a smaller equivalent-circle radius, caused more flow to be diverted through the bypass graft and less flow to go through the native aorta. The unaltered coarctation contour, as generated by the model construction process, had an equivalent circle radius of 1.38 mm. For an increase in equivalent-circle radius from 1.38 mm to 1.65 mm, 5% more blood flowed through the native aorta and 5% less blood flowed through the bypass graft. On the other hand, a decrease in equivalent-circle radius from 1.38 mm to 1.11 mm resulted in a 5%

increase in blood flow in the bypass graft and a corresponding decrease in blood flow in the native aorta.

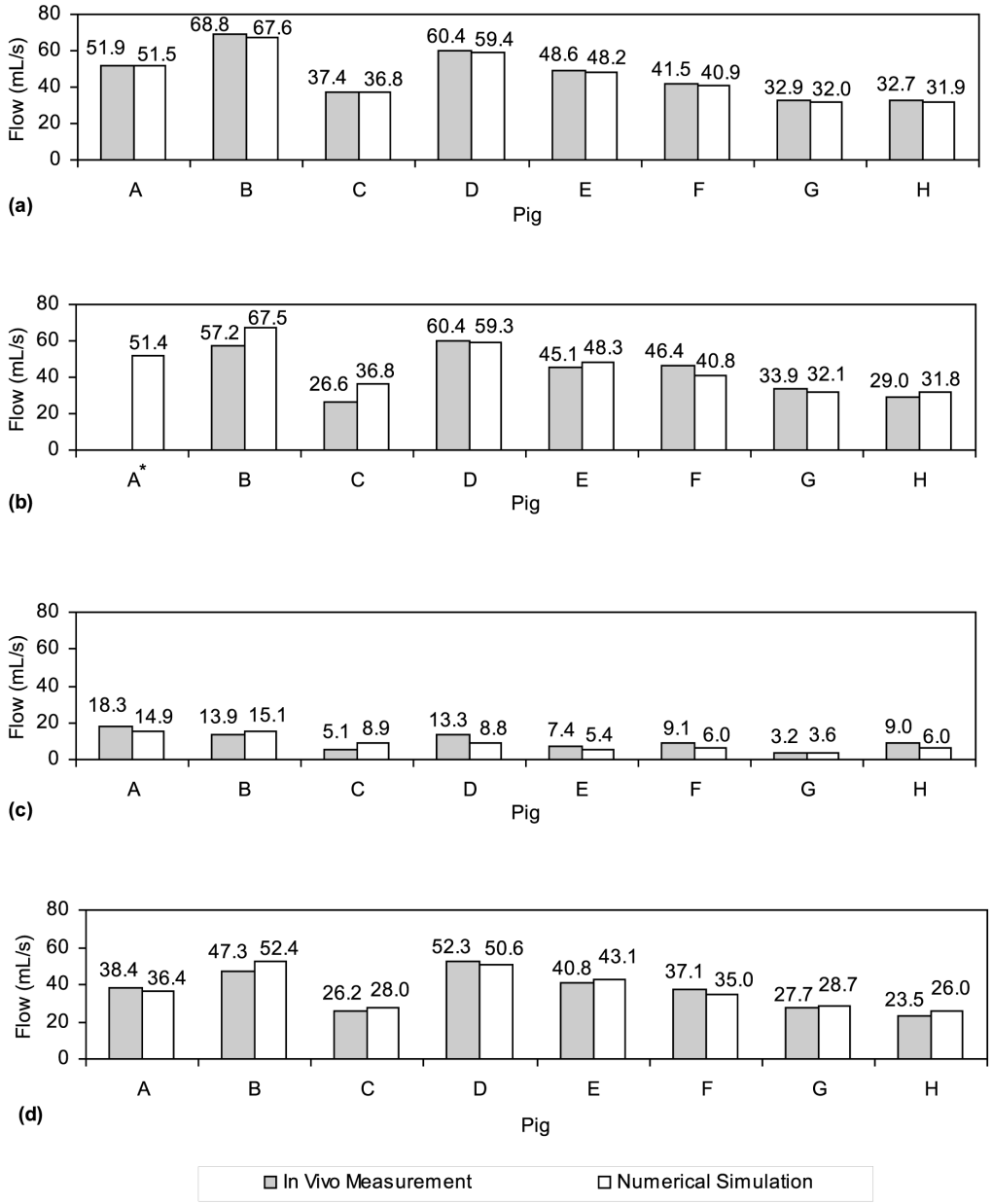
Heart rates for the animals were recorded every 10 to 20 minutes. The average heart rates for the animals with the bypass open ranged from 80 bpm to 123 bpm during the imaging portion of the experiment. During this time, the animals' heart rates varied, with the minimum variation in heart rate being 3 bpm and the maximum variation in heart rate being 29 bpm.

Pig	Inlet (mL/s)	Aorta (mL/s)	Graft (mL/s)	Outlet (mL/s)
A	5.2	7.8	2.2	n/a
B	3.3	2.1	2.5	3.7
C	2.3	1.4	1.8	2.1
D	5.8	3.9	4.4	3.3
E	3.8	2.7	3.7	3.4
F	2.8	1.7	3.2	2.7
G	4.3	2.8	3.9	2.2
H	5.4	4.4	7.1	2.8

Table 6.6: Theoretically computed standard deviations of flow measurements acquired with PC-MRI.

6.2.1.3 Discussion

Based on the eight animals studied, there is excellent agreement in flow rates and flow waveforms between the PC-MRI measurements and the numerical simulation results. The differences observed in the flow through the aorta and through the bypass are on the order of the theoretically computed standard deviations in PC-MRI-measured flows. The maximum absolute difference in branch-to-inlet blood flow ratio was 10.6%. The average absolute difference in the aorta-to-inlet blood flow ratio was only 6.0%, while that of the bypass-to-inlet blood flow ratio was only 5.4%. Furthermore, the flow waveforms generated from the numerical simulations and from the experimental data appeared similar in shape and amplitude, suggesting that in addition to being able to accurately predict the time-averaged flow rates, the numerical methods could also reasonably predict flow rates for a given time point in the cardiac cycle.



**In vivo* data not available

Figure 6.8: Comparison of average flow rates measured with PC-MRI and computed by numerical simulations for eight animals. Flow measurements are provided for the (a) inlet, (b) outlet, (c) aorta, and (d) graft locations, as indicated in Figure 6.1.

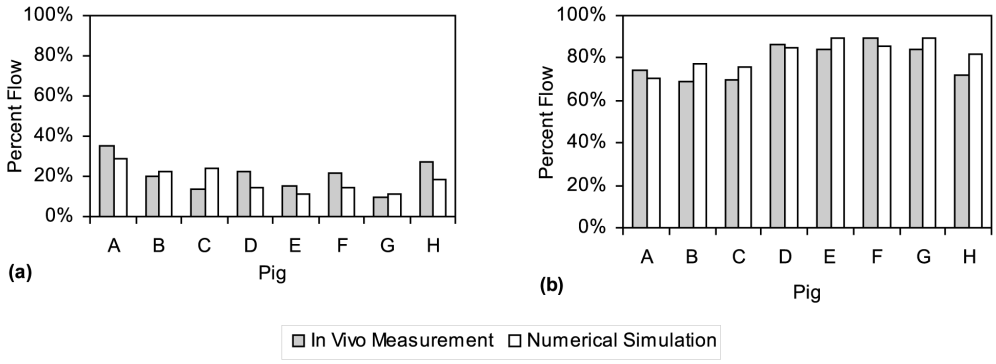


Figure 6.9: Comparison of flow distributions between PC-MRI flow measurements and numerically computed quantities. (a) shows the percentage of the inlet flow going through the native aorta, and (b) shows the percentage of the inlet flow going through the bypass graft.

The small differences that were observed between the simulation results and the PC-MRI measurements can be attributed to both physiological conditions and technological limitations. The accuracy of the geometric model that is constructed has a significant impact on the resulting computational flow values. As the sensitivity study performed on pig E showed, imprecise modeling of the aortic constriction could lead to variation in the flow distribution. If the constriction was modeled to be tighter than it actually was, then the predicted flow rate in the bypass graft would be higher than the *in vivo* measurement, while the flow rate in the native aorta would be lower. This could explain the results observed in pig E. Increasing the equivalent-circle radius of the contour used to model the coarctation by 0.27 mm, half the pixel resolution of the MRA data set, caused 5% more blood flow in the native aorta and 5% less blood flow in the bypass graft, resulting in better agreement with the *in vivo* measurements. Other assumptions made in modeling the blood and blood vessels, such as the aforementioned Newtonian approximation of blood viscosity, the use of an idealized inlet boundary condition, and a rigid wall assumption, could also cause discrepancies between the numerical results and the PC-MRI measurements. Improvements to the modeling methods used would allow for more realistic simulations that could test the effects of the simplifying assumptions that were used and potentially improve the agreement between the simulation and the *in vivo* flow results.

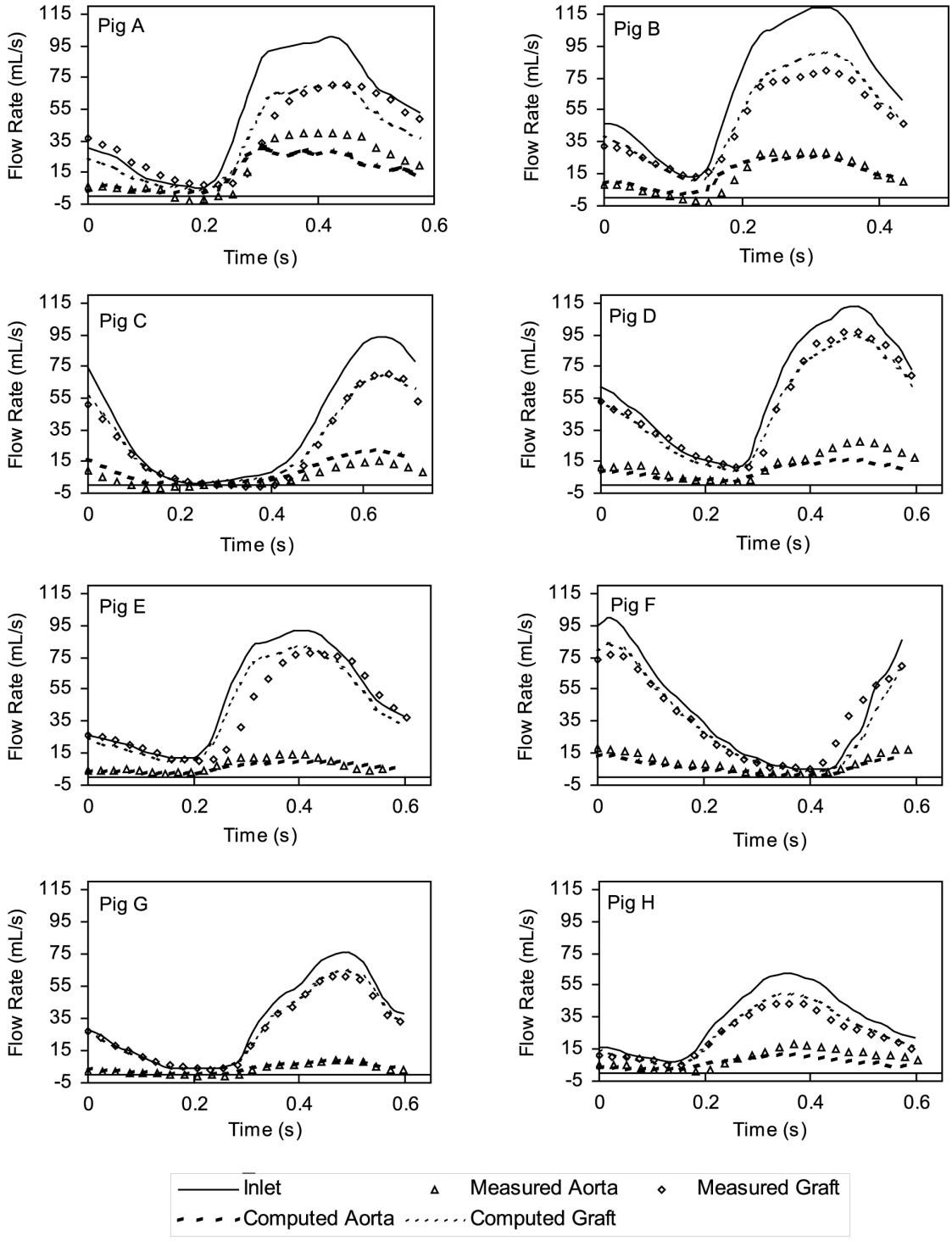


Figure 6.10: Comparison of flow waveforms acquired with PC-MRI and computed with numerical simulation techniques over one cardiac cycle for eight pigs.

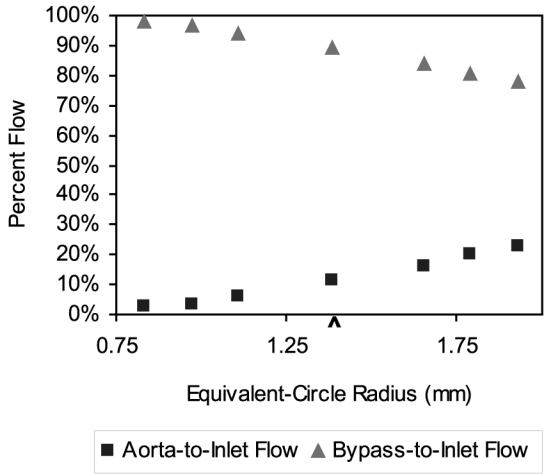


Figure 6.11: Sensitivity of the flow solutions to the equivalent-circle radius of the coarctation contour for pig E. The caret indicates the equivalent-circle radius of the original coarctation contour. The original coarctation contour was scaled to increase or decrease its equivalent-circle radius by 0.5, 0.75, or 1 pixel. As predicted theoretically, a tighter coarctation, which corresponds to smaller values of the equivalent-circle radius, caused more flow to be diverted through the bypass graft and less flow to go through the native aorta.

Changes in the animal's physiology and limitations of the MRI techniques could also lead to inconsistencies in the experimental measurements and account for some of the differences between the *in vivo* data and the numerical simulation results. Use of an inaccurate baseline correction during post-processing of the *in vivo* measurements could lead to offsets in the velocity measurements and account for differences between the MRI-measured and the numerically computed flow waveforms, although these differences are likely to be small. In these experiments, second-order baseline correction functions based upon regions that were relatively far from the aorta were used. The guidelines for baselining, described in Section 3.1, suggested using a zeroth- or first-order correction function based on regions close to the region of interest. Analysis of the baseline functions showed that the maximum coefficient for the second-order effects was 0.00575, so the second-order correction was minor, particularly in the center 20 pixels, where the vessel of interest was generally located, and in this case, similar to that of the first-order correction. The average baseline correction was small, generally less than 2 mL/s with the largest average baseline correction only being 4.6 mL/s. However, these small errors could account for differences such as that observed in the native aorta flow

waveforms for pigs C and F, in which the measured and computed waveforms appear to be offset from one another by a few mL/s.

It was also observed that the measured flow rates did not strictly conserve flow. For the *in vivo* data, the sum of the mean flows in the bypass graft and through the native aorta differed from the inlet flow by as much as 22% of the inlet flow, while the difference between the MR-measured inlet and outlet flows was as much as 28.9% of the inlet flow. Possible explanations for this include inaccuracies in the imaging method [141, 142] and the omission of outflow through small intercostal arteries due to experimental constraints. An alternative explanation is that the animal's physiology changed between image acquisitions at different locations. Monitoring of the animals showed that heart rate varied by as much as 28 bpm during the data acquisition for the bypass-open state. Since the PC-MRI images were not acquired at all four locations simultaneously, any change in the animal's heart rate or blood flow distribution would only affect measurements for a single location, potentially leading to an apparent lack of conservation of flow.

6.2.2 Predicting Velocity Patterns

6.2.2.1 Methods

6.2.2.1.1 Assessment of Available Data

The *in vitro* experiments of Chapters 4 and 5 demonstrated the importance of accurate inlet boundary conditions. Since helical blood flow patterns with significant in-plane velocity components are observed in the descending aorta [143], inlet boundary conditions based on measurements from this region, such as in this *in vivo* experiment, need to include all three-components of velocity. Figure 6.12 shows the helical flow patterns during diastole and the deceleration phase of systole at the inlet of pig G. In this experiment, three-components of velocity were acquired with the 2D cine PC-MRI sequences. Of the 8 pigs studied, only 4 had 3-components of velocity data at the inlet and at a minimum of two other locations (see Table 6.2 and Table 6.3): pig C, pig D, pig G, and pig H.

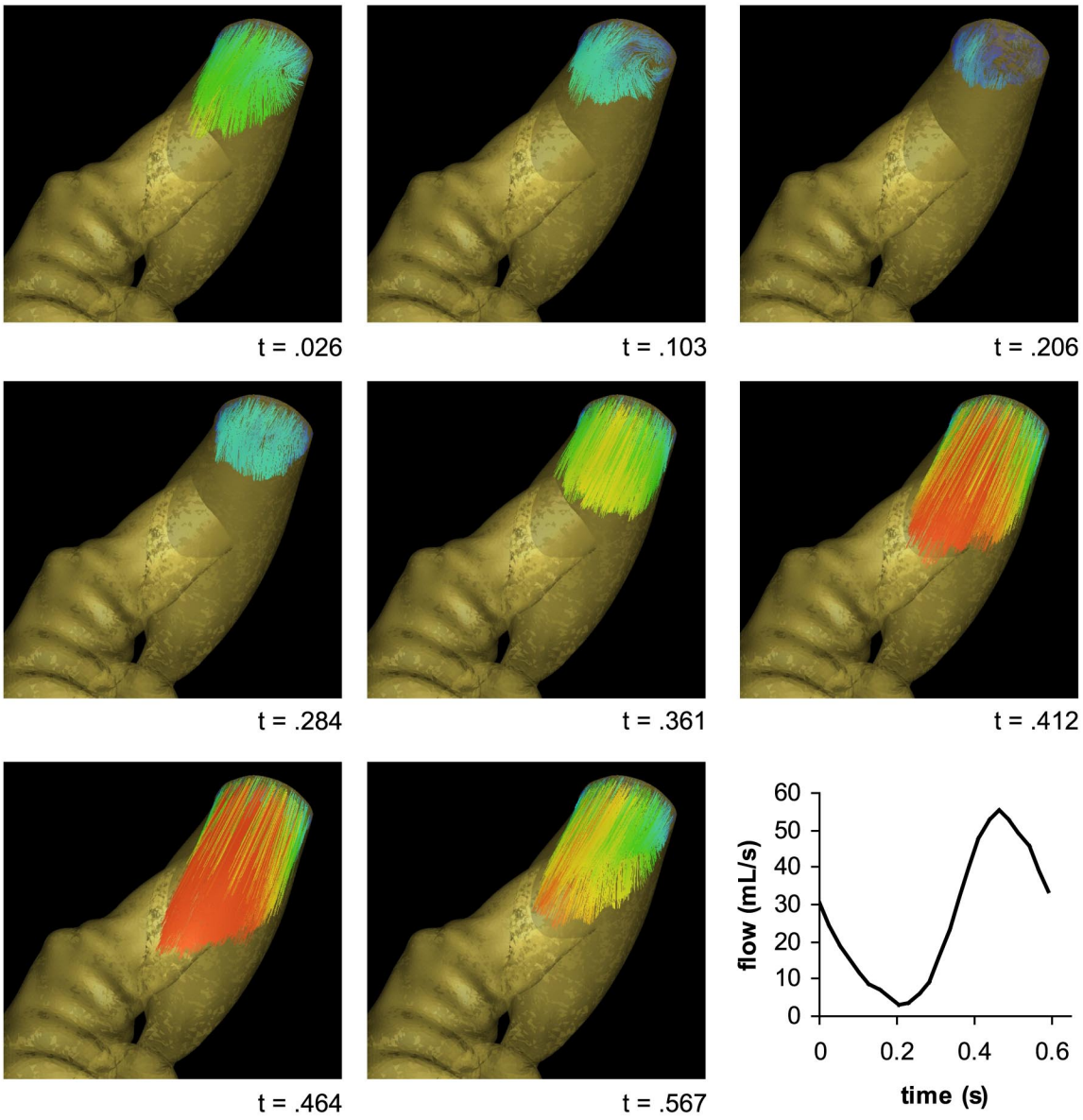


Figure 6.12: Velocity profile prescribed at inlet of numerical simulations for pig G. During diastole, a helical flow structure was observed.

For these initial *in vivo* comparisons, pig G was chosen because of its excellent signal-to-noise ratio (SNR) and its stable physiology. Table 6.7 lists the other factors considered in determining the suitability of the data for these comparison studies. The flow information in the table came from the segmented k-space data, and the SNR and standard deviations of velocity were computed using the method described in Section 2.2.3.5.

6.2.2.2 Numerical Simulations

The numerical simulations were run exactly as described in Section 6.2.1.1.1. Except at the inlet, the same boundary conditions and assumptions were made, and the only difference in the solver parameters was that residual control, a parameter that increases the stability of the numerical solutions but can also decrease the accuracy of the predicted velocity fields, was turned off. Also, the simulations described in this section ran for 23 cycles at 480 time steps per cycle, as compared with the 240 time steps per cycle for 5 cycles for the simulations of Section 6.2.1.

	Pig C	Pig D	Pig G	Pig H
Velocity Data Available	4 slice locations	4 slice locations (one slice has aliasing)	3 slice locations	4 slice locations
Difference between Inlet Flow and Sum of Flow through Aorta and Bypass Graft (mL/s)	6.17	5.26	1.98	0.19
Heart Rate during Experiment (bpm)	80.6 ± 4.1	101 ± 4	98.3 ± 2.1	104.7 ± 14
Maximum Change in Heart Rate during Experiment (bpm)	12	11	3	20
SNR	Inlet: 50.7 Aorta: 43.2 Graft: 59 Outlet: 41.8	Inlet: 29.2 Aorta: 26.6 Outlet: 29.0	Inlet: 71.1 Aorta: 36.2 Graft: 51.3	Inlet: 29 Aorta: 34.2 Graft: 44.2 Outlet: 53.2
Standard Deviation of Velocity (mm/s)	Inlet: 13.3 Aorta: 15.6 Graft: 19.1 Outlet: 26.9	Inlet: 23.1 Aorta: 25.4 Outlet: 38.7	Inlet: 9.5 Aorta: 18.7 Graft: 22	Inlet: 23.3 Aorta: 19.7 Graft: 15.3 Outlet: 12.7
Other Factors	Several intercostal arteries not ligated	One intercostal artery not ligated in region of interest. Animal physiology very unstable at end of experiment.		

Table 6.7: List of factors to assess usability of data for comparisons between numerically computed and PC-MRI-acquired velocity patterns.

The main difference between the simulations in Section 6.2.1 and those in this section was the inputs. Although the model for the velocity comparison simulation was constructed according to the process described in Section 6.2.1.1.1, two changes were made to improve the accuracy of the final geometry, which can noticeably affect the velocity patterns. First, grad-warp corrected MRA data was used (see Section 2.2.2.3 for more details about grad-warp correction). Secondly, more contours were included in the model in an attempt to capture details, such as the accordion-like structure of the bypass graft. Figure 6.13 shows the differences between the original and the improved model. A 1.1 million element mesh was created from the final improved model using automatic mesh generation software [117] (MeshSim, Simmetrix, Inc., Clifton Park, NY).

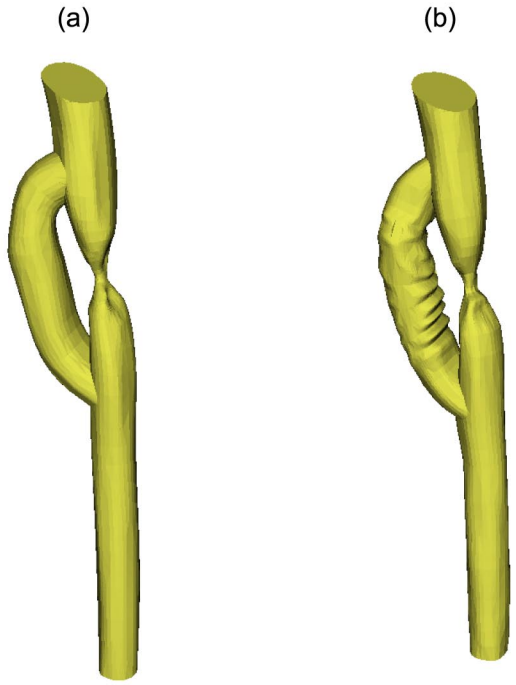


Figure 6.13: Models used for the numerical simulation of velocity patterns for Pig G. (a) Model used in comparisons of flow distribution, described in Section 6.2.1. (b) Model used in comparisons of velocity patterns, described in Section 6.2.2.

The inlet boundary condition for the velocity comparison experiment was based upon the first-order baseline-corrected 2D cine PC-MRI measurements, which provided both through-plane and in-plane velocity data. These velocities were mapped onto the inlet

mesh using the process described in Section 2.3.3.2.2. Fourier smoothing was performed using 12 Fourier components.

6.2.2.2.1 Data Analysis

Section 4.3 discussed the need for spatial and temporal averaging of the numerically computed velocities in order to fairly compare them with those measured with PC-MRI. As with the experiments described in Chapters 4 and 5, the simulation results for this experiment were averaged over 8 cycles and 5 slices, which spanned a thickness of 5 mm and were spaced 1.25 mm apart.

Because of the difficulty in accurately segmenting the *in vivo* PC-MRI data, comparisons were made to a masked version of the PC-MRI data. Within Geodesic, an initial segmentation of the PC-MRI data was obtained using an ellipse that completely enclosed the vessel of interest. This data was converted to an image file using Tecplot (Amtec Engineering, Inc., Bellevue, WA), and then Photoshop (Adobe Systems, Inc., San Jose, CA) was used to display only those velocities within the area of the corresponding slice through the geometric model. This contrasts with the way the data was displayed for the *in vitro* experiments, where the numerical simulations were mapped onto the PC-MRI segmentation. If that method were used for the *in vivo* experiment, clipping of the numerical simulation results occurred. Therefore, in order to view the complete velocity profiles from the numerical simulations, this comparison study masked the PC-MRI data using the contours from the geometric model.

6.2.2.3 Results

The average Reynolds number at the inlet of this problem was 689, with a minimum Reynolds number of 87 and a maximum Reynolds number of 1444. Figure 6.14 shows the velocity magnitudes for the numerical simulations at 4 different time points: deceleration, diastole, acceleration, and peak flow. The velocity magnitudes ranged from 0 to 1000 mm/s, a significantly larger range than in the *in vitro* experiments of Chapters 4 and 5. The stenosis was also much tighter than in the *in vitro* experiments, estimated to be a 94% decrease in cross-sectional area versus a 75% decrease in the *in vivo* experiments.

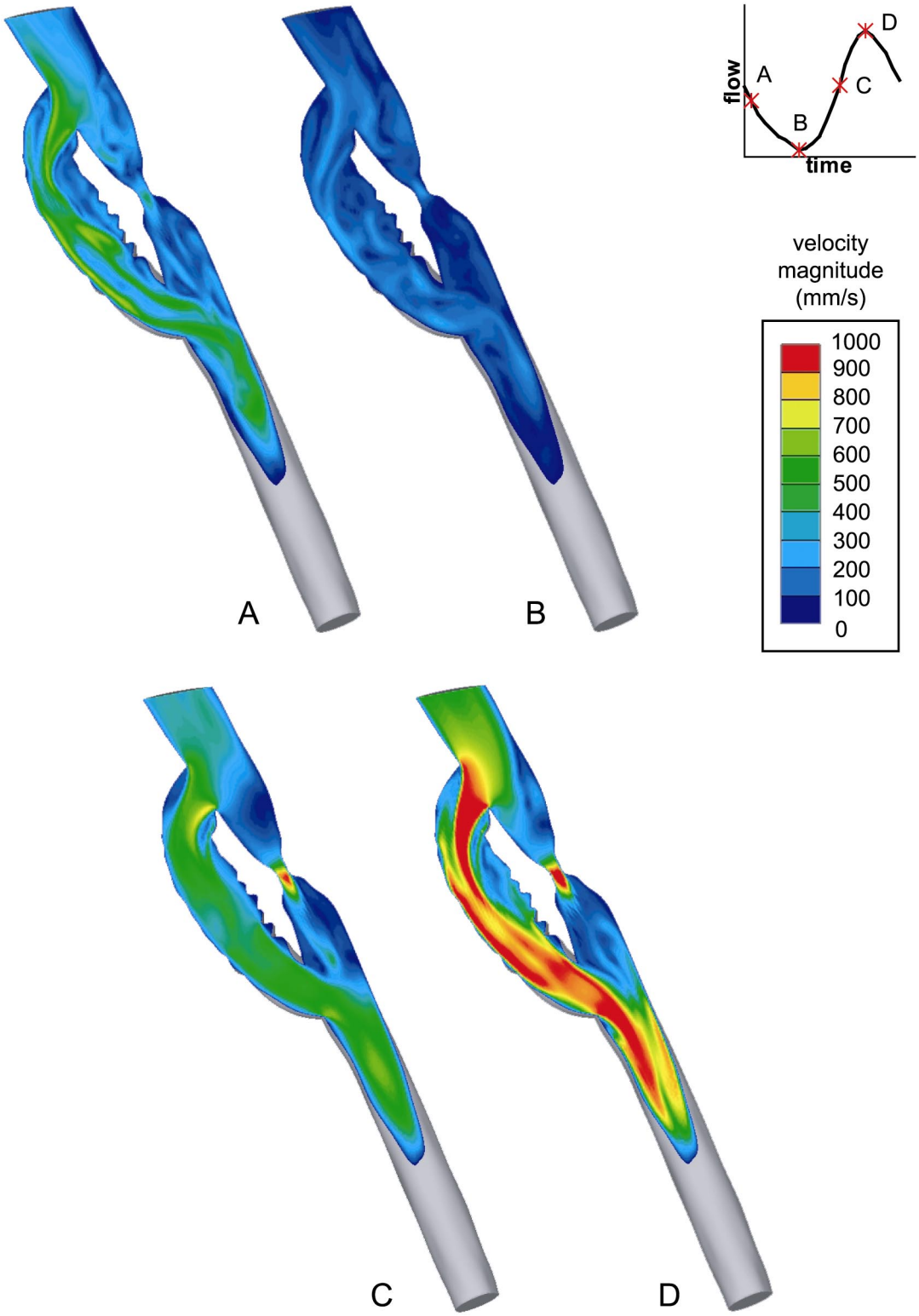


Figure 6.14: Velocity magnitudes from the numerical simulation of Pig G at 4 different time points: deceleration (A), diastole (B), acceleration (C), and peak flow (D).

6.2.2.3.1 Flow Comparisons

Although the primary focus of this section is on the velocity pattern comparison, it is important to verify that the flow distributions between the numerical computations and PC-MRI also compare favorably. If these are not similar, then it is unlikely that agreement between the velocity patterns will be obtained. Figure 6.15 plots the flow waveforms for both the numerical simulations and the PC-MRI measurements through the aorta and through the graft. Both the flow waveforms and the average flows agreed reasonably well. The average flow through the aorta was 2.4 mL/s, as measured with PC-MRI, and 2.2 mL/s, as predicted by the numerical simulations. Through the bypass graft, the average flows were 22.9 mL/s and 24.0 mL/s, according to PC-MRI and the numerical computations, respectively. Note that the peak of the aorta waveform, as measured with PC-MRI, occurs slightly before the peak of the inlet waveform, probably due to a small change in the physiology between these two data acquisitions.

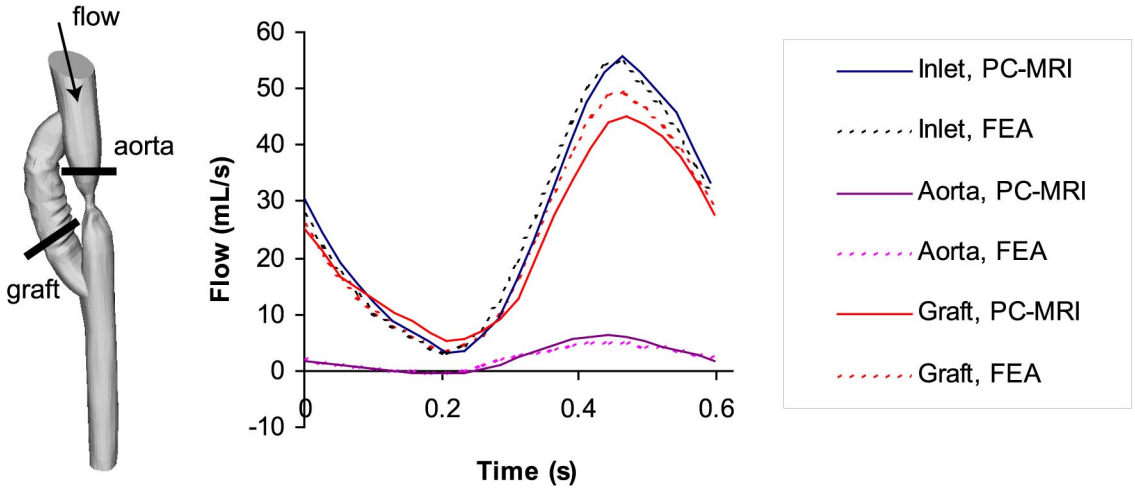


Figure 6.15: Comparison of flow waveforms from the numerical simulations and from PC-MRI.

Two useful measures when analyzing this data are flow periodicity and flow conservation. Figure 6.16 compares the flow waveforms from the numerical simulations for the average of cycles 8 to 15 and for the average of cycles 16 to 23. These waveforms were nearly identical with one another, indicating periodicity of the flows for these averaged results. In terms of flow conservation, the numerically computed flows at the inlet matched the sum of the flows through the aorta and the bypass graft (Figure 6.17).

The average flow at the inlet was 26.4 mL/s and the sum of the flows through the aorta and the graft was 26.3 mL/s, a difference of only 0.1 mL/s. However, the PC-MRI measurements showed a difference of 1.1 mL/s between these two quantities, measuring 26.4 mL/s at the inlet and 25.3 mL/s through the aorta and bypass graft. The discrepancies occurred primarily at peak flow, according to Figure 6.17, and are likely due to measurement errors or changes in the animal's physiology between successive acquisitions.

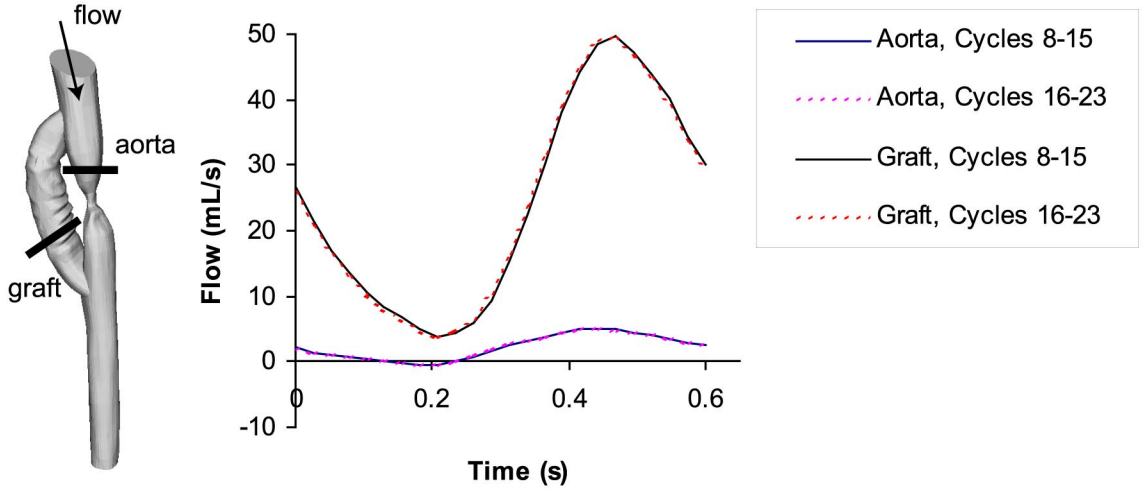


Figure 6.16: Periodicity of flow waveforms from averaged numerical simulation results.

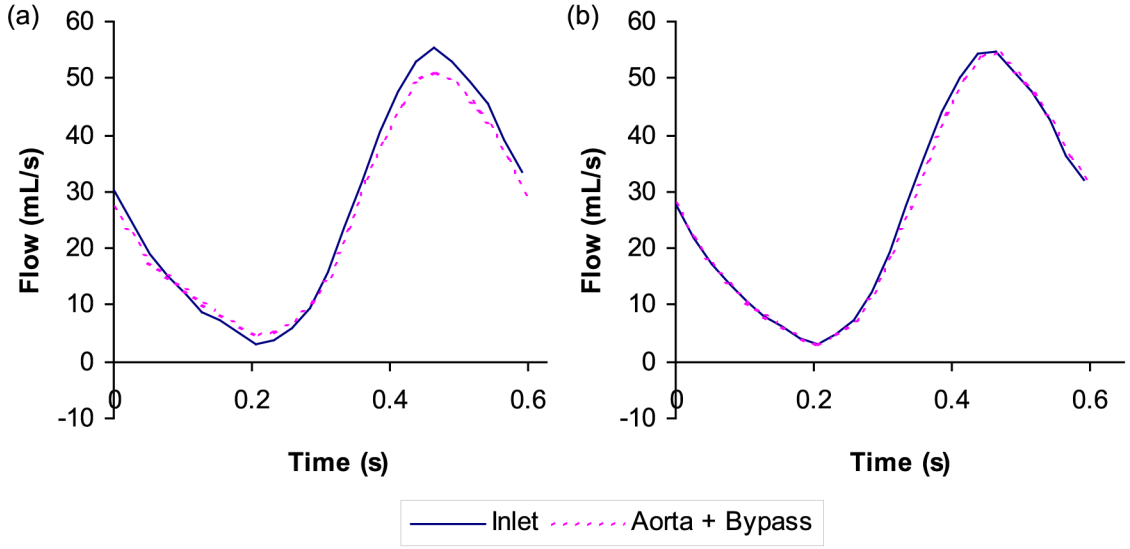


Figure 6.17: Comparison of flows at the inlet with sum of flows through the aorta and the bypass graft. (a) Based on PC-MRI measurements (b) Based on numerical simulations

6.2.2.3.2 Velocity Comparisons

Figure 6.18 and Figure 6.19 compare the through-plane velocity patterns for the numerical simulations and for the PC-MRI data at the aorta and at the bypass graft, respectively. Isocontour plots are shown at four different time points: deceleration, diastole, acceleration, and peak flow. Two sets of results are displayed for the numerical simulations: results from the average of cycles 8 to 15 and results from the average of cycles 16 to 23. The similarity between the velocity isocontours from these two sets of averaged results indicates that the velocities were fairly periodic. Differences were apparent during some time points, though, such as at peak flow in the aorta and during acceleration in the bypass graft.

In terms of comparisons with the PC-MRI data, the numerically computed results had similar overall velocity patterns. For instance, the peak in velocities during deceleration in the aorta occurred along the wall closest to the bypass with a region of negative velocities appearing along the opposite wall. However, the patterns between the numerical simulations and the PC-MRI measurements were slightly rotated from one another in this case. Likewise, the peak velocities for the simulations and the PC-MRI measurements occurred along the same wall during peak flow in the bypass graft but were rotated from one another. The greatest differences between the PC-MRI data and the numerical simulation results were during acceleration. Although the through-plane velocities had comparable magnitudes, the shape of the contours were noticeably more crescent-shaped in the numerical computations than in the PC-MRI measurements in the aorta, and in the bypass graft, the peak velocities occurred closer to the vessel center in the numerical results than they did in the measured data.

6.2.2.3.3 Sensitivity of Experimental Results

Two useful measures of the reliability of the PC-MRI data are its precision and its temporal resolution. In the previous experiments described in this thesis, the theoretically computed standard deviations were used as a measure of the precision of the velocity measurements. These were computed for pig G and given in Table 6.7. For both the aorta and bypass graft measurements, the theoretical standard deviation was approximately 20 mm/s. The number of independent time frames that could be acquired

was computed using Equation (2.28). Given the heart rate of 97 bpm at the inlet and a T_R of 30 ms, approximately five frames could be collected independently.

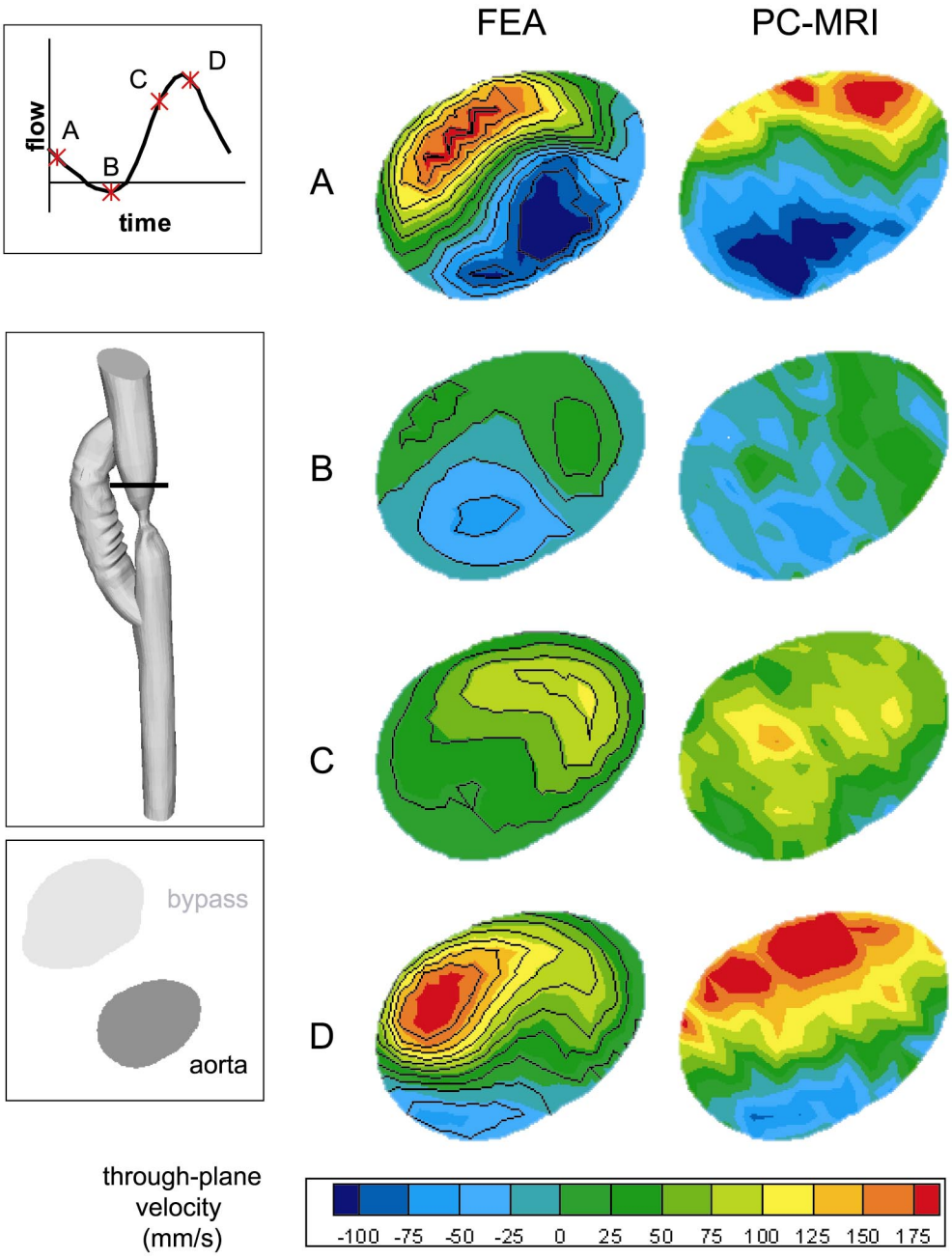


Figure 6.18: Comparisons of through-plane velocity patterns computed numerically using finite element analysis (FEA) and those acquired with PC-MRI in the aorta proximal to the coarctation. Four different time points are examined: deceleration (A), diastole (B), acceleration (C), peak flow (D). Two sets of results are shown for the numerical simulations: the color map results are an average of cycles 8 to 15; the black contour lines are an average of cycles 16 to 23.

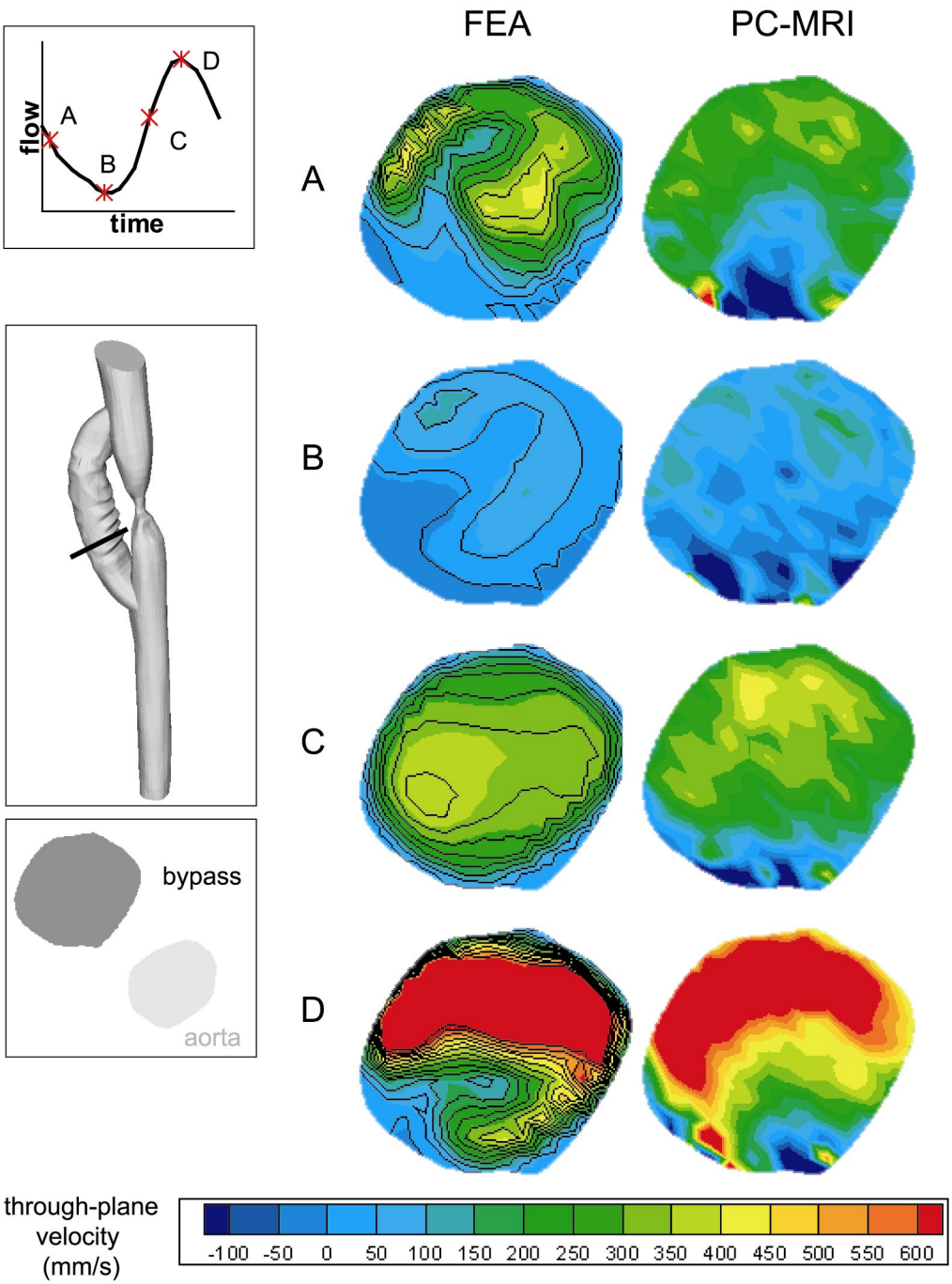


Figure 6.19: Comparisons of through-plane velocity patterns computed numerically using finite element analysis (FEA) and those acquired with PC-MRI in the bypass graft. Four different time points are examined: deceleration (A), diastole (B), acceleration (C), peak flow (D). Two sets of results are shown for the numerical simulations: the color map results are an average of cycles 8 to 15; the black contour lines are an average of cycles 16 to 23.

6.2.2.4 Discussion

The through-plane velocity comparisons between numerically predicted results and PC-MRI measurements were analyzed here for only one animal, but the results are encouraging, with the magnitudes of the through-plane velocities in excellent agreement. Furthermore, for most of the time points, the regions of low and high velocities in the two data sets corresponded well, although the agreement was not as favorable as in the low and high flow *in vitro* experiments. In addition to the differences between the *in vitro* and the *in vivo* experiments—the changes in physiology, the higher Reynolds numbers in the *in vivo* case, and the appropriateness of the approximations inherent in these numerical simulations, such as the rigid-walled vessel and the Newtonian fluid—the *in vivo* experiments had an additional challenge. The stenoses in the *in vivo* experiments were approximately 5% to 15% tighter than in the *in vitro* experiments. This would result in higher velocities and potentially more complex flow patterns downstream of the stenosis. Other imaging modalities, such as computed tomography (CT), may need to be considered in order to obtain accurate images of and to build accurate models of the tighter stenosis.

The time point that displayed the most noticeable difference between the velocity patterns was during acceleration. Since acceleration introduces errors into the PC-MRI measurements (see Section 2.2.3.1), the presence of significant discrepancies at this time point was to be expected. Acquiring data using a shorter T_E could potentially reduce some of these errors, depending on the slice select gradient. A shorter T_E would also minimize artifacts due to excited spins moving out of the slice thickness of interest prior to data acquisition. Other changes that could improve the accuracy of the PC-MRI measurements include a shorter T_R, now possible with the custom sequence used in the *in vitro* experiments described in Chapters 4 and 5, lower v_{enc} values, and a smaller bandwidth. Temporal resolution could also be improved by acquiring only one velocity component at a time, instead of three. The accuracy of this approach depends on the stability of the animal's physiology. Of course, there are trade-offs involved when setting the imaging parameters, e.g., modification of one parameter to achieve better

image quality could simultaneously increase the total scan time, an important consideration for *in vivo* experiments.

On the simulation side, the same factors that affect the flow distribution results affect the velocity patterns: an inaccurate geometric model and mathematical and physical approximations. These results also used a fairly coarse mesh of 1.1 million elements and ran with 480 time steps per cycle. Increasing the mesh size and/or the number of time steps per cycle could produce a more accurate solution. In addition, it has been shown that changes in the inlet velocity boundary condition will alter the velocity patterns. Specifically, Wood and colleagues found that modifications to the prescribed in-plane velocity components would cause rotations of the downstream velocity patterns [62], similar to that observed during deceleration in the aorta and during peak flow in the bypass graft. Lastly, the values used for the post-processing of the numerical simulations, such as the number of cycles to average together, were empirically chosen, and alternate quantities could change the velocity patterns and increase the similarities to the PC-MRI measurements.

6.2.3 Summary

This *in vivo* experiment demonstrated that numerical simulations could predict flow distributions and velocity patterns which were similar to that measured with PC-MRI. Based on results from eight animals, the average flow rates differed by less than 2.7 mL/s and the flow distributions were within 10.6% of each other. In terms of the velocity comparisons for the one animal, the magnitudes of the through-plane velocities were in excellent agreement and for most of the time points, the regions of low and high velocities in the two data sets corresponded well. Potential improvements in the agreement of the PC-MRI measurements to the numerical results could be achieved through changes in both the data acquisition as well as the numerical simulations. The current results are promising, though, and additional *in vivo* comparison studies would further strengthen the validity of using finite-element-based numerical simulations to predict flow distributions and velocity patterns.

6.3 Comparison of Physiology with Bypass Open and Closed

The validation study described in Section 6.2 utilized anatomic and physiologic data from the bypass-open state. However, in order for numerical simulation methods to be useful in predicting the flow conditions for different bypass surgeries, they need to utilize only pre-operative data, in this case, data corresponding to the bypass-closed state. Of particular interest is the difference in the flows and pressures at the inlet and outlet for the bypass-open and the bypass-closed states, since these are used as boundary conditions for the numerical simulations. In the following section, comparisons are made at the inlet and outlet locations for these two states. Heart rate information is also presented. The method of processing and comparing the data is explained in Section 6.3.1, while the results are presented in Section 6.3.2. Section 6.3.3 describes the sensitivity of the pressure measurements, and Sections 6.3.4 and 6.3.5 discuss the significance of the data.

6.3.1 Methods

Section 6.3.1.1 explains the method used for processing and comparing the pressure data, while Section 6.3.1.2 discusses how the flow data was analyzed. Section 6.3.1.3 focuses on the heart rate data.

6.3.1.1 Post-Processing and Comparison of Pressure Data

The pressure measurements were made with the pressure catheters described in Section 6.1.3. As mentioned above, these were inserted upstream of the inlet imaging plane (proximal) and downstream of the outlet imaging plane (distal). While pressure measurements obtained *in vivo* are cyclic in nature, for comparison and computational purposes, it is useful to extract a single representative cycle. In the case of an ideal, periodic waveform, all the cycles are exactly the same so any individual cycle accurately describes all the other cycles. Physiologic pressure measurements are far from ideal, though, as illustrated by the pressure measurements in Figure 6.20. In addition to measurement errors, variations in heart rate, respiration, and cardiac output will cause the pressure waveform to be aperiodic. In this case, a single representative cycle could be obtained by simply computing the average of all the individual cycles. The waveform

can be divided into individual cycles by using information from an external trigger signal, which is synchronized with the pressure waveform, or by identifying a common point in the cycle, such as the minimum or maximum of the cycle.

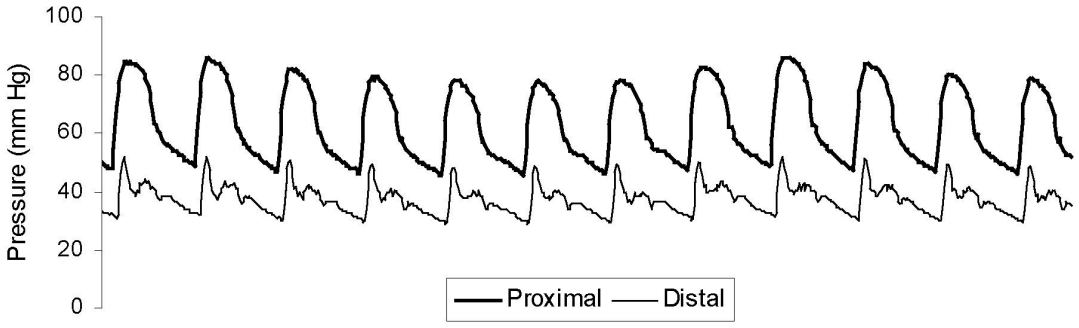


Figure 6.20: Pressure measurements acquired in the proximal and distal porcine aorta.

In this experiment, a MATLAB (The MathWorks, Inc., Natick, MA) program was written to identify the minimum points in a waveform and determine the individual cycles of the waveform (Figure 6.21(a)). While triggering information was available, the data did not provide consistent intervals, likely due to an occasional loss of signal. Furthermore, the plethysmograph location was often changed during the experiment because of signal loss, so the time delay between the trigger and a certain time point in the proximal or distal pressure waveform would vary. For these reasons, the minimum point in the proximal pressure waveform was used to divide both the proximal and distal waveforms into individual cycles.

Identification of the minimum points was done in two stages. The first stage required finding regions of the total waveform that were near the minimum of the waveform. A user-specified parameter determined the range of values that qualified as "near" the minimum. This parameter is especially useful for processing pressure data with respiratory effects, as is the case with the data in these experiments, since the cycle minimums increase and decrease with respiration. Regions that were separated by more than 3 points were assumed to belong to different cycles. The more-than-three-points separation was empirically determined and was needed to account for noise in the data. The second stage found the minimum within each region. These points were then used to determine the boundaries between individual cycles. In cases where multiple points were

associated with the minimum value, the point that occurred latest in time and closest to the rise in the waveform was used. Figure 6.21(a) shows a sample pressure waveform with the minimum points marked with x's. Using these minimum points, the pressure waveform was divided up into individual cycles, and averaged together, as shown in Figure 6.21(b). In order to perform the averaging, the cycles may need to be modified to be of the same length. The straightforward approach of truncating the longer cycles to be of the same length as the shortest cycle was used here. Typically, the cycle lengths only differed by one to three points. Compared with cycle lengths of at least 44 points, this was considered a minor and acceptable adjustment.

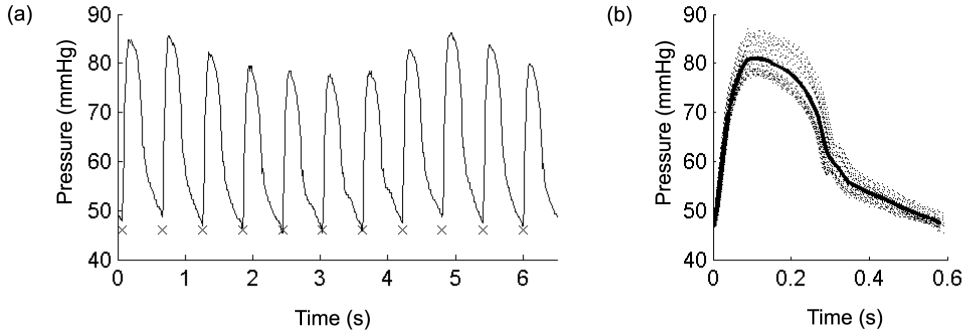


Figure 6.21: Obtaining an average representative cycle from a pressure waveform. (a) The minimum points of the waveform are identified and marked with an "x". The points are used to divide up the waveform into individual cycles. (b) The individual cycles, shown in the dotted lines, are averaged together to obtain a representative cycle, drawn in heavy black.

For comparison purposes, two quantities were computed for each waveform: the average pressure and the peak-to-peak pressure, which is simply the difference between the maximum and minimum pressure values. In most cases, multiple measurements were made for a given state (bypass-open or bypass-closed), so the average over these multiple measurements was used.

6.3.1.2 Flow

The custom software program vcalc was used to process the PC-MRI data to obtain flow waveforms. For all pigs except for Pig C, the through-plane flow was computed using the segmented k-space data for both the bypass-open (post-operative) and the bypass-closed (pre-operative) state. For Pig C, only 2D cine PC-MRI data was available, so flow information obtained from this data was used in the comparisons below. First-order

baseline correction factors, computed from the fatty and muscular regions in the image, were used in generating the flow waveforms, and a combination of thresholding and manual outlining techniques were used to determine the region of interest.

As with the pressure waveforms, the flow waveforms were characterized by their average and their peak-to-peak variation for comparison purposes. The measurements presented below represent the average of three waveforms: the inlet flow, the outlet flow, and the summation of the flow through the aorta and the graft (See Figure 6.1). Assuming that the flows through the vessels that branch off of the thoracic aorta were negligible, which should be true for most of the animals given that any noticeable intercostal arteries were ligated, then the inlet flow should be the same as the outlet flow and the sum of the aorta and graft flows.

6.3.1.3 Heart Rate

The heart rate information presented below was obtained from the anesthesia records that were maintained during the experiment. The measurements were obtained approximately every 15 minutes using the LifeWindow™ 6000 patient monitoring system (Digicare Biomedical Technology, Inc., West Palm Beach, FL) during the surgery portion of the experiment and the MRI-compatible patient monitoring system Magnitude® (Invivo Research, Inc., Orlando, FL) during the imaging portion of the experiment. For each pig, an average heart rate was computed for the bypass-open and the bypass-closed state. Note that Pig A's heart rate fluctuated between 40 to 90 beats per minute during the bypass-closed state, and a single number could not be obtained to represent the heart rate at a given time. For this reason, heart rate information is not provided for the bypass-closed state for Pig A.

6.3.2 Physiologic Results

Comparisons of the average and peak-to-peak pressure values for the bypass-open and bypass-closed state are shown in Figure 6.22. Measurements are given for both the proximal pressure, which was measured above the inlet flow plane, and the distal pressure, which was measured below the outlet flow plane. In all cases, the proximal pressure is greater than the distal pressure. Furthermore, the difference between the

average proximal and distal pressure is greater in the bypass-closed state than in the bypass-open state. A similar relationship is observed in terms of the peak-to-peak pressure measurements, where the proximal measurements are greater than the distal measurements. In all cases, the greatest peak-to-peak difference occurs with the proximal pressure waveform for the bypass-closed state, and the smallest difference is observed for the distal pressure waveform for the bypass-closed state. Note that pressure data was not available for all animals. For Pig A, errors were made in the data recording, so that the pressure measurements could not be identified. For Pig B, only one of the pressure catheters was functional, so only distal pressure measurements were obtained. With Pig G, the bypass graft did not occlude properly, so bypass-closed pressure measurements were not available for this animal.

Figure 6.23 shows the comparisons between flow measurements made under the bypass-open and bypass-closed conditions. Recall that these measurements were the average of the following (if the data were available): flow at the inlet, flow at the outlet, and the sum of flows through the aorta and the bypass. The average total flow for each pig with the bypass closed was slightly less than that with the bypass open. There was also a significant difference in the peak-to-peak variation of the flow waveforms, with the waveforms associated with the bypass-closed state showing much less variation than those of the bypass-open state. As mentioned previously, bypass-closed measurements were not available for Pig G. In addition, the bypass graft was slightly open in the "bypass closed" state for Pigs B and F, allowing a small amount of blood to flow through the graft. In these cases, the total flow was the sum of this small leak through the bypass and the flow through the aorta; in all other cases, the total flow for the bypass-closed state simply used the flow through the aorta.

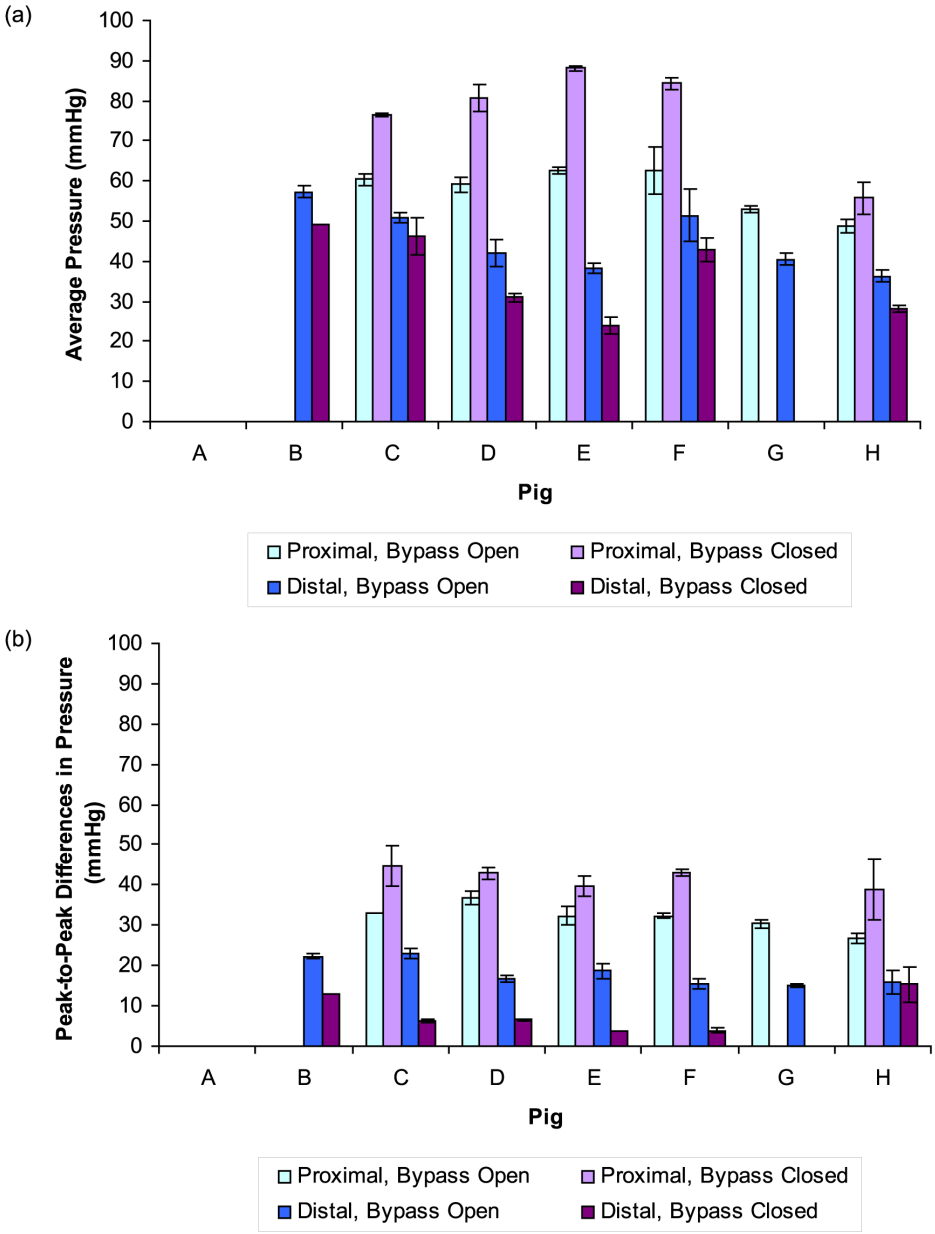


Figure 6.22: Comparison of pressure waveform characteristics for the bypass-open and bypass-closed state. (a) shows the change in the average pressure for both the proximal pressure, measured above the inlet flow plane, and the distal pressure, measured below the outlet flow plane. In all cases, the proximal pressure is greater than the distal pressure. Furthermore, the difference between the average proximal and distal pressure is greater in the bypass-closed state than in the bypass-open state. (b) demonstrates the changes in the peak-to-peak pressures for both the proximal and distal pressure waveforms. In all cases, the greatest difference occurs with the proximal pressure waveform for the bypass-closed state, and the smallest difference is observed for the distal pressure waveform for the bypass-closed state. The error bars represent ±1 standard deviation. Pressure data was not usable for Pig A, and only data from one of the pressure transducers was available for Pig B. Lastly, the bypass-closed state was not achieved for Pig G, so no data was available for this pig.

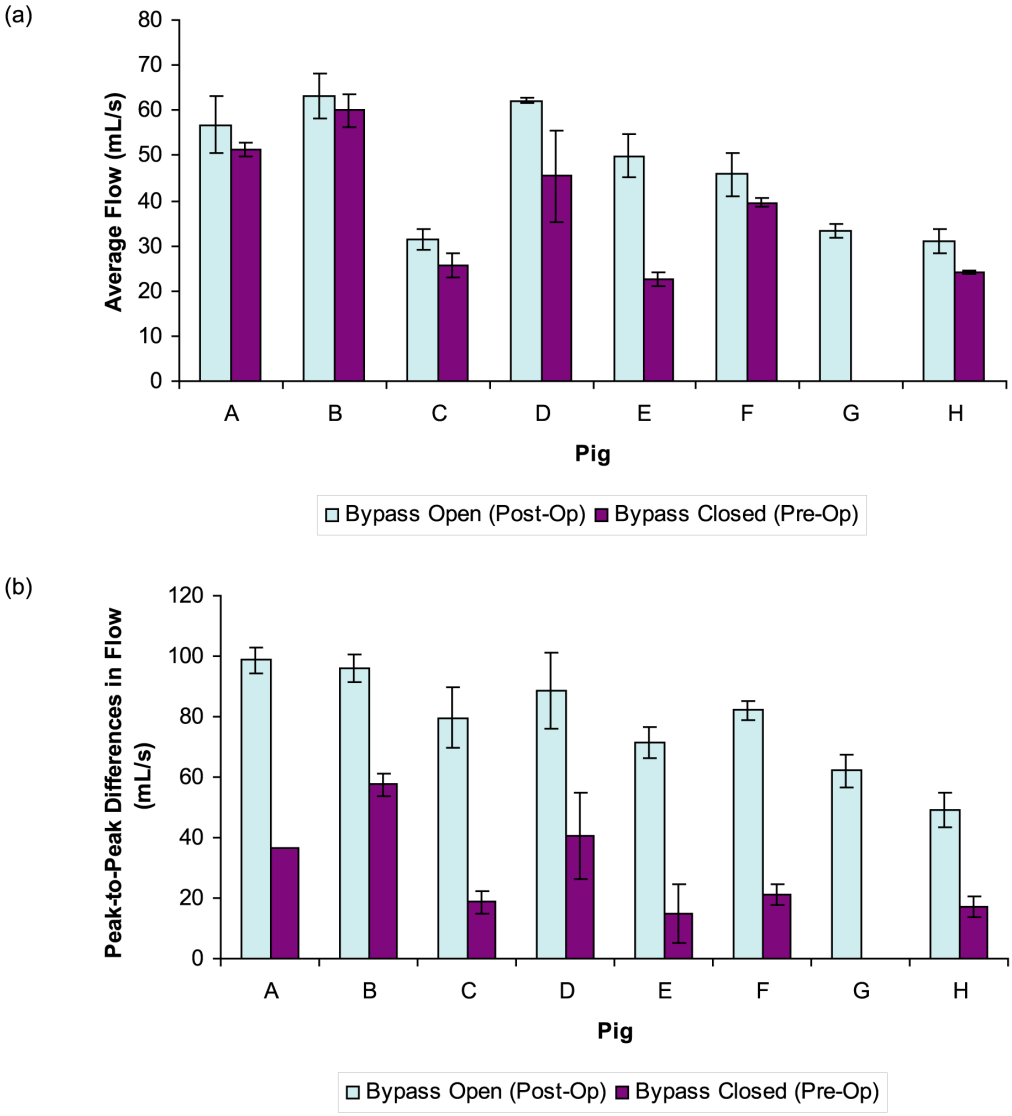


Figure 6.23: Comparison of flow waveform characteristics for the bypass-open and bypass-closed state. Note that the bypass was slightly open in the "bypass closed" state for Pigs B and F and that the bypass-closed state was not achieved for Pig G. (a) The average total flow through the aorta of each pig was slightly less with the bypass closed, as compared with the bypass-open condition. (b) There was a significant difference in the peak-to-peak variation of the flow waveforms, with the waveforms associated with the bypass-closed state showing much less variation than those of the bypass-open state. The error bars represent ±1 standard deviation.

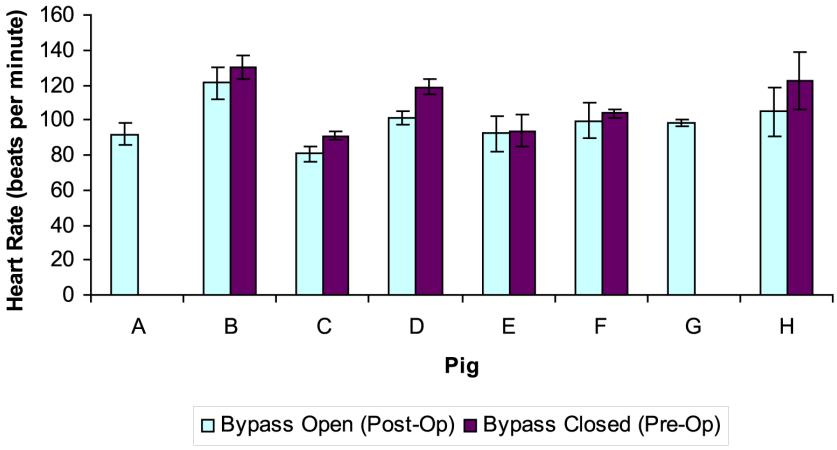


Figure 6.24: Comparison of average heart rates for the bypass-open and bypass-closed state. The heart rates for the bypass-closed state were slightly higher than the corresponding heart rates for the bypass-open state. Large fluctuations in the heart rate of Pig A in the bypass-closed state prevented the acquisition of data for this state, and the bypass-closed state was not achieved for Pig G.

Changes in the heart rate were less apparent. Figure 6.24 shows that the heart rates for the bypass-closed state were slightly higher than the corresponding heart rates for the bypass-open state. Large fluctuations in the heart rate of Pig A in the bypass-closed state prevented the acquisition of data for this state, and the bypass-closed state was not achieved for Pig G.

By analyzing the individual waveforms for each pig, a more detailed examination of the physiologic changes can be performed. Figure 6.25 shows the physiologic measurements for Pig F, which is representative of the waveforms observed in the other pigs. The data for all the pigs is presented in Appendix C. While the differences in the shapes of the flow waveforms for the bypass-open and the bypass-closed states are minimal, there is a noticeable difference in the shapes of the proximal pressure waveforms. The proximal waveform for the bypass-closed state has a sharp peak and two notches on either side of the main peak, whereas the proximal waveform for the bypass-open state has a broader peak and only the single notch following the main peak. In contrast, the distal pressure waveforms for the two different states are similar in shape, with a peak followed by a gentle rise in the pressure, a sharp drop, and then a gentle decrease in the pressure.

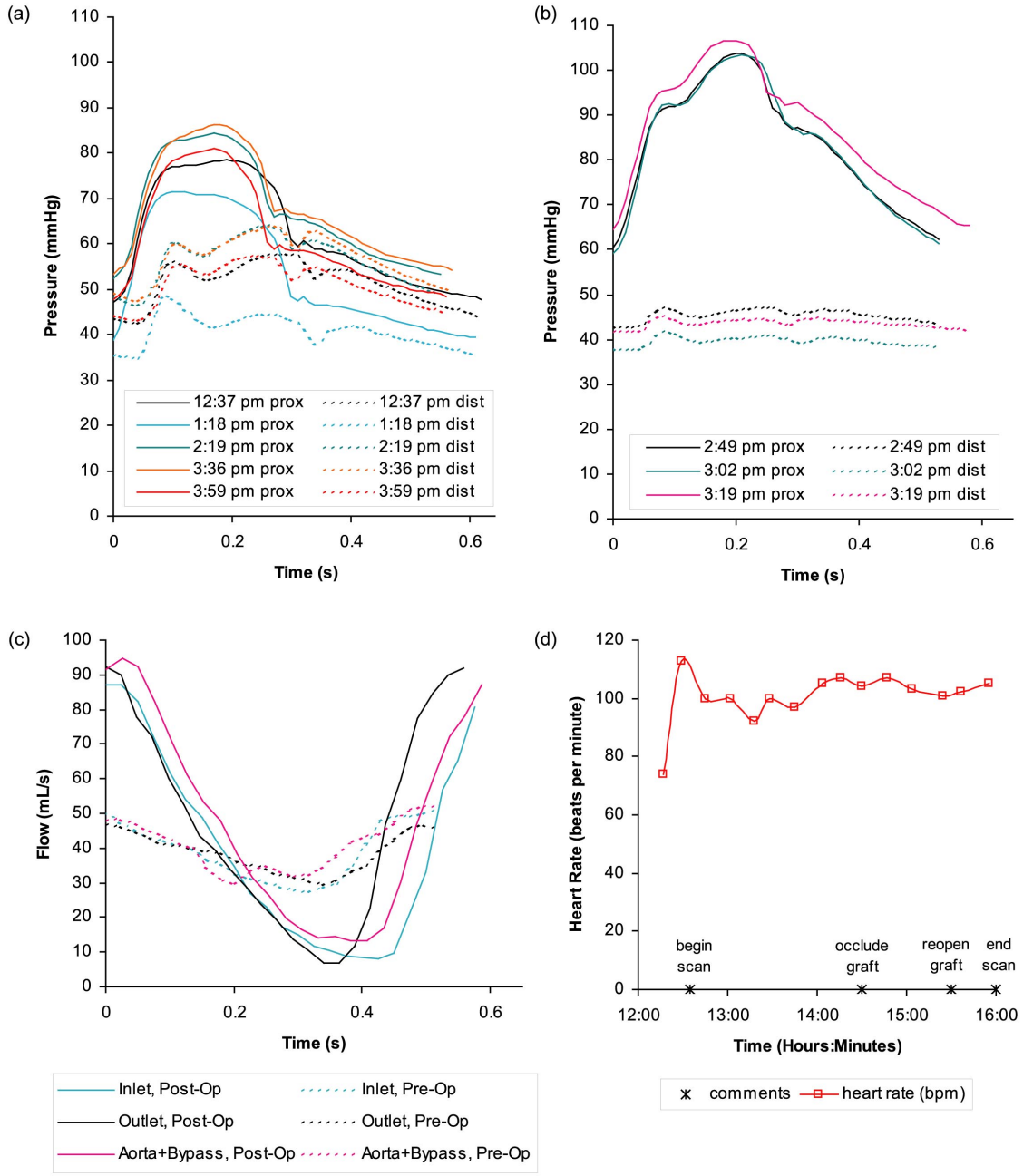


Figure 6.25: Physiologic changes observed in Pig F for the bypass-open and bypass-closed states. (a) Proximal (prox) and distal (dist) pressures measured at different times for the bypass-open state. (b) Proximal (prox) and distal (dist) pressures measured at different times for the bypass-closed state. (c) Total flow measurements, acquired with a segmented k-space PC-MRI sequence, for both the bypass open (Post-Op) and bypass closed (Pre-Op). (d) Variations in heart rate over the course of the experiment. Important events during the experiment are noted along the time axis.

6.3.3 Sensitivity of Pressure Measurements

In examining the pressure waveforms, it is useful to understand the variation present in the measurements. Over time, the pressure transducers will drift. The manufacturer cites a drift of less than 6 mmHg within 12 hours, and experimental data confirmed this. For the drift experiment, two pressure transducers were calibrated according to the method described in Section 6.1.3.2 and placed in vials of water. Periodic measurements were acquired using the system described in Section 6.1.3 over a 25-hour time period. The average pressure at each time point was then plotted against time to determine how much measurement drift had occurred (Figure 6.26). Transducer 1 had a 0.33 mmHg change in pressure over the first 12 hours and a 0.82 mmHg change over the entire experiment. The drift observed in transducer 2 was on the same scale: 1.12 mmHg over the first 12 hours and 1.85 mmHg over the entire experiment. The significance of this amount of drift will depend on the experiment. In the case of pressure measurements in a porcine aorta, where the pressures are on the order of tens of millimeters of mercury, a drift of 1.12 mmHg over 12 hours is relatively minor. The porcine experiments described here were conducted in under 10 hours.

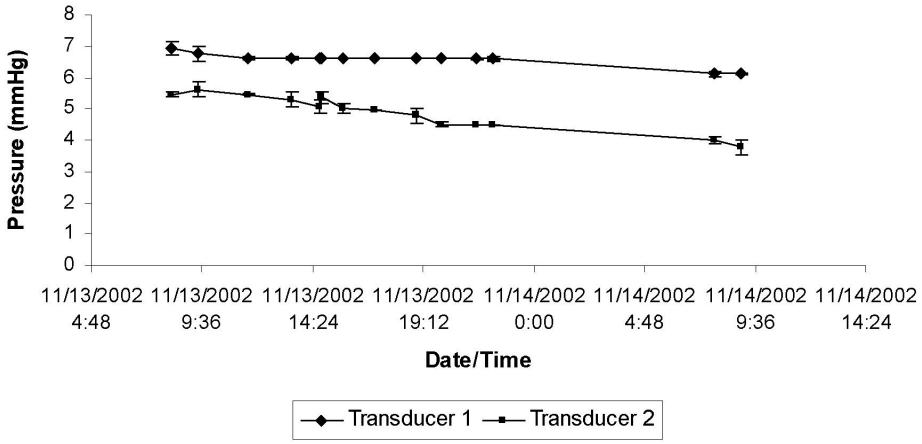


Figure 6.26: Determination of drift in pressure transducer measurements. Different transducers demonstrate different amounts of drift. The maximum difference observed in pressure measurement was 1.85 mmHg. The error bars indicate the standard deviation in pressure measurements for a given time point.

6.3.4 Discussion

Noticeable changes in physiology were measured between the bypass-open and the bypass-closed states. The physiology observed in these experiments are consistent with theory. As explained in Section 2.1.2, blood flow through vessels can be characterized by a resistance, based upon the radius of the vessel. A stenosed vessel would have a small radius, and thereby a very high resistance. With the bypass open, a parallel network of resistances exist, with a high resistance due to the stenosis and a low resistance due to the bypass (Figure 6.27). The total resistance due to the stenosis-bypass combination is

$$\frac{R_{stenosis} \cdot R_{bypass}}{R_{stenosis} + R_{bypass}} \tag{6.1}$$

where $R_{stenosis}$ is the resistance of the stenosis, and R_{bypass} is the resistance of the bypass. Since $R_{stenosis}$ is much greater than R_{bypass}, the total resistance can be approximated as R_{bypass}, which is lower than the resistance of the stenosis alone. These differences in resistances result in changes in the pressures and flows, as given by Equation (2.5). If there is an increase in resistance, either the pressure drops must increase and/or the flows must decrease. According to the measurements made in this study, changes in both pressures and flows occurred. In going from the bypass-open to the bypass-closed state, an increase in the difference between the average proximal and distal pressures, as well as a decrease in the average flows, was observed for all the pigs.

The increase in the pressure drop depended on changes in both the proximal and distal pressures. When the bypass, initially open, was closed, the distal pressure dropped and the proximal pressure increased. The change in the distal pressure could be attributed to the pressure drop across the stenosis, as well as to the downstream arterial dilation due to the endothelium response to changes in shear stress, which occur due to changes in flow. The increase in the proximal pressure corresponds to the heart's response to the higher total resistance seen in the bypass-closed state. This resistance is often referred to as the afterload. A higher afterload causes the heart to contract more forcefully, thereby producing a higher pressure.

The changes observed in the heart rate are also consistent with the theory that the bypass-closed condition results in a higher total resistance, or afterload. With the larger afterload, the heart needs to work harder to output the same amount of blood. One consequence of this was mentioned previously: the increase in the proximal pressure. Another consequence is a higher heart rate, since the heart is able to output more blood per beat.

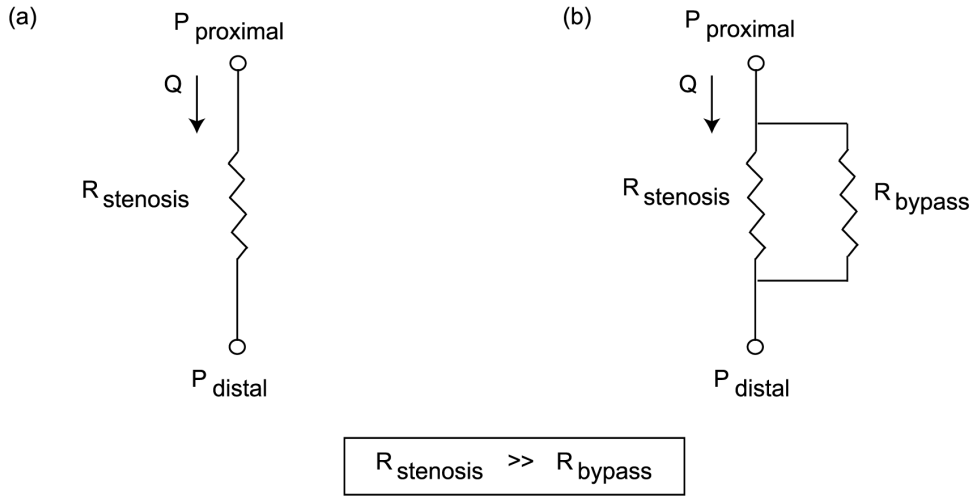


Figure 6.27: Circuit representations of (a) the stenosis (bypass-closed condition) and (b) the stenosis and bypass (bypass-open condition). The total resistance for the circuit in (a) is $R_{stenosis}$. For the circuit in (b), the total resistance is approximately R_{bypass}, assuming $R_{stenosis}$ is much greater than R_{bypass}. P represents pressure, and Q indicates flow.

The differences in the shapes of the physiologic waveforms can also be explained using an electrical analogue. Wave reflections, an idea introduced in Section 2.1.3, occur wherever there is an impedance mismatch, such as at points where the vessel diameter changes, and can amplify or diminish the pressure and flow waveforms, depending on the nature of the reflection. Since impedance at a frequency of 0 Hz is simply resistance, a basic analysis using the circuit models in Figure 6.27 can be performed to understand the changes observed in the physiologic waveforms when the bypass is opened or closed.

Again, the total resistance for the bypass-closed state is much greater than that of the bypass-open state. It is also reasonable to assume that both these resistances were greater than the resistance of the normal aorta upstream of the surgical area. Therefore, from Equation (2.10), the reflected pressure wave for the bypass-closed state will be greater

than that for the bypass-open state. Because the amplitude of the reflected pressure wave has the same sign as that of the incident wave, the amplitude of the final waveform, which is the summation of the reflected and incident waves, is greater than that of either of the individual waves. The larger amplitude of the reflected wave for the bypass-closed state could account for the extra peak and two notches, and therefore the larger peak-to-peak pressure, observed for the proximal pressure waveform. On the other hand, the downstream resistances for the bypass-open state are assumed to be larger than for the bypass-closed state, due to the endothelial response described previously. This would lead to a larger reflected pressure waveform, and subsequently, a larger peak-to-peak variation in the distal pressure waveform for the bypass-open state, as is observed in the data. While a similar analysis could be applied to the flow waveforms via Equation (2.11), [70] indicates that wave reflections do not have a large influence on the final flow waveforms, so the changes observed in the flow waveforms are likely just due to changes in afterloads.

6.3.5 Conclusion

Significant changes in physiology were observed between the bypass-open and the bypass-closed state. For the bypass-open state, the proximal pressures had a lower average and a smaller peak-to-peak difference. In contrast, the distal pressures had a higher average and a larger peak-to-peak difference. Overall, this results in a smaller pressure gradient for the bypass-open state, as compared with the bypass-closed state. The bypass-open state also produced higher average flows and higher peak-to-peak flow values. Furthermore, the heart rate was slightly lower for the bypass-open condition.

With the bypass-closed state representing a pre-operative condition and the bypass-open state representing a post-operative situation, the physiologic changes observed in these experiments are useful for developing a model to determine parameters needed for numerical simulations which are used to predict the outcomes of a bypass surgery. As discussed above, the differences observed in the pressures and flows between the bypass-open and the bypass-closed conditions qualitatively agree with current models of

impedance and wave reflection, suggesting that a method could be developed to quantitatively predict these waveforms for post-operative simulation purposes.

Chapter 7

Conclusions and Future Work

A conclusion is the place where you got tired thinking.
~Martin Henry Fischer

7.1 Contributions and Significance

While numerical simulations could potentially improve surgical outcomes through the predictions of flow distributions and velocity patterns, they must first be validated against direct experimental measurements. Previous *in vitro* and *in vivo* investigations have been limited in terms of the geometries and flow conditions studied and in the assumptions made for the numerical simulations. The comparison studies presented in this thesis expanded the range of conditions under which the numerical simulations have been evaluated and demonstrated the favorable agreement between the numerically computed results and the PC-MRI measurements.

Chapters 4 and 5 discussed results from *in vitro* experiments performed in a phantom model of a stenosed vessel with a bypass graft. This geometry, with the loop structure created by the bypass graft, was more complex than had previously been studied. Furthermore, the average Reynolds numbers at the inlet reached 766, higher than in other validation experiments. This higher Reynolds number resulted in complex flows that made the comparisons between the numerical simulations and the PC-MRI measurements more challenging. An important insight was the need for temporal averaging of the numerical results when comparing against PC-MRI measurements, particularly in regions of non-periodic velocities. Spatial averaging of the simulations was also necessary for

some locations. Excellent agreement in both the flow distributions and the through-plane velocity patterns was obtained for both the lower and higher Reynolds number problems for this geometry.

Chapter 6 described comparisons between the numerical simulations and PC-MRI for an *in vivo* experiment involving a similar geometry: a bypass graft sewn around a stenosis. Unlike many previous studies, the simulations in this study assumed no *a priori* knowledge of the flow distribution between vessels, and therefore are the first examples of the simultaneous prediction of flow distributions and velocity profiles in *in vivo*, subject-specific models. The high inlet Reynolds numbers and the complex geometries with the extremely tight stenosis and the loop structure further increased the difficulty in obtaining accurate solutions. Despite these challenges, reasonable agreement was obtained between the numerical results and the PC-MRI measurements. Based on results from eight animals, the average flow rates differed by less than 2.7 mL/s and the flow distributions were within 10.6% of each other. In terms of the velocity comparisons for the one animal, the magnitudes of the through-plane velocities were in excellent agreement, and for most of the time points, the regions of low and high velocities in the two data sets corresponded well.

In addition to the comparisons between the numerically computed results and PC-MRI, sensitivity studies were conducted for both the numerical simulations and the PC-MRI measurements. Chapter 3 examined the effect of imaging parameters, such as the repetition time and the angle of the prescribed plane, on the PC-MRI data. The influence of post-processing steps, such as baseline error correction and temporal smoothing, on the PC-MRI velocity measurements was also investigated. The sensitivity of the numerical simulation results to changes in geometry and inlet boundary conditions were discussed throughout Chapters 4 to 6.

Lastly, the hemodynamic conditions were quantified in the porcine model for the bypass-open versus bypass-closed state. Section 6.3 described the changes in the pressures, flows and heart rates under these different states. With the bypass closed, an increase in the pressure drop across the stenosis, an increase in the peak-to-peak proximal pressures, and a decrease in the peak-to-peak distal pressures were observed. Under the

bypass closed condition, a decrease in the average and peak-to-peak flows was also noticed. These findings are consistent with a resistance network model and suggest a possible method for predicting boundary conditions for numerical simulations for surgical planning purposes.

While it is unknown how accurate blood flow simulations need to be in order to be useful to physicians, the results of these experiments indicate that flow distributions and velocity patterns predicted using numerical simulations compare favorably with PC-MRI measurements. This suggests that given only input velocity information and a geometric model, computational methods can be used to predict flow rates and velocity patterns for bypass graft procedures similar to the ones studied in this thesis, an important development in the move towards simulation-based surgical planning. Investigations into the changes in boundary conditions under the bypass-open and bypass-closed states and the identification of limitations of PC-MRI and the numerical simulations provide a starting point for further research and development of simulation-based surgical planning techniques.

7.2 Recommendations for Future Investigations

One of the ultimate applications for these finite-element-based numerical simulations of blood flow is surgical planning. While the work presented in this thesis is a significant step towards the realization of this goal, considerable work remains to be done. Improvements in both the numerical simulations and the imaging technology, combined with further experiments, will be necessary before numerical predictions become clinically useful and accepted.

With the ever-increasing power of computers, some of the current limitations of the numerical simulations will naturally be overcome. Simulations will be able to be run in a more reasonable time period with larger mesh sizes and more time steps per cycle, leading to more accurate solutions. The improvements in computational power also make it more practical to increase the complexity of the simulations, allowing the incorporation of more physiologically realistic conditions, such as compliant vessel walls,

and potentially improving the accuracy of the simulation results for *in vivo* applications. One of the more difficult challenges will be the assignment of correct boundary conditions. In this work, the simulations used a geometry with a single inlet and outlet and simplifying assumptions that allowed a zero pressure boundary condition to be applied to the outlet. It is unclear as to what the appropriate boundary conditions would be for a multiple-outlet model. Furthermore, in order to use the numerical simulations for surgical planning, a model needs to be developed in which the boundary conditions for the post-operative model are predicted from information available from the pre-operative state.

Because numerical simulations for surgical planning purposes need to be patient-specific, they require accurate anatomic and physiologic data. The current imaging modality of choice for *in vivo* applications is MRI because it can simultaneously provide three-dimensional anatomic data and three-components of velocity within a given volume of space. However, there are limitations with this technique, including imaging artifacts inherent in the method. Developing PC-MRI sequences that utilize shorter T_R and T_E values will minimize some of these effects, particularly for regions of relatively high velocities. Improvements in the spatial resolution would also be useful for constructing more accurate geometric models, and the development of an efficient method to account for the variable range in velocities over a cardiac cycle could decrease the noisiness of the measurements.

One of the major drawbacks of PC-MRI is the spatial and temporal averaging that naturally occurs during data acquisition. In order to fairly compare the numerical simulation results against the PC-MRI measurements, the computed results were spatially and temporally averaged in an attempt to mimic what occurs with the PC-MRI data. However, few studies have examined PC-MRI measurements for non-periodic flow phenomena. Investigations into the exact nature of the PC-MRI measurements of non-periodic velocities and development of a similar method for post-processing the numerical results could yield better agreement than the current method of simple averaging and could potentially lead to other uses of the computational methods, such as simulating PC-MRI imaging artifacts. Ideally, though, an *in vivo* technique that provided

more instantaneous velocity measurements would replace, or be used in conjunction with, PC-MRI to validate the numerical simulation results, so that the accuracy of the computations for individual cycles could be assessed.

Lastly, and perhaps most importantly, additional experiments need to be conducted comparing the results of the numerical simulations to physical measurements. *In vitro* experiments are useful because they are much simpler and more controlled than *in vivo* experiments. In particular, it would be valuable to conduct *in vitro* experiments to determine the validity of the numerical simulation predictions when in-plane velocity components are prescribed at the inlet. Inaccurate in-plane components at the inlet have been suspected to cause differences between numerically computed velocity patterns and measured results. They may also be the reason that some simulation solutions diverge and cannot be run to completion. *In vivo* experiments for a broad range of geometries and flow conditions will also be needed to demonstrate the robustness of the numerical simulations for surgical planning purposes. With these additional validation studies and with the continuing advancements in numerical simulation methods and imaging techniques, numerical simulations will have a role in vascular surgery planning in the future.

Appendix A

Effect of Repetition Time on Flow Measurements

Preliminary experiments were conducted to assess the effect of the repetition time T_R on the PC-MRI acquired flow measurements. These experiments used the same set-up as that described in Section 3.2. The imaging parameters for the standard 2D cine PC-MRI sequence were: slice thickness = 5.0 mm, FOV = 240 x 240 mm^2, acquisition matrix of 256 x 256, T_E = 5.028 ms, NEX = 1, flip angle of 20^o, bandwidth of 16.0 kHz, an in-plane v_{enc} of 500 mm/s, and a through-plane v_{enc} of 1500 mm/s. Data was acquired using two different T_R values: 19 ms and 33 ms. In addition, a custom cine PC-MRI sequence with improvements that could potentially shorten the T_R values [124] was used to acquire flow measurements with the same imaging parameters as above except with an even shorter T_R of 10 ms, a T_E of 4.004 ms, and a bandwidth of 62.5 kHz. Additional measurements were acquired with a segmented k-space sequence with the following imaging parameters: slice thickness = 5.0 mm, FOV = 240 x 240 mm^2, acquisition matrix of 256 x 192, T_E = 3.3 ms, T_R = 7.1 ms, NEX = 1, flip angle of 30^o, bandwidth of 31.25 kHz, 4 views per segment, a through-plane v_{enc} of 1500 mm/s. These measurements were collected with the flow pump cycling at 75 cycles/minute and with the flow pump off. A first-order baseline error correction was determined from the flow-pump-off images, and the flow rates were computed using the custom software vcalc. The standard 2D cine PC-MRI sequences and the segmented k-space PC-MRI sequence were repeated for the flow pump cycling at 100 cycles/minute, and the data was processed as for the 75 cycles/minute measurements.

The results are shown in Figure A.1. In general, the effective temporal resolution was inversely related to the amount of dampening that occurred in the flow waveforms. An

inverse relationship was also observed between the average flows and the effective temporal resolution. For the 75 cycles/minute, the average flows were 17.9 mL/s, 21.7 mL/s, 23.9 mL/s, and 27.5 mL/s for the segmented k-space data, the custom cine PC-MRI measurements, the standard cine data (T_R=19 ms), and the standard cine data (T_R=33 ms), respectively. For the 100 cycles/minute, the average flows were 25.3 mL/s, 30.6 mL/s, and 34.1 mL/s for the segmented k-space data, the standard cine data (T_R=19 ms), and the standard cine data (T_R=33 ms), respectively.

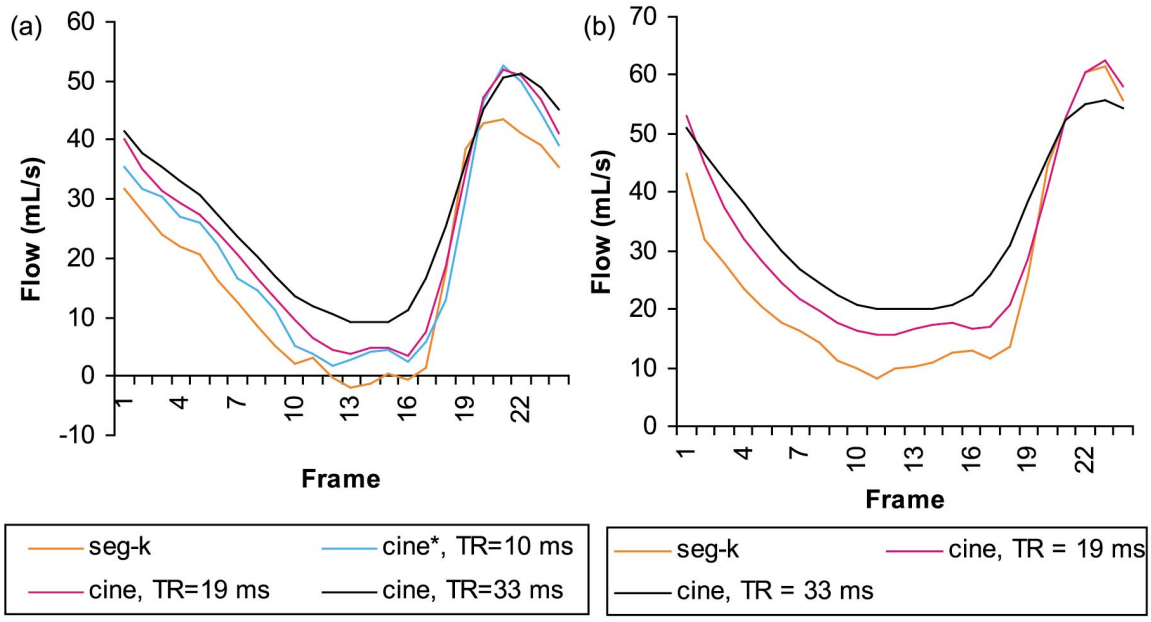


Figure A.1: Comparison of PC-MRI measurements for 2D-cine sequences with different T_R values for flow output at (a) 75 cycles/minute and (b) 100 cycles/minute. Measurements acquired using a segmented k-space sequence are provided as additional reference. The cine* sequence refers to the custom cine PC-MRI sequence that could potentially shorten the T_R values.

Appendix B

Spectrum Input File

```
ECHO
ECHO "Stanford Cardiovascular Biomechanics Lab
ECHO "======================================================="
ECHO
ECHO "    Flow in aorta"
ECHO
ECHO "Problem Description"
ECHO "-------------------"
ECHO "    Geometry:  Pig 12"
ECHO "                      "
ECHO "    Loading:   True velocity input, peak flow velocity =  cm/sec"
ECHO "                   zero pressure at output"
ECHO "    Materials: Blood"
ECHO "    Mesh:       nodes,  tetrahedral elements"
ECHO "    Analysis:  Nonlinear, transient, incompressible,"
ECHO "               isothermal"
ECHO "    Targets:   "
ECHO "               "
ECHO "               "
ECHO "    Units:     CGS"
ECHO
ECHO "Computational Resources"
ECHO "-----------------------"
ECHO "    Machine:   SGI Octane"
ECHO "    CPU:        hours"
ECHO "    Memory:    Mbytes"
ECHO "    Disk:       Mbytes"
ECHO

#-----------------------------------------------------------------------
# Problem and database
#-----------------------------------------------------------------------

DEFINE_PROBLEM               \
    name    = "pig12"      \
    title   = "Pulsatile flow in pig 12" \
    static  = off             \
    solid   = off            \
    type    = nonlinear      \
    dynamic = on            \
```

```
    fluid   = on             \
    parallel = on


# +-----------------------------------------------
# | TI-INCOMP-ISO
# +-----------------------------------------------

TIME_INTEGRATION_ALGORITHM     \
    equation = incompressible_isothermal \
    alpha    = 0.8             \
    gamma    = 0.7

#-----------------------------------------------------------------------
# State law for water
#-----------------------------------------------------------------------

DEFINE_STATE_LAW_MODEL         \
    name    = "blood"          \
    type    = constant_density \
    density = 1.06e+00

#-----------------------------------------------------------------------
# Viscous material properties
#-----------------------------------------------------------------------

DEFINE_MATERIAL_MODEL \
    name = "blood"    \
    type = fluid

    STRESS_MODEL                        \
        type      = constant_viscosity \
        viscosity = 0.04

    SCALAR_DIFFUSION_MODEL                       \
        diffusion_coefficient = 1.e-7

#-----------------------------------------------------------------------
# Fluid region
#-----------------------------------------------------------------------

DEFINE_REGION                          \
    name            = "fluid region" \
    type            = fluid          \
    state_law_model = "blood"        \
    num_processes   = 30

    DEFINE_EQUATION                          \
        type    = incompressible_isothermal \
        subtype = navier_stokes

    COORDINATE file = "coordinates"

#-----------------------------------------------------------------
```

```
# Continuum element set
#-----------------------------------------------------------------

    DEFINE_ELEMENT_SET                      \
        name           = "fluid elements" \
        shape          = four_node_tet\
        material_model = "blood"

        ELEMENT_NODES file = "connectivity"

        # +-------------------------------------------------
        # | TECHNOLOGY
        # +-------------------------------------------------

        ELEMENT_TECHNOLOGY                                  \
               residual_control = off
#               cfl_number = 10.0                            \

#-------------------------------------------------------------------------
# Inlet boundary conditions
#-------------------------------------------------------------------------

    DEFINE_NODAL_BOUNDARY_CONDITION_SET \
        name = "inlet nodes"

        INCLUDE_BOUNDARY_CONDITION_NODE file = "inlet.nbc"

        DEFINE_NODAL_BOUNDARY_CONDITION                 \
               type = user_defined                          \
               variable = x_velocity                   \
                   function_name = "Time-Space Varying NBC"

                   USER_NODAL_BOUNDARY_CONDITION_PARAMETERS value = 1

        DEFINE_NODAL_BOUNDARY_CONDITION                 \
               type = user_defined                          \
               variable = y_velocity                   \
                   function_name = "Time-Space Varying NBC"

                   USER_NODAL_BOUNDARY_CONDITION_PARAMETERS value = 2

        DEFINE_NODAL_BOUNDARY_CONDITION                 \
               type = user_defined                          \
               variable = z_velocity                   \
                   function_name = "Time-Space Varying NBC"

                   USER_NODAL_BOUNDARY_CONDITION_PARAMETERS value = 3



#-------------------------------------------------------------------------
# Outlet boundary conditions
#-------------------------------------------------------------------------
```

```
    DEFINE_ELEMENT_SET \
        name = "fluid elements"

        DEFINE_ELEMENT_BOUNDARY_CONDITION_SET \
            name  = "outlet_elements"        \
            shape = three_node_tri

            ELEMENT_BOUNDARY_CONDITION_NODES file = "outlet.ebc"

            DEFINE_ELEMENT_BOUNDARY_CONDITION    \
                type     = zero \
                variable = pressure

            DEFINE_ELEMENT_BOUNDARY_CONDITION    \
                type     = internally_defined    \
                variable = tangential_1_traction

            DEFINE_ELEMENT_BOUNDARY_CONDITION    \
                type     = internally_defined    \
                variable = tangential_2_traction

#-------------------------------------------------------------------------
# Wall boundary conditions
#-------------------------------------------------------------------------

    DEFINE_NODAL_BOUNDARY_CONDITION_SET \
        name = "wall nodes"

        INCLUDE_BOUNDARY_CONDITION_NODE file = "skin.nbc"

        DEFINE_NODAL_BOUNDARY_CONDITION \
            type     = zero             \
            variable = x_velocity

        DEFINE_NODAL_BOUNDARY_CONDITION \
            type     = zero             \
            variable = y_velocity

        DEFINE_NODAL_BOUNDARY_CONDITION \
            type     = zero             \
            variable = z_velocity

#-------------------------------------------------------------------------
# Initial conditions
#-------------------------------------------------------------------------

    DEFINE_NODAL_INITIAL_CONDITION \
        type     = zero            \
        variable = pressure

    DEFINE_NODAL_INITIAL_CONDITION \
        type     = zero            \
        variable = velocity
```

```
# +-------------------------------------------------
# | VISUALIZATION-OUTPUT
# +-------------------------------------------------

VISUALIZATION_OUTPUT                                  \
       pressure = on                                  \
       velocity = on                                  \
       time_step_frequency = 20                        \
       vorticity = off                                 \
       stress = on

#-----------------------------------------------------------------------
# Solution statistics output
#-----------------------------------------------------------------------

SOLVER_STATISTICS_OUTPUT                \
    time_step_frequency           = 20   \
    time_step_statistics          = on   \
    analysis_statistics           = on   \
    performance_statistics        = on   \
    two_norm_residual_information = on   \
    max_norm_residual_information = off  \
    time_increment_history        = on

#-----------------------------------------------------------------------
# Restart output every 50 steps
#-----------------------------------------------------------------------

RESTART_OUTPUT               \
    time_step_frequency = 240 \
    final_time          = on  \
    save                = 5

#-----------------------------------------------------------------------
----
# Solution strategy
#-----------------------------------------------------------------------
----

TIME_SEQUENCE                                  \
    final_time                         = 14.24    \
    initial_time_increment             = 0.00129   \
    max_time_steps                     = 11040   \
    exit_on_steady_state               = off   \
    exit_on_steady_state_delay         = 0  \
    automatic_time_increment_selection = off    \
    reform_lhs_initial_times           = 11040   \
    reform_lhs_frequency               = 1     \
    reform_lhs_on_divergence           = 1     \
    min_time_increment                 = 0    \
    max_time_increment                 = 1.0  \
    time_increment_increase_factor     = 1.2   \
    time_increment_increase_delay      = 10    \
```

```
    redo_time_step_decrease_factor     = 0.5 \
    redo_time_step_min_ratio           = 0.1  \
    redo_time_step_on_divergence       = 0    \
    cfl_control                        = off  \
    truncation_error_control           = on  \
    truncation_error_tol               = 0.1

#-------------------------------------------------------------------------
----
# Stagger setup
#-------------------------------------------------------------------------
----

STAGGER_CONTROL \
    stagger1                                = "incompressible velocity
analysis" \
    stagger2                                = "incompressible pressure
analysis" \
    min_iterations                          = 1 \
    max_iterations                          = 2\
    convergence_check                       = off \
    redo_time_step_on_divergence            = 0 \
    reform_lhs_initial_times                = 0 \
    reform_lhs_frequency                    = 0 \
    reform_lhs_on_divergence                = 1 \

DEFINE_STAGGER \
    name                                    = "incompressible velocity
analysis" \
    type                                    = augmented_lagrangian \
    activation_time                         = 0 \
    activation_interval                     = 0 \
    deactivation_time                       = 0 \

INCLUDE_EQUATION \
    type                                    = incompressible_isothermal
\
    variable                                = velocity \
    residual_convergence_check              = on \
    residual_convergence_tol                = 0.001 \
    residual_divergence_threshold           = 1 \
    residual_assumed_zero                   = 1e-10 \
    solution_increment_check                = on \
    solution_increment_convergence_tol      = 0.001 \
    solution_increment_divergence_threshold = 10 \
    solution_increment_assumed_zero         = 1e-10 \

AUGMENTED_LAGRANGIAN_PARAMETERS \
    min_iterations                          = 1 \
    max_iterations                          = 1 \
    convergence_check                       = on \
    redo_time_step_on_divergence            = 0 \
    reform_lhs_initial_times                = 0 \
    reform_lhs_frequency                    = 0 \
```

```
    reform_lhs_on_divergence                = 0 \
    lagrange_multiplier                     = on \

NONLINEAR_ITERATION_PARAMETERS \
    min_iterations                          = 1 \
    max_iterations                          = 1 \
    convergence_check                       = on \
    redo_time_step_on_divergence            = 0 \
    reform_lhs_initial_times                = 0 \
    reform_lhs_frequency                    = 0 \
    reform_lhs_on_divergence                = 0 \

GLOBAL_STAGGER_DRIVER \
    type                                    = gmres \
    num_krylov_vectors                      = 30 \
    max_gmres_cycles                        = 10 \
    convergence_tol                         = 0.02 \
    divergence_threshold                    = 0.1 \
    preconditioner                          = block_diagonal \

DEFINE_STAGGER \
    name                                    = "incompressible pressure
analysis" \
    type                                    = augmented_lagrangian \
    activation_time                         = 0 \
    activation_interval                     = 0 \
    deactivation_time                       = 0 \

INCLUDE_EQUATION \
    type                                    = incompressible_isothermal
\
    variable                                = pressure \
    residual_convergence_check              = on \
    residual_convergence_tol                = 0.001 \
    residual_divergence_threshold           = 1 \
    residual_assumed_zero                   = 1e-10 \
    solution_increment_check                = on \
    solution_increment_convergence_tol      = 0.001 \
    solution_increment_divergence_threshold = 10 \
    solution_increment_assumed_zero         = 1e-10 \

AUGMENTED_LAGRANGIAN_PARAMETERS \
    min_iterations                          = 1 \
    max_iterations                          = 1 \
    convergence_check                       = on \
    redo_time_step_on_divergence            = 0 \
    reform_lhs_initial_times                = 0 \
    reform_lhs_frequency                    = 0 \
    reform_lhs_on_divergence                = 0 \
    lagrange_multiplier                     = on \

NONLINEAR_ITERATION_PARAMETERS \
    min_iterations                          = 1 \
    max_iterations                          = 1 \
```

```
    convergence_check                       = on \
    redo_time_step_on_divergence            = 0 \
    reform_lhs_initial_times                = 0 \
    reform_lhs_frequency                    = 0 \
    reform_lhs_on_divergence                = 0 \

GLOBAL_STAGGER_DRIVER \
    type                                    = conjugate_gradient \
    max_iterations                          = 1394 \
    num_projection_vectors                  = 10 \
    convergence_tol                         = 0.1 \
    divergence_threshold                    = 10 \
    preconditioner                          = block_diagonal \

DEFINE_SUBDOMAIN \
    name                                    = "fluid subdomain" \

INCLUDE_REGION \
    type                                    = all_fluids \

SUBDOMAIN_STAGGER_SOLVER \
    stagger                                 = "incompressible velocity
analysis" \
    type                                    = implicit_iterative \
    subtype                                 = gmres \
    lhs_storage_type                        = matrix_free \
    preconditioner                          = none \

SUBDOMAIN_STAGGER_SOLVER \
    stagger                                 = "incompressible pressure
analysis" \
    type                                    = implicit_iterative \
    subtype                                 = conjugate_gradient \
    lhs_storage_type                        = matrix_free \
    preconditioner                          = none \


# +-------------------------------------------------
# | Execute Solver...
# +-------------------------------------------------


#RUN_SOLVER program = "/u/joyku/inp_bcs/userSlvKern"
RUN_SOLVER mode = batch

#RUN_SOLVER mode = data_check

#EndOfFile
```

Appendix C

Physiology Observed With Open and Occluded Bypass Grafts

A summary of the physiologic changes that occur with a bypass graft open (a condition that simulates a post-operative state) versus with a bypass graft closed (a situation similar to a pre-operative situation) was described in Section 6.3. In this appendix, detailed graphs of the pressures, flows, and heart rates are presented for each pig in that study.

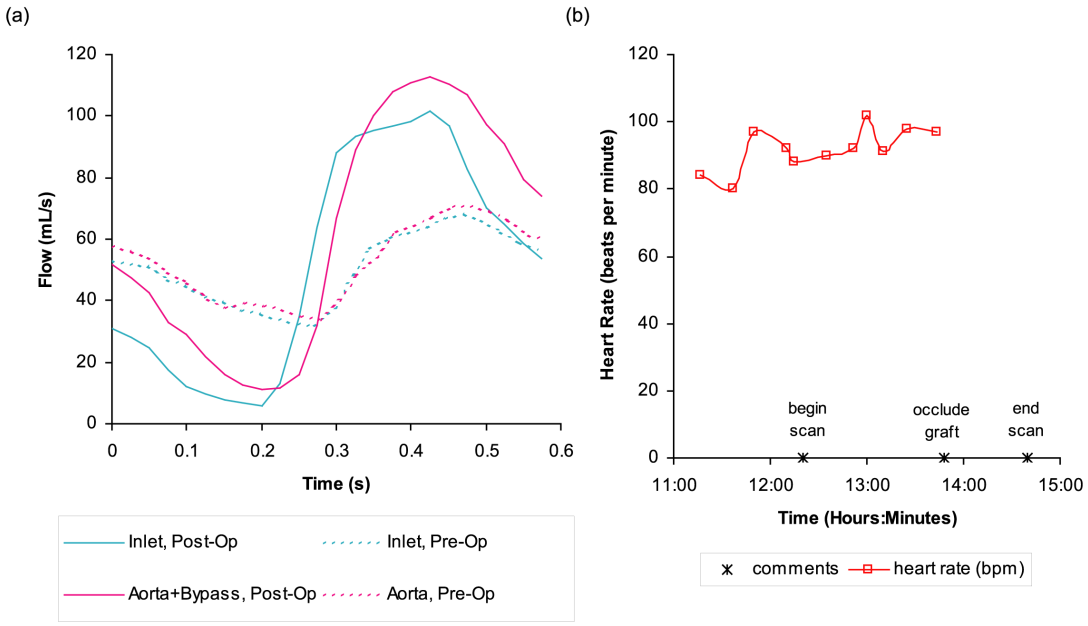


Figure C.1: Physiologic changes observed in Pig A for the bypass-open and bypass-closed states. Pressure data, outlet flow information, and heart rate information for the bypass-closed state were not available for this animal. (a) Total flow measurements, acquired with a segmented k-space PC-MRI sequence, for both the bypass open (Post-Op) and bypass closed (Pre-Op). (b) Variations in heart rate over the course of the experiment. Important events during the experiment are noted along the time axis.

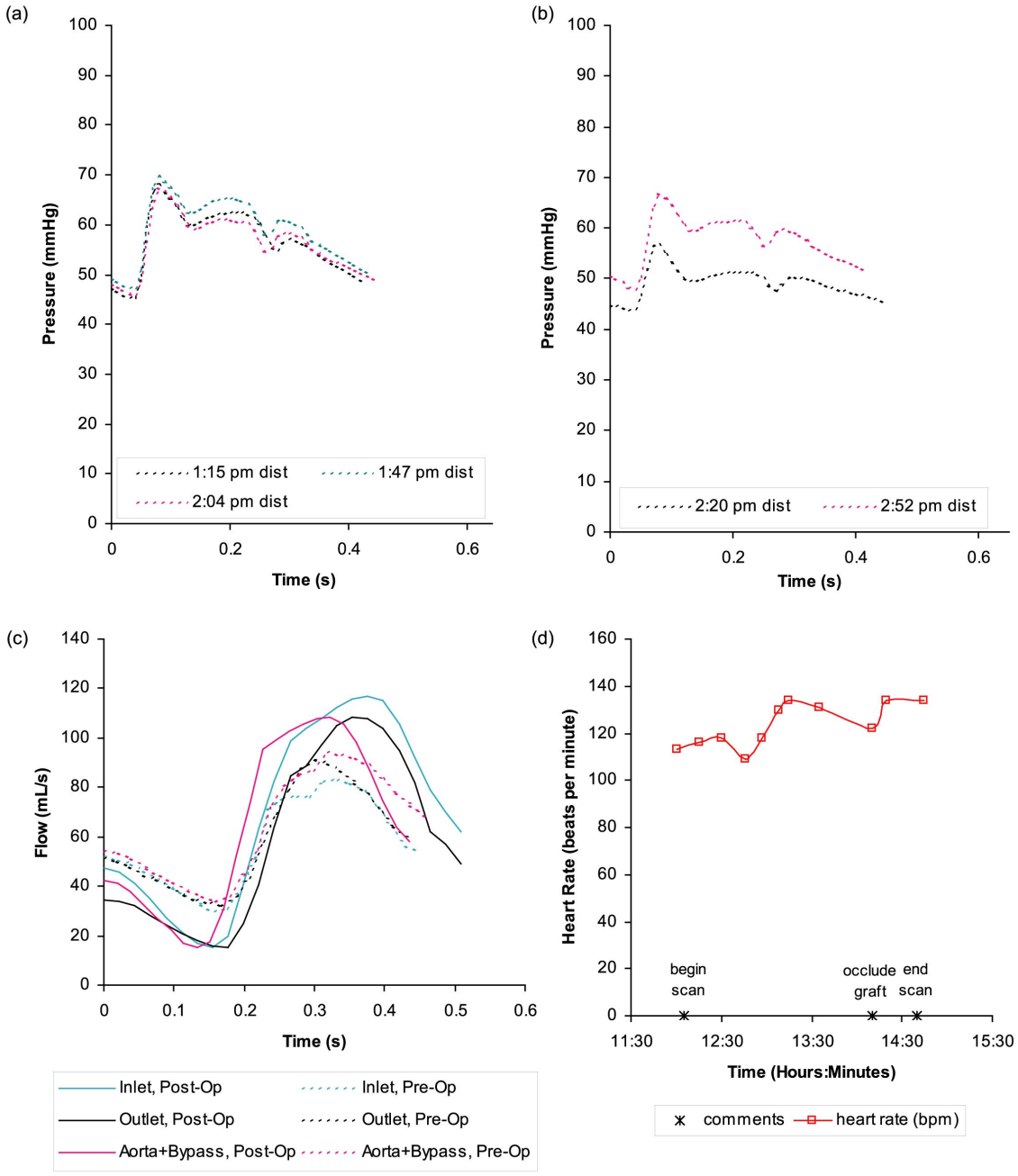


Figure C.2: Physiologic changes observed in Pig B for the bypass-open and bypass-closed states. (a) Distal pressures measured at different times for the bypass-open state. (b) Distal pressures measured at different times for the bypass-closed state. (c) Total flow measurements, acquired with a segmented k-space PC-MRI sequence, for both the bypass open (Post-Op) and bypass closed (Pre-Op). (d) Variations in heart rate over the course of the experiment. Important events during the experiment are noted along the time axis.

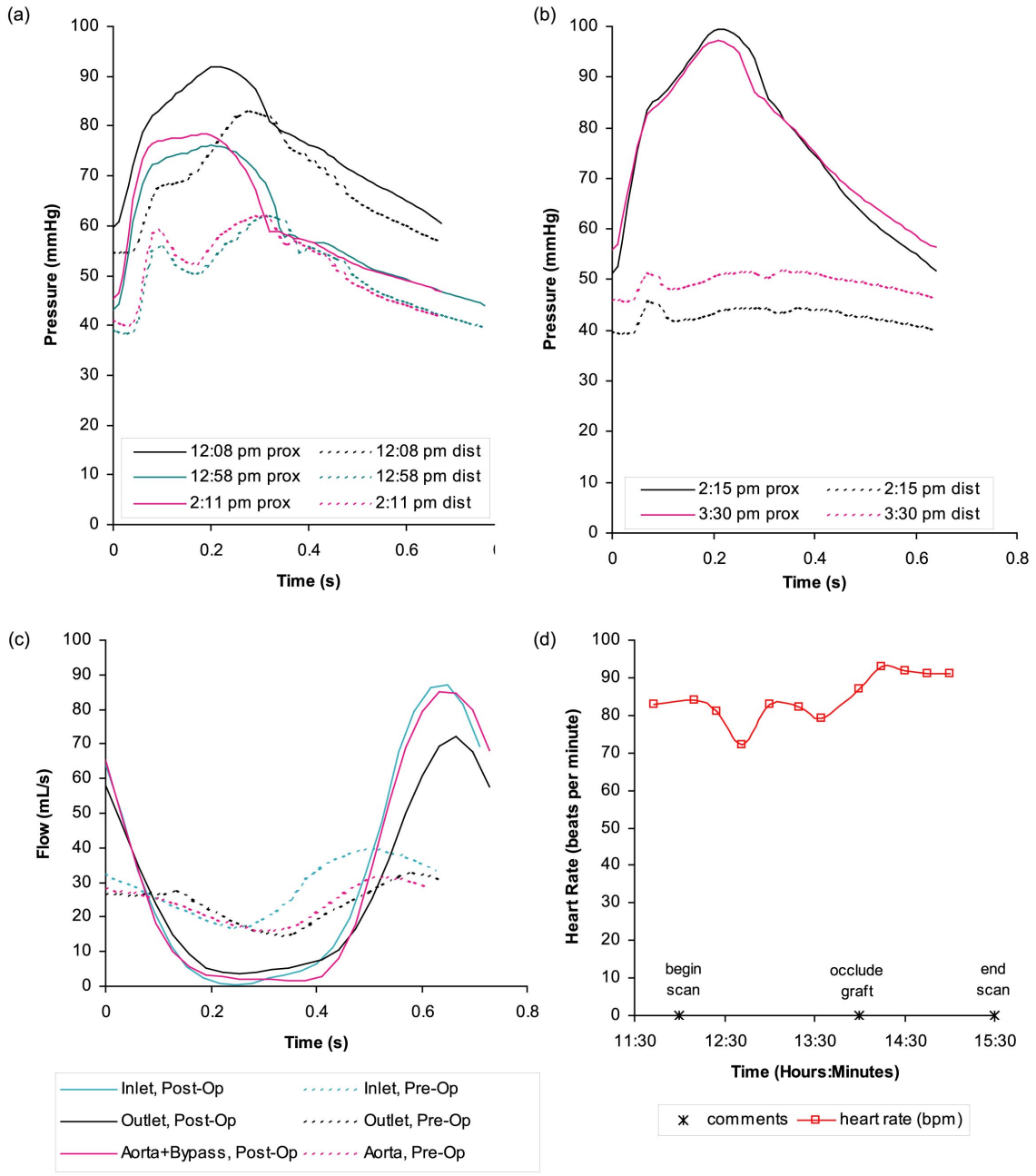


Figure C.3: Physiologic changes observed in Pig C for the bypass-open and bypass-closed states. (a) Proximal (prox) and distal (dist) pressures measured at different times for the bypass-open state. (b) Proximal (prox) and distal (dist) pressures measured at different times for the bypass-closed state. (c) Total flow measurements, acquired with a 2D cine PC-MRI sequence, for both the bypass open (Post-Op) and bypass closed (Pre-Op). (d) Variations in heart rate over the course of the experiment. Important events during the experiment are noted along the time axis.

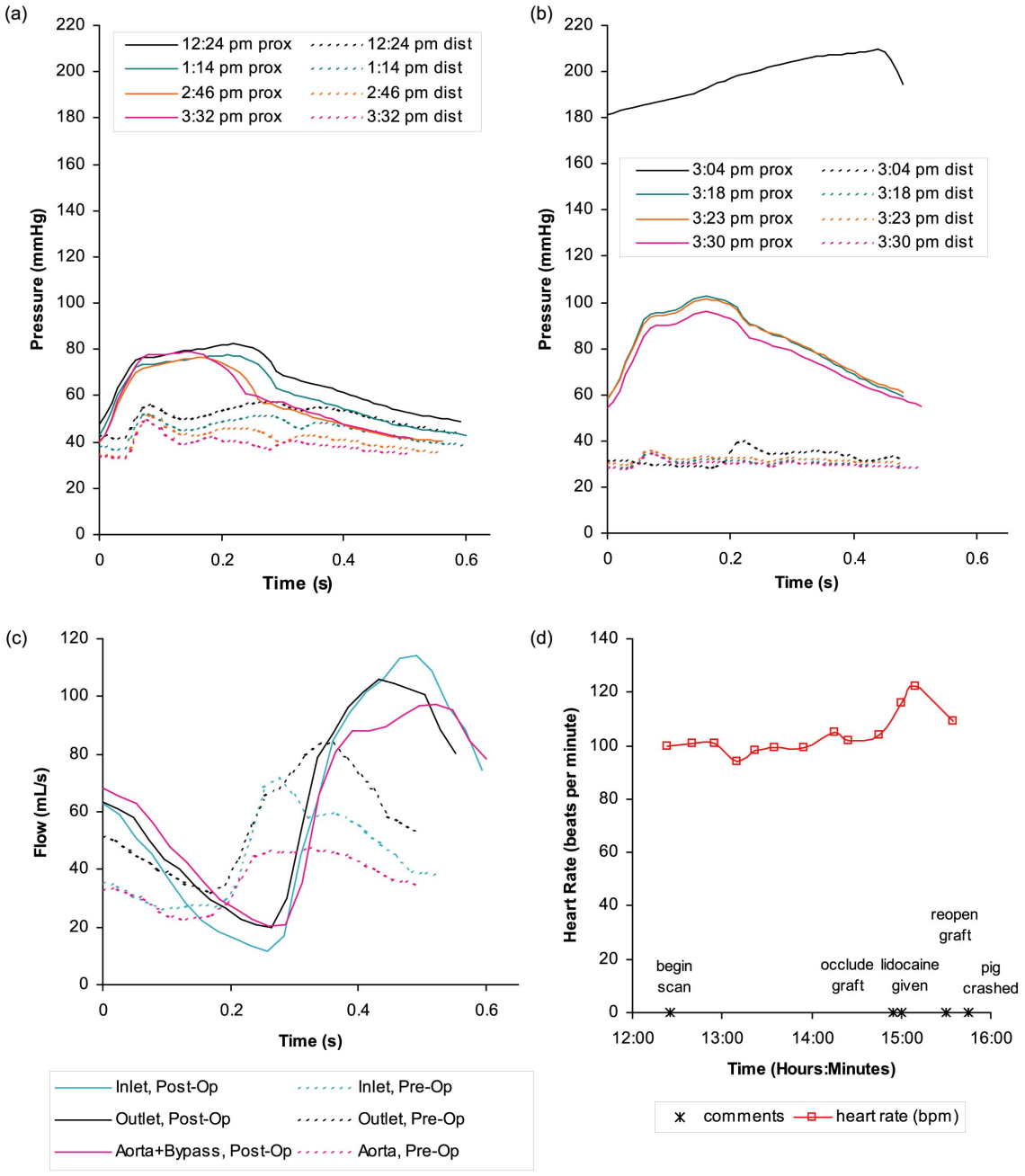


Figure C.4: Physiologic changes observed in Pig D for the bypass-open and bypass-closed states. (a) Proximal (prox) and distal (dist) pressures measured at different times for the bypass-open state. (b) Proximal (prox) and distal (dist) pressures measured at different times for the bypass-closed state. (c) Total flow measurements, acquired with a segmented k-space PC-MRI sequence, for both the bypass open (Post-Op) and bypass closed (Pre-Op). (d) Variations in heart rate over the course of the experiment. Important events during the experiment are noted along the time axis. Of particular interest is the administration of lidocaine at approximately 3 p.m., which is the likely cause of the large increase in the proximal pressure at 3:04 p.m.

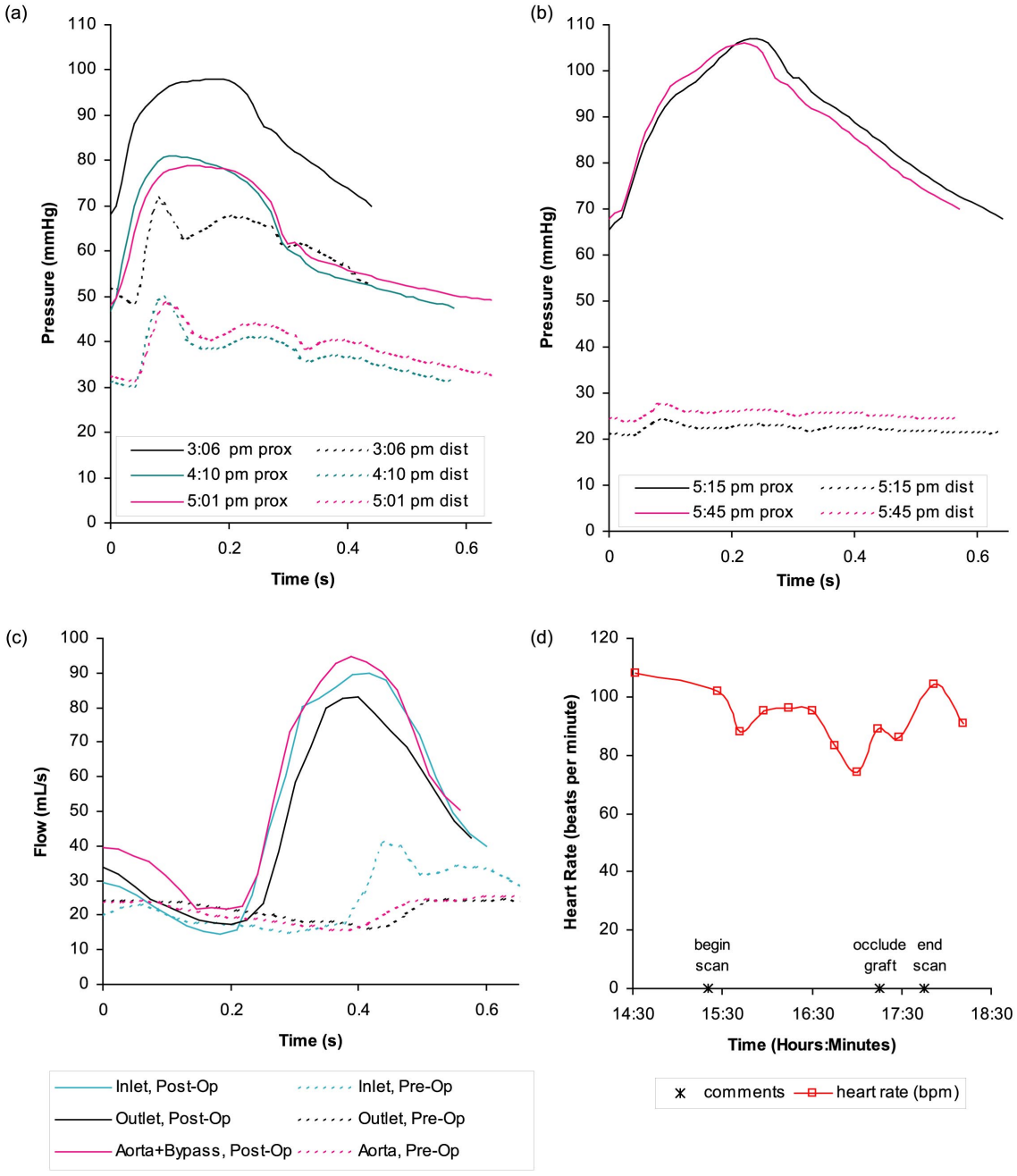


Figure C.5: Physiologic changes observed in Pig E for the bypass-open and bypass-closed states. (a) Proximal (prox) and distal (dist) pressures measured at different times for the bypass-open state. (b) Proximal (prox) and distal (dist) pressures measured at different times for the bypass-closed state. (c) Total flow measurements, acquired with a segmented k-space PC-MRI sequence, for both the bypass open (Post-Op) and bypass closed (Pre-Op). (d) Variations in heart rate over the course of the experiment. Important events during the experiment are noted along the time axis.

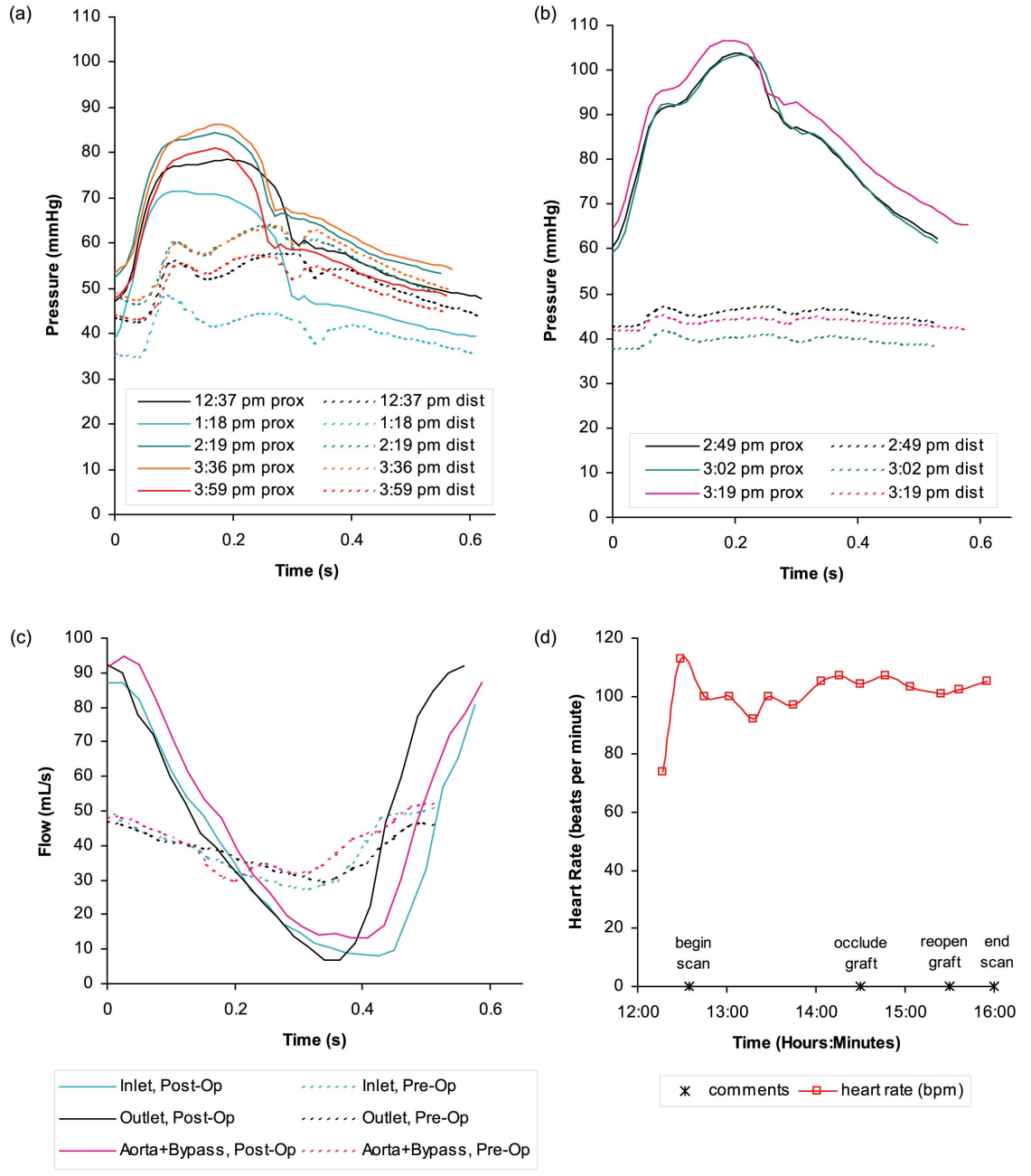


Figure C.6: Physiologic changes observed in Pig F for the bypass-open and bypass-closed states. (a) Proximal (prox) and distal (dist) pressures measured at different times for the bypass-open state. (b) Proximal (prox) and distal (dist) pressures measured at different times for the bypass-closed state. (c) Total flow measurements, acquired with a segmented k-space PC-MRI sequence, for both the bypass open (Post-Op) and bypass closed (Pre-Op). (d) Variations in heart rate over the course of the experiment. Important events during the experiment are noted along the time axis.

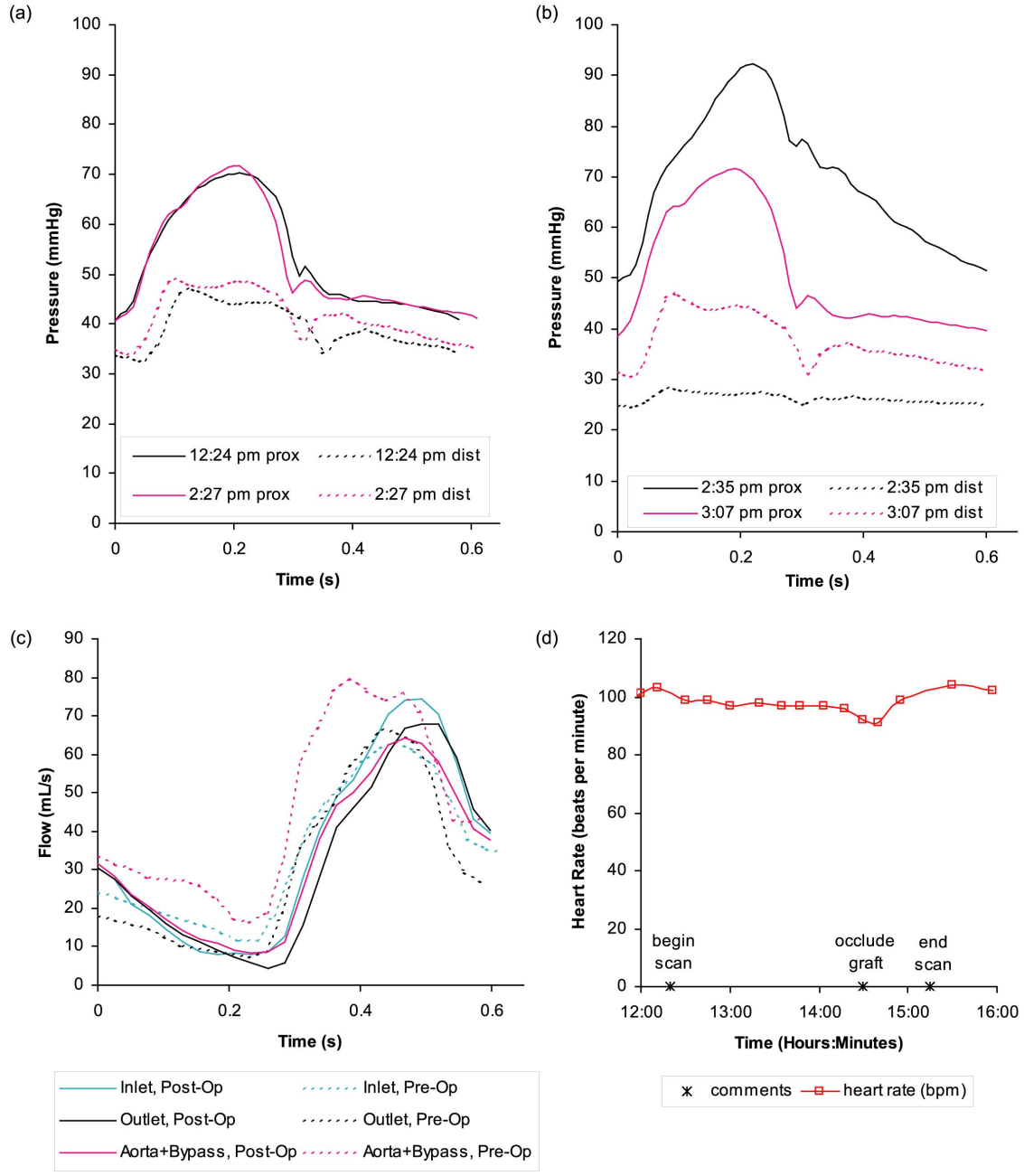


Figure C.7: Physiologic changes observed in Pig G for the bypass-open condition. Although measurements were made for what was assumed to be the bypass-closed state, a large amount of flow was measured through the bypass during this time, indicating that the bypass-closed state was not achieved. The similarity between the pressure measurements at 3:07 p.m. and those made at 12:24 p.m. and 2:27 p.m. also lend support to this belief. (a) Proximal (prox) and distal (dist) pressures measured at different times for the bypass-open state. (b) Proximal (prox) and distal (dist) pressures measured at different times during the assumed bypass-closed state. (c) Total flow measurements, acquired with a segmented k-space PC-MRI sequence, for both the bypass open (Post-Op) and attempted bypass closed (Pre-Op) condition. (d) Variations in heart rate over the course of the experiment. Important events during the experiment are noted along the time axis.

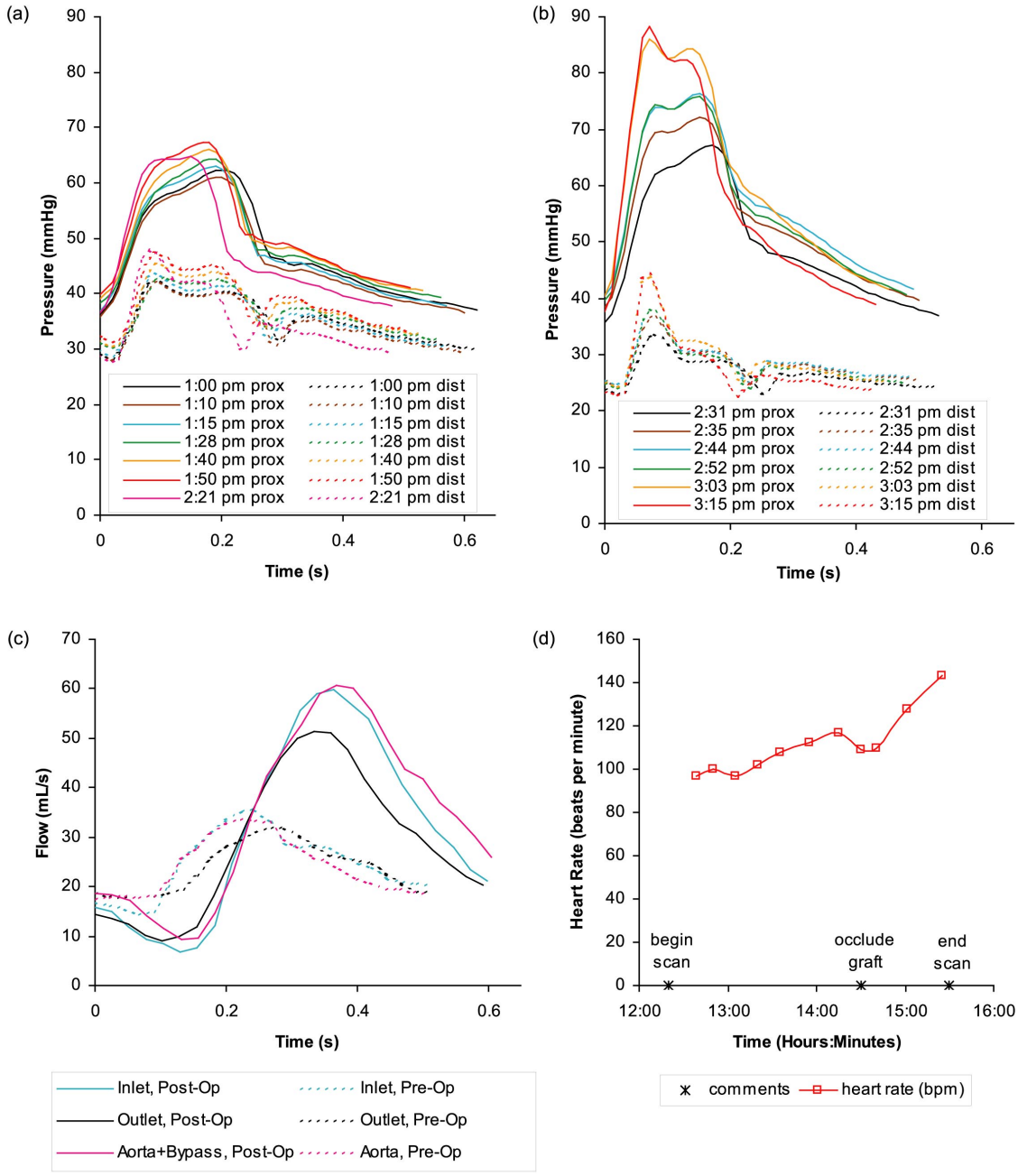


Figure C.8: Physiologic changes observed in Pig H for the bypass-open and bypass-closed states. (a) Proximal (prox) and distal (dist) pressures measured at different times for the bypass-open state. (b) Proximal (prox) and distal (dist) pressures measured at different times for the bypass-closed state. (c) Total flow measurements, acquired with a segmented k-space PC-MRI sequence, for both the bypass open (Post-Op) and bypass closed (Pre-Op). (d) Variations in heart rate over the course of the experiment. Important events during the experiment are noted along the time axis.

Bibliography

[1] B. Campanini (editor), "The World Health Report 2002: Reducing Risks, Promoting Healthy Life," World Health Organization, Geneva, Switzerland, 2002.

[2] American Heart Association, "Heart Disease and Stroke Statistics -- 2003 Update," American Heart Association, Dallas, Texas, 2002.

[3] C. K. Zarins, D. P. Giddens, B. K. Bharadvaj, V. S. Sottiurai, R. F. Mabon, and S. Glagov, "Carotid Bifurcation Atherosclerosis: Quantitative Correlation of Plaque Localization with Flow Velocity Profiles and Wall Shear Stress," *Circulation Research*, vol. 53, no. 4, pp. 502-514, 1983.

[4] H. S. Bassiouny, S. White, S. Glagov, E. Choi, D. P. Giddens, and C. K. Zarins, "Anastomotic Intimal Hyperplasia: Mechanical Injury or Flow Induced," *Journal of Vascular Surgery*, vol. 15, no. 4, pp. 708-717, 1992.

[5] R. S. Keynton, M. M. Evancho, R. L. Sims, N. V. Rodway, A. Gobin, and S. E. Rittgers, "Intimal Hyperplasia and Wall Shear in Arterial Bypass Graft Distal Anastomoses: An *In Vivo* Model Study," *Journal of Biomechanical Engineering*, vol. 123, pp. 464-473, 2001.

[6] C. K. Zarins and S. Glagov, "Artery Wall Pathology in Atherosclerosis," in *Vascular Surgery*, vol. 1, R. B. Rutherford, Ed., Fifth ed. Philadelphia, Pennsylvania: W.B. Saunders Company, 2000, pp. 313-333.

[7] C. G. Caro, J. M. Fitz-Gerald, and R. C. Schroter, "Atheroma and Arterial Wall Shear. Observation, Correlation and Proposal of a Shear Dependent Mass Transfer Mechanism for Atherogenesis," *Proceedings of the Royal Society of London. Series B: Biological Sciences*, vol. 177, no. 46, pp. 109-159, 1971.

[8] J. M. Ramstack, L. Zuckerman, and L. F. Mockros, "Shear-Induced Activation of Platelets," *Journal of Biomechanics*, vol. 12, no. 2, pp. 113-125, 1979.

[9] J. Popovic, *1999 National Hospital Discharge Survey: Annual Summary with Detailed Diagnosis and Procedure Data*, vol. 151. Hyattsville, Maryland: National Center for Health Statistics, 2001.

[10] L. L. Stept, W. R. Flinn, W. J. M. III, S. T. Bartlett, J. J. Bergan, and J. S. T. Yao, "Technical Defects as a Cause of Early Graft Failure After Femorodistal Bypass," *Archives of Surgery*, vol. 122, no. 5, pp. 599-604, 1987.

[11] D. B. Walsh, "Technical Adequacy and Graft Thrombosis," in *Vascular Surgery*, vol. 1, R. B. Rutherford, Ed., Fifth ed. Philadelphia, Pennsylvania: W.B. Saunders Company, 2000, pp. 708-725.

[12] G. E. Hajjar and W. J. Quinones-Baldrich, "The Polytetrafluoroethylene Graft for Infrainguinal Revascularization: Long-Term Results," in *Long-Term Results in Vascular Surgery*, J. S. T. Yao and W. H. Pearce, Eds. Norwalk, Connecticut: Appleton & Lange, 1993, pp. 215-224.

[13] D. C. Brewster, A. J. LaSalle, J. G. Robison, E. C. Strayhorn, and R. C. Darling, "Factors Affecting Patency of Femoropopliteal Bypass Grafts," *Surgery, Gynecology & Obstetrics*, vol. 157, no. 5, pp. 437-442, 1983.

[14] C. A. Erickson, J. B. Towne, G. R. Seabrook, J. A. Freischlag, and R. A. Cambria, "Ongoing Vascular Laboratory Surveillance Is Essential to Maximize Long-Term *In Situ* Saphenous Vein Bypass Patency," *Journal of Vascular Surgery*, vol. 23, no. 1, pp. 18-27, 1996.

[15] H. Dardik, K. Wengerter, F. Qin, A. Pangilinan, F. Silvestri, F. Wolodiger, M. Kahn, B. Sussman, and I. M. Ibrahim, "Comparative Decades of Experience with Glutaraldehyde-Tanned Human Umbilical Cord Vein Graft for Lower Limb Revascularization: An Analysis of 1275 Cases," *Journal of Vascular Surgery*, vol. 35, no. 1, pp. 64-71, 2002.

[16] A. Nevelsteen, R. Suy, W. Daenen, A. Boel, and G. Stalpaert, "Aortofemoral Grafting: Factors Influencing Late Results," *Surgery*, vol. 88, no. 5, pp. 642-653, 1980.

[17] A. D. Whittemore, M. C. Donaldson, and J. A. Mannick, "Ten-Year Patency of Autogenous Vein Bypass Grafts," in *Long-Term Results in Vascular Surgery*, J. S. T. Yao and W. H. Pearce, Eds. Norwalk, Connecticut: Appleton & Lange, 1993, pp. 243-246.

[18] B. S. Glickman, J. P. Rehm, and B. T. Baxter, "Arterial Aneurysms: Etiologic Considerations," in *Vascular Surgery*, vol. 1, R. B. Rutherford, Ed. Philadelphia, Pennsylvania: W.B. Saunders Company, 2000, pp. 373-386.

[19] H. Gaylis and G. Dewar, "Anastomotic Aneurysms: Facts and Fancy," *Surgery Annual*, vol. 22, no., pp. 317-339, 1990.

[20] J. M. Edwards, S. A. Teefey, R. E. Zierler, and T. R. Kohler, "Intraabdominal Paraanastomotic Aneurysms After Aortic Bypass Grafting," *Journal of Vascular Surgery*, vol. 15, no. 2, pp. 344-353, 1992.

[21] P. J. van Den Akker, R. Brand, R. van Schilfgaarde, J. H. van Bockel, and J. L. Terpstra, "False Aneurysms After Prosthetic Reconstructions for Aortoiliac Obstructive Disease," *Annals of Surgery*, vol. 210, no. 5, pp. 658-666, 1989.

[22] L. Zhang, M. Moskovitz, S. Piscatelli, M. T. Longaker, and J. W. Siebert, "Hemodynamic Study of Different Angled End-to-Side Anastomoses," *Microsurgery*, vol. 16, no. 2, pp. 114-117, 1995.

[23] P. E. Hughes and T. V. How, "Effects of Geometry and Flow Division on Flow Structures in Models of the Distal End-to-Side Anastomosis," *Journal of Biomechanics*, vol. 29, no. 7, pp. 855-872, 1996.

[24] M. Ojha, R. S. C. Cobbold, and K. W. Johnston, "Influence of Angle on Wall Shear Stress Distribution for an End-to-Side Anastomosis," *Journal of Vascular Surgery*, vol. 19, no. 6, pp. 1067-1073, 1994.

[25] R. S. Keynton, S. E. Rittgers, and M. C. Shu, "The Effect of Angle and Flow Rate Upon Hemodynamics in Distal Vascular Graft Anastomoses: An In Vitro Model Study," *Journal of Biomechanical Engineering*, vol. 113, no. 4, pp. 458-63, 1991.

[26] A. J. Greenstein and J. A. Mannick, "Effect of Restricted Outflow on the Early Patency of Arterial Grafts," presented at 22nd Annual Sessions of the Forum on Fundamental Surgical Problems, 32nd Clinical Congress of the American College of Surgeons, San Francisco, CA, 1966.

[27] R. A. Yeager, R. W. Hobson II, T. G. Lynch, Z. Jamil, B. C. Lee, K. Jain, and R. Keys, "Analysis of Factors Influencing Patency of Polytetrafluoroethylene Prostheses for Limb Salvage," *Journal of Surgical Research*, vol. 32, no. 5, pp. 499-506, 1982.

[28] S. S. White, C. K. Zarins, D. P. Giddens, H. Bassiouny, F. Loth, S. A. Jones, and S. Glagov, "Hemodynamic Patterns in Two Models of End-to-Side Vascular Graft Anastomoses: Effects of Pulsatility, Flow Division, Reynolds Number, and Hood Length," *Journal of Biomechanical Engineering*, vol. 115, no. 1, pp. 104-111, 1993.

[29] H. M. Crawshaw, W. C. Quist, E. Serallach, C. R. Valeri, and F. W. LoGerfo, "Flow Disturbance at the Distal End-to-Side Anastomosis. Effect of Patency of the Proximal Outflow Segment and Angle of Anastomosis," *Archives of Surgery*, vol. 115, no. 11, pp. 1280-1284, 1980.

[30] X. Li and S. E. Rittgers, "Hemodynamic Factors at the Distal End-to-Side Anastomosis of a Bypass Graft with Different POS:DOS Flow Ratios," *Journal of Biomechanical Engineering*, vol. 123, pp. 270-276, 2001.

[31] S. E. Rittgers and G. H. Bhambhani, "Doppler Color Flow Images of Iliofemoral Graft End-to-Side Distal Anastomotic Models," *Ultrasound in Medicine and Biology*, vol. 19, no. 4, pp. 257-267, 1993.

[32] H. Sakuma, K. Takeda, and C. B. Higgins, "Fast Magnetic Resonance Imaging of the Heart," *European Journal of Radiology*, vol. 29, no. 2, pp. 101-113, 1999.

[33] B. N. Steele, J. Wan, J. P. Ku, T. J. R. Hughes, and C. A. Taylor, "In Vivo Validation of a One-Dimensional Finite Element Method for Predicting Blood Flow in Cardiovascular Bypass Grafts," *IEEE Transactions on Biomedical Engineering*, vol. 50, no. 6, pp. 649-656, 2003.

[34] K. Perktold and G. Rappitsch, "Computer Simulation of Local Blood Flow and Vessel Mechanics in a Compliant Carotid Artery Bifurcation Model," *Journal of Biomechanics*, vol. 28, no. 7, pp. 845-856, 1995.

[35] C. A. Taylor, T. J. R. Hughes, and C. K. Zarins, "Finite Element Modeling of Three-Dimensional Pulsatile Flow in the Abdominal Aorta: Relevance to Atherosclerosis," *Annals of Biomedical Engineering*, vol. 26, no. 6, pp. 1-14, 1998.

[36] C. R. Ethier, D. A. Steinman, X. Zhang, S. R. Karpik, and M. Ojha, "Flow Waveform Effects on End-to-Side Anastomotic Flow Patterns," *Journal of Biomechanics*, vol. 31, no. 7, pp. 609-617, 1998.

[37] M. Hofer, K. Rappitsch, W. Perktold, W. Trubel, and H. Schima, "Numerical Study of Wall Mechanics and Fluid Dynamics in End-to-Side Anastomoses and Correlation to Intimal Hyperplasia," *Journal of Biomechanics*, vol. 29, no. 10, pp. 1297-1308, 1996.

[38] D. A. Steinman, J. B. Thomas, H. M. Ladak, J. S. Milner, B. K. Rutt, and J. D. Spence, "Reconstruction of Carotid Bifurcation Hemodynamics and Wall Thickness Using Computational Fluid Dynamics and MRI," *Magnetic Resonance in Medicine*, vol. 47, no. 1, pp. 149-159, 2002.

[39] D. Lee and J. J. Chiu, "Intimal Thickening Under Shear in a Carotid Bifurcation - A Numerical Study," *Journal of Biomechanics*, vol. 29, no. 1, pp. 1-11, 1996.

[40] D. A. Steinman, Ethier, C.R., Zhang X., Karpik S., "Effects of Local Geometry on Anastomotic Flow Patterns," *Advances in Bioengineering*, vol. 28, pp. 433-434, 1994.

[41] M. Lei, C. Kleinstreuer, and J. Archie Jr., "Geometric Design Improvements for Femoral Graft-Artery Junctions Mitigating Restenosis," *Journal of Biomechanics*, vol. 29, no. 12, pp. 1605-1614, 1996.

[42] D. Fei, J. Thomas, and S. Rittgers, "The Effect of Angle and Flow Rate Upon Hemodynamics in Distal Vascular Graft Anastomoses: A Numerical Study," *Journal of Biomechanical Engineering*, vol. 116, pp. 331-336, 1994.

[43] C. A. Taylor, M. T. Draney, J. P. Ku, D. Parker, B. N. Steele, K. Wang, and C. K. Zarins, "Predictive Medicine: Computational Techniques in Therapeutic Decision-Making," *Computer Aided Surgery*, vol. 4, no. 5, pp. 231-247, 1999.

[44] F. J. H. Gijsen, E. Allanic, F. N. van de Vosse, and J. D. Janssen, "The Influence of the Non-Newtonian Properties of Blood on the Flow in Large Arteries: Unsteady Flow in a 90^{o} Curved Tube," *Journal of Biomechanics*, vol. 32, no. 7, pp. 705-713, 1999.

[45] F. J. H. Gijsen, F. N. van de Vosse, and J. D. Janssen, "The Influence of the Non-Newtonian Properties of Blood on the Flow in Large Arteries: Steady Flow in a Carotid Bifurcation Model," *Journal of Biomechanics*, vol. 32, no. 6, pp. 601-608, 1999.

[46] R. Botnar, G. Rappitsch, M. B. Scheidegger, D. Leipsch, K. Perktold, and P. Boesiger, "Hemodynamics in the Carotid Artery Bifurcation: A Comparison Between Numerical Simulations and In Vitro MRI Measurements," *Journal of Biomechanics*, vol. 33, pp. 137-144, 2000.

[47] S. Z. Zhao, X. Y. Xu, P. Papathanasopoulou, and I. Marshall, "Combined MRI Measurement and CFD Simulation of Pulsatile Flow in a Carotid Artery Bifurcation Phantom," presented at International Society for Magnetic Resonance in Medicine Tenth Scientific Meeting and Exhibition, Honolulu, Hawai'i, USA, 2002.

[48] K. Perktold, M. Hofer, G. Rappitsch, M. Loew, B. D. Kuban, and M. H. Friedman, "Validated Computation of Physiologic Flow in a Realistic Coronary Artery Branch," *Journal of Biomechanics*, vol. 31, no. 3, pp. 217-228, 1998.

[49] J. S. Cole, "Pulsatile, Non-Newtonian Blood Flows through Typical Arterial Bypass Graft Models," in *School of Aeronautical Engineering*. Belfast, Northern Ireland, United Kingdom: The Queen's University of Belfast, 2000.

[50] Y. Sun, D. O. Hearshen, G. W. Rankin, and A. M. Haggar, "Comparison of Velocity-Encoded MR Imaging and Fluid Dynamic Modeling of Steady and

Disturbed Flow," *Journal of Magnetic Resonance Imaging*, vol. 2, no. 4, pp. 443-52, 1992.

[51] B. Newling, S. J. Gibbs, J. A. Derbyshire, D. Xing, L. D. Hall, D. E. Haycock, W. J. Frith, and S. Ablett, "Comparisons of Magnetic Resonance Imaging Velocimetry with Computational Fluid Dynamics," *Journal of Fluids Engineering*, vol. 119, pp. 103-109, 1997.

[52] C. A. Taylor, T. J. R. Hughes, and C. K. Zarins, "Finite Element Modeling of Blood Flow in Arteries," *Computer Methods in Applied Mechanics and Engineering*, vol. 158, pp. 155-196, 1998.

[53] M. Lei, D. Giddens, S. Jones, F. Loth, and H. Bassiouny, "Pulsatile Flow in an End-to-Side Vascular Graft Model: Comparison of Computations with Experimental Data," *Journal of Biomechanical Engineering*, vol. 123, no. 1, pp. 80-87, 2001.

[54] D. A. Steinman, R. Frayne, X. D. Zhang, B. K. Rutt, and C. R. Ethier, "MR Measurement and Numerical Simulation of Steady Flow in an End-to-Side Anastomosis Model," *Journal of Biomechanics*, vol. 29, no. 4, pp. 537-542, 1996.

[55] C. R. Ethier, S. Prakash, D. A. Steinman, R. L. Leask, G. G. Couch, and M. Ojha, "Steady Flow Separation Patterns in a 45 Degree Junction," *Journal of Fluid Mechanics*, vol. 411, pp. 1-38, 2000.

[56] Y. Papaharilaou, D. J. Doorly, and S. J. Sherwin, "Assessing the Accuracy of Two-Dimensional Phase-Contrast MRI Measurements of Complex Unsteady Flows," *Journal of Magnetic Resonance Imaging*, vol. 14, pp. 714-723, 2001.

[57] C. Bertolotti, V. Deplano, J. Fuseri, and P. Dupouy, "Numerical and Experimental Models of Post-Operative Realistic Flows in Stenosed Coronary Bypasses," *Journal of Biomechanics*, vol. 34, no. 8, pp. 1049-1064, 2001.

[58] Q. Long, X. Y. Xu, M. Bourne, and T. M. Griffith, "Numerical Study of Blood Flow in an Anatomically Realistic Aorto-Iliac Bifurcation Generated from MRI Data," *Magnetic Resonance in Medicine*, vol. 43, no. 4, pp. 565-576, 2000.

[59] Q. Long, X. Y. Xu, B. Ariff, S. A. Thom, A. D. Hughes, and A. V. Stanton, "Reconstruction of Blood Flow Patterns in a Human Carotid Bifurcation: a Combined CFD and MRI Study," *Journal of Magnetic Resonance Imaging*, vol. 11, no. 3, pp. 299-311, 2000.

[60] X. Y. Xu, M. W. Collins, and C. J. Jones, "Flow Studies in Canine Artery Bifurcations Using a Numerical Simulation Method," *Journal of Biomechanical Engineering*, vol. 114, no. 4, pp. 504-511, 1992.

[61] A. Leuprecht, K. Perktold, S. Kozerke, and P. Boesiger, "Combined CFD and MRI Study of Blood Flow in a Human Ascending Aorta Model," *Biorheology*, vol. 39, pp. 425-429, 2002.

[62] N. B. Wood, S. J. Weston, P. J. Kilner, A. D. Gosman, and D. N. Firmin, "Combined MR Imaging and CFD Simulation of Flow in the Human Descending Aorta," *Journal of Magnetic Resonance Imaging*, vol. 13, pp. 699-713, 2001.

[63] F. Migliavacca, P. J. Kilner, G. Pennati, G. Dubini, R. Pietrabissa, R. Fumero, and M. R. de Leval, "Computational Fluid Dynamic and Magnetic Resonance Analyses of Flow Distribution Between the Lungs After Total Cavopulmonary Connection," *IEEE Transactions on Biomedical Engineering*, vol. 46, no. 4, pp. 393-399, 1999.

[64] D. E. Brooks, J. W. Goodwin, and G. V. F. Seaman, "Interactions Among Erythrocytes Under Shear," *Journal of Applied Physiology*, vol. 28, no. 2, pp. 172-177, 1970.

[65] H. H. Lipowsky, S. Usami, and S. Chien, "*In Vivo* Measurements of "Apparent Viscosity" and Microvessel Hematocrit in the Mesentery of the Cat," *Microvascular Research*, vol. 19, no. 3, pp. 297-319, 1980.

[66] R. L. Whitmore, *Rheology of the Circulation*. Oxford, England: Pergamon Press Ltd., 1968.

[67] R. Fahraeus and T. LIndqvist, "The Viscosity of the Blood in Narrow Capillary Tubes," *American Journal of Physiology*, vol. 96, no. 3, pp. 562-568, 1931.

[68] Y. C. Fung, *Biomechanics: Mechanical Properties of Living Tissues*, 2nd ed. New York: Springer-Verlag, 1993.

[69] P. L. Altman and D. S. Dittmer, "Respiration and Circulation." Bethesda, Maryland: Federation of American Societies for Experimental Biology, 1971.

[70] W. W. Nichols and M. F. O'Rourke, *McDonald's Blood Flow in Arteries. Theoretical, Experimental and Clinical Principles*, 4th ed. New York, NY: Oxford University Press, 1998.

[71] J. S. Stroud, S. A. Berger, and D. Saloner, "Influence of Stenosis Morphology on Flow through Severely Stenotic Vessels: Implications for Plaque Rupture," *Journal of Biomechanics*, vol. 33, no. 4, pp. 443-455, 2000.

[72] D. Bluestein, C. Gutierrez, M. Londono, and R. T. Schoephoerster, "Vortex Shedding in Steady Flow Through a Model of an Arterial Stenosis and Its

Relevance to Mural Platelet Deposition," *Annals of Biomedical Engineering*, vol. 27, no. 6, pp. 763-773, 1999.

[73] R. M. Hoogeveen, C. J. G. Bakker, and M. A. Viergever, "Limits to the Accuracy of Vessel Diameter Measurement in MR Angiography," *Journal of Magnetic Resonance Imaging*, vol. 8, no. 6, pp. 1228-1235, 1998.

[74] A. J. Evans, D. B. Richardson, R. Tien, J. R. MacFall, L. W. Hedlund, E. R. Heinz, O. Boyko, and H. D. Sostman, "Poststenotic Signal Loss in MR Angiography: Effects of Echo Time, Flow Compensation, and Fractional Echo," *American Journal of Neuroradiology*, vol. 14, no. 3, pp. 721-729, 1993.

[75] D. Saloner, K. Ong, J. H. Rapp, and ACSCEPT investigators, "Overestimation of Carotid Stenosis on Contrast-Enhanced MRA," presented at International Society for Magnetic Resonance in Medicine Tenth Scientific Meeting and Exhibition, Honolulu, Hawai'i, USA, 2002.

[76] M. T. Draney, M. T. Alley, B. T. Tang, N. M. Wilson, R. J. Herfkens, and C. A. Taylor, "Importance of 3D Nonlinear Gradient Corrections for Quantitative Analysis of 3D MR Angiographic Data," presented at International Society for Magnetic Resonance in Medicine Tenth Scientific Meeting and Exhibition, Honolulu, Hawai'i, USA, 2002.

[77] G. L. Nayler, D. N. Firmin, and D. B. Longmore, "Blood Flow Imaging by Cine Magnetic Resonance," *Journal of Computer Assisted Tomography*, vol. 10, no. 5, pp. 715-722, 1986.

[78] N. J. Pelc, R. J. Herfkens, A. Shimakawa, and D. R. Enzmann, "Phase Contrast Cine Magnetic Resonance Imaging," *Magnetic Resonance Quarterly*, vol. 7, no. 4, pp. 229-254, 1991.

[79] J. O. Fredrickson and N. J. Pelc, "Time-Resolved MR Imaging by Automatic Data Segmentation," *Journal of Magnetic Resonance Imaging*, vol. 4, no. 2, pp. 189-196, 1994.

[80] M. H. Buonocore and L. Gao, "Experimental Study of the Effects of "Fractional" Gating on Flow Measurements," *Magnetic Resonance in Medicine*, vol. 31, no. 4, pp. 429-436, 1994.

[81] C. Thomsen, M. Corsten, L. Sondergaard, O. Henriskon, and F. Stahlberg, "A Segmented K-Space Velocity Mapping Protocol for Quantification of Renal Artery Blood Flow During Breath-Holding," *Journal of Magnetic Resonance Imaging*, vol. 5, no. 4, pp. 393-401, 1995.

[82] R. Frayne and B. K. Rutt, "Frequency Response of Retrospectively Gated Phase-Contrast MR Imaging: Effect of Interpolation," *Journal of Magnetic Resonance Imaging*, vol. 3, no. 6, pp. 907-917, 1993.

[83] D. N. Ku, C. L. Biancheri, R. I. Pettigrew, J. W. Peifer, C. P. Markou, and H. Engels, "Evaluation of Magnetic Resonance Velocimetry for Steady Flow," *Journal of Biomechanics*, vol. 112, pp. 464-472, 1990.

[84] R. Frayne, D. A. Steinman, C. R. Ethier, and B. K. Rutt, "Accuracy of MR Phase Contrast Velocity Measurements for Unsteady Flow," *Journal of Magnetic Resonance Imaging*, vol. 5, no. 4, pp. 428-431, 1995.

[85] M. B. Robertson, U. Kohler, P. R. Hoskins, and I. Marshall, "Quantitative Analysis of PC MRI Velocity Maps: Pulsatile Flow in Cylindrical Vessels," *Magnetic Resonance Imaging*, vol. 19, pp. 685-695, 2001.

[86] S. E. Maier, D. Meier, P. Boesiger, U. T. Moser, and A. Vieli, "Human Abdominal Aorta: Comparative Measurements of Blood Flow with MR Imaging and Multigated Doppler US," *Radiology*, vol. 171, no. 2, pp. 487-492, 1989.

[87] J. M. Siegel, Jr., J. N. Oshinski, R. I. Pettigrew, and D. N. Ku, "The Accuracy of Magnetic Resonance Phase Velocity Measurements in Stenotic Flow," *Journal of Biomechanics*, vol. 29, no. 12, pp. 1665-1672, 1996.

[88] D. A. Steinman, C. R. Ethier, and B. K. Rutt, "Combined Analysis of Spatial and Velocity Displacement Artifacts in Phase Contrast Measurements of Complex Flows," *Journal of Magnetic Resonance Imaging*, vol. 7, pp. 339-346, 1997.

[89] M. Markl, M. T. Draney, and N. J. Pelc, "Analysis and Correction of the Effect of Spatial Gradient Field Distortions on Velocity Measurements with Phase Contrast MRI," presented at International Society for Magnetic Resonance in Medicine Tenth Scientific Meeting and Exhibition, Honolulu, Hawai'i, USA, 2002.

[90] N. J. Pelc, F. G. Sommer, K. C. P. Li, T. J. Brosnan, R. J. Herfkens, and D. R. Enzmann, "Quantitative Magnetic Resonance Flow Imaging," *Magnetic Resonance Quarterly*, vol. 10, no. 3, pp. 125-147, 1994.

[91] C. Kondo, G. R. Caputo, R. Semelka, E. Foster, A. Shimakawa, and C. B. Higgins, "Right and Left Ventricular Stroke Volume Measurements with Velocity-Encoded Cine MR Imaging: In Vitro and In Vivo Validation," *American Journal of Roentgenology*, vol. 157, pp. 9-16, 1991.

[92] A. J. Evans, F. Iwai, T. A. Grist, H. D. Sostman, L. W. Hedlund, C. E. Spritzer, R. Negro-Vilar, C. A. Beam, and N. J. Pelc, "Magnetic Resonance Imaging of Blood

Flow with a Phase Subtraction Technique. In Vitro and In Vivo Validation," *Investigative Radiology*, vol. 28, no. 2, pp. 109-115, 1993.

[93] T. R. McCauley, C. S. Pena, C. K. Holland, T. B. Price, and J. C. Gore, "Validation of Volume Flow Measurements with Cine Phase-Contrast MR Imaging for Peripheral Arterial Waveforms," *Journal of Magnetic Resonance Imaging*, vol. 5, no. 6, pp. 663-668, 1995.

[94] L. Sondergaard, F. Stahlberg, C. Thomsen, A. Stensgaard, K. Lindvig, and O. Henriksen, "Accuracy and Precision of MR Velocity Mapping in Measurement of Stenotic Cross-Sectional Area, Flow Rate, and Pressure Gradient," *Journal of Magnetic Resonance Imaging*, vol. 3, no. 2, pp. 433-437, 1993.

[95] P. Summers, M. Drangova, A. Papadaki, D. W. Holdsworth, and B. K. Rutt, "Multi-site Comparison of Accuracy, Linearity and Precision in MR Flow Measurements," presented at International Society for Magnetic Resonance in Medicine Ninth Scientific Meeting and Exhibition, Glasgow, Scotland, UK, 2001.

[96] G. P. Chatzimavroudis, J. N. Oshinski, R. H. Franch, P. G. Walker, A. P. Yoganathan, and R. I. Pettigrew, "Evaluation of the Precision of Magnetic Resonance Phase Velocity Mapping for Blood Flow Measurements," *Journal of Cardiovascular Magnetic Resonance*, vol. 3, no. 1, pp. 11, 2001.

[97] L. R. Pelc, N. J. Pelc, S. C. Rayhill, L. J. Castro, G. H. Glover, R. J. Herfkens, D. C. Miller, and R. B. Jeffrey, "Arterial and Venous Blood Flow: Noninvasive Quantitation with MR Imaging," *Radiology*, vol. 185, no. 3, pp. 809-812, 1992.

[98] D. N. Firmin, G. L. Nayler, R. H. Klipstein, S. R. Underwood, R. S. O. Rees, and D. B. Longmore, "In Vivo Validation of MR Velocity Imaging," *Journal of Computer Assisted Tomography*, vol. 11, no. 5, pp. 751-756, 1987.

[99] H. Zhang, S. S. Halliburton, J. R. Moore, O. P. Simonetti, P. R. Schvartzman, R. D. White, and G. P. Chatzimavroudis, "Ultrafast Flow Quantification with Segmented k-Space Magnetic Resonance Phase Velocity Mapping," *Annals of Biomedical Engineering*, vol. 30, no. 1, pp. 120-128, 2002.

[100] V.-P. Poutanen, R. Kivisaari, A.-M. Hakkinen, S. Savolainen, P. Hekali, and C.-G. Standertskjold-Nordenstam, "Multiphase Segmented K-Space Velocity Mapping in Pulsatile Flow Waveforms," *Magnetic Resonance Imaging*, vol. 16, no. 3, pp. 261-270, 1998.

[101] V. S. Lee, C. E. Spritzer, B. A. Carroll, L. G. Pool, M. A. Bernstein, S. K. Heinle, and J. R. MacFall, "Flow Quantification Using Fast Cine Phase-Contrast MR Imaging, Conventional Cine Phase-Contrast MR Imaging, and Doppler

Sonography: In Vitro and In Vivo Validation," *American Journal of Roentgenology*, vol. 169, no. 4, pp. 1125-1131, 1997.

[102] R. L. Wolf, R. L. Ehman, S. J. Riederer, and P. J. Rossman, "Analysis of Systemic and Random Error in MR Volumetric Flow Measurements," *Magnetic Resonance in Medicine*, vol. 30, no. 1, pp. 82-91, 1993.

[103] C. Tang, D. D. Blatter, and D. L. Parker, "Accuracy of Phase-Contrast Flow Measurements in the Presence of Partial-Volume Effects," *Journal of Magnetic Resonance Imaging*, vol. 3, no. 2, pp. 377-85, 1993.

[104] K. C. Wang, "Level Set Methods for Computational Prototyping with Application to Hemodynamic Modeling," in *Electrical Engineering*. Stanford, CA: Stanford University, 2001.

[105] N. M. Wilson, "Geometric Algorithms and Software Architecture for Computational Prototyping: Applications in Vascular Surgery and MEMS," in *Mechanical Engineering*. Stanford, CA: Stanford University, 2002.

[106] N. J. Pelc, M. A. Bernstein, A. Shimakawa, and G. H. Glover, "Encoding Strategies for Three-Direction Phase-Contrast MR Imaging of Flow," *Journal of Magnetic Resonance Imaging*, vol. 1, no. 4, pp. 405-413, 1991.

[107] E. P. Durand, O. Jolivet, E. Itti, J. Tsau, and J. Bittoun, "Precision of Magnetic Resonance Velocity and Acceleration Measurements: Theoretical Issues and Phantom Experiments," *Journal of Magnetic Resonance Imaging*, vol. 13, no. 3, pp. 445-451, 2001.

[108] M. T. Draney, "In Vivo Quantification of Vessel Wall Motion and Cyclic Strain Using Cine Phase Contrast Magnetic Resonance Imaging," in *Mechanical Engineering*. Stanford, CA: Stanford University, 2003.

[109] C. J. G. Bakker, R. M. Hoogeveen, and M. A. Viergever, "Construction of a Protocol for Measuring Blood Flow by Two-Dimensional Phase-Contrast MRA," *Journal of Magnetic Resonance Imaging*, vol. 9, no. 1, pp. 119-127, 1999.

[110] J. S. Milner, J. A. Moore, B. K. Rutt, and D. A. Steinman, "Hemodynamics of Human Carotid Artery Bifurcations: Computational Studies with Models Reconstructed from Magnetic Resonance Imaging of Normal Subjects," *Journal of Vascular Surgery*, vol. 28, no. 1, pp. 143-156, 1998.

[111] M. H. Friedman, O. J. Deters, F. F. Mark, C. B. Bargeron, and G. M. Hutchins, "Arterial Geometry Affects Hemodynamics. A Potential Risk Factor for Atherosclerosis," *Atherosclerosis*, vol. 46, no. 2, pp. 225-231, 1983.

[112] J. R. Cebral and R. Lohner, "From Medical Images to Anatomically Accurate Finite Element Grids," *International Journal for Numerical Methods in Engineering*, vol. 51, no. 8, pp. 985-1008, 2001.

[113] D. Magee, A. Bulpitt, and E. Berry, "Level Set Methods for the 3D Segmentation of CT Images of Abdominal Aortic Aneurysms," presented at Medical Image Understanding and Analysis, Birmingham, England, 2001.

[114] H. M. Ladak, J. S. Milner, and D. A. Steinman, "Rapid Three-Dimensional Segmentation of the Carotid Bifurcation from Serial MR Images," *Journal of Biomechanical Engineering*, vol. 122, no. 1, pp. 96-99, 2000.

[115] E. Bekkers and C. Taylor, "Image-Based, Direct Three Dimensional Vascular Modeling," presented at 2003 Summer Bioengineering Conference, Key Biscayne, Florida, 2003.

[116] J. Mackerle, "2D and 3D Finite Element Meshing and Remeshing. A Bibliography (1990-2001)." *Engineering Computations*, vol. 18, no. 8, pp. 1108-1197, 2001.

[117] M. S. Shephard, "Meshing Environment for Geometry-Based Analysis," *International Journal for Numerical Methods in Engineering*, vol. 47, no. 1-3, pp. 169-190, 2000.

[118] J. R. Womersley, "An Elastic Tube Theory of Pulse Transmission and Oscillatory Flow in Mammalian Arteries," Wright Air Development Center TR 56-614, January 1957.

[119] C. A. Taylor, "A Computational Framework for Investigating Hemodynamic Factors in Vascular Adaptation and Disease," in *Mechanical Engineering*. Stanford, CA: Stanford University, 1996, pp. 97.

[120] T. J. R. Hughes, *The Finite Element Method. Linear Static and Dynamic Finite Element Analysis*. Mineola, New York: Dover Publications, Inc., 2000.

[121] Centric Engineering Systems, Inc. (now part of Ansys, Inc., Cannonsburg, PA), "*Spectrum* Solver Solution Methods Theory," 1993.

[122] H. M. Hilber, T. J. R. Hughes, and R. L. Taylor, "Improved Numerical Dissipation for Time Integration Algorithms in Structural Dynamics," *Earthquake Engineering and Structural Dynamics*, vol. 5, no. 3, pp. 283-292, 1977.

[123] P. J. Roache, *Verification and Validation in Computational Science and Engineering*. Albuquerque, New Mexico, USA: Hermosa Publishers, 1998.

[124] Personal communication with M. Markl via e-mail, Subject: mVINNIE sequence, 2003.

[125] G. N. Palafox, R. B. Wicker, and C. J. Elkins, "Rapid In-Vitro Physiologic Flow Experimentation Using Rapid Prototyping and Particle Image Velocimetry," presented at 2003 ASME Summer Bioengineering Meeting, Key Biscayne, Florida, 2003.

[126] C. J. Elkins, J. K. Eaton, and R. B. Wicker, "Rapid Experimentation in Complex Internal Flow Passages using SLA and MRV," presented at 4th ASME / JSME Joint Fluids Engineering Conference, Honolulu, Hawaii, 2003.

[127] F. M. White, *Fluid Mechanics*. New York, NY: McGraw-Hill Book Company, 1986.

[128] M. T. Alley, R. Y. Shifrin, N. J. Pelc, and R. J. Herfkens, "Ultrafast Contrast-Enhanced Three-Dimensional MR Angiography: State of the Art," *Radiographics*, vol. 18, no. 2, pp. 273-285, 1998.

[129] J. A. Moore, B. K. Rutt, S. J. Karlik, K. Yin, and C. R. Ethier, "Computational Blood Flow Modeling Based on In Vivo Measurements," *Annals of Biomedical Engineering*, vol. 27, no. 5, pp. 627-640, 1999.

[130] V. Favier and C. A. Taylor, "Modeling Blood Flow in a Porcine Aorta Bypass Graft: Toward Physiological Conditions," *Center for Turbulence Research Annual Research Briefs*, pp. 219-230, 2001.

[131] J. G. Myers, J. A. Moore, M. Ojha, K. W. Johnston, and C. R. Ethier, "Factors Influencing Blood Flow Patterns in the Human Right Coronary Artery," *Annals of Biomedical Engineering*, vol. 29, no. 2, pp. 109-120, 2001.

[132] D. A. Steinman, "Image-Based Computational Fluid Dynamics Modeling in Realistic Arterial Geometries," *Annals of Biomedical Engineering*, vol. 30, no. 4, pp. 483-497, 2002.

[133] Y. Liu, Y. Lai, A. Nagaraj, B. Kane, A. Hamilton, R. Greene, D. D. McPherson, and K. B. Chandran, "Pulsatile Flow Simulation in Arterial Vascular Segments with Intravascular Ultrasound Images," *Medical Engineering & Physics*, vol. 23, no. 8, pp. 583-595, 2001.

[134] A. M. A. Khalifa and D. P. Giddens, "Characterization and Evolution of Post-Stenotic Flow Disturbances," *Journal of Biomechanics*, vol. 14, no. 5, pp. 279-296, 1981.

[135] M. M. Swindle and A. C. Smith, "Comparative Anatomy and Physiology of the Pig," *Scandinavian Journal of Laboratory Animal Science*, vol. 25, pp. 1-10, 1998.

[136] Personal communication with M. T. Draney via e-mail, Subject: Notes on pigs 1-3, 2003.

[137] "Pathology Report, Study Number 01-1965," Pathology Services, Department of Comparative Medicine, Stanford University, Stanford, CA May 11, 2001.

[138] K. L. Wedding, M. T. Draney, R. J. Herfkens, C. K. Zarins, C. A. Taylor, and N. J. Pelc, "Measurements of *In Vivo* Vessel Wall Motion and Strain with Cine Phase Contrast MRI," presented at International Society for Magnetic Resonance in Medicine 8th Scientific Meeting and Exhibition, Denver, CO, 2000.

[139] Millar Instruments, "Millar Mikro-Tip Catheter Pressure Transducer Instructions for Use" Houston, Texas: Millar Instruments, Inc.

[140] Meriam Instrument, "350 Smart Manometer Operating Instructions" Cleveland, Ohio: Meriam Instrument.

[141] M. H. Buonocore and H. Bogren, "Factors Influencing the Accuracy and Precision of Velocity-Encoded Phase Imaging," *Magnetic Resonance in Medicine*, vol. 26, no. 1, pp. 141-154, 1992.

[142] K. W. Moser, E. C. Kutter, J. G. Georgiadis, R. O. Buckius, H. D. Morris, and J. R. Torczynski, "Velocity Measurements of Flow through a Step Stenosis Using Magnetic Resonance Imaging," *Experiments in Fluids*, vol. 29, pp. 438-447, 2000.

[143] H. G. Bogren and M. H. Buonocore, "4D Magnetic Resonance Velocity Mapping of Blood Flow Patterns in the Aorta in Young vs. Elderly Normal Subjects," *Journal of Magnetic Resonance Imaging*, vol. 10, no. 5, pp. 861-869, 1999.